

Amrinder Pal Singh Dhillon

Evaluation of Strain Hardened Austenitic Corrosion Resistant Alloys' Susceptibility to Hydrogen Induced Stress Cracking (HISC)

Master's thesis in Materials science and engineering

Supervisor: Roy Johnsen

Co-supervisor: Xu Lu

July 2022

Amrinder Pal Singh Dhillon

Evaluation of Strain Hardened Austenitic Corrosion Resistant Alloys' Susceptibility to Hydrogen Induced Stress Cracking (HISC)

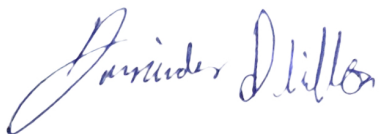
Master's thesis in Materials science and engineering
Supervisor: Roy Johnsen
Co-supervisor: Xu Lu
July 2022

Norwegian University of Science and Technology
Faculty of Engineering
Department of Mechanical and Industrial Engineering

Preface

This master thesis was written in accordance with the course TMM4960 and the two years masters program Materials science and engineering at the Norwegian University of Science and Technology (NTNU), Trondheim. This work has been conducted at the Department of Mechanical and Industrial Engineering, where professor Roy Johnsen has been the main supervisor together with postdoctoral researcher Xu Lu from NTNU and principal engineer Atle Qvale from Subsea Design as co-supervisors. The project was created by Equinor and Subsea Design in collaboration with NTNU and has been related to the topic of robust material selection for the energy sector.

I want to extend gratitude to Roy Johnsen, Xu Lu and Atle Qvale for assistance with experimental work, fruitful discussions and theoretical guidance. A sincere thank you is also extended to Cristian Torres Rodríguez for guidance within localized corrosion testing, hydrogen pre-charging procedure and other lab related difficulties I have encountered. In addition, credit to Pål Christian Skaret for assistance with tensile testing at the Department of Material Science and Engineering. Finally, I would like to thank my great friends Chido Nnoli and Ruben Gran Nykaas for their friendship and support through out my time in Trondheim.



Amrinder Pal Singh Dhillon

July 7, 2022, Trondheim

Date and location

Abstract

It has through the following work by the means of slow strain rate testing (SSRT) and stepwise constant loading (SCL) been carried out an investigation of four different strain hardened nickel alloys susceptibility to hydrogen induced stress cracking (HISC). The alloys in question have been a high strength and low strength version of P750 with ultimate tensile strengths of 1269 MPa and 979 MPa, respectively. In addition, the new austenitic versatile grades UNS N08034 (A31+) and UNS N08935 (Sanicro35) have been candidates of interest. The specimens have during in-situ hydrogen charging in both procedures been cathodically polarized simulating cathodic protection (CP) in seawater environment. Fracture surfaces of in-situ hydrogen charged specimens have been examined and compared to inert air tested specimens as a part of the overall evaluation. In addition, hydrogen measurements have been conducted.

According to results obtained from in-situ hydrogen charging in both SSRT and SCL, the influence of hydrogen embrittlement (HE) had a minimal effect on the yield strength and ultimate tensile strength of the alloys. In contrast, the ductility was notoriously affected for some of the alloy candidates. It was revealed that the high strength version of P750 exhibited a superior resistance against HISC with an average loss of 0.35% in fracture strain, hence maintaining 98% of the fracture strain obtained from testing in air environment. The alloy achieved the highest plastic elongation ratio of 95.98%. The A31+ did according to the fractography study suffered severe transgranular cracking combined with brittle flat facets in both edge and central areas of the fracture surface indicating high degree of HE. Despite the latter, the alloy suffered a relatively small loss in fracture strain of 1.7%, thus maintaining 91% of the fracture strain obtained from SSRT in air. The plastic elongation ratio was 88.59% indicating A31+ being another alloy with low susceptibility to HISC.

It has been the low strength version of P750 and Sanicro35 which relatively have suffered the greatest reductions in ductility with losses of 4.19% and 8.65%, followed by their respective plastic elongations of 79.10% and 60.73%. The Sanicro35 managed to maintain 65% of the fracture strain from SSRT in air, while low strength P750 managed to maintain 82%.

Sammendrag

Det har i dette arbeidet ved hjelp av slow strain rate testing (SSRT) og stepwise constant loading (SCL) blitt gjennomført en undersøkelse av fire forskjellige arbeidsherdede nikkellegeringer hvor deres respektive sensitivitet mot hydrogensprøhet har stått i fokus. To av legeringene i dette arbeidet har vært en høy styrke og lav styrke versjon av P750, hvor deres respektive bruddstyrker henholdsvis har vært 1269 MPa og 979 MPa. De relativt nye austenittiske og allsidige gradene UNS N08034 (A31+) og UNS N08935 (Sanicro35) har også vært kandidater av interesse i dette arbeidet. Prøvestykkene har under in-situ hydrogenlading i begge mekaniske prosedyrer blitt katodisk polarisert hvor katodisk beskyttelse i sjøvannsmiljø har blitt simulert. Bruddoverflater av in-situ hydrogenladede prøver har blitt undersøkt og sammenlignet med bruddflater av prøvestykker testet i inert luftmiljø som en del av den samlede evalueringen. Det har også gjennom dette arbeidet blitt gjennomført hydrogenmålinger.

I følge resultater oppnådd fra in-situ hydrogenlading i både SSRT og SCL, hadde påvirkningen av hydrogensprøhet en minimal effekt på flytspenningen og bruddstyrken til legeringene. Duktiliteten derimot har vært svært påvirket for noen av legeringene. Det fremkommer at høy-styrke versjonen av P750 besitter en overlegen motstand mot hydrogensprøhet utfra et gjennomsnittlig tap på 0.35% i bruddtøyning og følgelig opprettholder 98% av bruddtøyningen oppnådd fra testing i luftmiljø. Legeringen oppnådde det høyeste plastiske forlengelsesforholdet på 95.98%. A31+ opplevde i følge fraktografistudien alvorlig transgranulær sprekkdannelse kombinert med sprø flate fasetter i både kant- og sentrale områder av bruddoverflaten, indikasjoner på høy grad av hydrogensprøhet. Til tross for sistnevnte, led legeringen et relativt lite tap i bruddtøyning på 1.7%, og følgelig beholdt 91% av bruddtøyningen i luft fra SSRT. Det plastiske forlengelsesforholdet var på 88.59% og følgelig indikerer at A31+ også er en legering med lav sensitivitet mot hydrogen indusert sprekkdannelse.

Det har vært lav-styrke versjonen av P750 og Sanicro35 som relativt sett har opplevd de største reduksjonene i duktilitet med hver deres respektive tap på 4.19% og 8.65%, etterfulgt av deres respektive plastiske forlengelsesforhold på 79.10% og 60.73%. Sanicro35 klarte å opprettholde 65% av bruddtøyningen fra SSRT i luft, mens lavstyrke P750 klarte å opprettholde 82%.

List of Figures

1.1.1 Illustration describing the positioning of bridge alloys in terms of nickel content compared to traditional nickel alloy grades and stainless steel [1].	2
2.1.1 Evans diagrams with and without galvanic coupling [5].	5
2.1.2 Potential-pH and Evans diagrams.	6
2.1.3 Galvanic series for different alloys with saturated calomel electrode (SCE) as reference electrode.	6
2.2.1 Expected potential development from 2.2.1a) Anodic potentiodynamic polarization according to ASTM G61 and 2.2.1b) ASTM G48 Method C	8
2.3.1 Illustration showing the three main factors needed to initiate HISC [12].	9
2.3.2 Traditional microstructure to a PH nickel alloy with precipitates on 2.3.2a) grain boundaries and as dispersed phases in the nickel matrix and 2.3.2b) γ' as homogeneous distributed phases in the nickel matrix [16].	10
2.3.3 Results obtained by Qvale et al.[19] describing the effect of a decrease in potential resulting in fracture loss and intergranular cracking of UNS N07725.	12
2.3.4 Schematic presentation of defects in metal and accumulation of hydrogen atoms. Where a) trap sites for hydrogen in the surface, b) in the subsurface and c) lattice sites. At e) representing a edge dislocation hydrogen segregation is expected, d) being the grain boundaries and f) for vacancies [24].	14
2.3.5 Illustration of the HEDE mechanism where (i) atomic hydrogen is placed in lattice, (ii) atomic hydrogen being absorbed and located at the crack tip and (iii) hydrogen is absorbed at the particle-matrix interface [22].	16
2.3.6 Schematic illustration of the HELP mechanism including a microvoid coalescence process with plasticity localized and located in regions with high hydrogen concentration [22].	17
2.4.1 Illustration of experimental setup for hydrogen pre-charging [25].	18
2.4.2 Typical stress-strain behavior for SSRT carried out in air and during in-situ hydrogen charging [21].	19
2.4.3 Stress-strain behaviours as function of time for a smooth and notched sample of A830 from SCL-testing and CLV obtained by experimental work conducted by Heimseter [26].	20
2.7.1 Plastic Elongation ratio of model alloys in comparison to production heat of Alloy UNS N07718 [27].	23
2.7.2 %RA for different precipitations conditions of UNS N07718 [17]	24
2.7.3 HISC evaluation of UNS N07718 and UNS N07725 by Stenerud [28].	25

2.7.4 Relationship between %RA ratios and yield strength for selected PH and strain hardened nickel alloys [30].	27
2.7.5 Evaluation of A975 to HE susceptibility carried out by Chitwood et al. [31].	28
3.3.1 Machine drawings of test specimen for SCL-testing and SSRT.	31
3.3.2 Images showing the original pipe materials for the alloys with positioning of where sample extraction occurred.	32
3.3.3 Image of two milled and test ready specimens for HISC testing.	33
3.4.1 Specimen geometry for tensile testing.	34
3.5.1 Experimental setup of hydrogen pre-charging at 80°C	35
3.6.1 Experimental setup of SSRT in seawater environment simulating CP. . . .	36
3.6.2 Experimental setup of SSRT in air environment.	37
3.9.1 Images showing test samples from the alloys investigated. From left to right: P750-H.S, P750-L.S, A31, Sanicro35 and 25%Cr SDSS.	38
3.9.2 Illustration of experimental setup for ASTM G48 Method C [34].	39
3.10. Measurements of average diameter of cross section in SEM post fracture. .	40
4.1.1 Standard tensile testing of P750-H.S, P750-L.S, A31+ and Sanicro35 . . .	41
4.2.1 Stress-strain behaviour obtained from SSRT in air and in-situ hydrogen charging for P750-H.S, P750-L.S, A31+ and Sanicro35.	42
4.2.2 YS and FS from SSRT in air and from in-situ hydrogen charging.	44
4.2.3 %RA and fracture strain obtained from SSRT in air and in-situ hydrogen charging.	46
4.2.4 HE indicators obtained from SSRT describing degree of embrittlement and mechanical ductility loss for alloys investigated.	47
4.3.1 Stress-strain behaviour as a function of time obtained from SCL-testing during in-situ hydrogen charging for P750-H.S, P750-L.S, A31+ and Sanicro35.	48
4.3.2 %RA and fracture strain obtained from in-situ hydrogen charging in SCL.	49
4.5.1 Hydrogen uptake in P750-H.S, P750-L.S, A31+ and Sanicro35 post SCL-test.	50
4.6.1 Fracture surface overview of P750-H.S from SSRT in air environment. . . .	51
4.6.2 Fracture surface overview of P750-L.S from SSRT in air environment. . . .	52
4.6.3 Fracture surface overview of A31+ from SSRT in air environment.	53
4.6.4 Fracture surface overview of Sanicro35 from SSRT in air environment. . . .	54
4.6.5 Overview of fracture surfaces for P750-H.S from in-situ hydrogen charging in SSRT.	55
4.6.6 Overview of fracture surfaces for P750-L.S from in-situ hydrogen charging in SSRT.	56
4.6.7 Overview of fracture surfaces for A31+ from in-situ hydrogen charging in SSRT.	57
4.6.8 Overview of fracture surfaces for Sanicro35 from in-situ hydrogen charging in SSRT.	58
4.6.9 Overview of fracture surfaces for P750-H.S from in-situ hydrogen charging in SCL.	59
4.6.10 Overview of fracture surfaces for P750-L.S from in-situ hydrogen charging in SCL.	60
4.6.11 Overview of fracture surfaces for A31+ post in-situ hydrogen charging in SCL.	61
4.6.12 Overview of fracture surfaces for Sanicro35 from in-situ hydrogen charging in SCL.	62

4.6.13	Overview of secondary cracking for P750-H.S from in-situ hydrogen charging in SSRT.	63
4.6.14	Overview of secondary cracking for P750-H.S from in-situ hydrogen charging in SCL.	64
4.6.15	Overview of secondary cracking for P750-L.S from in-situ hydrogen charging in SSRT.	65
4.6.16	Overview of secondary cracking for P750-L.S from in-situ hydrogen charging in SCL.	67
4.6.17	Overview of secondary cracking for A31+ from in-situ hydrogen charging in SSRT.	69
4.6.18	Overview of secondary cracking for A31+ from in-situ hydrogen charging in SCL.	71
4.6.19	Overview of secondary cracking for Sanicro35 from in-situ hydrogen charging in SSRT.	73
4.6.20	Overview of secondary cracking for Sanicro35 from in-situ hydrogen charging in SCL.	75
4.7.1	Microscopical overview of P750-H.S.	77
4.7.2	Microscopical overview of P750-L.S.	78
4.7.3	Microscopical overview of A31+.	79
4.7.4	Microscopical overview of Sanicro35.	80
4.7.5	EDS evaluation of P750-H.S.	81
4.7.6	EDS evaluation of P750-L.S	82
4.7.7	Microstructure overview of A31+ obtained through SEM.	83
4.7.8	EDS evaluation of detected inclusion in A31+.	83
4.7.9	EDS evaluation of secondary phase detected in A31+.	84
4.7.10	EDS evaluation of Sanicro35.	84
4.7.11	EDS evaluation of 25%Cr SDSS.	85
4.8.1	Potential development and temperature increase as a function of time for alloys investigated by ASTM G48 Method C.	87
5.6.1	Correlation between CPT and PReN for alloys investigated.	95

List of Tables

- 2.1.1 Corrosion potentials for typical sacrificial anodes with reference to Ag/AgCl [6]. 7
- 2.7.1 Precipitation conditions of four different heats of UNS N07718 [27]. 22
- 2.7.2 Precipitation conditions and morphologies of UNS N07718 [17]. 23
- 2.7.3 Hydrogen measurements from hydrogen pre-charging study conducted by Burille et al.[21]. 26

- 3.2.1 Chemical composition in wt% for alloys investigated. 30
- 3.2.2 Chemical composition in wt% for alloys investigated. 30
- 3.2.3 Mechanical properties of alloys investigated in longitudinal direction at RT.
* = Grain size determined according to ASTM E112. 31

- 4.1.1 Key mechanical properties of alloys investigated obtained from tensile testing at RT. 42
- 4.2.1 Key mechanical properties for alloys investigated obtained from SSRT. . . . 43
- 4.2.2 An overview of mean cross section areas pre and post fracture, %RA and plastic elongation for each alloy sample used during SSRT. 45
- 4.2.3 HE indicators. 46
- 4.3.1 Initial and incremental loading values for each alloy during SCL. 47
- 4.3.2 An overview of key mechanical properties and %RA for alloys investigated obtained from SCL. 48
- 4.4.1 Comparison of key mechanical properties and %RA between SSRT and SCL for all four alloys. 50
- 4.7.1 Grain diameter and the corresponding ASTM grain size for the alloys investigated. 76
- 4.8.1 Overview of PREn for each alloy, weight difference and CPT achieved post ASTM G48 testing. 88

- 5.5.1 An overview of RARs, hydrogen uptakes and plastic elongations ratios for strain hardened and PH nickel alloys.* = Mean value. 94

- S1 Key values from EDS analysis on P750-H.S 135
- S2 Key values from EDS analysis of P750-L.S 135
- S3 Key values from EDS analysis of detected inclusion in the microstructure of A31. 135
- S4 Key values from EDS analysis of detected secondary phase in the microstructure of A31. 136
- S5 Key values from EDS analysis of Sanicro35. 136
- S6 Key values from EDS analysis of 25%Cr SDSS. 136

List of abbreviations

BCT	body centered tetragonal
BSE	Back Scattered Electrons
CLT	Constant load testing
CP	Cathodic protection
CPT	Critical pitting temperature
CRA	Corrosion resistant alloys
EAC	Environmental assisted cracking
EDS	Energy dispersive Spectroscopy
FCC	Face-centered cubic
FS	Fracture strength
HCP	hexagonal close-packed
HE	Hydrogen embrittlement
hede	Hydrogen Enhanced Decohesion
HEI	Hydrogen embrittlement index
HELP	Hydrogen Enhanced Local Plasticity
HER	Hydrogen evolution Reaction
HISC	Hydrogen induced stress cracking
OCP	open circuit potential
ORR	Oxygen reduction Reaction
PH	Precipitation hardened
PREn	Pitting resistance equivalent number.
RA	Reduction in area
RAR	Reduction in area ratio
RT	Room Temperature
SCE	Saturated calomel Electrode
SCL	Stepwise constant loading
SDSS	Super duplex stainless steel
SE	Secondary Electrons
SEM	Scanning electron Microscopy
SHE	Standard hydrogen Electrode
SSRT	Slow Strain rate testing
TEM	Transmission electron microscopy

List of nomenclature

D	Lattice diffusion coefficient
D_0	The pre-exponential factor for lattice diffusion
	plastic elongation
E	Potential
E^0	Standard reduction potential
E^{rev}	Reversible potential
E_{corr}	Corrosion potential
E_{pit}	Pitting potential
I	Current
I_{corr}	Corrosion current
J	Diffusion flux
R	Gas constant
	plastic elongation ratio
T	Temperature
γ''	Gamma double prime [-]
γ'	Gamma prime
i	Current density
$wt\%$	Weight percentage

Contents

Preface	I
Abstract	III
Sammendrag	V
Figures	VII
Tables	XI
Abbreviations	XIII
Nomenclature	XV
1 Introduction	1
1.1 Historical background and motivation	1
1.2 Research objectives and scope	2
1.3 Outline	3
2 Theory	4
2.1 Corrosion	4
2.1.1 Electrochemistry and thermodynamics	4
2.1.2 Cathodic protection	5
2.1.3 Localized corrosion	7
2.2 Localized corrosion testing	8
2.3 Hydrogen Induced Stress Cracking	8
2.3.1 HISC as a phenomena	8
2.3.2 Hydrogen entry and defect interaction	13
2.3.3 Diffusion of hydrogen	14
2.3.4 Hydrogen embrittlement mechanisms	15
2.4 Experimental methods for HISC study	17
2.4.1 Hydrogen pre-charging	17
2.4.2 Slow strain rate testing	18
2.4.3 Stepwise constant loading	19
2.5 HE indicators	20
2.6 Metallographic characterization	21
2.7 HISC in corrosion resistant alloys - A literature review	22
2.7.1 Precipitation hardened austenitic nickel alloys	22
2.7.2 Strain hardened austenitic nickel alloys	25

3	Experimental work	29
3.1	Chemicals and apparatus	29
3.2	Strain hardened austenitic Ni alloys	30
3.3	Test specimen for HISC testing	31
3.4	Tensile testing	33
3.5	Hydrogen pre-charging	34
3.6	Slow strain rate testing	35
3.6.1	Hydrogen charged samples	35
3.6.2	Air tested samples	36
3.7	Stepwise constant loading	37
3.8	Hydrogen measurements	38
3.9	Localized corrosion testing	38
3.9.1	Sample preparation	38
3.9.2	Experimental setup	38
3.10	SEM	39
3.10.1	Fractography	39
3.10.2	EDS	40
3.11	Microstructure imaging	40
4	Results	41
4.1	Tensile testing	41
4.2	Slow strain rate testing	42
4.3	Stepwise constant loading	47
4.4	Comparison of SSRT and SCL	49
4.5	Hydrogen uptake	50
4.6	Fractography	51
4.6.1	Air environment - SSRT	51
4.6.2	In-situ hydrogen charged	54
4.6.3	Secondary cracking	62
4.7	Microstructure evaluation	76
4.7.1	Microstructure overview	76
4.7.2	EDS analysis	80
4.8	Localized corrosion testing	85
5	Discussion	89
5.1	Sources of error	89
5.2	Slow strain rate testing	89
5.3	Stepwise constant loading	91
5.4	Fracture surfaces and secondary cracking	92
5.5	Comparison of strain hardened and PH grades.	93
5.6	Localized corrosion testing and characterization	94
6	Conclusion	96
7	Future work	98
	Bibliography	99
8	Appendix	103

Chapter 1

Introduction

1.1 Historical background and motivation

High strength precipitation hardened (PH) nickel alloys are widely used in subsea and downhole oil and gas applications for their excellent combination of mechanical properties, toughness and corrosion resistance in sour environments as well as traditionally being considered typical material selection for high pressure - high temperature services. However as strength increases and due to their microstructural features, these alloys may also become more susceptible to failure mechanisms associated with hydrogen absorption. In recent years resistance to Hydrogen Induced Stress Cracking (HISC) due to Hydrogen Embrittlement (HE) have become a research topic of increasing interest to the industry due to a number of reported failures of different high strength PH nickel alloy grades. According to investigations of several failures related to HISC, one of the main sources resulting in presence of atomic hydrogen have shown to be cathodic protection (CP) consisting of sacrificial anodes. The clear correlation between CP as the hydrogen source and the presence of precipitates as secondary phases in the nickel matrix and in the grain boundaries, have been established to be a crucial factor resulting in the increased susceptibility to HISC under tension loading.

As a result, a category of alloys classified as the "bridge alloys" are being considered as a potential substitution. A category consisting of alloys filling the gap between traditional stainless steel and high strength nickel alloys, Figure 1.1.1. The basis for this consideration are cost optimization due to the lower content of nickel, microstructure cleanliness and phase stability potentially increasing the HE resistance. Thereby, in recent times the focus have been shifted towards strain hardened nickel alloys being the focus alloys of this thesis work.

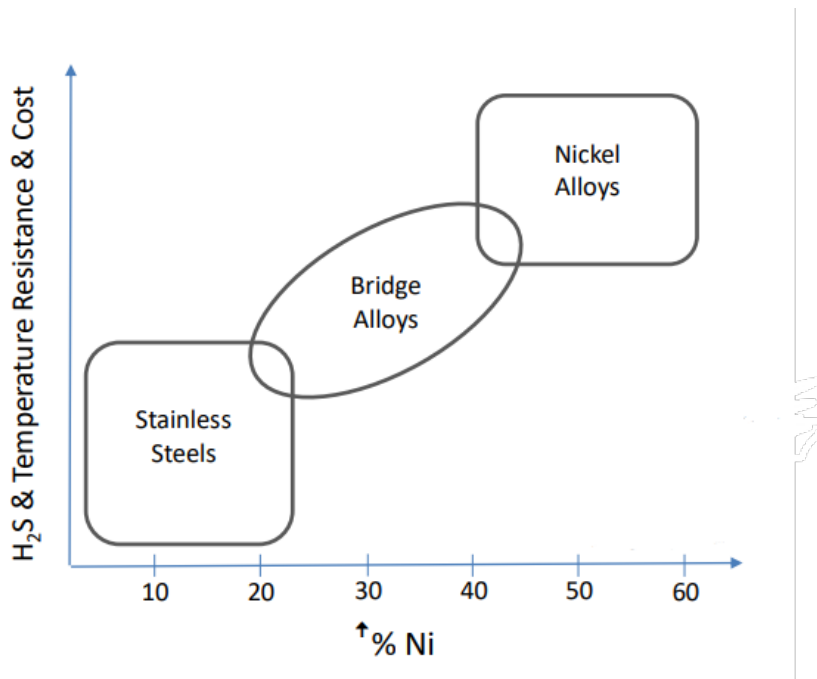


Figure 1.1.1: Illustration describing the positioning of bridge alloys in terms of nickel content compared to traditional nickel alloy grades and stainless steel [1].

1.2 Research objectives and scope

In recent years at NTNU in collaboration with both Subsea Design and Equinor, notable experimental work has been conducted on PH nickel alloys. Several interesting findings on how their different microscopical features subjected to HE are affecting the mechanical behaviour of these alloys, have been added to the overall data collection. However, during this thesis work the main objective would be to investigate the mechanical performance of high strength strain hardened austenitic nickel alloys with high microstructure cleanliness when cathodically polarized to $-1100 \text{ mV}_{Ag/AgCl}$ simulating CP in seawater environment. The different alloys susceptibility to HISC will be evaluated using slow strain rate testing (SSRT) and stepwise constant loading (SCL) followed by fractography to achieve an overview of secondary cracking and other microscopical HISC related characteristics. The alloys susceptibility to HISC will be rated in accordance with defined HE indicators. The microscopical examination conducted by the use of scanning electron microscopy (SEM) and energy dispersive spectroscopy (EDS) along with critical pitting temperatures (CPT) obtained according to ASTM G48 Method C from the specialization project during the fall semester have been included in this thesis.

1.3 Outline

- **Chapter 1:** Introduction describes historical background and motivation, main research objectives, scope of project and outline of the work.
- **Chapter 2:** Theory describes the fundamental concepts of HISC, HE, typical indicators used in literature to rate HE susceptibility, experimental methods used in HISC testing and methods used for microscopical examination. In addition, a literature review where results on both PH and strain hardened nickel alloys obtained by different authors are presented and discussed.
- **Chapter 3:** Experimental covers utilized equipment, chemicals, introduction of alloys in focus, processes of sample preparation for HISC and corrosion testing. Description of experimental methods carried out to investigate the mechanical performance of alloys in focus during in-situ hydrogen charging is also included.
- **Chapter 4:** Results provides the key correlations obtained from HISC testing and fractography study. Results from localized corrosion testing obtained in the specialization project have also been included.
- **Chapter 5:** Discussion of results and key correlations in regards to HISC susceptibility of alloys in focus. The results have been compared to literature.
- **Chapter 6:** Conclusion of the work and its significance.
- **Chapter 7:** Future works explores avenues for further research.
- **Chapter 8:** References presents literature used for theoretical background and context.
- **Chapter 9:** Appendix contains material certificates, material data sheets, risk assessments and quantitative overview of the EDS evaluation of each alloy sample.

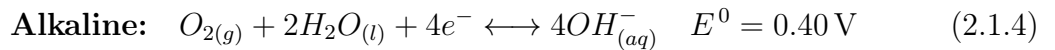
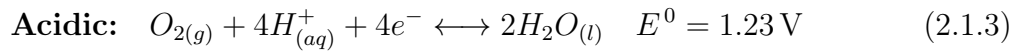
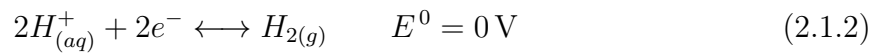
Chapter 2

Theory

2.1 Corrosion

2.1.1 Electrochemistry and thermodynamics

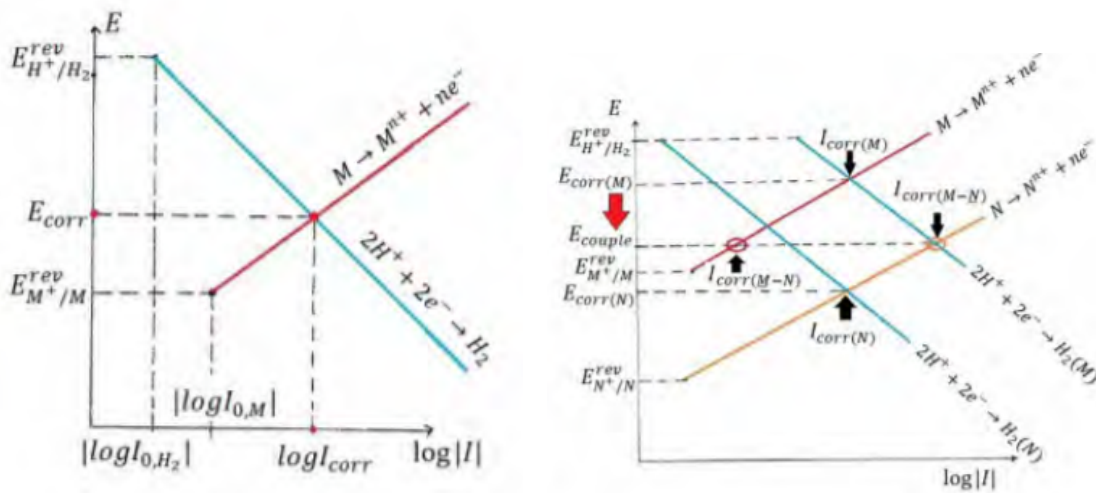
Corrosion is a degradation process of a metal as a result of charge transfer reactions occurring simultaneously on the metal surface. The scheme of electrochemical reactions would consist of oxidation of an arbitrary metal atom in the given alloy according to equation 2.1.1 where their associated reduction reactions such as hydrogen evolution reaction (HER) and oxygen reduction reaction (ORR) can occur, equations 2.1.2, 2.1.3, 2.1.4 respectively. Although, the given environment will impact both potential and pH which consequently would influence which reduction reaction that will be the dominating cathode reaction [2]. As described in 1.2, due to the scope and research objectives of this thesis the main focus would be on HER originating from a CP system consisting of sacrificial anodes.



The electrode potential is usually far from the reversible potentials for any of the reactions occurring on a metal surface [3, 2]. According to charge conservation and mixed potential theory, in order to avoid the accumulation of charge on a freely-immersed electrode the sum of all of oxidation currents must be equal to the sum of all of reduction currents [4]. Any electrode immersed in an electrolyte will naturally achieve a potential referred to as open circuit potential (OCP) or corrosion potential (E_{corr}), which fulfills this requirement. By comparing the E_{corr} to a metals calculated $E_{\text{electrode}}^{\text{rev}}$ the possibility of corrosion and corrosion rate can be assessed. In Figure 2.1.1a the red and blue line represents the anodic

reaction of the metal and HER, respectively. Both reactions are occurring on the metal surface and the corrosion rate is measured in current, consequently in current density as constant area is assumed. The intersection between the anodic and cathodic tafel curve represents the corrosion current (I_{corr}) and E_{corr}

In most cases within offshore design two metals with different degree of nobility are electrically connected creating a galvanic coupling. From a pure electrochemical standpoint this leads to a formation of four half-cell reactions, two on each metal surface. In such case, the potential gets stabilized at an E_{couple} as indicated with red arrow in Figure 2.1.1b. It appears that a decrease in potential from $E_{corr,M}$ to E_{couple} also results in a decrease in corrosion rate of the noble metal ($I_{corr,M}$). Consequently, this would lead to an increase in corrosion rate of the active metal ($I_{corr,N}$) in a coupling compared to the corrosion rate the same metal would experience without the coupling indicated by the orange circle. This described concept is the driving principle in galvanic corrosion [4, 3].

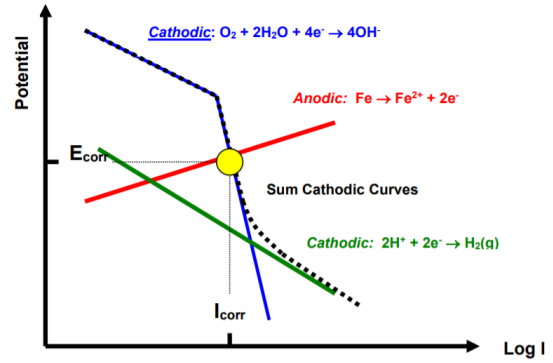
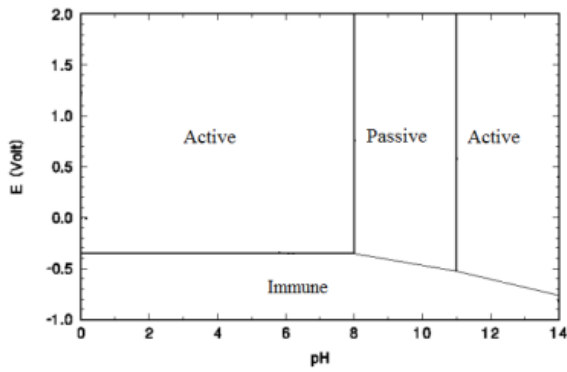


(a) Evans diagram for a single metal with HER as the dominating reduction reaction. (b) Evans diagram describing a galvanic coupling of two metals with their respective HER as the dominating reduction reactions.

Figure 2.1.1: Evans diagrams with and without galvanic coupling [5].

2.1.2 Cathodic protection

CP from sacrificial anodes is based on the principles of galvanic corrosion. The more active metal is connected to the noble metal which is intended to be protected. As the corrosion potential for a given alloy would appear in the active region in Figure 2.1.2a, a lowering of the potential from the the active into the immune region through reducing the corrosion rate by utilizing sacrificial anodes is by definition cathodic protection, Figure 2.1.2b [3].



(a) Potential-pH diagram for an arbitrary metal at 25°C. (b) Evans diagram for iron including ORR and HER as the cathodic reactions.

Figure 2.1.2: Potential-pH and Evans diagrams.

In order to reduce the potential into the immune region, installing sacrificial anodes with a potential more negative than the corrosion potential would be required. Typical industry practice in terms of material selection for anodes is zinc, aluminum or magnesium which would have their respective corrosion potentials.

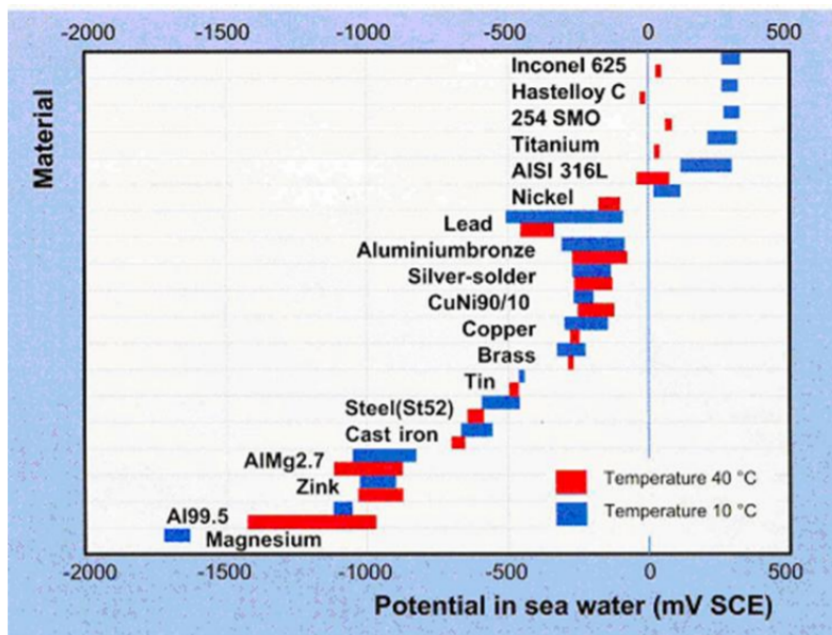


Figure 2.1.3: Galvanic series for different alloys with saturated calomel electrode (SCE) as reference electrode.

The proper protection of different engineering alloys is achieved when the chosen sacrificial anodes are able to cathodically polarize the given alloy past a certain protection threshold defined as protection potential (E_p). However, a careful material selection for anode material is essential. A polarized potential more negative than a range of -1050 to -1100 mV_{Ag/AgCl} can potentially contribute to HER becoming the dominating reduction reaction consequently leading to generation of hydrogen gas that can be absorbed into the metal. The high content of dissolved hydrogen in the alloy combined with an aggressive loadcase

consisting of tensile or residual stresses, failure due to HISC can be expected. This might be the case when using sacrificial anodes consisting of magnesium. According to Table 2.1.1, magnesium has more negative corrosion potential than zinc and aluminium hence making magnesium a more toxic alternative as CP purely in terms of hydrogen generation. Thus, making sacrificial anodes of zinc and aluminium the standard industry practice [6, 3]. A more tailored elaboration of CP resulting in HISC is provided in 2.3.1.

Table 2.1.1: Corrosion potentials for typical sacrificial anodes with reference to Ag/AgCl [6].

Material	Potential (mV vs Ag/AgCl)
Zn	-1050
Al	-1050
Mg	1600

2.1.3 Localized corrosion

Corrosion resistant alloys (CRAs) with their chemical composition are highly corrosion resistant due to their passive films consisting of oxide layers which forms naturally on the metal surface. However, such passive layers are susceptible to localized breakdown leading to an accelerated dissolution of the underlying alloy. Furthermore, if an attack initiates on an open surface it would be referred to as pitting corrosion while if on an occluded site then by definition crevice corrosion. For an initiation of pitting, a potential increase which exceeds a critical value defined as the pitting potential (E_{pit}) is required [7]. Typical pitting corrosion is caused by passive film breakdown due to the presence of aggressive anionic species, where chloride ions usually are the root cause. Parameters such as chemical composition of the alloy, temperature and surface conditions are to be considered as important factors as well [8].

Especially the concentrations of chromium and the molybdenum plays a vital role on maintaining the protective passive film hence the high resistance against pitting corrosion. Typical observed pattern of pitting attacks indicates that pits tend to initiate where some form of chemical or physical heterogeneity in form of inclusions, second phase particles, solute segregated grain boundaries or some form of mechanical damage exist on the sample surface [7, 9]. As majority of engineering alloys do contain all or many of such defects existing on the metal surface, it is expected that pits would tend to form at these defects being more susceptible sites [7, 10].

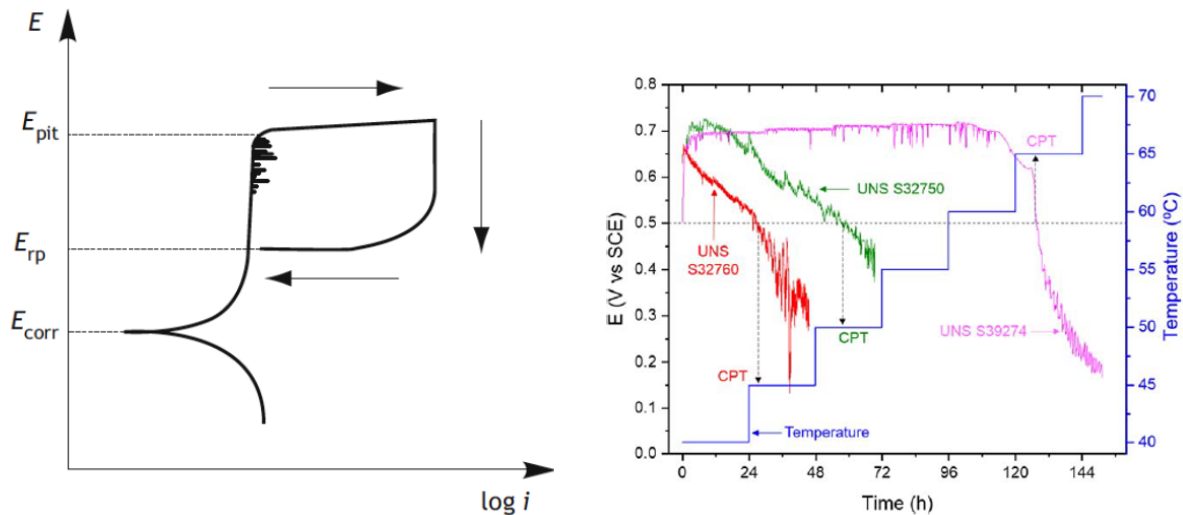
Similarly to metallurgy and alloy composition, temperature is an important parameter to be considered as many metals do not experience pitting below certain temperatures. This effect can be observed either by varying the temperature at a range of fixed applied potential or by varying the potential for a range of constant temperature experiments [10]. At higher temperatures, the pitting potential decreases with increasing temperature and chloride concentration. It is standard industry practice to determine the CPTs in order to rate the alloys susceptibility to pitting corrosion. In order to estimate the pitting index for steel alloys and assess the effects of chemical composition on pitting resistance, the pitting resistance equivalent number (PREn) can be calculated according to equation 2.1.5 [10]. Where the different components represents the mass fraction in percent of chromium, molybdenum and nitrogen. Although, PREn only gives a quantitatively estimate of the

resistance to localized corrosion.

$$PREn = \%Cr + 3.3 \cdot \%Mo + 16 \cdot \%N \quad (2.1.5)$$

2.2 Localized corrosion testing

Different test methods depending on parameters in focus can be conducted to assess a metal's susceptibility to localized corrosion. More specifically, in order to obtain important parameters such as the repassivation potential (E_{rp}), passive current density (i_{pass}), E_{corr} and E_{pit} cyclic potentiodynamic polarization according to ASTM G61 standard can be conducted. Whereas in order to determine CPT certain test methods according to ASTM G48 would be the viable options. The latter standard is used to determine both pitting and crevice resistance of CRAs in chloride containing environment by immersion in a 6% $FeCl_3$ solution. The standard is classified into six test methods based on how temperature adjustments are conducted during testing. The test can either be conducted by a fixed test temperature or adjusted in intervals. In Figure 2.2.1 typical potential development for both ASTM G61 and G48 Method C is illustrated.



(a) Typical polarization curve for an active-passive metal illustrating different regions of determination of corrosion-, pitting- and repassivation potential [10]. (b) Typical potential development and incremental temperature increase as a function of time for 25%Cr super duplex stainless steel (SDSS) alloys in 6% $FeCl_3$ [11].

Figure 2.2.1: Expected potential development from 2.2.1a) Anodic potentiodynamic polarization according to ASTM G61 and 2.2.1b) ASTM G48 Method C

2.3 Hydrogen Induced Stress Cracking

2.3.1 HISC as a phenomena

HISC in metal alloys is a form of HE occurring as a result of three main factors working together. This being a specific source the atomic hydrogen is originating from, the given alloys susceptibility to hydrogen and the material being exposed to a relatively rigorous

load case consisting of local stress and strain levels above the materials threshold, Figure 2.3.1. HISC has been a serious challenge for several alloys that initially have been viewed as the ideal material selection for typical oil and gas applications and consequently their respective offshore environments [12, 13]. As the three elements have to be in place simultaneously to initiate HISC, the path to determine the full overview of the causes resulting in HE can therefore be challenging. Especially the environment and material susceptibility for both PH and strain hardened nickel alloys, as the main drivers are to be described in detail in the following.

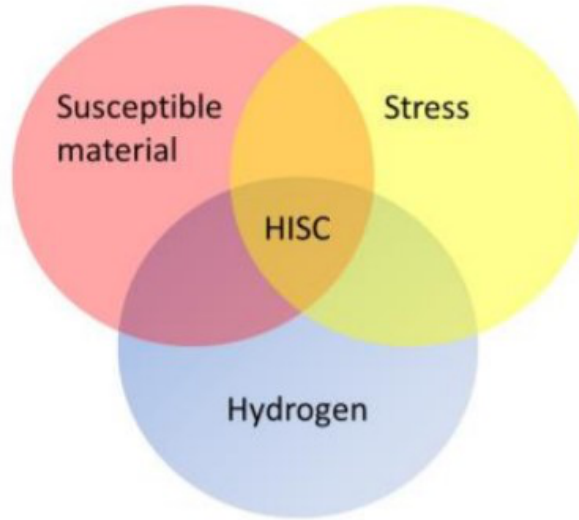
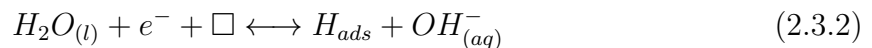


Figure 2.3.1: Illustration showing the three main factors needed to initiate HISC [12].

Environment

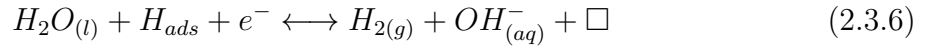
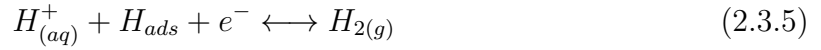
There can be several sources to generation of atomic hydrogen in an environment for a given alloy. For instant, this could be the welded zones of the material, processes for surface treatments involving acid use, coating processes and corrosion. When utilizing CP both ORR and HER becomes the possible reduction reactions, equations 2.3.1 and 2.3.2. During HER, formation of atomic hydrogen occurs according to equation 2.3.3 [12].



Where the hollow square represents a surface site available for hydrogen adsorption [14].

The formation of atomic hydrogen which occurs results in being adsorbed from the metal surface, but can recombine to hydrogen gas and get absorbed into the steel lattice. The

hydrogen produced undergoes a chemisorption step on the metal surface resulting in diffusion of hydrogen into the metal, equation 2.3.4. However, the hydrogen which do not absorbs into the steel lattice follow the adsorption process according to equations 2.3.5 and 2.3.6.



Material susceptibility in PH and strain hardened nickel alloys

The influence of both the microstructure and alloy elements on the materials behavior towards HE is of utmost importance. PH nickel alloys have different precipitates in the shape of phases existing on the grain boundaries and as their own dispersed phases in a high-nickel matrix integrated in the microstructure, Figure 2.3.2 [15, 16] . The precipitate gamma prime (γ') consist of $Ni_3(Al, Ti)$ with a face-centered cubic structure (FCC) in the nickel matrix and provides notable strengthening to the alloy. Both the particle size of γ' and the volume of γ' phase relative to the nickel matrix leads to an increase in mechanical strength and hardness of the alloy. The amount of γ' formed during processing is a function of alloy elements such as aluminum, titanium and niobium. Although, a supersaturation of Ti and Nb can lead to a transformation of γ' . Ti-rich metastable γ' can transform to the eta phase (η) consisting of Ni_3Ti with a hexagonal close-packed phase (HCP) structure. While excessive Nb leads to a transformation of γ' to γ'' and the η phase with a body centered tetragonal crystal (BCT) structure consisting of Ni_3Nb . Both γ' and γ'' would be present simultaneously at peak hardness [13].

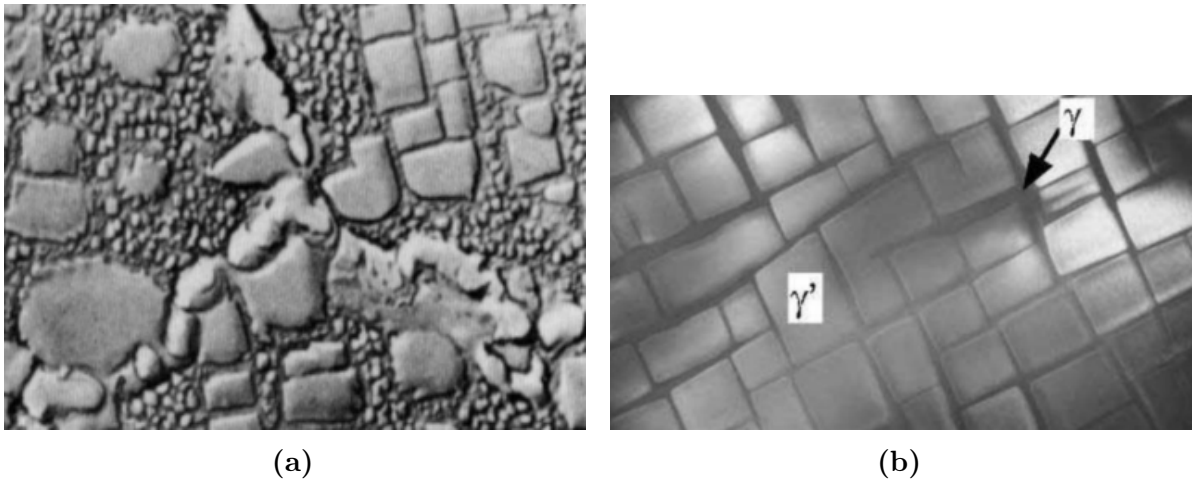


Figure 2.3.2: Traditional microstructure to a PH nickel alloy with precipitates on 2.3.2a) grain boundaries and as dispersed phases in the nickel matrix and 2.3.2b) γ' as homogeneous distributed phases in the nickel matrix [16].

It is widely accepted that the microstructure of these alloys plays an important role in their sensitivity to HE [13]. Several different conclusions have been reached on their susceptibility towards HISC, but one particular microscopical feature that has been quite common during microscopical examination is the grain boundary decoration, also known as grain boundary coverage. It is strongly being argued if the HISC sensitivity is related to carbide-matrix interfaces behaving as irreversible hydrogen trapping sites. Several authors have also pointed out the effect of the secondary strengthening phases γ' and γ'' and other grain boundary phases such as δ -, σ - and η -phase affecting the HE resistance. Furthermore, quite extensive work has been conducted particularly with PH nickel alloys such as UNS N07718, UNS 07725 and UNS N07716.

It was by Liu et al. [17] through a comparison of UNS N07718 with different precipitation conditions of the γ'' and δ -phase fabricated through different heat treatments, that both precipitates played a significant role in affecting the HE sensitivity of UNS N07718. A possible explanation for the increase in HE sensitivity due to the γ'' phase, would be that it has a higher lattice misfit resulting in higher trapping of hydrogen. It was shown that percent loss of reduction in area (RA) decreased with a decreasing fraction of γ'' . According to the experimental work carried out by Liu et al. [17], it appears that moving dislocations could transport more hydrogen to the δ /matrix interface, hence leading the micro-cracks to initiate at these sites due to the brittleness caused by the relatively large hydrogen accumulation. This results in a higher HISC sensitivity as these micro-cracks will merge and enhance the propagation of the primary crack. The fractography conducted reveals that local transgranular cleavages were initiated from the δ /matrix interfaces in the presence of pre-charged hydrogen. However, the actual interaction between trapped hydrogen in the grain boundary decoration and moving dislocations is still not fully understood. In addition, the contribution of the different microstructural elements is difficult to establish since as heat treatments are used to produce different microstructures and thus several parameters are simultaneously modified and no single effect can be studied properly [18, 13, 17].

While in the case of UNS N07725, an extensive root cause investigation of a subsea failure involving metallic seals revealed that the brittle nature of the fracture surface indicated environmental assisted cracking (EAC). Further investigation through experimental work conducted by Qvale et al. [19] led to discovering that the presence of full grain boundary decoration σ -phase assisted the crack initiation and propagation and reducing the overall fracture resistance of the alloy. In order to determine the effect of the interaction between atomic hydrogen and σ -phase on the mechanical performance of the alloy, a correlation between reduction in fracture load and in situ hydrogen charging in means of incremental step loading was obtained, Figure 2.3.3a. The correlation is clear, revealing that as the applied potential decreases the reduction in fracture load increases indicating that as the alloy is coupled to CP, the probability of HISC increases. The interaction between atomic hydrogen and σ /matrix interface is also being revealed in the fractography study showing intergranular cleavage in the fracture surface, Figures 2.3.3b

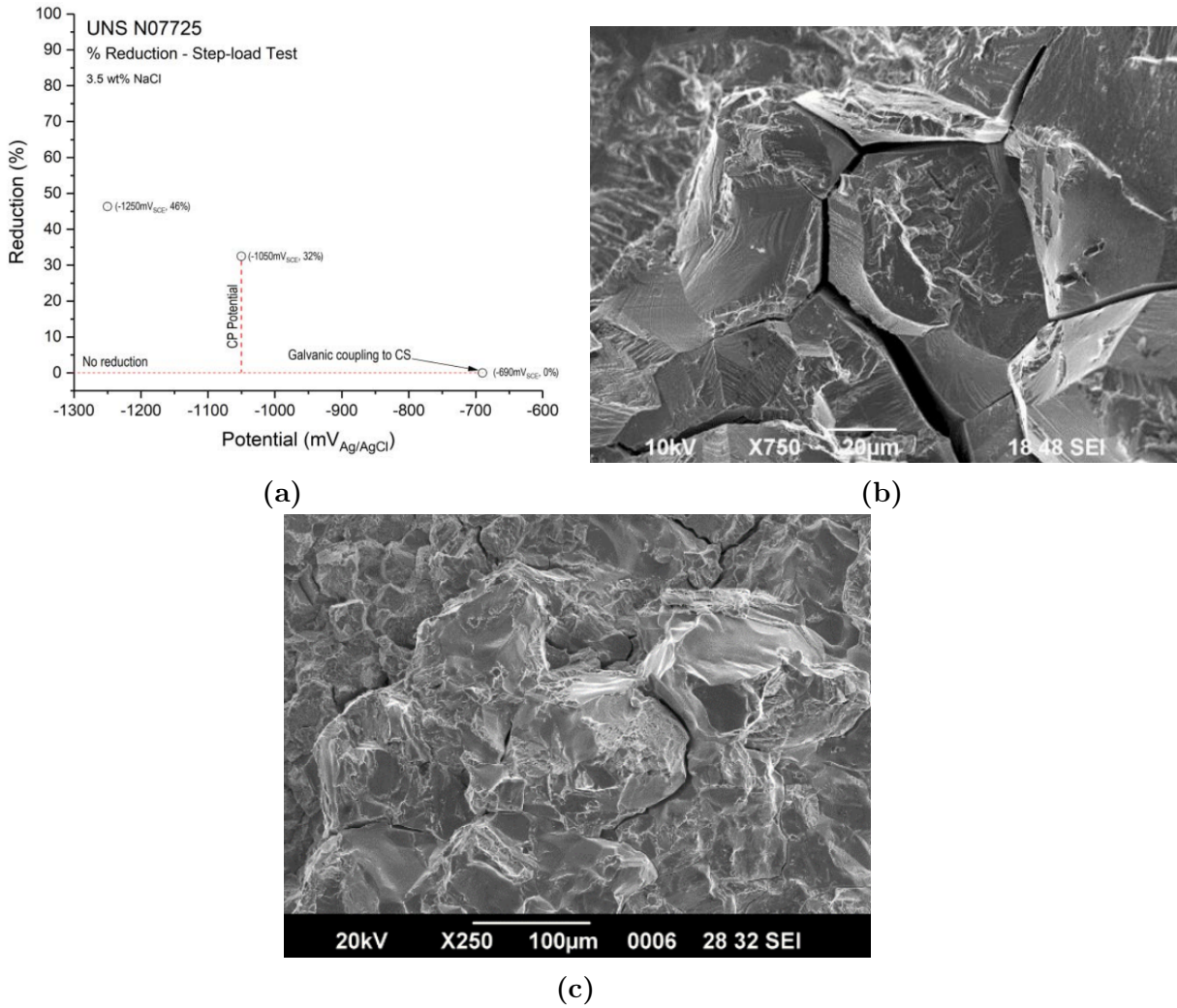


Figure 2.3.3: Results obtained by Qvale et al.[19] describing the effect of a decrease in potential resulting in fracture loss and intergranular cracking of UNS NO7725.

The strain hardened nickel alloys compared to PH due to the differences in their respective production methods, do not possess any precipitates on grain boundaries or any dispersed phases in the microstructure [16, 15]. The strain hardened nickel alloys are strengthened by the means of plastic deformation referred to as cold work. The strengthening through cold work is realized by developing an excessive amount of dislocations leading to an increase in dislocation density which disturbs further plasticity flow and motion of already existing dislocations. Defects such as grain boundaries would also contribute to hinder further dislocation movement [20]. As grain boundaries separates grains with different orientations, it leads to higher amount of energy required for the dislocations in motion to change to a different slip plane hence disturbing plasticity flow. More grain boundaries can be achieved through decreasing the grain diameter and consequently increasing the yield strength according to Hall–Petch equation, equation 2.3.7 [20, 15]. Typical production methods based on cold work are cold extrusion and cold rolling which are carried out at room temperature (RT).

$$\sigma_y = \sigma_0 + k_y \cdot d^{-\frac{1}{2}} \quad (2.3.7)$$

It has according to Burille et al. [21] been concluded that the relationship between the plastic deformation behaviour and HISC of the single phased strain-hardened UNS N08830 alloy is connected to the motion and mobility of dislocations transporting hydrogen. The experimental work conducted by the authors revealed that the specimens when in-situ hydrogen charged during SSRT experienced a lower fracture strain compared to when tested in an inert air environment. As the alloy is single-phased with high microstructure cleanliness, hydrogen enhanced localized plasticity (HELP) is being considered as the dominating HE mechanism.

From the above introduction it is clear that the microstructure of PH Ni alloys plays an important role in their sensitivity to HISC. More specifically, microscopical features such as the content of strengthening phases like γ'' and grain boundary decoration such as δ - and σ -phase. An overview of how different microscopical features in PH hardened and strain hardened nickel alloys interact with hydrogen and consequently affect their mechanical behavior has been provided in a literature review, section 2.7.

2.3.2 Hydrogen entry and defect interaction

Entry

The very first step of HE is the entrance of atomic hydrogen into the alloy, a process dependent on several parameters. The overall gas-solid interaction can although be described by three steps being the physisorption, chemisorption and absorption. Physisorption can be described as the physical bonding of gas molecules to the surface of a solid. The weak bonding is made at relatively low temperatures and does not involve any surface reaction. However, for the chemisorption step a chemical reaction between the surface atoms and the adsorbent molecules occur according to the reaction scheme described in the section 2.3.1. During absorption, the products of the chemisorption step is incorporated into the bulk lattice of the metal through diffusion [22].

Hydrogen interaction with defects in metal

- **Point defects**

The vacancy is arguably the simplest defect in metals consisting of a an available lattice site. Atomic hydrogen is strongly bound to this imperfection in most metals and the interaction has been investigated in depth for a long time. In regards to point defects the hydrogen atoms would have a choice between vacancy or interstitial placement [22].

- **Dislocations**

An understanding of the interactions between hydrogen and moving dislocations in metals is of considerable importance due to the influence of these effects on plastic flow and hydrogen mobility within the given material. The hydrogen is attached to dislocations and moves through the lattice structure as dislocation motion occurs during plastic deformation, where it can be trapped by different sort of traps. In regards to HISC, the hydrogen can be transported into the plastic zone in front a crack tip resulting in brittleness due to hydrogen accumulation[22, 23]

- **Hydrogen solubility and trapping**

In addition to typical vacancy takeover and interstitial placement in the lattice structure, the hydrogen can also be absorbed into other sites called reversible and irreversible traps.

These sites can be described as localized regions where hydrogen atoms experience a stronger attraction to instead of other lattice sites. In addition to the internal boundaries and moving dislocations, microstructures consisting of precipitates as their own dispersed phases in a matrix, inclusions or as secondary phase grain boundary decoration such as in PH nickel alloys, possess a strong ability to trap atomic hydrogen. Such trap ability would result in a delay the hydrogen transport. However, HE can still occur as the trapped hydrogen would start to decrease interatomic bond strength resulting hydrogen enhanced decohesion (HEDE) becoming the dominating HE mechanism, hence leading to an intergranular crack initiation, section 2.3.4. The given trap site is to be considered reversible when the atomic hydrogen manages to get unlocked from the traps. Typical reversible traps would be dislocations and vacancies. While, in irreversible traps the atomic hydrogen experiences higher resistance to detach from the trap site, hence higher trap energy is required. In addition, it can be argued that the increase in number of trapping sites leads to an increased hydrogen solubility in a material. The number of trap sites would tend to increase with applied stress due to formation of dislocations during plastic deformation [22, 23, 20].

A summary of hydrogen interaction with the different defects mentioned above can be described according by Figure 2.3.4

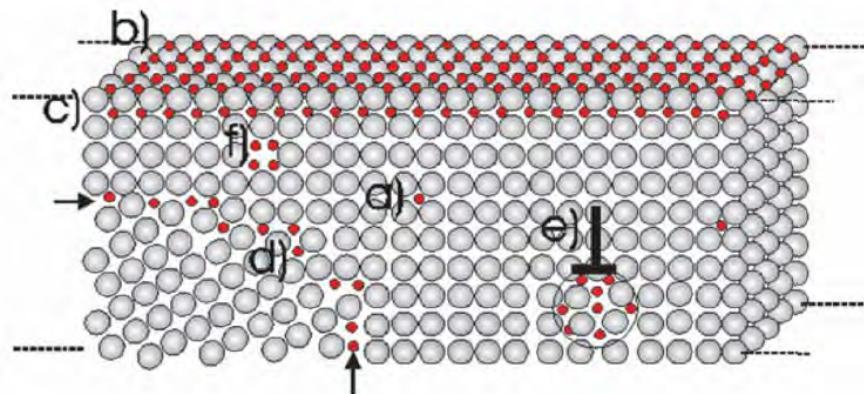


Figure 2.3.4: Schematic presentation of defects in metal and accumulation of hydrogen atoms. Where a) trap sites for hydrogen in the surface, b) in the subsurface and c) lattice sites. At e) representing a edge dislocation hydrogen segregation is expected, d) being the grain boundaries and f) for vacancies [24].

2.3.3 Diffusion of hydrogen

Diffusion can be described as random movement of particles due to concentration differences. When steady-state in regards to time is assumed, diffusion can be described according to Fick's first law, equation 2.3.8.

$$J = -D \frac{dC}{dx} \quad (2.3.8)$$

Where $\frac{dC}{dx}$ being the concentration gradient, C the concentration of the diffusion component, D the diffusion coefficient and J the diffusion flux.

A hydrogen atom is the smallest of all atoms thus resulting in atomic hydrogen having high mobility at room temperature. Although, the mobility of the atoms is affected by several parameters such as temperature, electrochemical conditions, microstructural and lattice features, the global and local stress-strain relationship hence plastic deformation. The main transport mechanism of hydrogen in steels resulting in the lattice diffusion is the interstitial jumping of the atoms, hence also making the crystal structure an important microstructural feature affecting the diffusion process. The BCC crystal structure allows a high diffusion rate and low solubility due to an open lattice structure. whereas, the austenitic FCC provides a low diffusion rate and high solubility due its relatively more packed lattice. If no defects in the metal is assumed the diffusion process can be described by Fick's second law, equation 2.3.9 [24, 20, 12]

$$\frac{\partial C}{\partial t} = D \frac{\partial^2 C}{\partial x^2} \quad (2.3.9)$$

Where C being the hydrogen concentration, t the time and x the distance of component diffused into the metal. D is the lattice diffusion coefficient defined according to equation 2.3.10

$$D = D_0 e^{-\frac{Q_a}{RT}} \quad (2.3.10)$$

Where Q_a is the activation energy, R the gas constant, T the temperature and D_0 the pre-exponential factor for the lattice diffusion.

2.3.4 Hydrogen embrittlement mechanisms

The mechanisms for hydrogen embrittlement has been widely discussed and has not yet been fully understood. There are several proposed mechanisms in the literature, where the most recognized are HELP and HEDE.

Hydrogen Enhanced Decohesion

As mentioned, the HEDE mechanism is believed to be a HE mechanism where atomic hydrogen at interstitial lattice sites reduces the interatomic bond strength at the crack tip. The decrease in the interatomic bond strength thus results in a decreased required energy to achieve fracture. The mechanism promotes a reduction of cohesive energy leading to a tensile separation of the atoms, Figure 2.3.5. The high localized concentration of hydrogen in the crack tip can also be assisted by the HELP mechanism through the hydrogen bearing dislocation pile up at grain boundaries resulting in grain boundary decohesion. The latter is especially unfortunate in the presence of secondary phase grain boundary coverage as the precipitate/matrix interface traps the atomic hydrogen [22, 24].

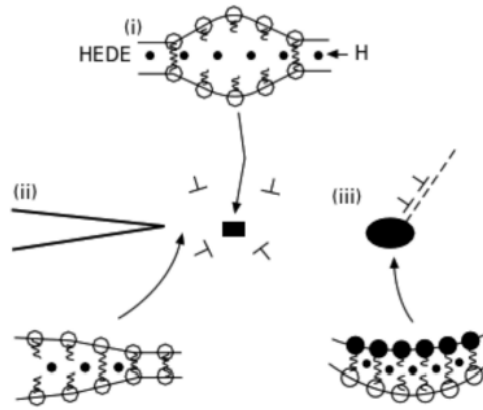


Figure 2.3.5: Illustration of the HEDE mechanism where (i) atomic hydrogen is placed in lattice, (ii) atomic hydrogen being absorbed and located at the crack tip and (iii) hydrogen is absorbed at the particle-matrix interface [22].

Hydrogen Enhanced Localized Plasticity

The HELP mechanism is believed to be based on the increased mobility of dislocations due to an elastic shielding effect. The hydrogen shields dislocation motion from interacting with other microstructural obstacles which can disturb plasticity flow, which as mentioned can be other dislocations, solute atom or grain boundaries. As the resistance to dislocation is reduced, the velocities of the dislocations are increased. The presence of hydrogen near a crack tip due to hydrostatic stresses increase the amount of dislocation motion in the region of the crack tip, Figure 2.3.6. Furthermore, the dislocation pileup leads to a localized softening of the material. Further crack growth is then to be expected as the softening leads to more localized microvoids coalescence compared to an air environment. As a result on a macroscopic scale, the fracture surface will appear brittle leaving a quasi cleavage clean facet consisting of the microcavities.

Investigations through in situ transmission electron microscopy (TEM) have revealed an increase in dislocation mobility in the presence of hydrogen. According to these observations, stationary dislocations gained motion and an increased velocity when hydrogen was introduced [22].

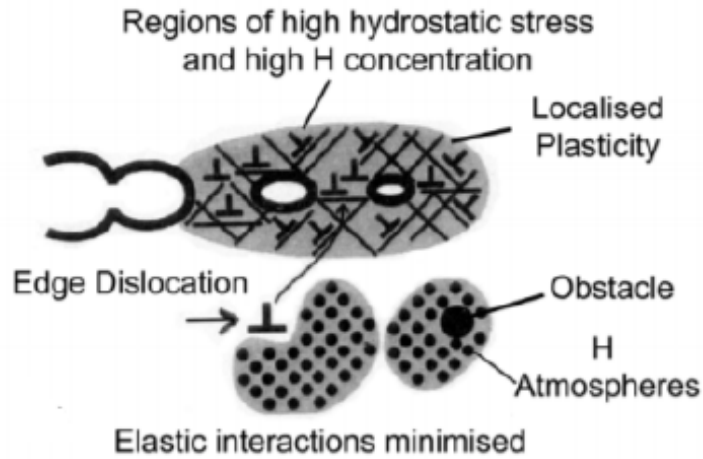


Figure 2.3.6: Schematic illustration of the HELP mechanism including a microvoid coalescence process with plasticity localized and located in regions with high hydrogen concentration [22].

2.4 Experimental methods for HISC study

2.4.1 Hydrogen pre-charging

In order to effectively evaluate the susceptibility of an alloy to HE, it is required to ensure sufficient amount of hydrogen in the microstructure during mechanical evaluation, hence hydrogen pre-charging traditionally being the first step in HISC examination [21]. This practice has also been performed by both Gjelseng [25] and Heimseter [26] during their respective experimental work related to their thesis at NTNU.

Heimseter [26] organized the experimental setup by placing several samples simultaneously in the glass autoclave with a temperature sensor, counter electrode and ion-bridge. The glass autoclave is by the ion-bridge connected to a separately positioned reference electrode. The separate positioning is in order to avoid any ion-membrane damage to occur due to the elevated temperature of the electrolyte. The pre-charging was conducted in 3.5 wt% NaCl solution at a temperature of 80°C for 7 days where Pt and Ag/AgCl was used as counter and reference electrodes, respectively. The setup is connected to a potentiostat which maintains a potential of $-1100 \text{ mV}_{Ag/AgCl}$ to ensure the formation of hydrogen on sample surface, Figure 2.4.1.

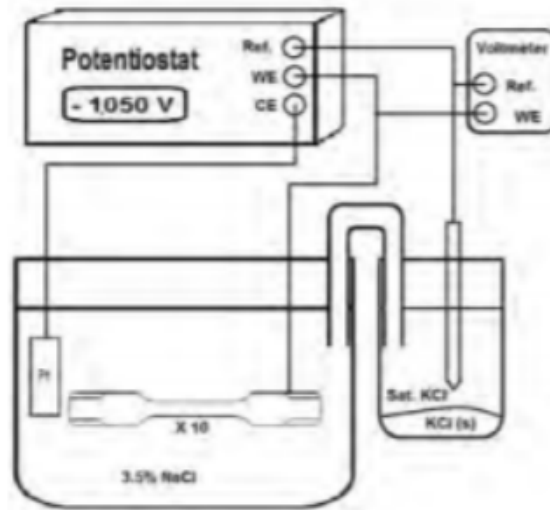


Figure 2.4.1: Illustration of experimental setup for hydrogen pre-charging [25].

2.4.2 Slow strain rate testing

SSRT is a test method where the main objective is to investigate the materials susceptibility to EAC. The method is performed by applying constant strain to the sample and parameters such as failure loading, temperature, elongation (%EL) and time can be measured. In order to assess the susceptibility to EAC the testing can be executed by simulating different environments. During the mechanical evaluation environments such as air, liquid environments (seawater, fresh water) and galvanic conditions (sacrificial anodes) are possible to simulate. Heimseter [26] performed SSRT while cathodically polarizing the samples to $-1100 \text{ mV}_{Ag/AgCl}$ in 3.5 wt% NaCl solution. During this work, the testing was carried out according to ASTM G129, NACE TM0198 and ASTM F1624 which covers the procedures for SSRT, specimen design and strain rate, respectively [26]. Typical stress-strain behaviour of metals in air and in-situ hydrogen charging during SSRT are illustrated in Figure 2.4.2.

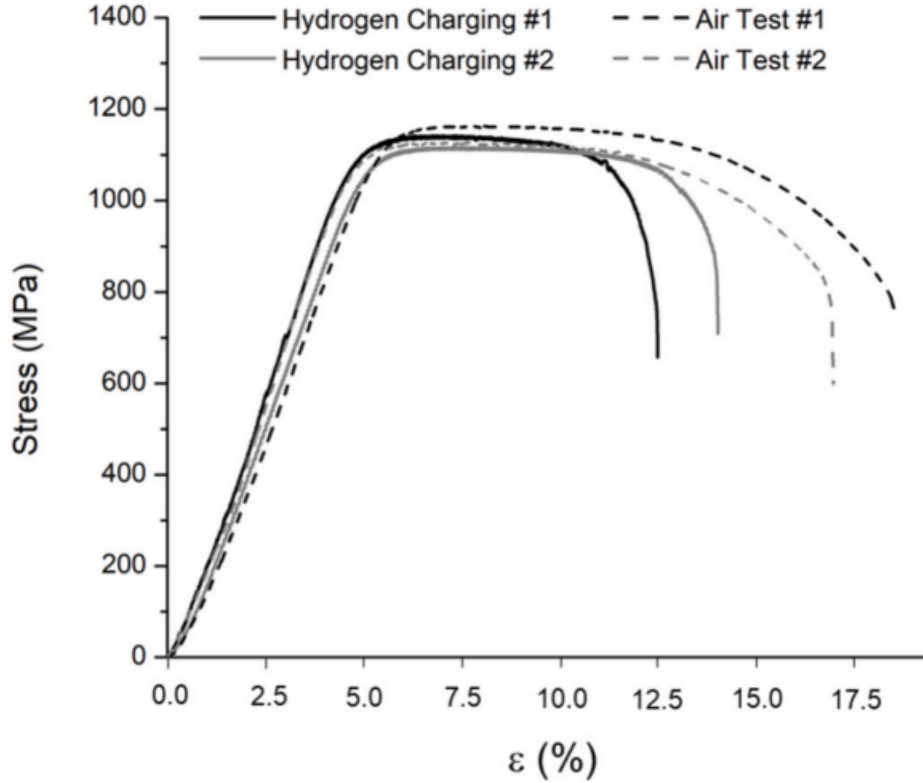
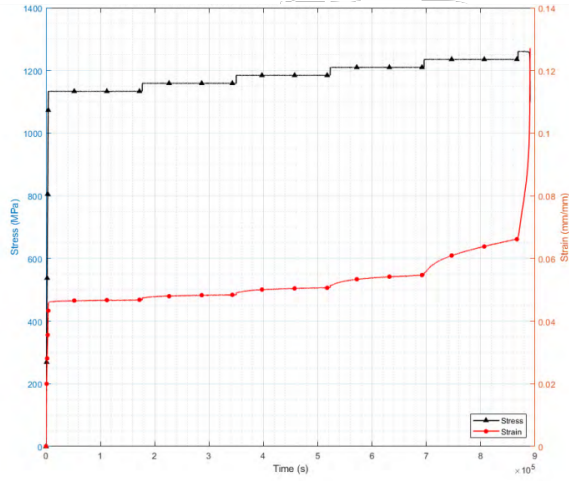


Figure 2.4.2: Typical stress-strain behavior for SSRT carried out in air and during in-situ hydrogen charging [21].

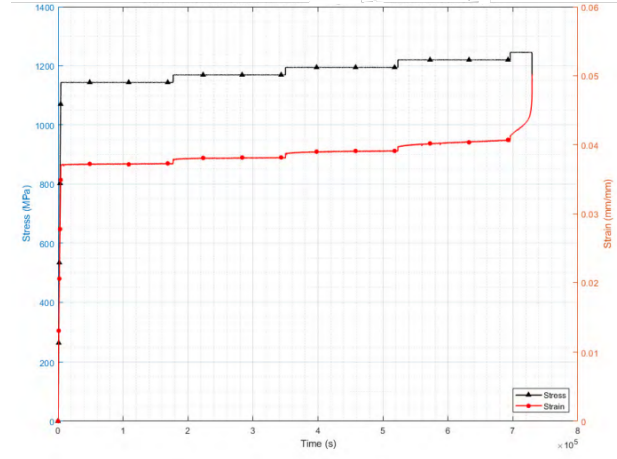
2.4.3 Stepwise constant loading

Constant load testing (CLT) is a testing method similar to SSRT in terms of assessing parameters such as failure loading, temperature, elongation and time period while investigating the susceptibility to EAC. Moreover, different procedures within CLT is developed over the past years. Extensive work on developing CLT have especially been carried out through joint industry project executed by SINTEF and Det Norske Veritas (DNV) [14]. The Cortest proof rings applied by Gjelseng [25], SCL and constant load verification (CLV) performed by Heimseter [26] are all methods based on similar intention of determining critical stress-strain levels while introducing EAC.

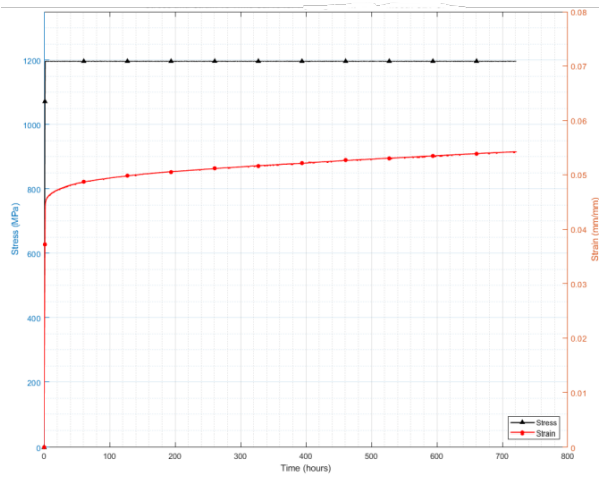
When utilizing the Cortest proof rings the sample is fastened to two metal rings and manually tightened to create a constant load on the sample. Moreover, in practice the test method introduces a challenge with creep. As a result, a difficulty with achieving a constant load on the sample can occur. The SCL procedure is executed by loading the sample to a predetermined % of the samples ultimate tensile strength (UTS) followed by maintaining the load for a set time period. The load is increased incrementally according to predetermined % of UTS. The process is continued until failure is achieved. CLV is carried out by applying a load which is predetermined % of UTS and maintained until failure occurs or when the testing is stopped. Variations in loading levels and test duration may vary. Typical stress-strain behavior as a function of time for both SCL and CLV test are illustrated in Figure 2.4.3.



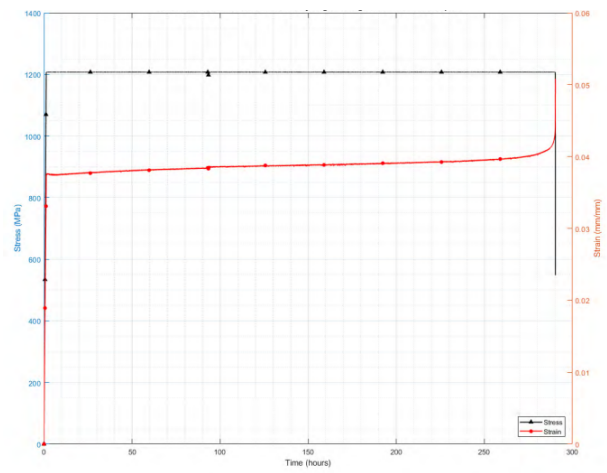
(a) SCL-testing of smooth sample



(b) SCL-testing of a notched sample.



(c) CLV of a smooth sample.



(d) CLV of a notched sample.

Figure 2.4.3: Stress-strain behaviours as function of time for a smooth and notched sample of A830 from SCL-testing and CLV obtained by experimental work conducted by Heimseter [26].

2.5 HE indicators

During this study certain indicators are used to determine the alloys susceptibility to HE, which are presented in the following.

RA is defined as reduction of the mean cross section area post failure, equation 2.5.1. As a ductile fracture leaves a fracture surface with relatively low cross section area due to necking, results in the understanding that high RA being interpreted as a ductile fracture being the case. In contrast, low RA indicating occurrence of a relatively more brittle fracture.

$$RA = \frac{A_0 - A_{min}}{A_0} \quad (2.5.1)$$

Where A_0 and A_{min} are the cross section areas pre and post testing, respectively.

The RA-values are further used to determine the RAR-values, an parameter traditionally used by several authors to determine the degree of HE embrittlement. The RAR-value includes the mean cross section areas of the gauge sections to specimens tested in inert air environment and in-situ hydrogen charging, equation 2.5.2.

$$RAR = \frac{RA_{Hyd}}{RA_{Air}} \quad (2.5.2)$$

Where RA_{Hyd} and RA_{Air} are the RA-values obtained from testing in air and in-situ hydrogen charging, respectively.

While RA-values and RAR-ratio quantitatively estimates the degree of HE embrittlement, other parameters such as hydrogen embrittlement index (HEI), plastic elongation ratio (RE,p) and fracture strain may be used to describe the effect of HE embrittlement on the mechanical performance, equations 2.5.3 and 2.5.4. HEI and RE,p have a opposite correlation. As the HEI increases, the less susceptible the alloy become to HE while an increase in RE,p would be interpreted as increased susceptibility to HE. During this study, the HEI-values have been calculated in accordance with ASTM G129. It was by Bothina et al. during the study on correlation of HE and microstructure of UNS N07718 defined a set threshold of 45% for elongation ratio between inert and aggressive environments. The criteria was used to measure resistance against HE for different heats of UNS N07718 with different precipitate conditions. Heats with elongation ratios higher than 45% were considered acceptable. On the other, Burille et al. measured the HEI of UNS N08830 with equation 2.5.5. The threshold set by Burille et al, was defined as an strain to fracture index (F(%)) lower than 50% indicated low vulnerability to HE.

$$HEI = \frac{E_{Plastic,air} - E_{Plastic,hyd}}{E_{Plastic,air}} \quad (2.5.3)$$

Where $E_{Plastic,air}$ and $E_{Plastic,hyd}$ are the plastic elongation values obtained from testing in air and in-situ hydrogen charging, respectively.

$$RE, p = \frac{E_{Plastic,hyd}}{E_{Plastic,air}} \quad (2.5.4)$$

Where $E_{Plastic,air}$ and $E_{Plastic,hyd}$ are the plastic elongation values obtained from testing in air and in-situ hydrogen charging, respectively.

$$F(\%) = \frac{\epsilon_{air} - \epsilon_{hyd}}{\epsilon_{air}} \quad (2.5.5)$$

Where ϵ_{air} and ϵ_{hyd} are the strain values obtained from testing in air and in-situ hydrogen charging, respectively.

2.6 Metallographic characterization

Scanning electron microscopy

SEM is an microscopical instrument which conducts digital imaging by the use of an intense electron beam targeted upon the surface of the sample which is being examined. The electrons are accelerated from a filament connected to a radiation source. As the beam interacts with the sample it scatters and various signals are being produced which in return gets recorded by different detectors. The different signals are secondary electrons (SE), backscatter electrons (BSE) and X-ray radiation and whereas each signal are being recorded by their respective detector. SEM provides information about chemical composition and a overview of surface topography.

Energy dispersive spectroscopy

EDS is an analytical technique in SEM used to determine the chemical composition of a sample. The sample is exposed to an intense electron current which in return emits characteristic X-rays that provides information about the chemical composition. The analysis is performed by the X-ray detector.

2.7 HISC in corrosion resistant alloys - A literature review

2.7.1 Precipitation hardened austenitic nickel alloys

Similarly to initially mentioned Liu et al.[17], Bothina et al.[27] carried out similar experimental work investigating how different fractions of γ' and γ'' in different heats of UNS N07718 altered the resistance against HE. The evaluation of susceptibility to HE was conducted by SSRT in accordance with NACE TM0198 where the aggressive environment consisted of 0.5M sulfuric acid solution while simulating CP. It was believed by the authors to use water as inert reference environment to achieve better temperature control compared to media such as air or glycerol. The precipitate condition of the four different heats were modified according to Table 2.7.1.

Table 2.7.1: Precipitation conditions of four different heats of UNS N07718 [27].

Heat	A	B	C	D
Fraction of γ' (%)	9.26	4	3.87	9.02
Fraction of γ'' (%)	8.5	0	11.7	4.34

One of the main HE indicators used during this study was an acceptance criterion of plastic elongation ratio being $\geq 45\%$, which was used to rate the HE resistance of the different heats. It appears from Figure 2.7.1 that higher volume fractions of γ'' precipitates and/or lower volume fractions of γ' precipitates were reported to have deleterious effects on the hydrogen embrittlement resistance [27].

It was concluded by the authors that the FCC γ'' phase was not responsible for the embrittlement of the model alloys, since heat with microstructure consisting of only this phase did not present any reduction in ductility after being strained during CP. The latter being the description of Heat B with an 101.8% plastic elongation ratio. In contrast, a dramatic reduction in ductility occurred for Heat C due to opposite fraction of the hardening phases combined with the presence of δ -phase decoration on the grain boundaries. The assumption of high gamma prime/gamma double prime ratio being a

factor to increasing HE resistance is also being confirmed according to Heat D reaching a plastic elongation ratio of 92.1%.

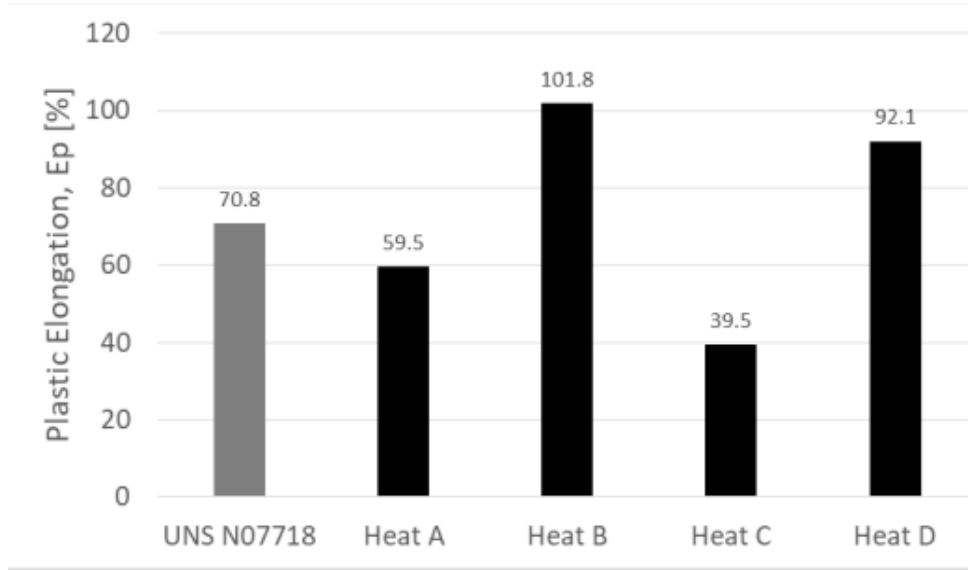


Figure 2.7.1: Plastic Elongation ratio of model alloys in comparison to production heat of Alloy UNS N07718 [27].

Especially the effect of grain boundary decoration by the δ -phase combined with modified composition of γ' and γ'' on HE sensitivity was further analyzed by the initially mentioned authors Liu et al.[17]. The investigation consisted of four different precipitation conditions provided in Table 2.7.2. The heats were divided in two different heat treatments where condition 1 was a δ -free aged specimen, condition 4 a conventionally aged specimen, condition 5 a delta free annealed alloy and the 6 a conventionally annealed alloy.

Table 2.7.2: Precipitation conditions and morphologies of UNS N07718 [17].

Precipitation condition	Precipitation morphology
1	γ' , free of δ and γ''
4	$\delta + \gamma'' + \gamma'$
5	free of δ , γ'' and γ'
6	$\gamma'' + \gamma'$, free of δ

It appears from the Figure 2.7.2 that the heat 1 and 5 with δ -free modified microstructures had much larger %RAs despite being hydrogen charged indicating low degree of embrittlement. Furthermore, in terms of loss in %RA the δ -free annealed alloy suffered a loss of 6.83% being relatively low compared to the conventionally annealed specimen which suffered a loss of 44.3%. The δ -free aged specimen experienced a loss of 29.41%, whereas the conventionally aged specimen with the relatively highest loss of 68.90%. It was from the results obtained concluded that the large decrease in HE sensitivity was due to the presence of δ -phase as grain boundary decoration. It was believed by the authors that the loss in %RAs for the delta free specimens was similarly to Bothina et al.[27] due to the γ'/γ'' -ratios [17].

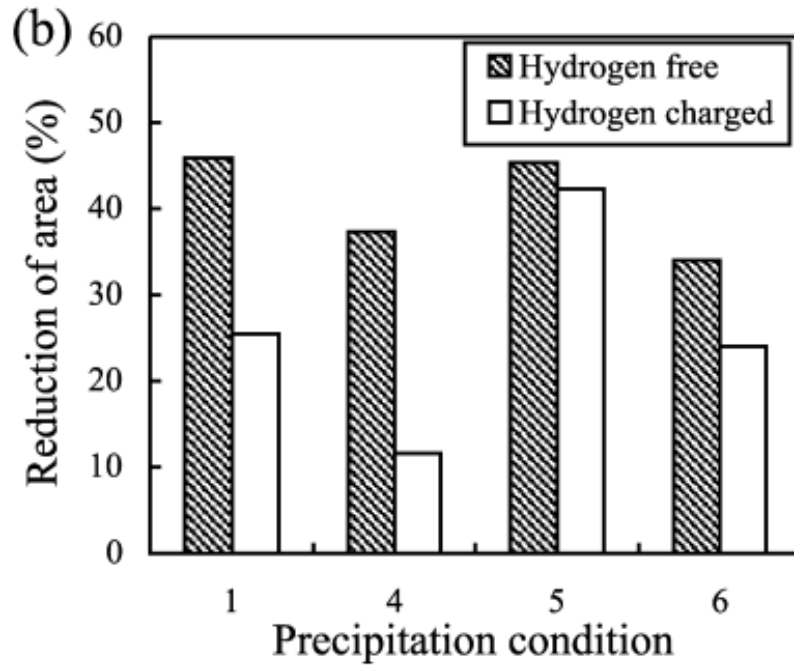
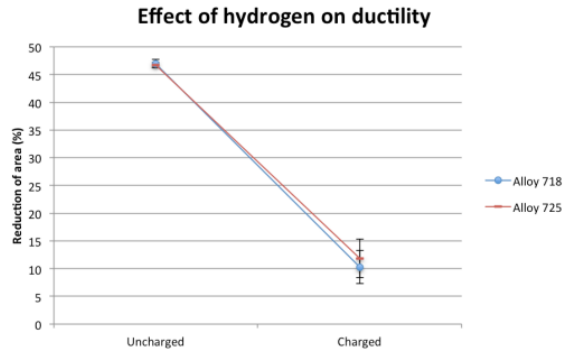
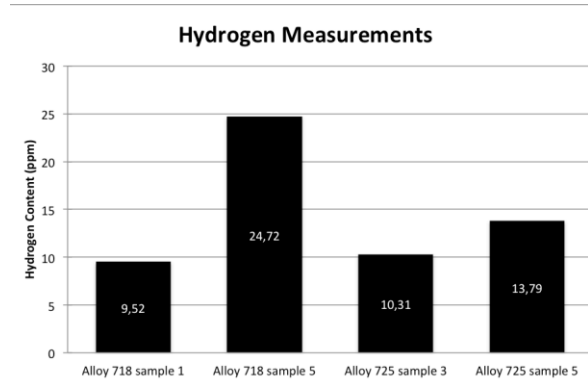


Figure 2.7.2: %RA for different precipitations conditions of UNS N07718 [17] .

The HE susceptibility of UNS N07718 and UNS N07725 was also investigated through incremental step loading and hydrogen uptake measurements by Stenerud [28]. During this study hydrogen charged samples of both alloys were exposed to tensile stresses with the main objective to establish critical stress levels for HISC initiation. It was also by Stenerud[28] similarly to both Liu et al. [17] and Bothina et al.[27] verified that UNS N07718 suffers a severe ductility loss when being subjected to HE, Figure 2.7.3a. It was concluded by Stenerud [28] that the strength of both alloys was reduced, although the ductility was reduced to a larger extent. The author obtained RAR-values of $78.08 \pm 6.13\%$ and $74.63 \pm 6.90\%$ for UNS N07718 and UNS N07725, respectively. According to the results obtained from incremental step loading combined with the UNS N07718 being the candidate with the highest hydrogen uptake from Figure 2.7.3b, the UNS N07725 alloy seemed be to relatively more resistant against HISC.



(a) A drop in %RA for UNS N07718 and UNS N07725 when subjected to HE through hydrogen charging compared to a reference environment.



(b) Roy hydrogen uptake

Figure 2.7.3: HISC evaluation of UNS N07718 and UNS N07725 by Stenerud [28].

However, as initially mentioned and similarly to UNS N07718 challenges with grain boundary decoration has also been the case for UNS N07725. It was concluded through the root cause investigation of a subsea failure involving metallic seals consisting of the latter alloy the presence of σ -phase was considered the causative factor for the observed embrittlement. During the study conducted by Qvale et al.[19] the UNS N07725 showed the highest susceptibility to HISC with a fracture load reduction of 49% when compared to baseline tested in air as reference environment. According to the fractography study, remnants of the σ -phase were found along the crack surface. It was concluded by the authors that more research was needed to understand the thermomechanical and heat treatment conditions which would lead to an optimal microstructure exhibiting an increased resistance against HE.

2.7.2 Strain hardened austenitic nickel alloys

The UNS N08830 alloy which initially was mentioned is a cold worked and single phased alloy which possess high strength and good toughness with a chemical composition resulting in high microstructural stability. The latter combined with high yield strength has led the alloy to become an ideal candidate for drilling tools operating under harsh oil and gas downhole environments capable of producing hydrogen [29, 30]. In addition, a cost saving is expected as the alloy possesses higher iron and reduced nickel content compared to the above mentioned PH nickel alloys. Since the relatively high price of nickel has been an influencing factor on final material selection within the energy sector, the development of such alloy has been desirable.

The investigation of UNS N08830 to HISC susceptibility was conducted by Burille et al.[21] by the means of SSRT with a strain rate $5.2 \cdot 10^{-8} s^{-1}$. As there is still some debate in the literature regarding time period for the hydrogen pre-charging procedure, the authors carried out a study experimenting with different time periods of 1,7 and 14 days followed by hydrogen concentration measurements. The specimens were charged by in H_2SO_4 0.5M water solution at 40 °C.

The hydrogen concentration was also measured for a sample which firstly was pre-charged

for 7 days followed by in-situ hydrogen charging in SSRT, thus compared to hydrogen concentrations of specimens which exclusively was pre-charged. It clearly appears from Table 2.7.3 that when comparing hydrogen pre-charging for 14 days to a total period of 15 days including the pre-charging procedure and SSRT, that hydrogen concentrations of 39 ± 11.8 and 56 ± 6.6 is reached, respectively. It is being believed by the authors that the increased value may be due to the effect of hydrogen transport by dislocations under strain during in-situ hydrogen charging. More specifically, when the hydrogen uptake occurs solely during the pre-charging procedure, diffusion becomes the dominating parameter controlling the mass transport to bulk of the material. However, it is believed that a mixed effect involving both diffusion and hydrogen transport thorough dislocation motion would be responsible for the flux of atomic hydrogen from the surface and further to the center of the specimen when strain is applied. According to the results obtained from SSRT, approximately similar YS and FS was achieved. In contrast, a clear reduction in ductility occurred for the in-situ charged specimens in comparison to the specimens tested in air resulting in F(%) and RAR of 25.3% and 42.1% respectively, indicating high resistance against HE.

Table 2.7.3: Hydrogen measurements from hydrogen pre-charging study conducted by Burille et al.[21].

Condition	Days	Hydrogen uptake (ppm)
Pre-charging	1	5 ± 0.2
Pre-charging	7	32 ± 5.2
Pre-charging	14	39 ± 11.8
Pre-charging + In-situ charging	15	56 ± 6.6

Similar work on UNS N08830 has also been carried out by Stefansson et.al [30] through SSRT. However, the pre-charging procedure was similar to Heimseter [26] described in section ??, and a higher strain rate of $1 \cdot 10^{-6} s^{-1}$ was used. The latter was only the case for specimens with rectangular cross section. During this study, susceptibility to HE of both smooth and notched specimens were investigated. It was revealed from SSRT that the ductility of notched samples were reduced by half compared to the smooth samples both in air and during in-situ hydrogen charging. The latter is due to the notch providing a pre-crack. However, it appears from the SSRT that the smooth specimen during this study compared to the results obtained by Burille et al.[21] had an RAR of 55.2% which also seem to have performed well. The authors calculated an elongation ratio of 85% which also has met the acceptance criterion defined by Bothina et al.[27]. An comparison of the RARs for UNS N08830 with different specimen geometries to UNS N07725 and UNS N07718 along with cold worked Alloy 625 have been provided in Figure 2.7.4. It appears that the PH nickel alloys have the lowest RARs, indicating highest degree of embrittlement and high sensitivity to HISC.

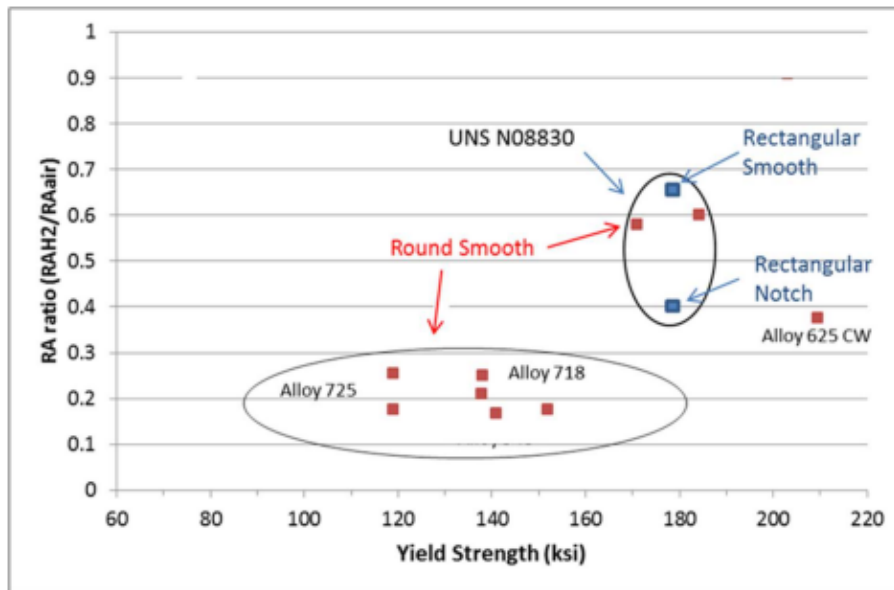
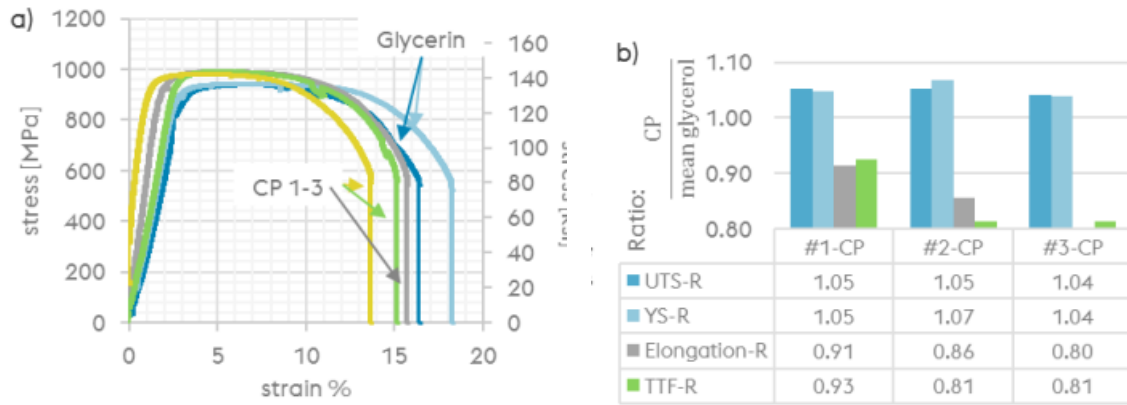


Figure 2.7.4: Relationship between %RA ratios and yield strength for selected PH and strain hardened nickel alloys [30].

In addition to UNS N08830, an increasing interest have also taken place for cold worked alloys such as A975 and UNS N07022 in terms of susceptibility to HISC.

The A975 alloy is a super austenitic stainless steel in CW condition which commonly has been used for drilling application due to the combination of high fatigue life and strength combined with the increased pitting resistance. By the experimental work carried out by Chitwood et al. [31], the susceptibility to HISC of A975 was investigated by the means of SSRT. The testing procedure were carried out in accordance with NACE TM0198. The results obtained from the experimental work carried out by the authors are provided in Figure 2.7.5. Two tests in glycerin has been used as reference when comparing to in-situ hydrogen charged specimens. In Figure 2.7.5b, key mechanical properties along with plastic elongation ratio and time to fracture ratio have been provided. In comparison to the uncharged specimens, all three tests conducted during in-situ hydrogen charging reveals an increase in YS and UTS ratios considering the CP and air environments, which may be due to hydrogen diffusion into the dislocation cores. The time to fracture and elongation ratios indicates that the alloy managed to maintain more than 80% of its ductility during in-situ hydrogen charging. It was concluded by the authors that the alloy possessed excellent resistance to HE.



(a) Stress-strain behavior of CW A975 obtained from SSRT in glycerin as reference environment and during in-situ hydrogen charging at 40 °C [31]. (b) Mechanical ratios comparing the uncharged and hydrogen charged specimens.

Figure 2.7.5: Evaluation of A975 to HE susceptibility carried out by Chitwood et al. [31].

UNS N07022 in CW condition is another strain hardened nickel alloy which has been considered as an ideal alloy candidate for the sour, aggressive and high pressure-high temperature environments in offshore oil and gas applications. Experimental work was carried out by Caron et al. [32] using SSRT with a strain rate of $1 \cdot 10^{-6} s^{-1}$ in both air and under CP, similarly to Stefansson et al. [30]. The authors used the ratio of fracture strains obtained from in-situ hydrogen charging and testing in air being $\geq 45\%$ for alloys to be considered as candidates with low HE susceptibility. The UNS N07022 achieved a ratio of 70% indicating that the alloy exhibited high resistance to HISC.

Chapter 3

Experimental work

3.1 Chemicals and apparatus

During the experimental work conducted in this study the following chemicals and equipment have been utilized.

Chemicals

- Iron(III)-chloride hexahydrate
- Hydrochloric acid
- Potassium chloride
- Ethanol (98% purity)
- Acetone

Equipment

- Struers-Unitom-Cutting machine
- Buehler MetaServ-250-Grinding machine
- Ivium-n-Stat potentiostat from Ivium Technologies
- VMP3 multichannel potentiostat from BioLogic Science Instruments
- SAM-50 precision channel logger from BioLogic Science Instruments
- SiC grinding paper from Struers
- Ultrasonic cleaner from VWR
- Heating element and temperature sensor from
- Pt wires
- Struers-LaboSystem-Grinding/polishing machine
- Polishing cloth of 1 and 3 μm from Struers
- SEM-QUANTA 650 FEG
- Ag/AgCl (saturated KCl) reference electrode
- Cormet C-176 SSRT Systems - Slow Strain Rate Test machine

3.2 Strain hardened austenitic Ni alloys

Four different strain hardened austenitic iron based nickel alloys have been provided by Schoeller-Bleckmann, Sandvik and VDM Metals. All four alloys have been strain hardened by the mentioned suppliers. The P750 alloys which during this work will be referred to as P750-L.S (P750 Low Strength) and P750-H.S (P750 High Strength) with their respective UTS of 979 MPa and 1269 MPa respectively, have been supplied by Schoeller-Bleckmann and fabricated through cold working. Both A31+ (UNS N08034) and Sanicro35 (UNS N08935) were supplied by VDM Metals and Sandvik, respectively. Sanicro35 were produced through cold work, whereas the A31+ through cold forging. In this thesis work, the 25%Cr SDSS (UNS S32750) alloy has been used as a comparable reference during localized corrosion testing and was provided by NTNU. The chemical composition in wt% of alloy elements for the materials investigated is provided in Tables 3.2.1 and 3.2.2. The tables are based on the alloys respective material certificates in Appendix A. Different data sheet for the alloys have been provided in Appendix B.

Table 3.2.1: Chemical composition in wt% for alloys investigated.

Alloy	UNS	Heat nr.	C	Mn	Cr	Ni	Mo	N	Fe
P750-H.S	Not applicable	Y11954	0.015	2.83	27.25	29.37	3.22	0.28	Balanced
P750-L.S	Not applicable	K10448	0.013	2.51	27.19	29.48	3.15	0.28	Balanced
A31+	UNS N08034	344059	0.004	2.04	26.50	34.00	6.58	0.23	Balanced
Sanicro35	UNS N08935	560812	<0.030	0.90	27.20	35.10	6.30	0.28	Balanced
25%Cr SDSS	UNS S32750	-	<0.030	<1.20	<26	<8	<5	<0.32	Balanced

Table 3.2.2: Chemical composition in wt% for alloys investigated.

Alloy	S	Si	Cu	P
P750-H.S	0.00	0.25	0.12	0.02
P750-L.S	0.00	0.33	0.00	0.02
A31+	<0.002	0.01	1.21	0.013
Sanicro35	<0.020	0.20	0.20	<0.030
25%Cr SDSS	0.02	0.80	50.00	0.04

Both P750-L.S and P750-H.S are austenitic Cr-Ni-N-steels with high pitting resistance while maintaining high mechanical strength for typical high pressure-high-temperature applications within oil and gas industry. The Sanicro35 is a Ni-Fe-Cr-Mo-N-steel combining features of a super austenitic stainless steel and a nickel alloy. The grade has high corrosion resistance due to the relatively higher molybdenum content for service in sea-water applications and other highly corrosive environments. A31+ is Ni-Fe-Cr-Mo-steel with high resistance against inter-crystalline corrosion where typical fields of application are chemical processes with aggressive sour environments. Mechanical properties in the longitudinal direction is obtained at RT and provided in Table 3.2.3 from Appendix Certificates. During the following sections the 0.2% offset YS will be referred to as YS.

Table 3.2.3: Mechanical properties of alloys investigated in longitudinal direction at RT.
 * = Grain size determined according to ASTM E112.

Alloy	0.2% offset YS (MPa)	UTS (MPa)	Elongation (%)	Hardness (BHN)	Grain size*
P750-H.S	1227	1268	17	380	3-4
P750-L.S	917	979	26	310	1-3
A31+	989	1082	24	300	-
Sanicro35	917	1067	29	310	-

3.3 Test specimen for HISC testing

Test specimen for HISC were prepared at the Department of Mechanical and Industrial Engineering at NTNU. The test samples were milled according to NACE TM0198 and from their each respective pipe material shown in Figures 3.3.1 and 3.3.2, respectively. For HISC testing a total of 7 samples from each alloy were milled, where a total of 4 were tested in SSRT, 1 for SCL and 2 used as back up samples in case of procedure errors during experimental work. The length and average diameter of the gauge sections did slightly deviate from the machine drawing in Figure 3.3.1. For the software procedure in SCL-testing and during SSRT, the length and the average diameter are important parameters which have to be inserted, hence was measured by the use of a digital caliper. The measurements were done of the marked areas described in Figure 3.3.3

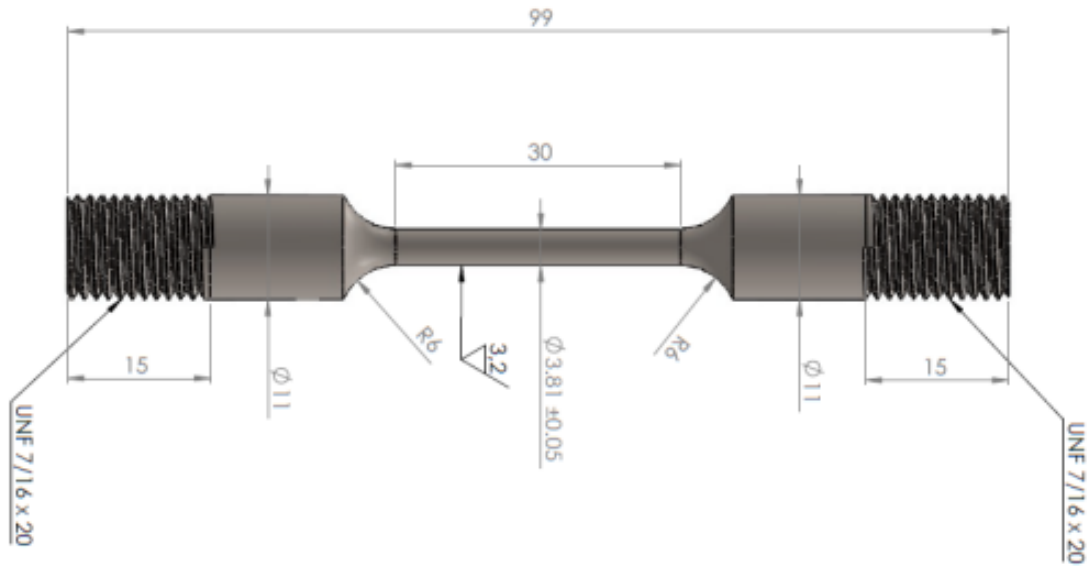


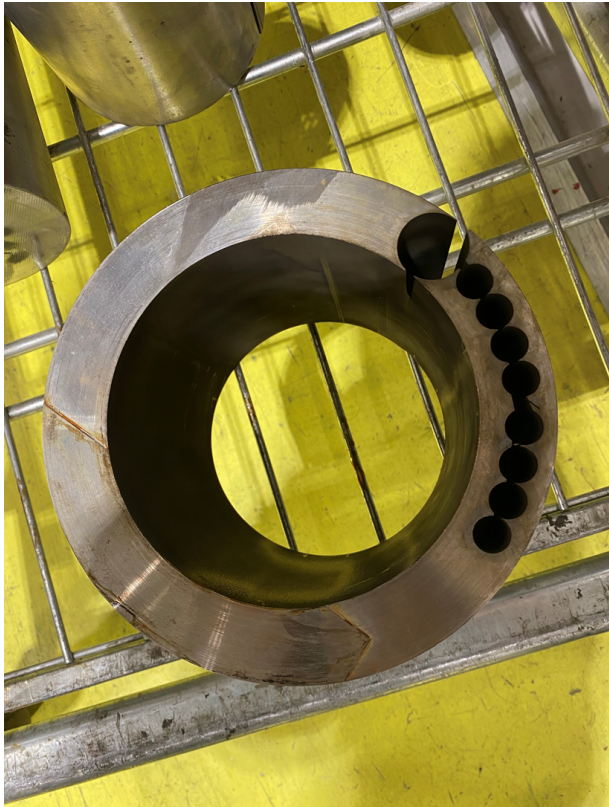
Figure 3.3.1: Machine drawings of test specimen for SCL-testing and SSRT.



(a) P750-H.S



(b) P750-L.S



(c) A31+



(d) Sanicro35

Figure 3.3.2: Images showing the original pipe materials for the alloys with positioning of where sample extraction occurred.



Figure 3.3.3: Image of two milled and test ready specimens for HISC testing.

3.4 Tensile testing

In order to determine the key mechanical properties of the alloys in focus, standard tensile test was conducted at the Department of Materials Science and Engineering, NTNU. The testing was carried out by the use of Walter and Bai Universal Test-machine with a loading capacity of 100 kN. The testing procedure allowed a strain rate of 2 mm/min at RT, where an extensometer of 25 mm was used to measure the elongation of the test specimen during test duration. Specifically for tensile testing only 1 sample from each alloy was milled and tested. Specimen for tensile testing is provided in Figure 3.4.1.

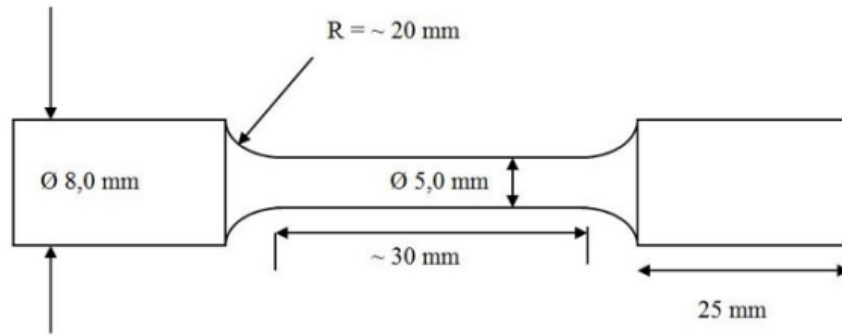


Figure 3.4.1: Specimen geometry for tensile testing.

3.5 Hydrogen pre-charging

In order to ensure the presence of hydrogen in the sample before SSRT and SCL-testing, hydrogen pre-charging was performed. The pre-charging procedure was conducted by cathodically polarizing the samples to $-1100 \text{ mV}_{Ag/AgCl}$ at a temperature of $80 \text{ }^\circ\text{C}$ for 7 days in 3.5% NaCl solution. Before immersing the samples into the electrolyte, their gauge sections were lightly grinded with P1000 grinding paper followed by cleaning with distilled water and 1 minute of ultrasonic ethanol bath. The samples were fitted with copper wires to ensure electrical contact and fastened by heat shrinking tubing. The intention with the latter was also to reduce area exposed to the electrolyte in order to achieve more concentrated effects of HISC in the gauge sections of samples during mechanical evaluation, Figure 3.5.1b.

During this project, multiple samples from the different alloys have been pre-charged simultaneously. The experimental setup has been consisting of the respective samples placed in the glass autoclave with an Pt counter electrode, temperature sensor and the ion-bridge connecting the separately positioned reference electrode Ag/AgCl, Figure 3.5.1. The reference electrode was immersed in KCl solution. The latter solution was prepared by dissolving KCl (170 g) in distilled water (500 mL). The separate positioning of the reference electrode is to avoid potential damage to the ion membrane of the reference electrode due to the elevated temperature. The content of the glass autoclave was connected to a potentiostat which contributed to the cathodic polarization to $-1100 \text{ mV}_{Ag/AgCl}$ ensuring the presence of hydrogen in the samples. The procedure was inspected everyday during the procedure run in case of removal of air bubbles accumulated in the ion bridge. After a complete pre-charging, the samples were taken out of the glass autoclave where the tubing was removed before being rinsed with distilled water and ethanol. The samples were stored in a freezer with a temperature of -20°C to eliminate the diffusion rate of hydrogen out of the charged samples.

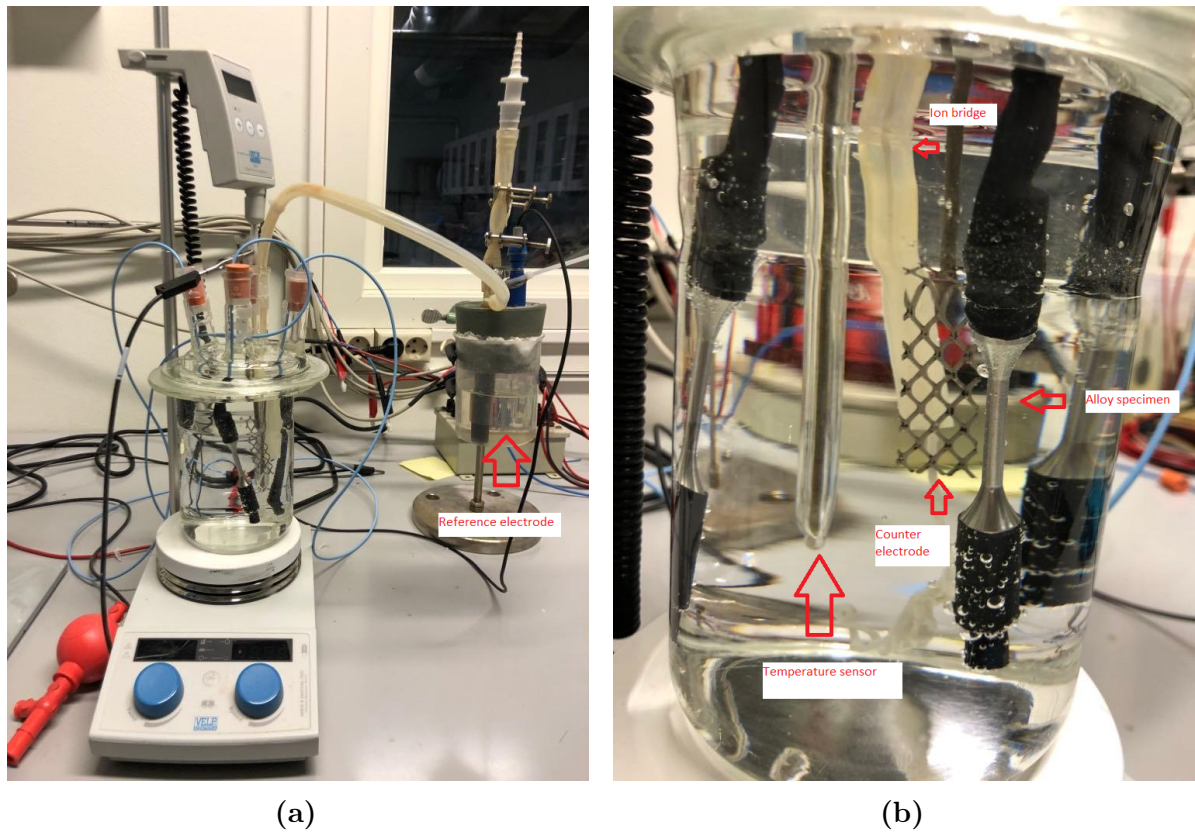


Figure 3.5.1: Experimental setup of hydrogen pre-charging at 80°C

3.6 Slow strain rate testing

SSRT was executed with main aim to assess the mechanical behaviour of the alloys in focus with respect to EAC. The different environments that have been simulated during testing is a seawater and an inert air environment. The samples tested in the air environment have during this work been used as the comparable baseline. Testing in seawater environment consisted of the alloy sample being immersed in 3.5% NaCl electrolyte while conducting a cathodic polarization to $-1100 \text{ mV}_{Ag/AgCl}$ in order to simulate CP. The mechanical evaluation was executed using a Cornet C-176 SSRT Test-machine. The test machine are connected to logging tools which transfer recorded data during test duration to a computer to be processed. Independent of if SSRT or SCL are to be performed, necessary inputs such as a mean cross section area of the gauge section to the alloy sample, length of the gauge section, initial strain rate, load limits, elongations limits and recording intervals have to be added. The initial strain rate used for every alloy sample during SSRT was $1 \cdot 10^{-6} \text{ s}^{-1}$.

3.6.1 Hydrogen charged samples

In terms of sample preparation for SSRT with seawater environment, a complete hydrogen pre-charging, removal of heat shrink tubing and further cleaning with distilled water and ethanol have been necessary. The mean diameter and length of the gauge section to the sample was measured using a caliper followed by being connected to a potentiostat as the working electrode alongside with Ag/AgCl and Pt as reference and counter electrodes,

respectively. The glass container is then closed and filled with 3.5% NaCl through the funnel. The complete setup is then left for 1 hour for the alloy sample to reach RT and to ensure a stabilized potential of $-1100 \text{ mV}_{Ag/AgCl}$, Figure 3.6.1. Test parameters such as the mean diameter and length of the gauge section followed by a calculated cross section area are inserted. The sample is subjected to a small force of 20-50 newtons pre logging. Both the displacement and force are zeroed by determining a start position before the logging starts. During test duration both the potential against Ag/AgCl and force applied according to the movement controller are inspected daily. As failure was achieved, the fractured sample parts were taken out of the container and cleaned with distilled water and ethanol. In order to decrease the hydrogen diffusion rate out of the sample, both parts were placed in a freezer with a temperature of -20°C for later microscopical investigation in SEM.

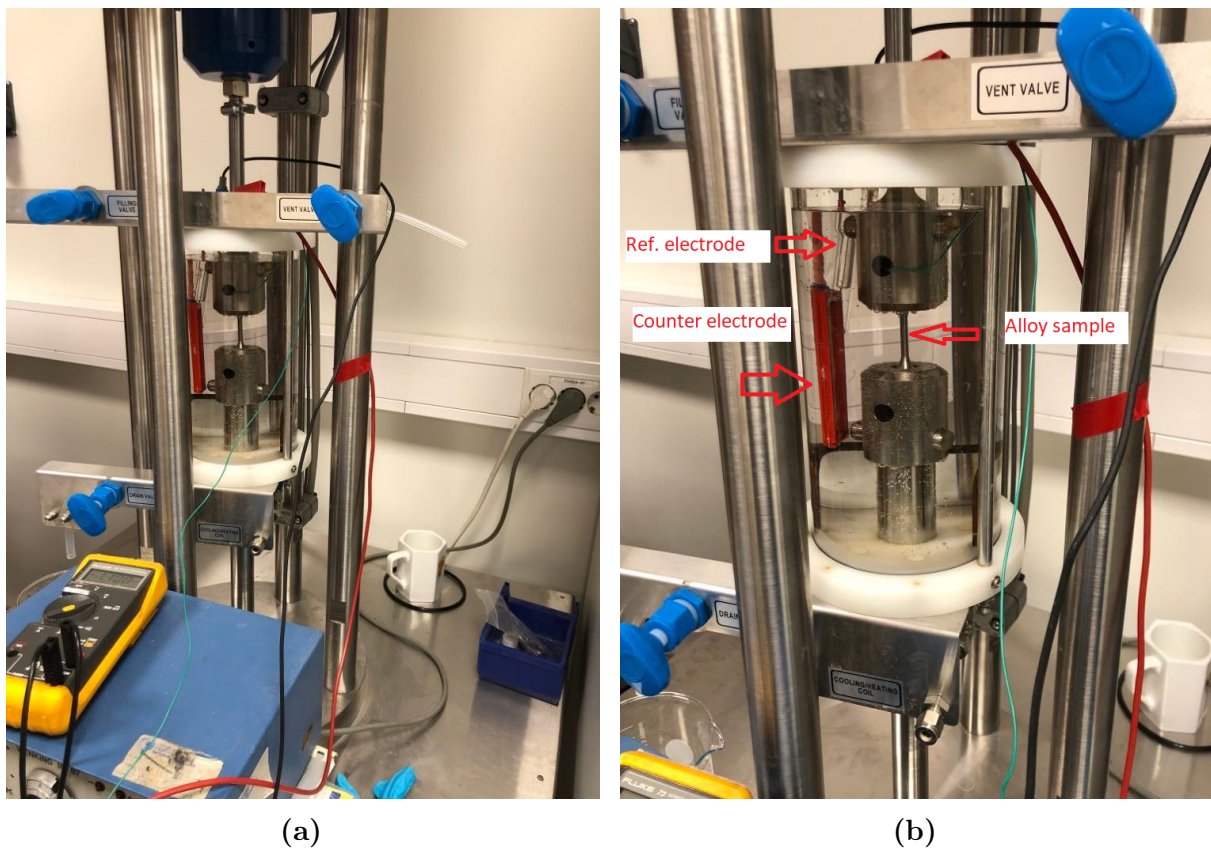


Figure 3.6.1: Experimental setup of SSRT in seawater environment simulating CP.

3.6.2 Air tested samples

In order to produce the comparable baseline, alloy samples with similar specimen geometry have been tested in an air environment. Before the experimental setup, the given alloy sample was prepared by light grinding of the gauge section using SiC paper with a roughness grade P1000 followed by cleaning with distilled water and ethanol. Measurements of the gauge section in terms of mean diameter and length was done using a caliper and inputted in the SSRT software. Both the software procedure and the mechanical fastening of the alloy sample are similar to the hydrogen charged samples. However, the experimental setup do not involve the glass container with the electrolyte and other electrodes, Figure 3.6.2. After the fastening, a force of 20-50 newtons is applied pre logging. Both the displacement

and force are zeroed by determining a start position before the logging starts. As failure occurred, the fractured sample was taken out and stored in a plastic bag at RT.

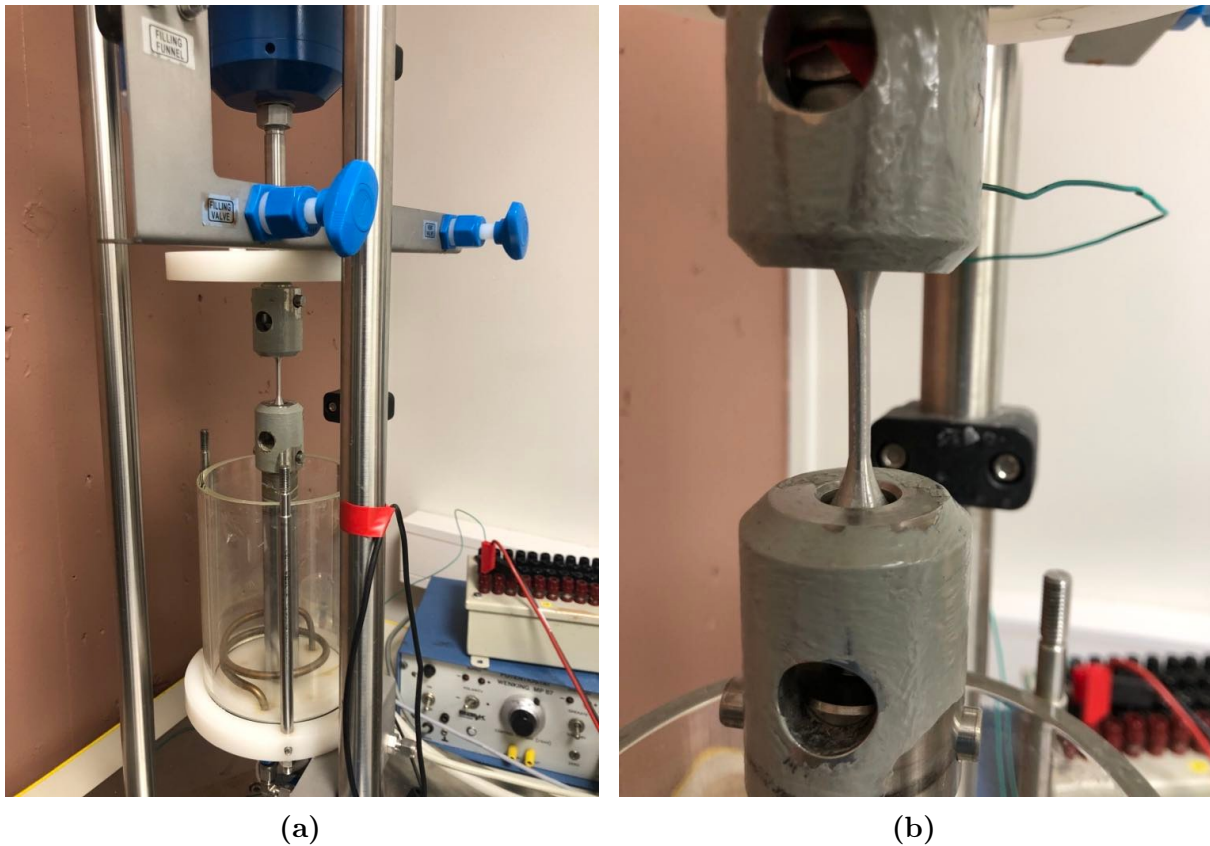


Figure 3.6.2: Experimental setup of SSRT in air environment.

3.7 Stepwise constant loading

In order to establish critical stress-strain levels while simulating CP in seawater environment SCL-testing of hydrogen charged samples has been executed. As described in section 2.4 test parameters such as initial loading and an incremental load is necessary. The basis for this experimental procedure has been that initial loading for each alloy sample has been 90% of the average FS obtained from in-situ hydrogen charging in SSRT for the same respective alloy with a hold time of 48 hours. Furthermore, where added increments have been 2% of same average FS every 24 hours until failure is reached.

The alloy samples have been hydrogen pre-charged according to procedure described in section 3.5. Both the sample preparation and experimental setup has been carried out in the same way as SSRT, section 3.6. However, the software procedure does somewhat differ. The first program to be added was the initial loading for 48 hours, then a program which executes the added incremental loads every 24 hour followed by a loop function which repeats the defined program before the loop. It was for every test run pre-defined that the loop is to repeat the increment program until failure is achieved. Necessary parameters to insert before recording was the initial and incremental loading values respectively corresponding to 90% and 2% of the average FS for the given sample obtained from SSRT and an increase in loading of 250 N/min until planned loads are reached. The inserted

loading values for each alloy is provided in section 4.3. As failure is reached, the fractured sample is to be stored in a freezer with a temperature of $-20\text{ }^{\circ}\text{C}$ to eliminate the diffusion rate of hydrogen out of the sample.

3.8 Hydrogen measurements

In order to quantify the total hydrogen content, hot extraction test was performed on in-situ hydrogen charged samples in SCL. The test was conducted using a G4 Phoenix DH setup.

3.9 Localized corrosion testing

3.9.1 Sample preparation

The samples were cut in circular shape from their respective alloy bars using Struers-Unitom-Cutting machine, where the alloy bars were milled and extracted out from their respective pipe materials, Figures 3.9.1 and 3.3.2.



(a) P750-H.S, P750-L.S and A31+



(b) Sanicro35 and 25%Cr SDSS

Figure 3.9.1: Images showing test samples from the alloys investigated. From left to right: P750-H.S, P750-L.S, A31, Sanicro35 and 25%Cr SDSS.

The sample preparation for localized corrosion testing was done by wet grinding the samples in Buehler MetaServ-250 grinding machine using SiC paper following a P80-P500 roughness order. Each grinding paper was cleaned by distilled water to ensure no grinding particles was embedded in the surface. The samples was then cleaned using ultrasonic bath for 5 minutes in a beaker containing ethanol followed by being rinsed by cold tap water and ethanol. The samples were dried in warm air, weighed for later weight loss determination and stored for a minimum of 24 hours at RT before testing.

3.9.2 Experimental setup

The CPT was obtained for P750-H.S, P750-L.S, Sanicro35, A31+ and 25%Cr SDSS in accordance to ASTM G48 Method C [33]. Two samples of each alloy were tested simultaneously during each testing duration. The preparation of electrolyte was done

according to ASTM G48 standard by dissolving iron(III)-chloride hexahydrate (6% $FeCl_3 \cdot 6H_2O$, 68.72 g) and adding reagent grade concentrated (36.5-38.0%, 16 mL) hydrochloric acid (HCl) in distilled water (600 mL). The reference electrode used was Ag/AgCl submerged in KCl solution.

The experimental setup was organized by placing the prepared electrolyte on a heating element in which a temperature sensor and the salt bridge were inserted. The samples were connected to the reference electrode and to their respective channels which logged the development of OCP during test duration, before being immersed into the electrolyte. The electrical connection was achieved by attaching a Pt wire through the holes in samples and clamped with the channel wires, Figure 3.9.2. The starting temperature for each test run was set to 50°C. Until any pitting was observed, the temperature was incrementally increased by 5°C every 12. hour. The experiment was to be stopped if the samples would experience a permanent potential drop below +450 mV_{Ag/AgCl} or if the sample would not experience any pitting even at a temperature of 85°C for a duration of 12 hours or more. Pitting initiation was defined at this potential drop and further temperature increase is not recommended according to the standard. After end of test, the samples were to be removed from the solution and cleaned with distilled water and ethanol. The cleaned samples would finally be weighed in order to determine any weight difference.

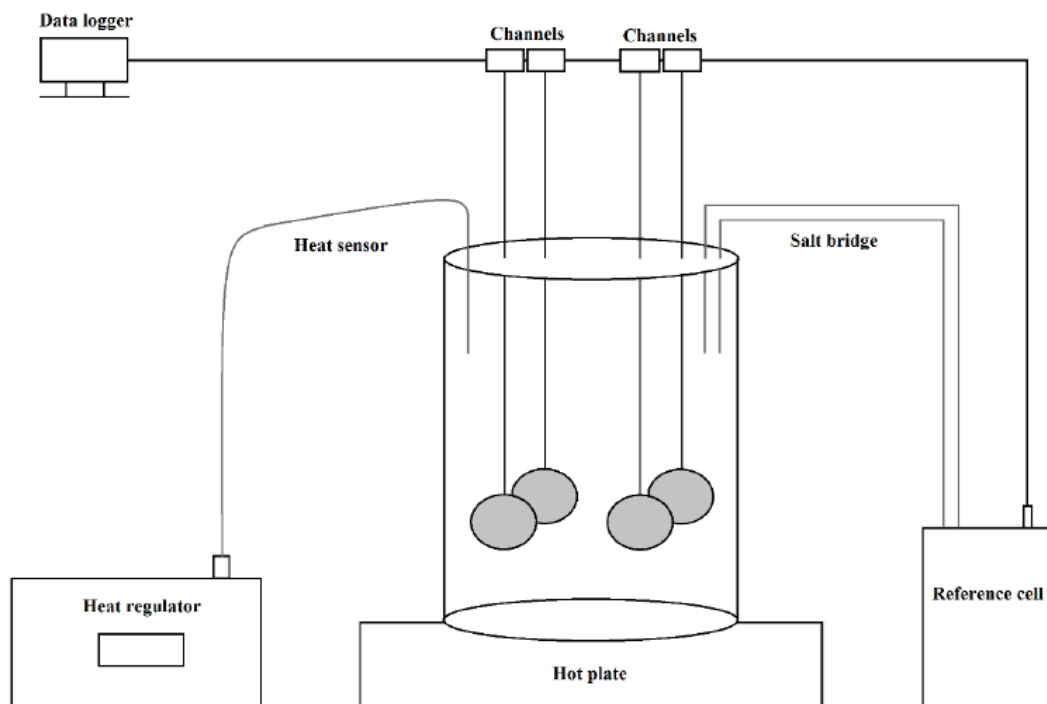


Figure 3.9.2: Illustration of experimental setup for ASTM G48 Method C [34].

3.10 SEM

3.10.1 Fractography

Fractography is carried out using a Quanta FEG 650 Scanning Electron Microscope. To gain best possible overview of fracture topology and secondary cracks, imaging was performed both normal and parallel to the fracture surfaces. Mean cross section area

post fracture was calculated using mean diameter of the cross section determined in SEM, Figure 3.10.1.

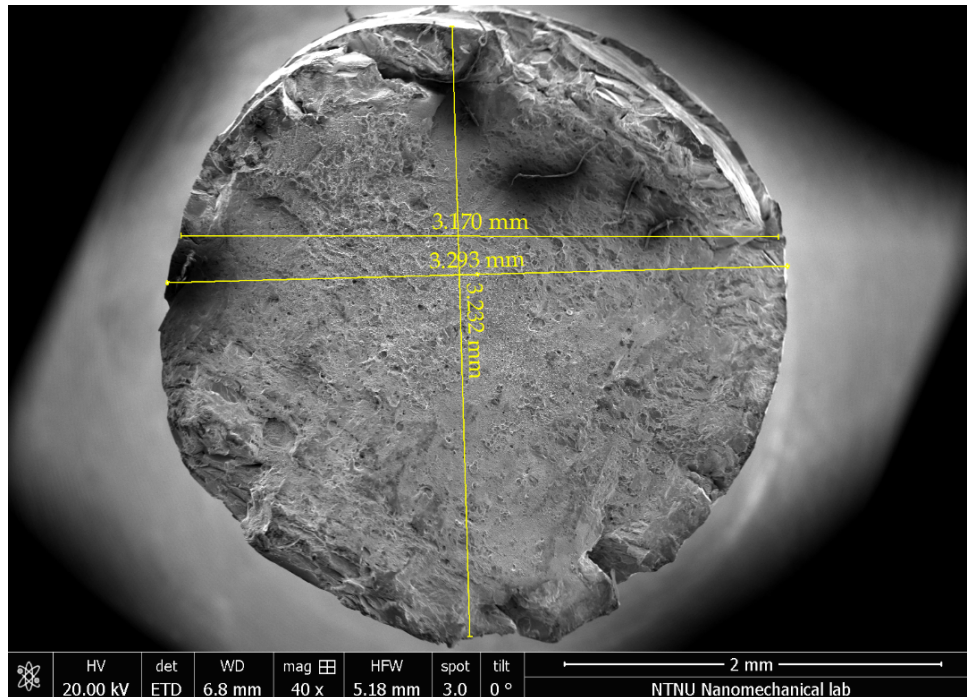


Figure 3.10.1: Measurements of average diameter of cross section in SEM post fracture.

3.10.2 EDS

The metallographic examination was carried out to characterize the materials microstructure, furthermore analyze and investigate the detected precipitates. The examination was performed using Quanta FEG 650 Scanning Electron Microscope where both SE and BSE detectors were utilized. As some inclusions were detected in the microstructure in each alloy sample, further chemical assessment of these precipitates was done by the use of EDS.

3.11 Microstructure imaging

An overview of the microstructure was achieved by optical microscopy. The sample preparation was carried out by wet grinding of samples in the Buehler MetaServ-250 grinding machine using SiC paper according to a roughness order of P80-P4000 followed by a separate polishing routine. The latter was done in Struers-LaboSystem-Grinding machine and consisted of polishing with a magnetic polishing cloth with 3 and 1 μm diamond suspension followed by oxide polishing suspension. As it can be challenging to reveal nickel alloys microstructure due to their high hardness an etching procedure was performed. The samples were etched with 20% Oxalic acid for 15-20 seconds with a applied potential of 5 V. Grain size of each alloy sample has been calculated using the Jeffries method in accordance with ASTM E112.

Chapter 4

Results

4.1 Tensile testing

Key mechanical properties of the alloys in focus were obtained through standard tensile testing and are intentionally presented to provide an overview of the mechanical performance of each alloy from their respective pipe material. By comparison to the mechanical data in Table 3.2.3 obtained from Appendix A, the deviation in terms of UTS and YS is small for all four alloys. Although, in terms of %EL specifically for the P750-H.S some notable variation according to Tables 4.1.1 and 3.2.3 have occurred. As it appears in Figure 4.1.1 the P750-H.S is the most brittle alloy and relatively low %EL is to be expected, however a difference of 8% in %EL is notable significant. Hence, a retest of P750-H.S where the sample had the same geometry as a HISC testing specimen was conducted. The stress-strain behaviour for the latter is displayed as the dotted line in Figure 4.1.1, where an %EL of 15.6% was reached. The latter result is more in accordance with values provided by the material suppliers in Appendix A. The variations in %EL with sample geometry for the P750-H.S is subject to uncertainty.

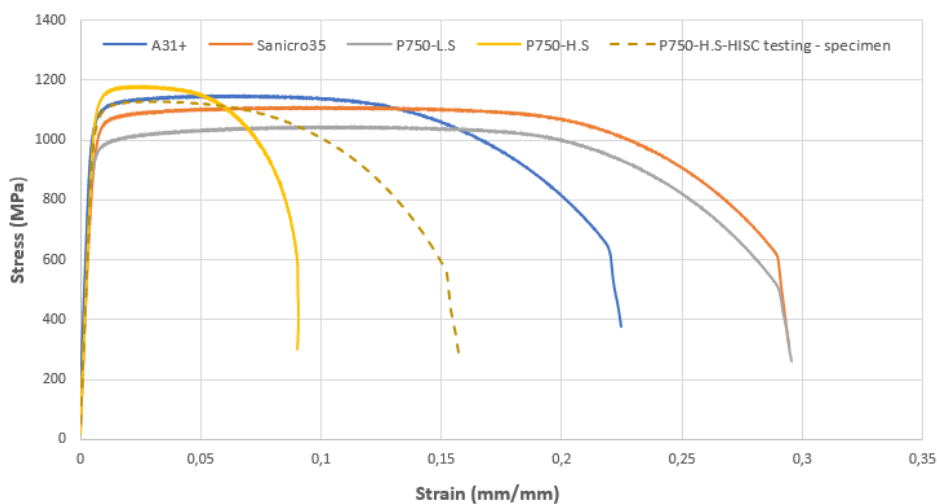


Figure 4.1.1: Standard tensile testing of P750-H.S, P750-L.S, A31+ and Sanicro35

Table 4.1.1: Key mechanical properties of alloys investigated obtained from tensile testing at RT.

Alloy	Youngs modulus (GPa)	0.2% offset YS (MPa)	UTS (MPa)	Fracture strain (-)	EL (%)	YS/UTS (%)
P750-H.S	193	1112	1178	0.09	9	94
P750-L.S	190	946	1044	0.295	30	91
A31+	208	1065	1147	0.224	22	93
Sanicro35	141	1041	1106	0.294	29	94

4.2 Slow strain rate testing

According to the stress-strain curves obtained from SSRT in Figure 4.2.1, it clearly appears that the alloys Sanicro35 and P750-L.S in Figures 4.2.1d and 4.2.1b respectively, have experienced relatively the largest loss in fracture strain. According to Table 4.2.1, both Sanicro35 and P750-L.S experienced a loss in fracture strain of 8.65% and 4.19% respectively, from in-situ hydrogen charging. The same pattern in terms of a decrease is also occurring in %EL and YS/FS-ratio for both alloys. In contrast, the loss in fracture strain from in-situ hydrogen charging for P750-H.S and A31+ have been 0.35% and 1.7%, respectively. Only a minimal decrease in terms of %EL and YS/FS-ratio has occurred for the latter alloys in comparison to P750-L.S and Sanicro35.

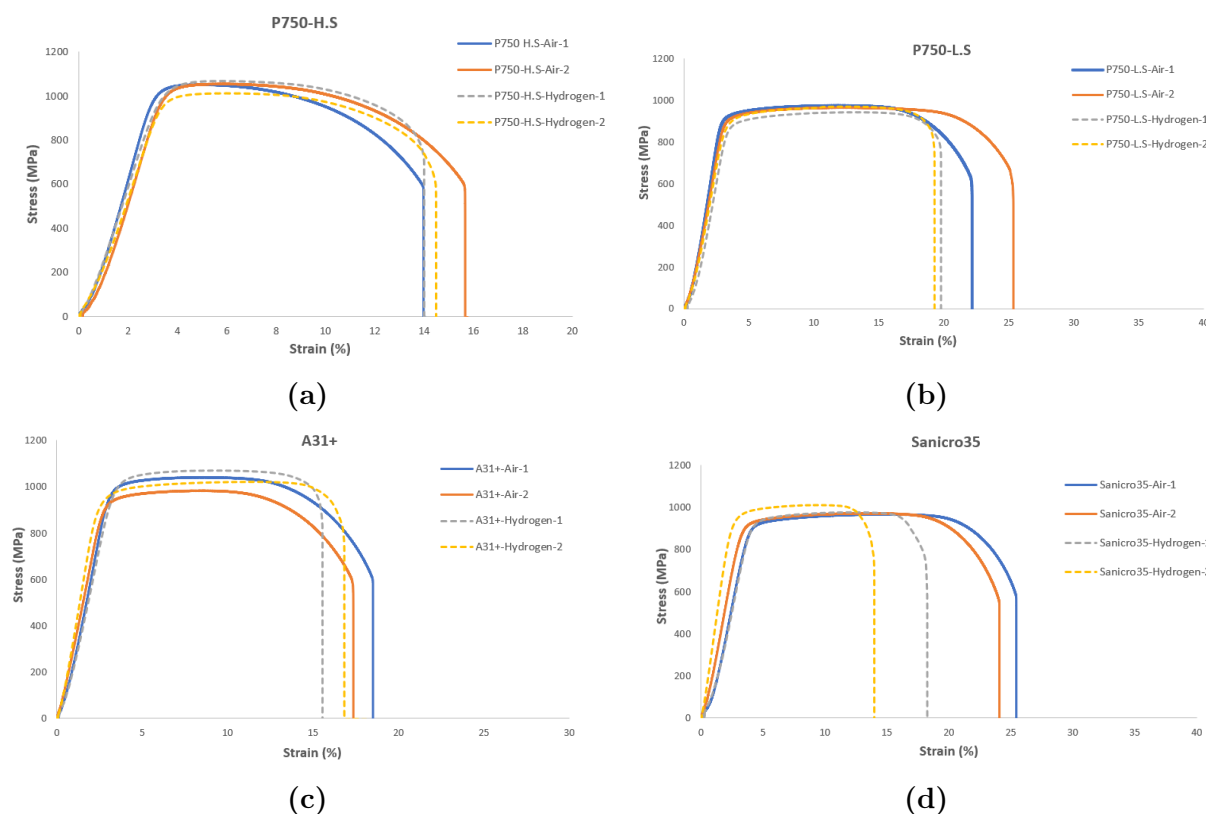


Figure 4.2.1: Stress-strain behaviour obtained from SSRT in air and in-situ hydrogen charging for P750-H.S, P750-L.S, A31+ and Sanicro35.

Table 4.2.1: Key mechanical properties for alloys investigated obtained from SSRT.

	Alloy	YS (MPa)	FS (MPa)	Fracture strain (%)	EL(%)	YS/FS (%)
Average SD	P750-H.S-Air-1	991.00	1051.00	14.00	14.00	94.29
	P750-H.S-Air-2	959.00	1054.00	15.10	15.00	90.99
		975.00	1052.50	14.55	14.50	92.64
		22.63	2.12	0.78	0.71	2.34
Average SD	P750-H.S-Hydrogen-1	952.00	1067.00	14.00	14.00	89.22
	P750-H.S-Hydrogen-2	940.00	1011.00	14.40	14.40	92.98
		946.00	1039.00	14.20	14.20	91.10
		8.49	39.60	0.28	0.28	2.66
Average SD	P750-L.S-Air-1	877.00	974.00	22.17	22.10	90.04
	P750-L.S-Air-2	857.00	964.00	25.30	25.30	88.90
		867.00	969.00	23.74	23.70	89.47
		14.14	7.07	2.21	2.26	0.81
Average SD	P750-L.S-Hydrogen-1	816.00	942.00	19.80	19.80	86.62
	P750-L.S-Hydrogen-2	804.00	969.00	19.30	19.30	82.97
		810.00	955.50	19.55	19.55	84.80
		8.49	19.09	0.35	0.35	2.58
Average SD	A31+-Air-1	936.00	1040.00	18.40	18.40	90.00
	A31+-Air-2	884.00	983.00	17.30	17.30	89.93
		910.00	1011.50	17.85	17.85	89.96
		36.77	40.31	0.78	0.78	0.05
Average SD	A31+-Hydrogen-1	928.00	1070.00	15.50	15.50	86.73
	A31+-Hydrogen-2	887.00	1021.00	16.80	16.80	86.88
		907.50	1045.50	16.15	16.15	86.80
		28.99	34.65	0.92	0.92	0.10
Average SD	Sanicro35-Air-1	860.00	967.00	25.40	25.40	88.93
	Sanicro35-Air-2	850.00	971.00	24.10	24.10	87.54
		855.00	969.00	24.75	24.75	88.24
		7.07	2.83	0.92	0.92	0.99
Average SD	Sanicro35-Hydrogen-1	840.00	977.00	18.20	18.20	85.98
	Sanicro35-Hydrogen-2	882.00	1011.00	14.00	14.00	87.24
		861.00	994.00	16.10	16.10	86.61
		29.70	24.04	2.97	2.97	0.89

For both P750-H.S and P750-L.S the variations in YS and FS when tested in air and from in-situ hydrogen charging are relatively small according to Figure 4.2.2 and Table 4.2.1. P750-H.S experienced a decrease of 29 MPa and 13.5 MPa in terms of YS and FS, respectively. While for P750-L.S the loss in YS and FS was 57 MPa and 14 MPa, respectively. However, in the case of A31+ and Sanicro35 a slight increase in FS from in-situ hydrogen charging occurred indicating a hardening effect for both alloys. The YS for the latter alloys from in-situ hydrogen charging experienced a minimal change. Due to these observations and as described in 2.5, the degree of susceptibility to HE will be measured according to parameters describing the mechanical ductility loss and degree of embrittlement.

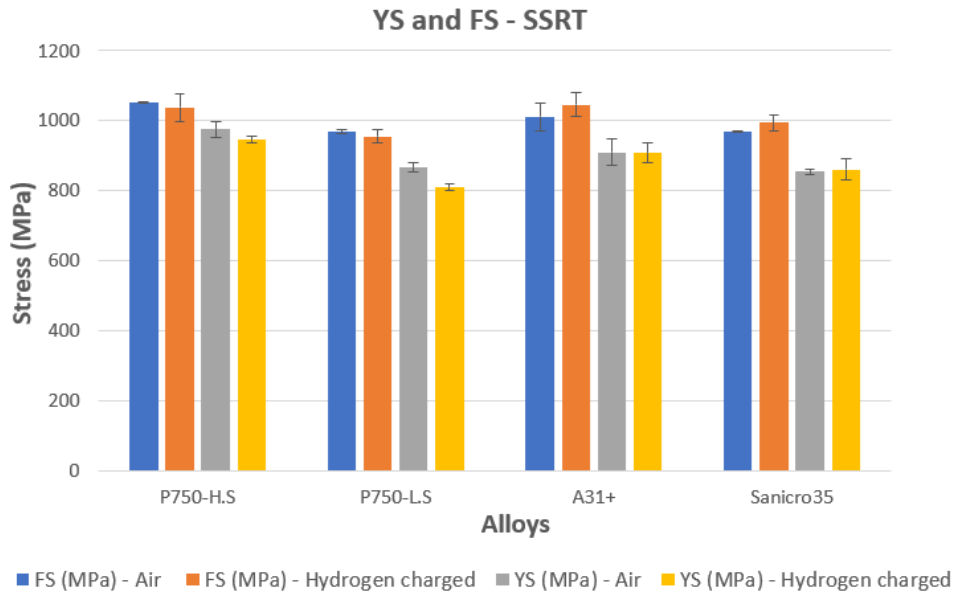


Figure 4.2.2: YS and FS from SSRT in air and from in-situ hydrogen charging.

It appears from Figure 4.2.3 with regards to loss in fracture strain in both environments, that Sanicro35 and P750-L.S have suffered the greatest ductility loss. However, the degree of embrittlement according to %RA and RAR do not correlate with the mechanical ductility loss. In terms of loss in %RA, A31+ and Sanicro35 appears to be the most affected alloys indicating highest degree of embrittlement. The A31+ alloy experiences a loss of 40.96% whereas Sanicro35 a loss of 40.12%. The loss in %RA for P750-H.S appears to be 37.31%, while 29.06% for P750-L.S.

Table 4.2.2: An overview of mean cross section areas pre and post fracture, %RA and plastic elongation for each alloy sample used during SSRT.

	Alloy sample	Area ₀ - pre fracture (mm ²)	Area _{min} - post fracture (mm ²)	RA (%)	E _p (mm)
Average	P750-H.S-Air-1	11.04	2.66	75.92	2.77
	P750-H.S-Air-2	11.34	2.63	76.81	2.99
SD				76.37	2.88
				0.62	0.15
Average	P750-H.S-Hydrogen-1	11.40	9.07	20.36	2.73
	P750-H.S-Hydrogen-2	11.34	4.79	57.75	2.80
SD				39.06	2.76
				26.44	0.05
Average	P750-L.S-Air-1	11.16	3.46	68.97	4.80
	P750-L.S-Air-2	11.04	3.53	68.04	5.58
SD				68.51	5.19
				0.66	0.55
Average	P750-L.S-Hydrogen-1	11.34	6.29	44.54	4.20
	P750-L.S-Hydrogen-2	10.98	7.21	34.36	4.01
SD				39.45	4.10
				7.19	0.14
Average	A31+-Air-1	11.34	3.17	72.02	3.86
	A31+-Air-2	11.40	3.22	71.72	3.60
SD				71.87	3.73
				0.21	0.18
Average	A31+-Hydrogen-1	11.22	7.94	29.23	3.09
	A31+-Hydrogen-2	11.34	7.64	32.59	3.52
SD				30.91	3.30
				2.38	0.31
Average	Sanicro35-Air-1	11.46	3.17	72.31	5.38
	Sanicro35-Air-2	11.16	3.27	70.72	5.16
SD				71.52	5.27
				1.13	0.16
Average	Sanicro35-Hydrogen-1	10.75	7.07	34.26	3.59
	Sanicro35-Hydrogen-2	11.04	7.89	28.54	2.81
SD				31.40	3.20
				4.04	0.55

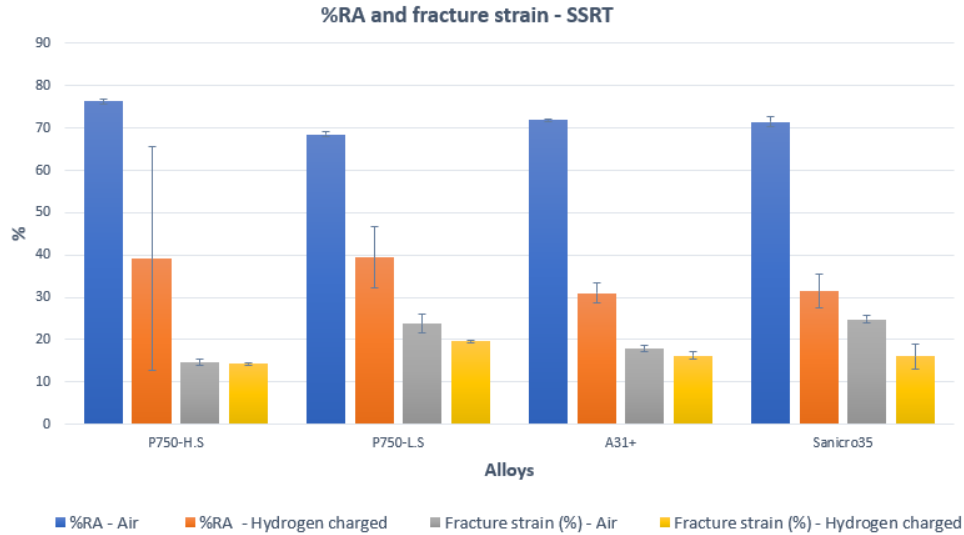


Figure 4.2.3: %RA and fracture strain obtained from SSRT in air and in-situ hydrogen charging.

According to the HE indicators defined in this study, it appears from Figure 4.2.4 and Table 4.2.3 that Sanicro35 and P750-L.S experienced greatest degree of ductility loss consequently highest degree of HE sensitivity with their highest values of HEI and lowest plastic elongation ratios. These results correlates with their respective plastic deformation behaviors appearing in Figure 4.2.1 confirming the lower fracture strains from in-situ hydrogen charging. However, in terms of RAR both A31+ and Sanicro35 seems to be the alloys which have experienced the highest degree of embrittlement.

Table 4.2.3: HE indicators.

Alloy	RAR (%)	RE _p (%)	HEI (%)
P750-H.S	51.14	95.98	4.02
P750-L.S	57.59	79.10	20.90
A31+	43.00	88.59	11.41
Sanicro35	43.91	60.73	39.27

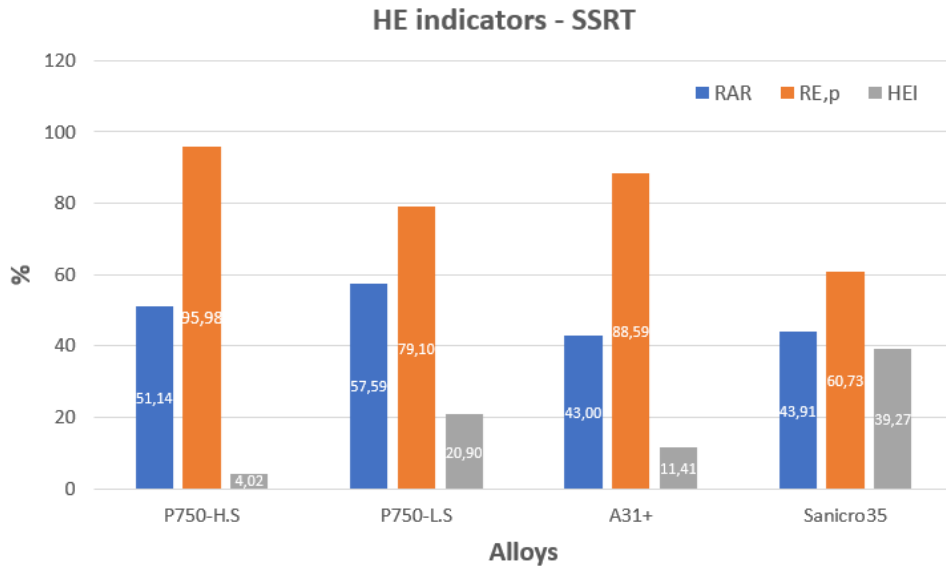


Figure 4.2.4: HE indicators obtained from SSRT describing degree of embrittlement and mechanical ductility loss for alloys investigated.

4.3 Stepwise constant loading

SCL was carried out based on FS values obtained from in-situ hydrogen charging in SSRT. Initial and incremental load values used for each alloy are provided in Table 4.3.1. According to both Table 4.3.1 and Figure 4.3.1, P750-H.S with a FS of 1050 MPa has maintained 101% of the FS obtained from in-situ hydrogen charging in SSRT. The testing period for P750-H.S was an exposure time of 11 increments equivalent to 16 days. Similarly, both Sanicro35 and P750-L.S reached 100% of their respective FS from SSRT. The exposure time was 5 and 6 increments, equivalent to approximately 6 and 8 days for Sanicro35 and P750-L.S respectively. A31+ reached 98% of FS from SSRT with an exposure time of 5 increments lasting 6.5 days.

Table 4.3.1: Initial and incremental loading values for each alloy during SCL.

Alloy	Initial loading (MPa)	Initial loading (N)	Incremental load (MPa)	Incremental load (N)
P750-H.S	935	10268	21	228
P750-L.S	860	9438	19	210
A31+	941	10554	21	235
Sanicro35	895	9981	20	222

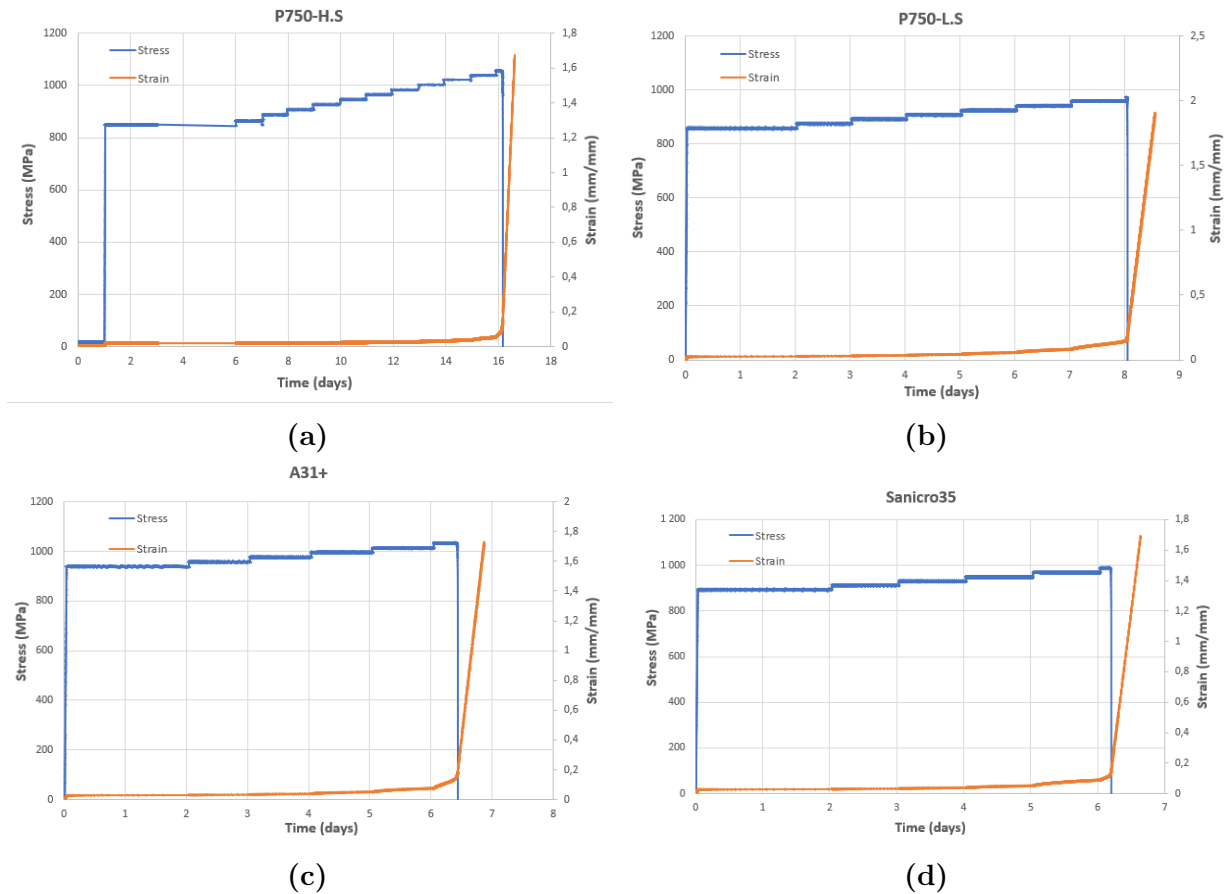


Figure 4.3.1: Stress-strain behaviour as a function of time obtained from SCL-testing during in-situ hydrogen charging for P750-H.S, P750-L.S, A31+ and Sanicro35.

It appears from Figure 4.3.2 that P750-H.S experienced greatest degree of embrittlement with an %RA of 20.25%, followed by Sanicro35 with 32.39%, A31+ with 35.07% and lastly P750-L.S with 38.62%. In regards to fracture strain, the variation across the four alloys is minimal.

Table 4.3.2: An overview of key mechanical properties and %RA for alloys investigated obtained from SCL.

Alloy	FS (MPa)	Fracture strain (%)	%EL	%RA
P750-H.S	1050	14	14	20.25
P750-L.S	961	16	16	38.62
A31+	1031	17	17	35.07
Sanicro35	989	18	18	32.39

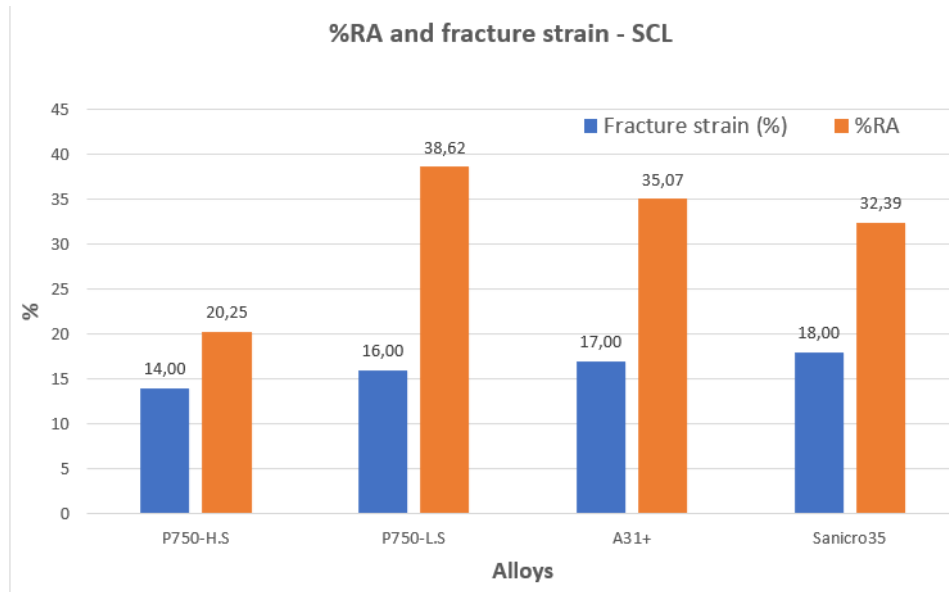


Figure 4.3.2: %RA and fracture strain obtained from in-situ hydrogen charging in SCL.

4.4 Comparison of SSRT and SCL

The average values for FS, %RA, %EL and fracture strain from in-situ hydrogen charging in SSRT and SCL are provided in Table 4.4.1. It is to be noted that the P750-H.S maintained its FS of 1050 MPa post SCL, which was within the standard deviation when tested in SSRT despite the significantly longer testing period of 16 days. Likewise, the %EL and fracture strain remained the same. The average test period for each alloy sample when SSRT was performed in air and during in-situ hydrogen charging was 2-3 days. However, a further reduction in %RA of 18.81% post SCL in comparison to SSRT has occurred. Although, the drop in %RA do appear within the relatively larger standard deviation for %RA in-situ hydrogen charging in SSRT occurring in Figure 4.2.3. Similarly to the P750-H.S, the A31+ maintained its FS of 1031 MPa and appears within the standard deviation occurring from SSRT. In terms of %RA, a slight increase from 30.91% post SSRT to 35.07% in SCL did occur. Variation in both fracture strain and %EL is minimal. P750-L.S did experience a minor ductility loss with a decrease of 3.5% in fracture strain as well as reaching a FS of 961 MPa. Sanicro35 maintained a FS of 989 MPa which is within the standard deviation from SSRT as well as the %RA and fracture strain, thus not experiencing any decreased ductility compared to results from SSRT.

Table 4.4.1: Comparison of key mechanical properties and %RA between SSRT and SCL for all four alloys.

Test	Alloy	FS (MPa)	RA (%)	%EL	Fracture strain (%)
SSRT	P750-H.S	1039 ± 39.60	39.06 ± 26.44	14.20 ± 0.28	14.20 ± 0.28
SSRT	P750-L.S	955.50 ± 19.09	39.45 ± 7.19	19.55 ± 0.35	19.55 ± 0.35
SSRT	A31+	1045,50 ± 34.65	30.91 ± 2.38	16.15 ± 0.92	16.15 ± 0.92
SSRT	Sanicro35	994 ± 24.04	31.40 ± 4.04	16.10 ± 2.97	16.10 ± 2.97
SCL	P750-H.S	1050	20.25	14	14
SCL	P750-L.S	961	38.62	16	16
SCL	A31+	1031	35.07	17	17
SCL	Sanicro35	989	32.39	18	18

4.5 Hydrogen uptake

The hydrogen content in alloy samples from in-situ hydrogen charging in SCL has been measured and provided in Figure 4.5.1. It appears that Sanicro35 and A31+ have the largest hydrogen concentrations with 96.64 ppm and 78.01 ppm respectively, followed by the P750-L.S with 65.70 ppm and P750-H.S with 39.57 ppm. It is to be noted that these results are subject to uncertainty as only one sample of each alloy has been investigated.

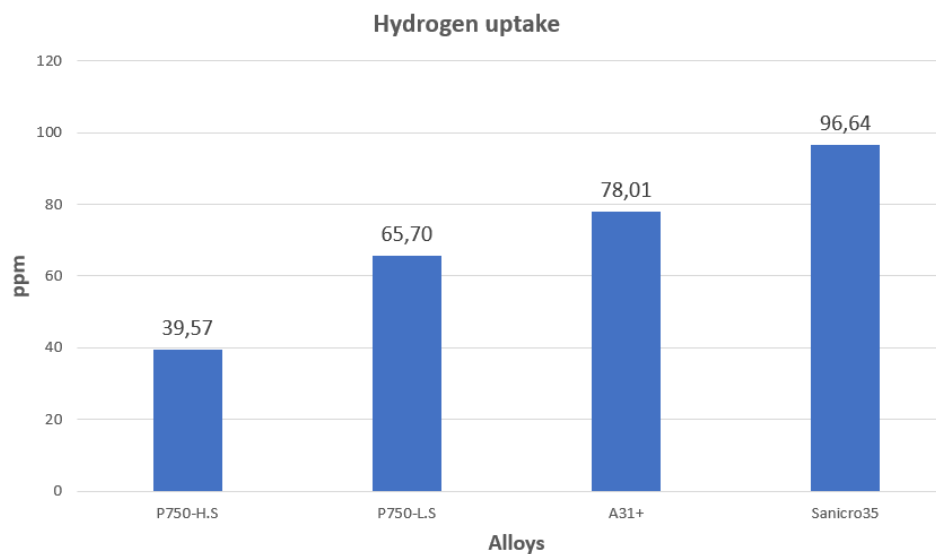


Figure 4.5.1: Hydrogen uptake in P750-H.S, P750-L.S, A31+ and Sanicro35 post SCL-test.

4.6 Fractography

4.6.1 Air environment - SSRT

In the following fractography of alloys post SSRT in air environment is presented. From Figures 4.6.1, 4.6.2, 4.6.3 and 4.6.4 it clearly appears from the alloys respective central and edge areas in their fracture surfaces that a high concentration of dimples have occurred indicating a ductile void collapse. The latter combined with the high degree of necking which the alloys have experienced during plastic deformation before the final fractures have occurred confirms the ductile fracture behaviours, Figures 4.6.1a, 4.6.2a, 4.6.3a and 4.6.4a. The high degree of necking is also being confirmed by the high %RA for alloys tested in air in Figure 4.2.3. Hence, no brittle features have been observed in the fracture surfaces or in the alloys respective gauge sections from SSRT in air environment.

P750-H.S

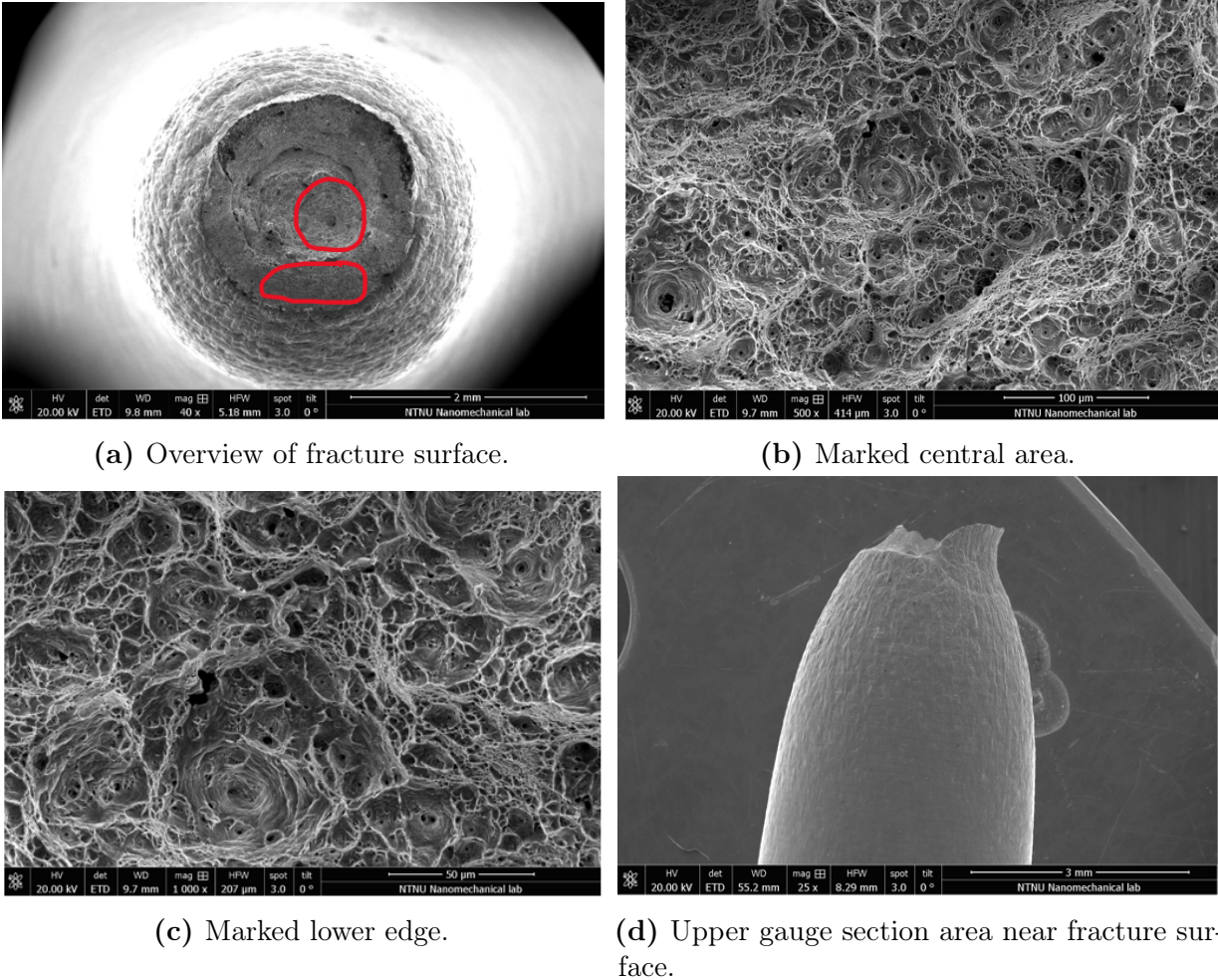
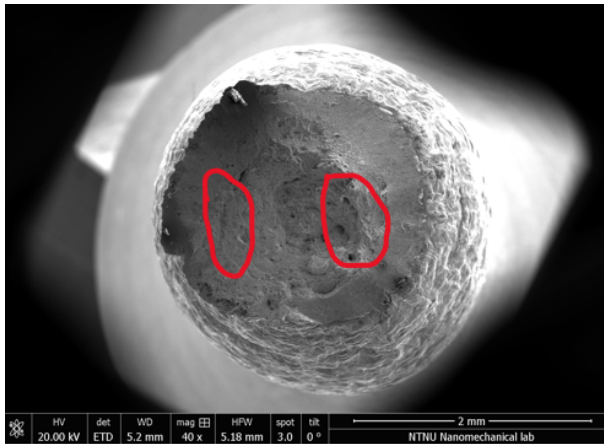
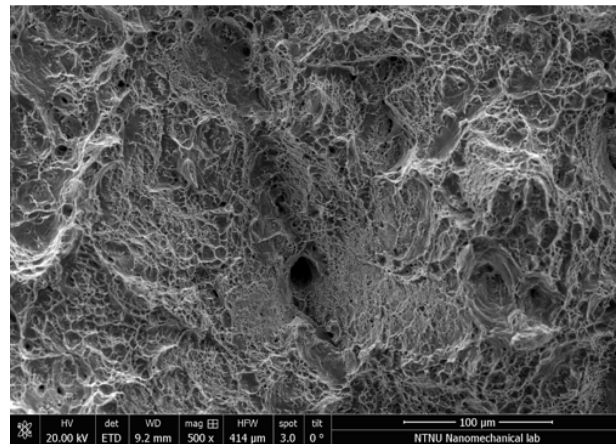


Figure 4.6.1: Fracture surface overview of P750-H.S from SSRT in air environment.

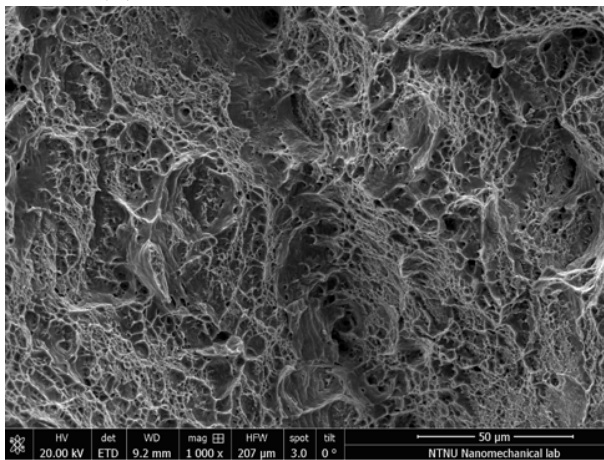
P750-L.S



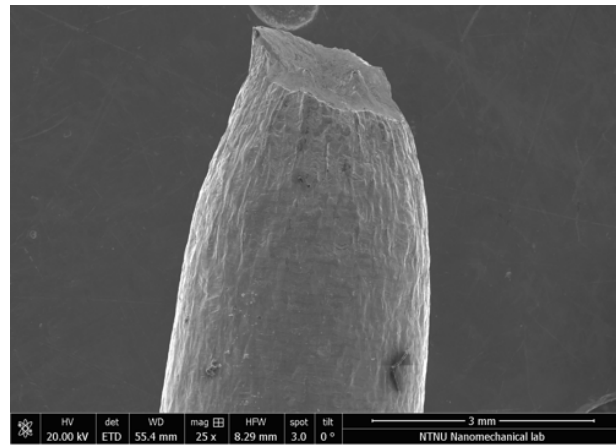
(a) Overview of fracture surface.



(b) Marked central area.



(c) Marked left edge.



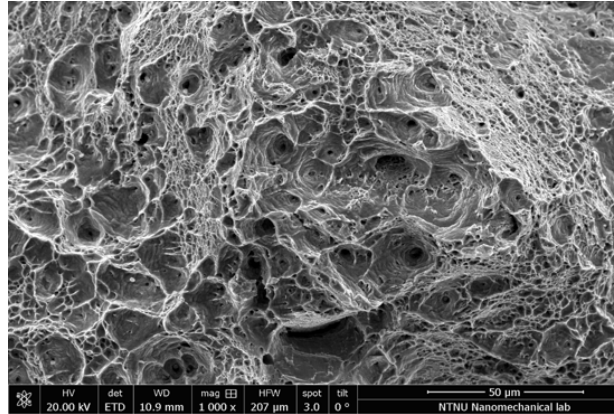
(d) Upper gauge section area near fracture surface.

Figure 4.6.2: Fracture surface overview of P750-L.S from SSRT in air environment.

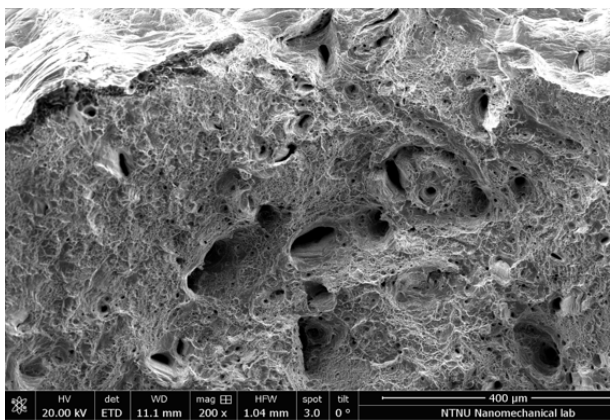
A31+



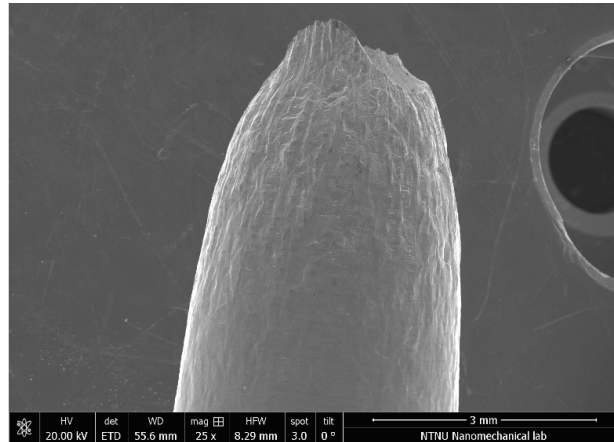
(a) Overview of fracture surface.



(b) Marked central area.



(c) Marked upper edge.



(d) Upper gauge section area near fracture surface.

Figure 4.6.3: Fracture surface overview of A31+ from SSRT in air environment.

Sanicro35

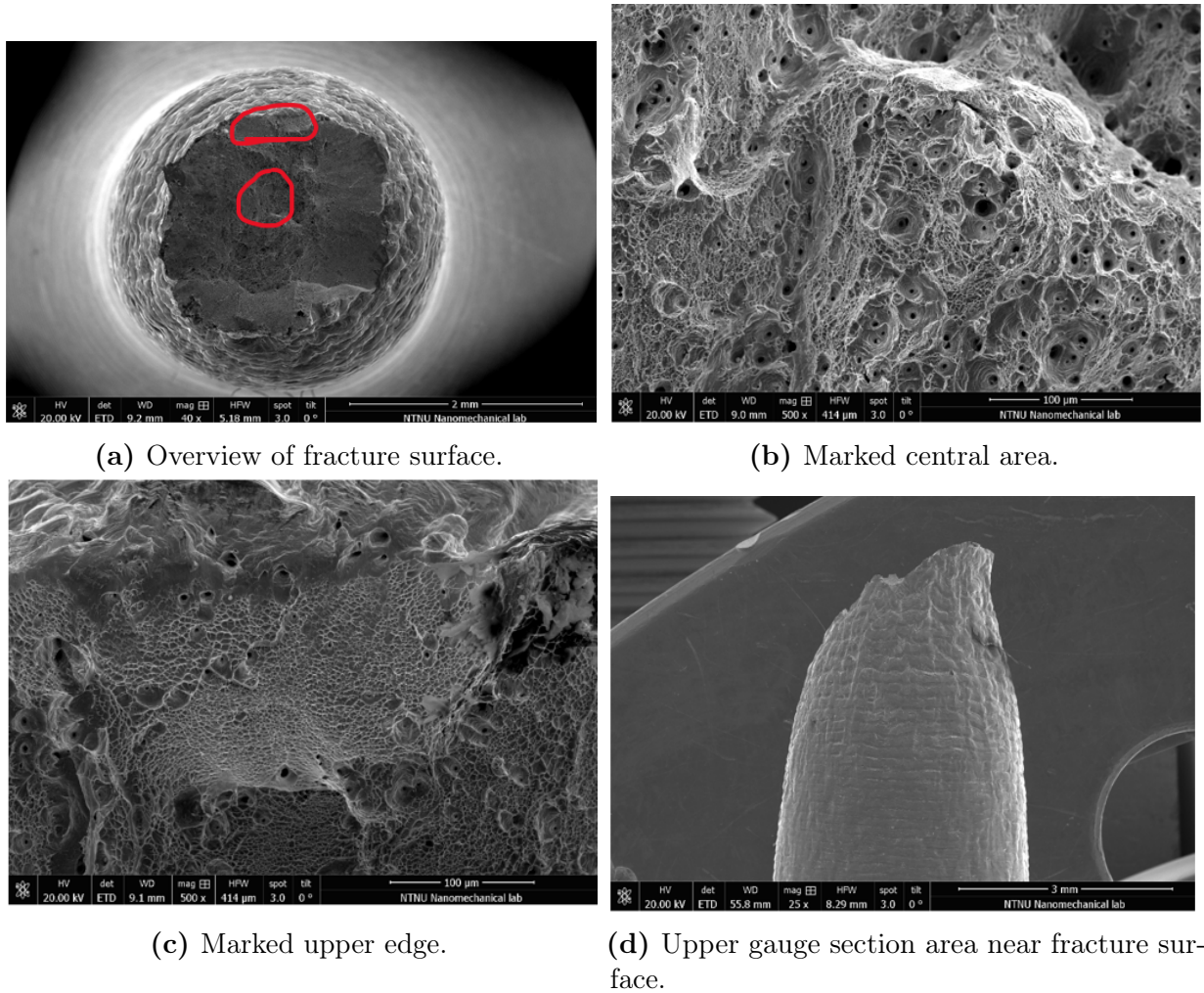


Figure 4.6.4: Fracture surface overview of Sanicro35 from SSRT in air environment.

4.6.2 In-situ hydrogen charged

In the following, an overview of the fracture surfaces with an emphasis on certain interest areas revealing brittle features due to HE has been provided. The following section is divided in alloy samples from in-situ hydrogen charging in SSRT and SCL.

SSRT

P750-H.S

It appears from Figure 4.6.5 that the P750-H.S experienced less necking from in-situ hydrogen charging indicating that the hydrogen had an embrittlement effect. However, Figure 4.6.5c does reveal that the degree of embrittlement from the edge area and towards the centrum of the fracture surface has varied indicating a brittle to ductile transition. In regards to the central area of the fracture surface, it appears from Figure 4.6.5b that a relatively high concentration of voids indicating a ductile fracture morphology has been maintained post failure, similarly to testing of P750-H.S in air. In contrast, some transgranular cracking has occurred on the edge area indicating relatively higher

concentrations of hydrogen in these sites, Figure 4.6.5d

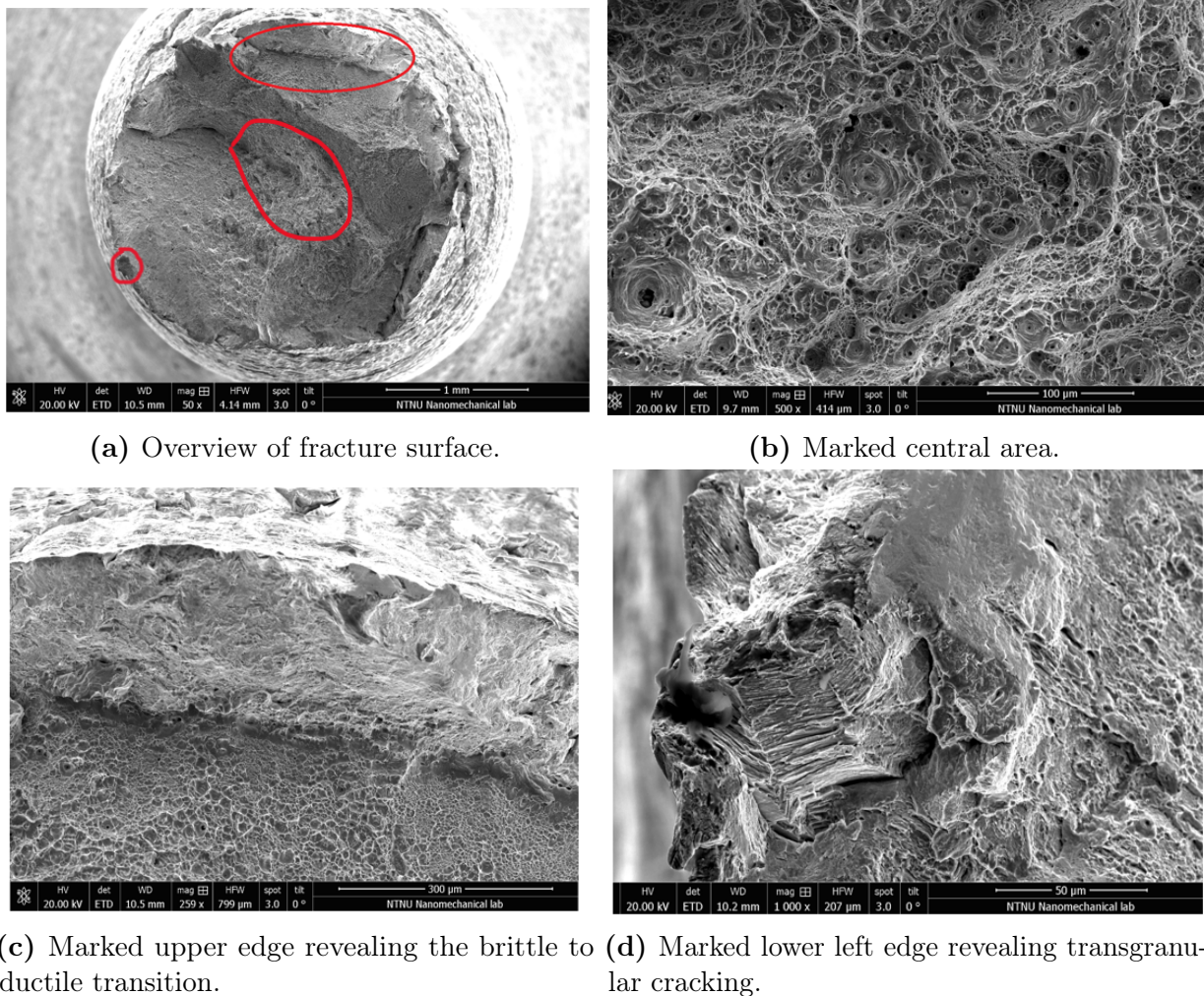
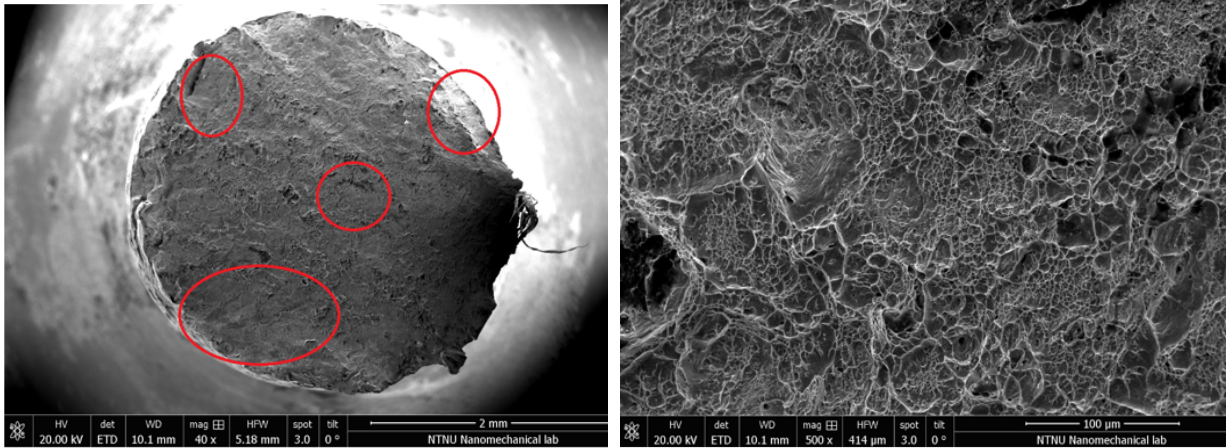


Figure 4.6.5: Overview of fracture surfaces for P750-H.S from in-situ hydrogen charging in SSRT.

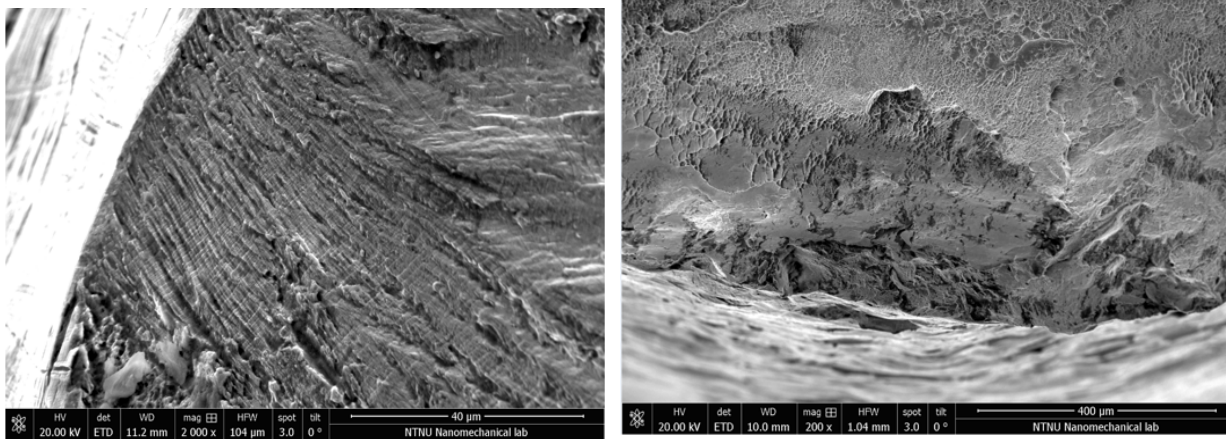
P750-L.S

For the P750-L.S mostly of the embrittlement has occurred on the edges of the fracture surface resulting in the river pattern indicating transgranular cracking, Figure 4.6.5d. Similarly to the P750-H.S, a brittle to ductile transition has occurred from the marked upper right edge area and towards the central area, Figure 4.6.6d. From Figure 4.6.6b, relatively high concentration of dimples indicates that the central area of the alloy sample remained ductile during in-situ hydrogen charging and post fracture. It is to be noted that the transgranular cracking in all marked edge areas for P750-L.S appears to be relatively much more severe than the P750-H.S alloy.



(a) Overview.

(b) Marked central area.



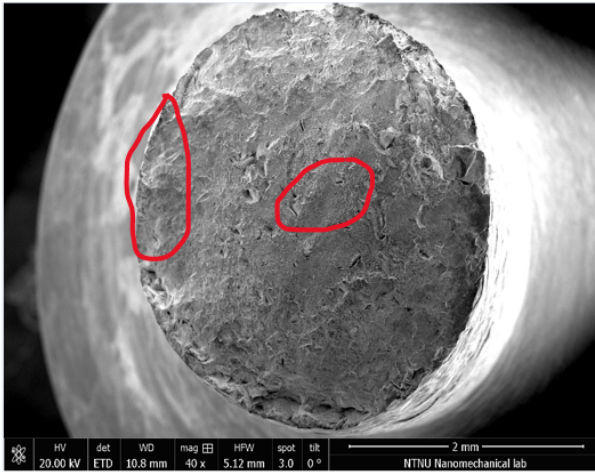
(c) Marked lower ledge revealing transgranular cracking.

(d) Marked upper right edge area revealing the brittle to ductile transition.

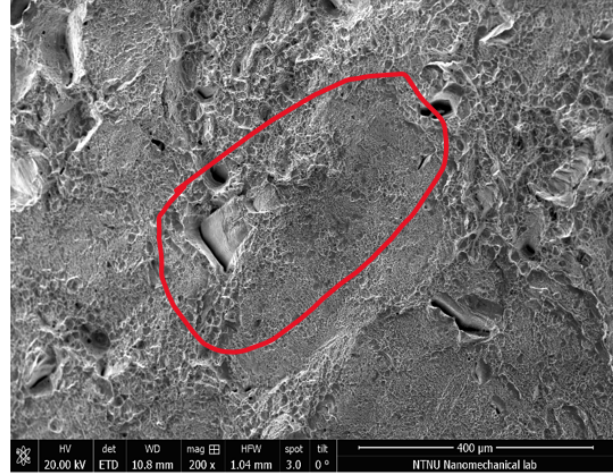
Figure 4.6.6: Overview of fracture surfaces for P750-L.S from in-situ hydrogen charging in SSRT.

A31+

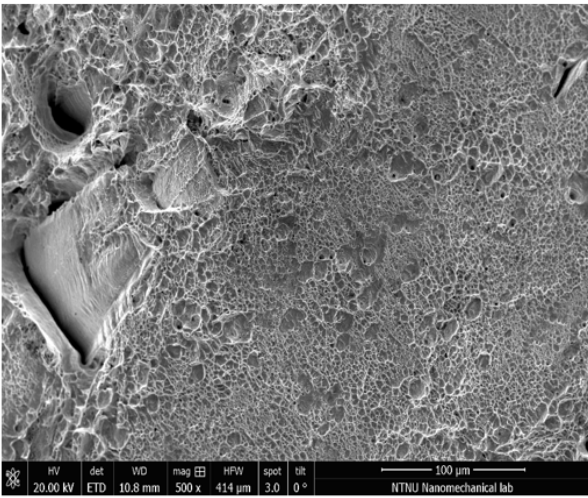
In the case of A31+, it can visually according to the marked central area in Figure 4.6.7b be argued that the ductile morphology has not appeared to be as clear compared to both P750 alloys. Moreover, the A31+ with less ductile morphology in the central area in combination with having relatively larger loss in %RA according to Figure 4.2.3 confirms higher degree of HE embrittlement when compared to the latter alloys. Especially in Figure 4.6.7c which is the marked central area with higher magnification, a brittle flat facet indicating relatively larger hydrogen accumulation in this specific site has occurred. In addition to the relatively largely affected central area, the marked edge area has also suffered more severe transgranular cracking compared to both P750 alloys, Figure 4.6.7e.



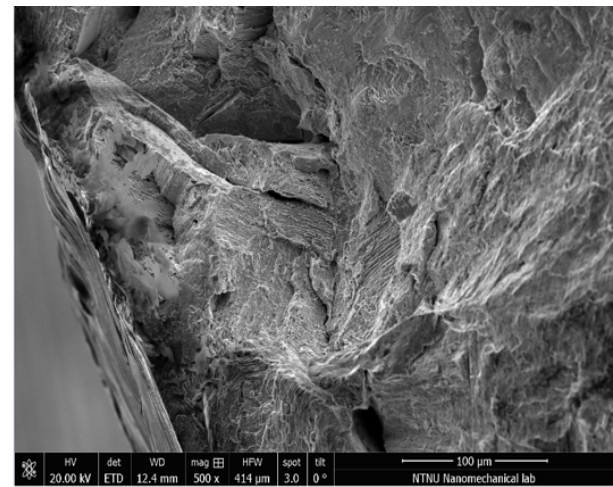
(a) Overview of fracture surface.



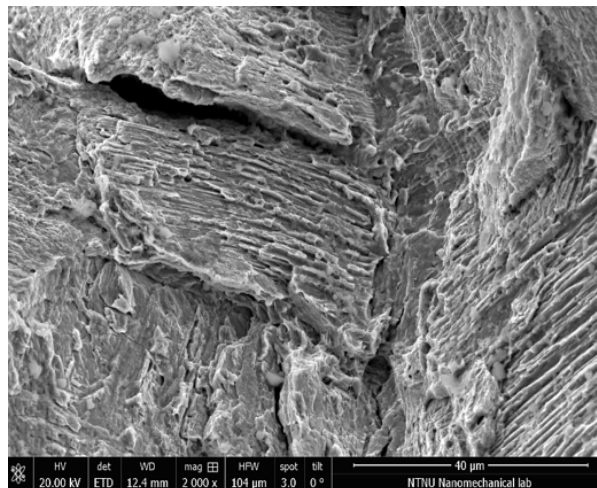
(b) Marked central area.



(c) Marked central area with 500X magnification.



(d) Marked left edge revealing transgranular cracking.

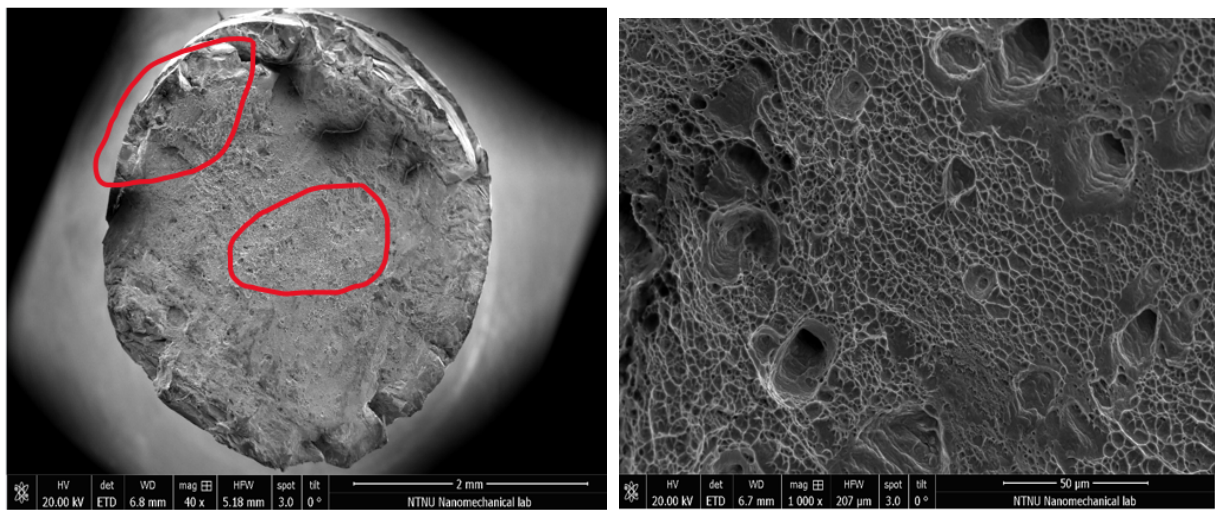


(e) Marked left edge revealing transgranular cracking with 2000X magnification.

Figure 4.6.7: Overview of fracture surfaces for A31+ from in-situ hydrogen charging in SSRT.

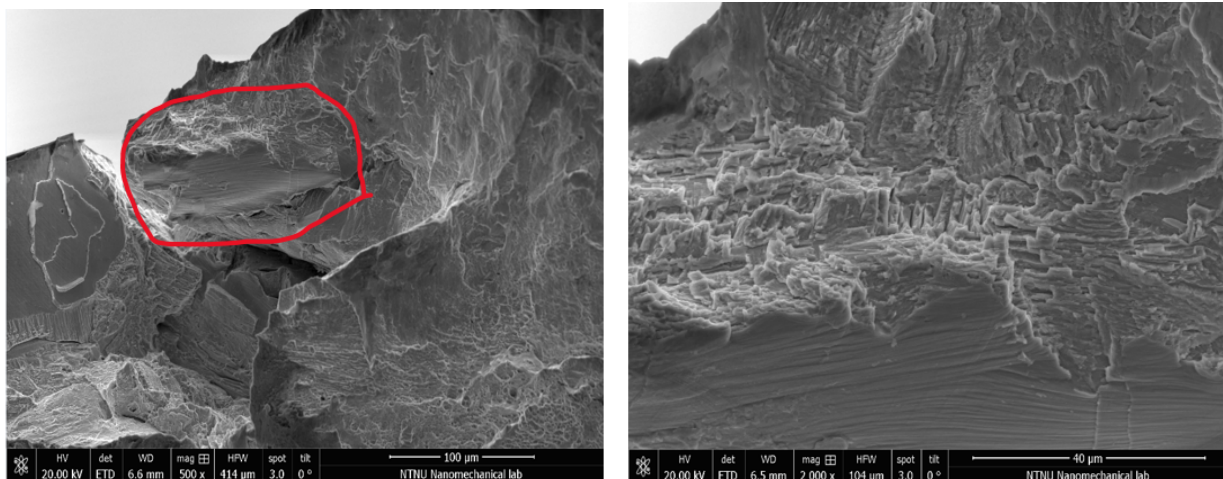
Sanicro35

Similarly to the A31+, the Sanicro35 experienced much more severe transgranular cracking in the edge areas compared to both P750 alloys. According to Figures 4.6.8c and 4.6.8d, much smoother brittle facets have occurred indicating relatively larger hydrogen accumulation in the marked edge compared to the central area. The relatively higher degree of embrittlement is also being confirmed by the larger drop in %RA compared to the P750 alloys. Similarly to A31+, the Sanicro35 has the lowest RAR indicating high sensitivity to embrittlement. On the other hand, the central area of the Sanicro35 did consist of much deeper voids and pure visually relatively clearer ductile fracture morphology indicating less hydrogen diffusion to the central sites compared to the A31+.



(a) Overview of fracture surface.

(b) Marked central area.



(c) Marked left ledge revealing transgranular cracking.

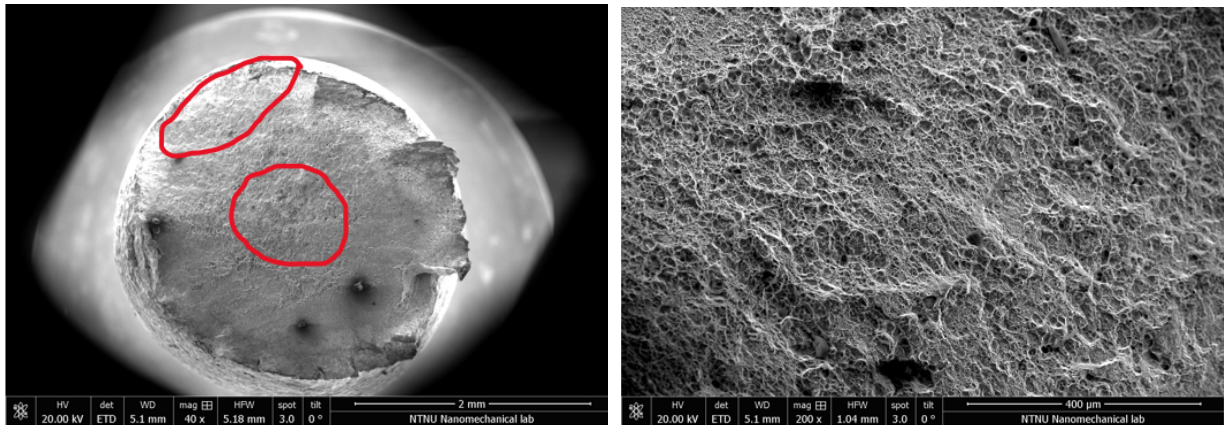
(d) Marked left edge revealing transgranular cracking with 2000X magnification.

Figure 4.6.8: Overview of fracture surfaces for Sanicro35 from in-situ hydrogen charging in SSRT.

SCL

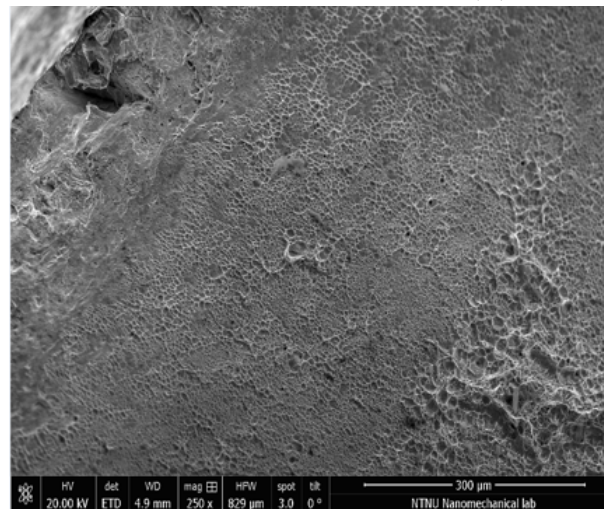
P750-H.S

The significantly longer testing period of 16 days before fracture was achieved for P750-H.S during in-situ hydrogen charging in SCL, did have a notable effect on the alloy in terms higher degree of embrittlement. The latter is especially being confirmed by the considerably longer brittle to ductile transition occurring in Figure 4.6.9c when compared to the transition occurring in Figure 4.6.5c during in-situ hydrogen charging in SSRT. The longer brittle to ductile transition post SCL has also correlated with the relatively lower %RA occurring in Figure 4.3.2, which as described has resulted in a reduction of 18.8% in %RA when comparing in-situ hydrogen charging in SCL with SSRT.



(a) Overview of fracture surface.

(b) Marked central area.



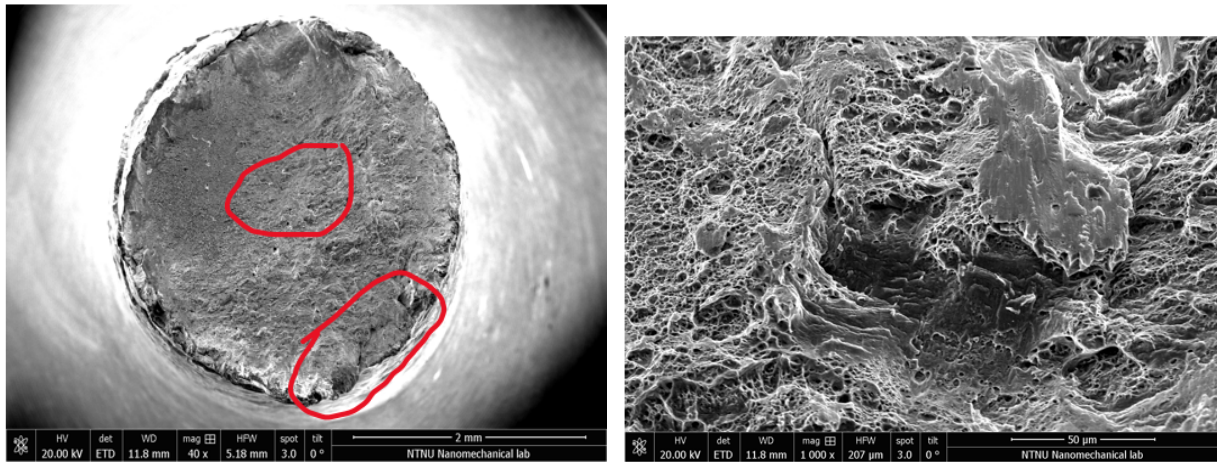
(c) Marked upper edge revealing the brittle to ductile transition.

Figure 4.6.9: Overview of fracture surfaces for P750-H.S from in-situ hydrogen charging in SCL.

P750-L.S

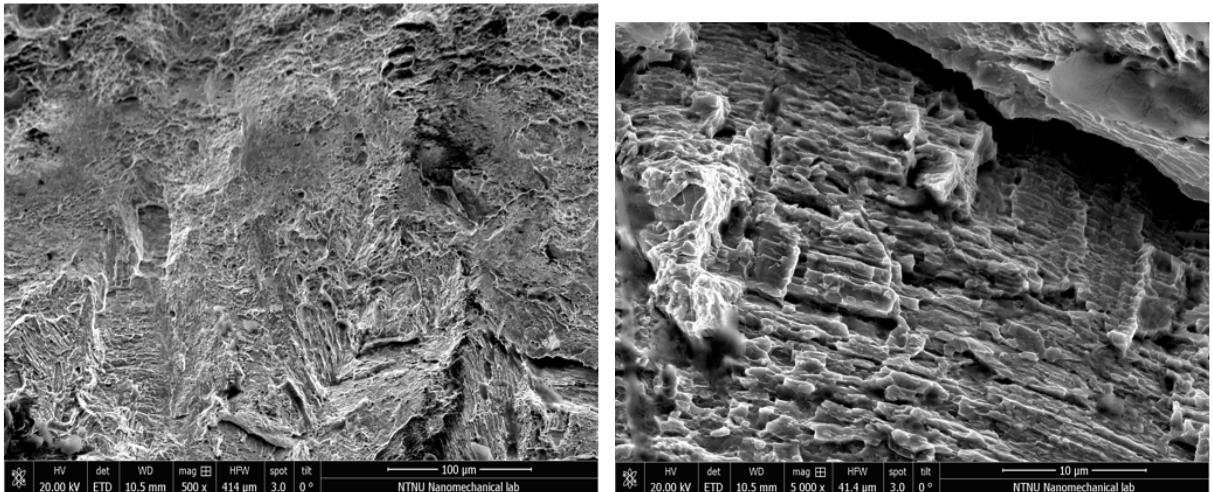
In contrast to the P750-H.S, the testing period for P750-L.S was approximately 8 days and the difference in %RA in comparison to SSRT has been minimal. However, it appears from Figure 4.6.9b that the deep dimples indicating the ductile central area which has been the case during SSRT, is no longer the dominating feature as some brittle facets have

occurred indicating hydrogen accumulation in central sites. Moreover, the transgranular cracking occurring in Figures 4.6.10c and 4.6.10d in the lower marked edge area seems to be much more severe compared to post SSRT.



(a) Overview.

(b) Marked central area.



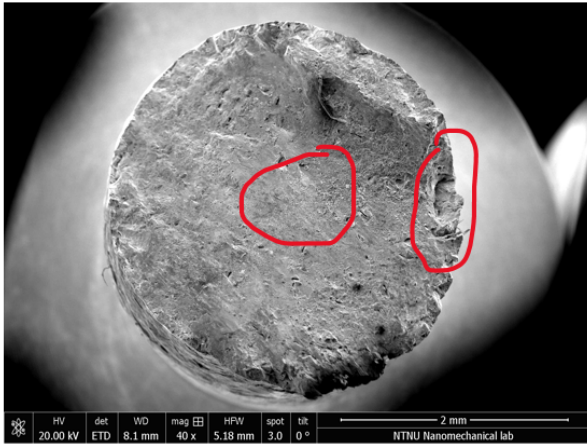
(c) Marked lower edge revealing the transgranular cracking.

(d) Different zone in the marked lower edge revealing the transgranular cracking

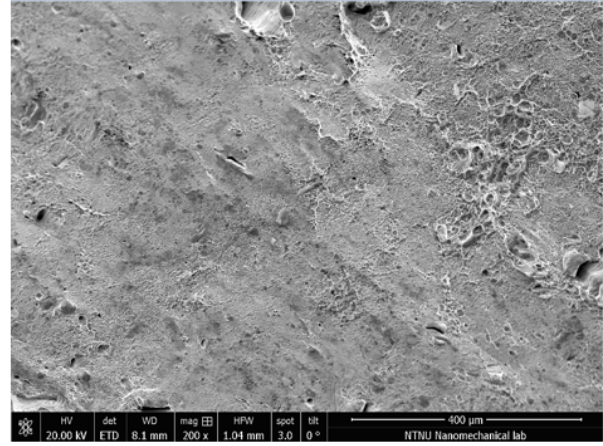
Figure 4.6.10: Overview of fracture surfaces for P750-L.S from in-situ hydrogen charging in SCL.

A31+

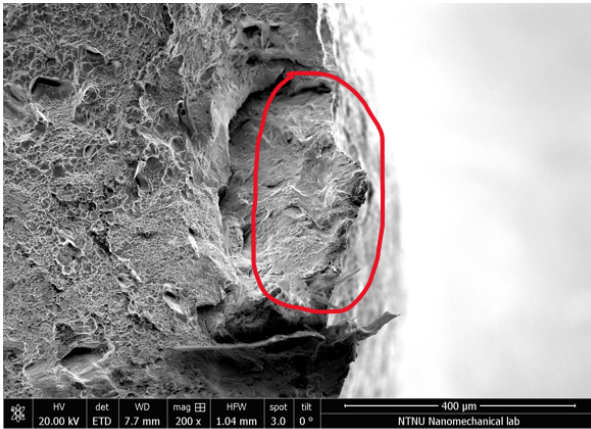
Similarly to Figure 4.6.7, the ductile morphology in terms of voids in the central area has been reduced dramatically from in-situ hydrogen charging, Figure 4.6.11b. In addition to being one of the alloys with the lowest %RA post SCL, brittle facets have occurred in the marked edge area indicating relatively larger hydrogen concentrations, Figure 4.6.11d. No brittle to ductile transition is observed for A31+ post SCL.



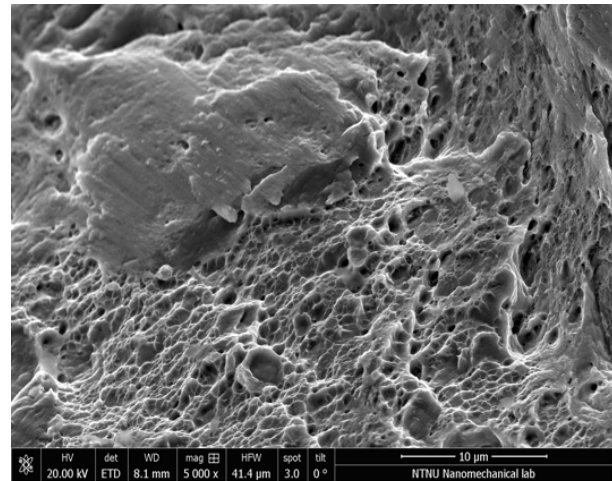
(a) Overview of fracture surface.



(b) Marked central area.



(c) Marked right edge.



(d) Marked right edge with a 5000X magnification revealing a brittle flat facet.

Figure 4.6.11: Overview of fracture surfaces for A31+ post in-situ hydrogen charging in SCL.

Sanicro35

In contrast to A31+, the central area of Sanicro35 maintained the ductile features indicating that the higher degree of embrittlement similarly to the outcome post SSRT only occurred in the edge areas, Figure 4.6.12b. However, in regards to the edge areas quite smooth flat facets have occurred in more areas in the edges compared to post SSRT indicating several zones in the edge area with relatively high hydrogen accumulation, Figures 4.6.12c and 4.6.12d.

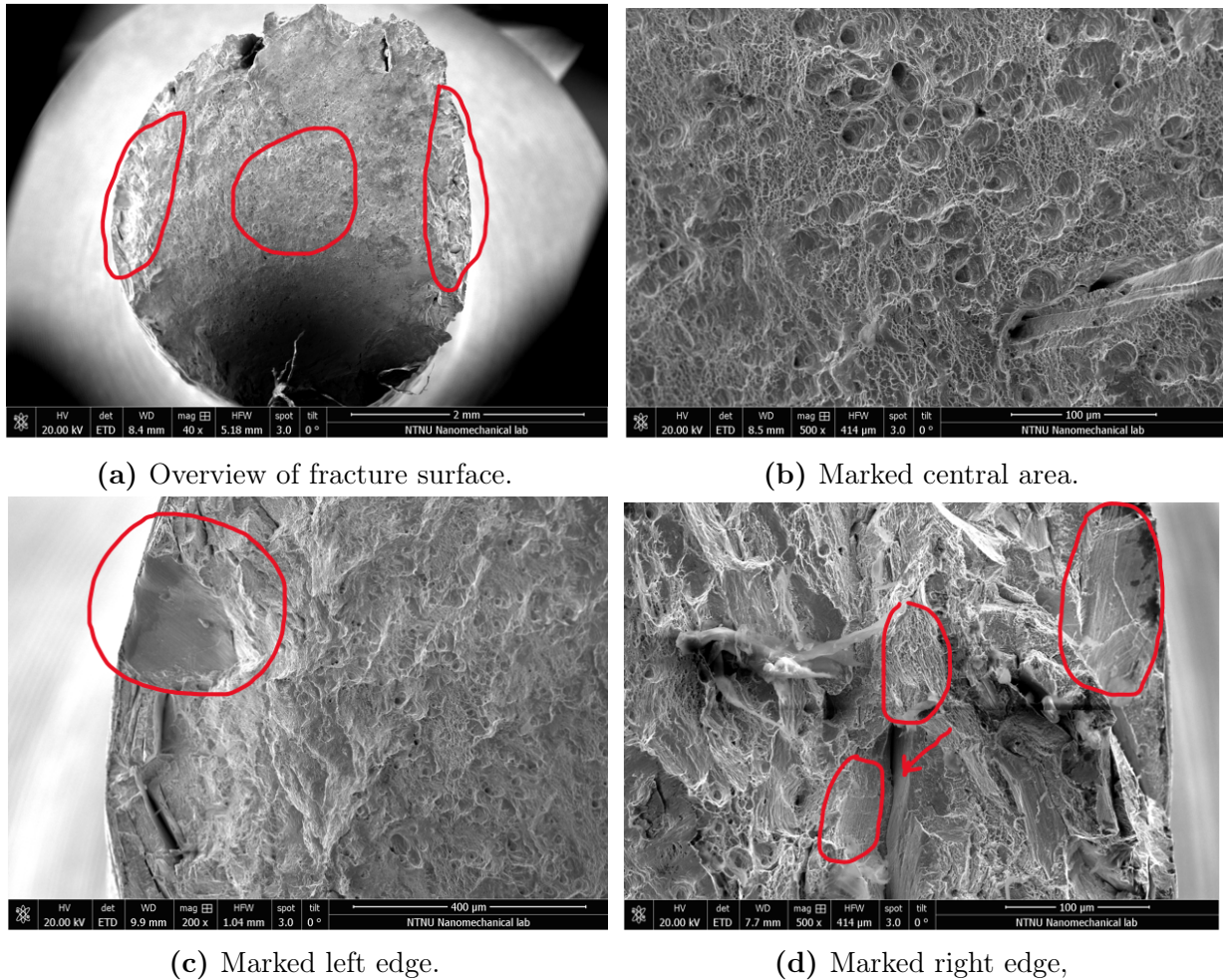


Figure 4.6.12: Overview of fracture surfaces for Sanicro35 from in-situ hydrogen charging in SCL.

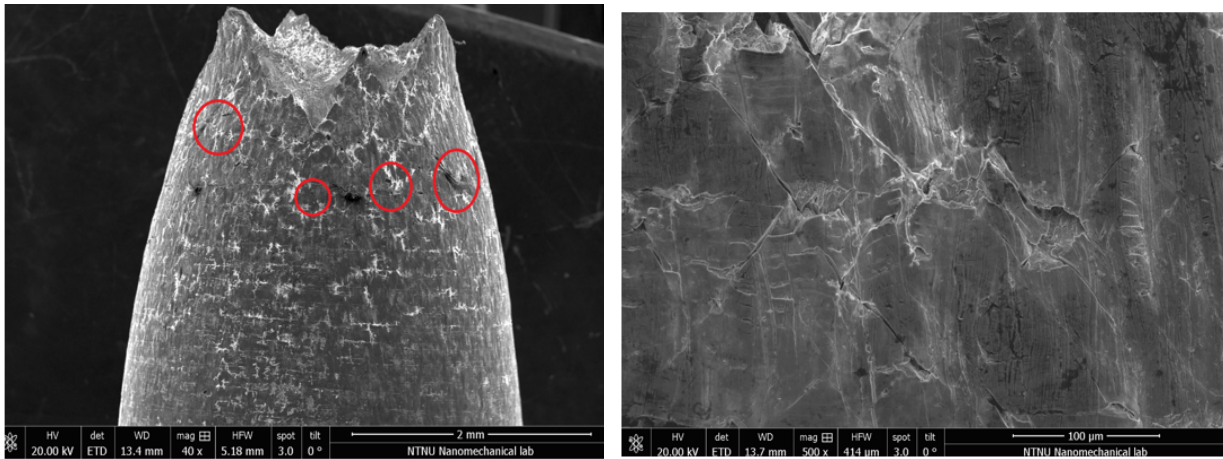
4.6.3 Secondary cracking

In the following an overview of the presence of secondary cracking for in-situ hydrogen charged samples post SCL and SSRT is provided. The following section describes the similarities and differences in the fracture surfaces of the secondary cracks and other HISC related characteristics which have occurred post SCL and SSRT for each alloy.

P750-H.S

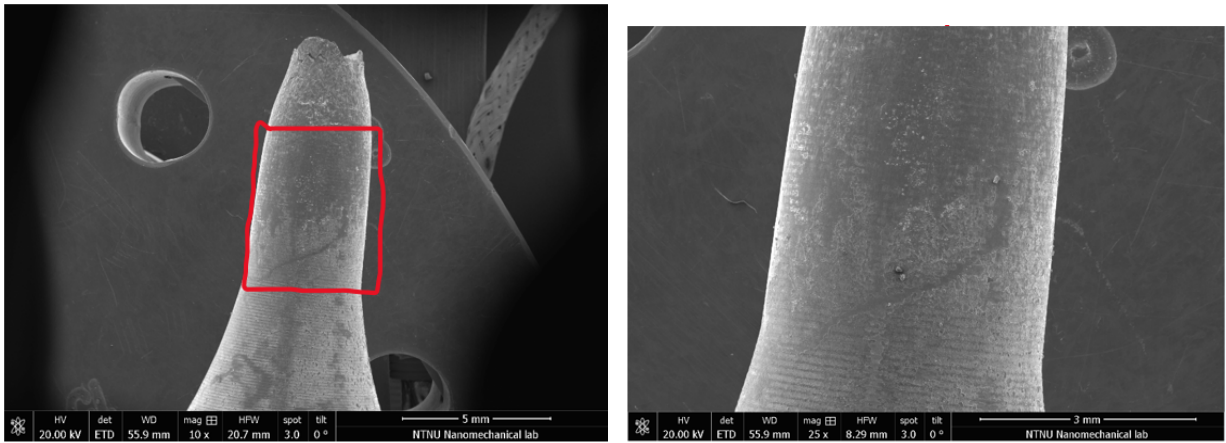
SSRT

It appears from Figure 4.6.13 that P750-H.S from in-situ hydrogen charging has experienced secondary cracking. Although, these have only appeared near the fracture surface whereas the marked area in the gauge section in Figure 4.6.13d do not consist of any brittle features or secondary cracks.



(a) Overview of secondary cracks near fracture surface.

(b) One of the marked areas in 4.6.13a showing the typical crack appearance for all the marked areas.



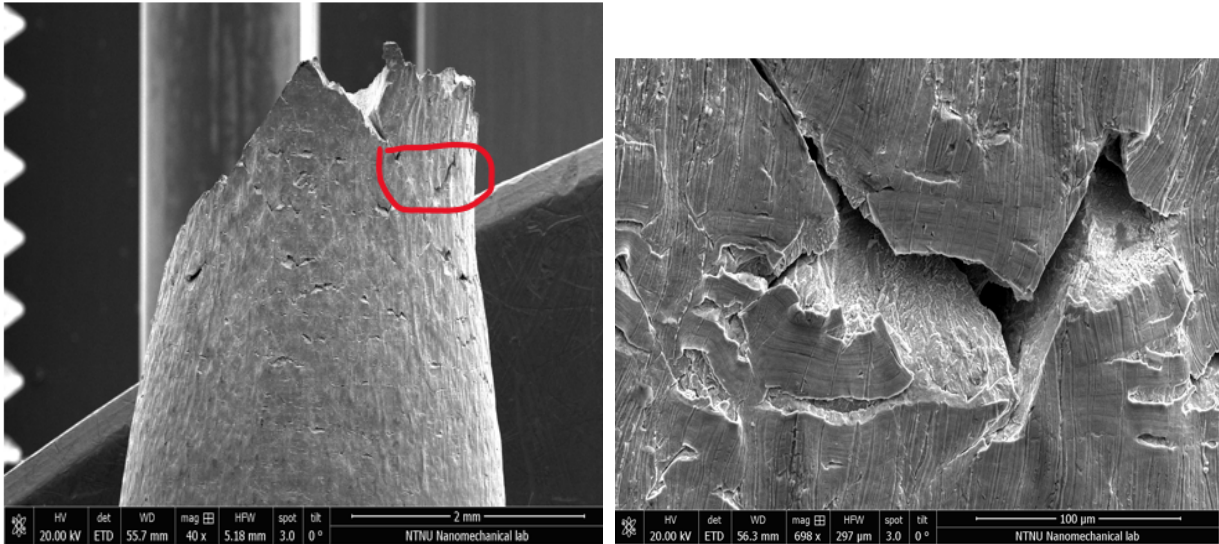
(c) Overview of the gauge section.

(d) Overview of the gauge section with a 25X magnification.

Figure 4.6.13: Overview of secondary cracking for P750-H.S from in-situ hydrogen charging in SSRT.

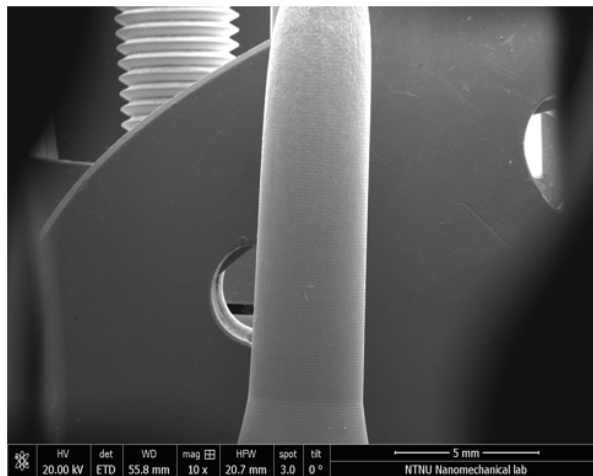
SCL

From Figure 4.6.14, it appears that the approximate concentration of secondary cracks has not changed post SCL for P750-H.S. However, much more severe transgranular cracking has occurred on the fracture surface of the marked secondary crack, Figure 4.6.14b. The latter may be due to significant longer test period before final fracture occurred. No secondary cracks further down the gauge section were observed, Figure 4.6.14c.



(a) Overview of secondary cracks near fracture surface.

(b) Secondary crack in marked area.



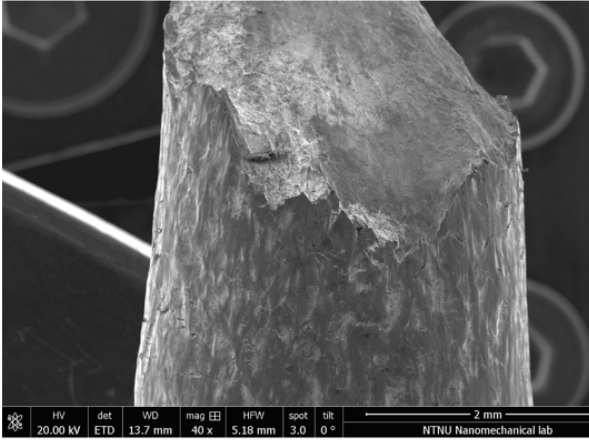
(c) Overview of gauge section.

Figure 4.6.14: Overview of secondary cracking for P750-H.S from in-situ hydrogen charging in SCL.

P750-L.S

SSRT

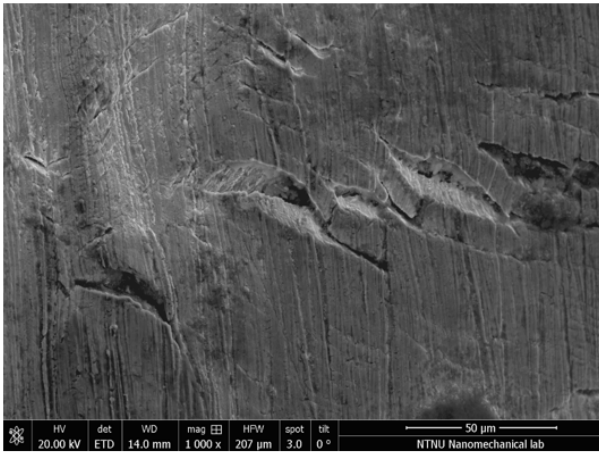
Similarly to P750-H.S, approximately same concentration of secondary cracks have occurred in the P750-L.S. However, the fracture surfaces of these cracks consists of traces of river pattern indicating to some degree aggressive transgranular cracking, Figures 4.6.15b and 4.6.15c. Brittle features or presence of secondary cracking further down the gauge section was not observed according to Figure 4.6.15e.



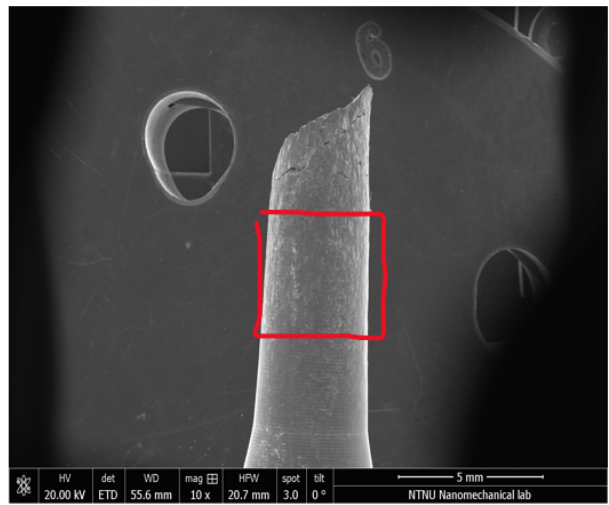
(a) Overview of secondary cracks near fracture surface.



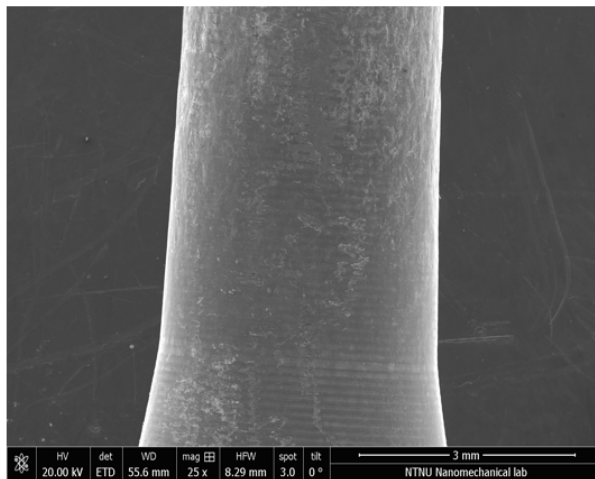
(b) Secondary crack in marked area.



(c) Secondary crack in marked area with 1000X magnification.



(d) Overview of gauge section.

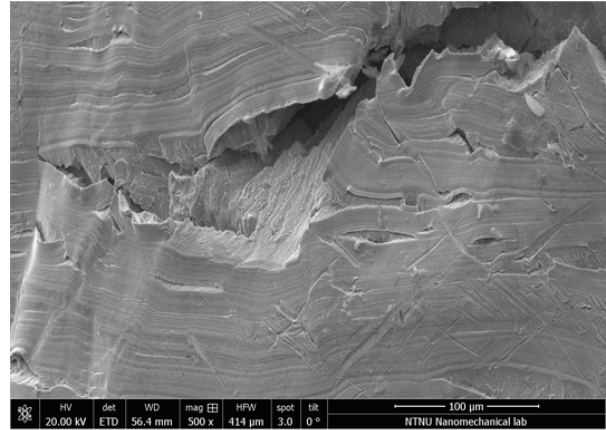
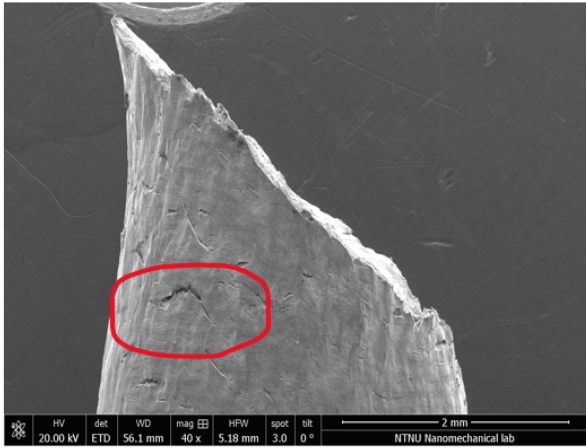


(e) Overview of gauge section with 25X magnification.

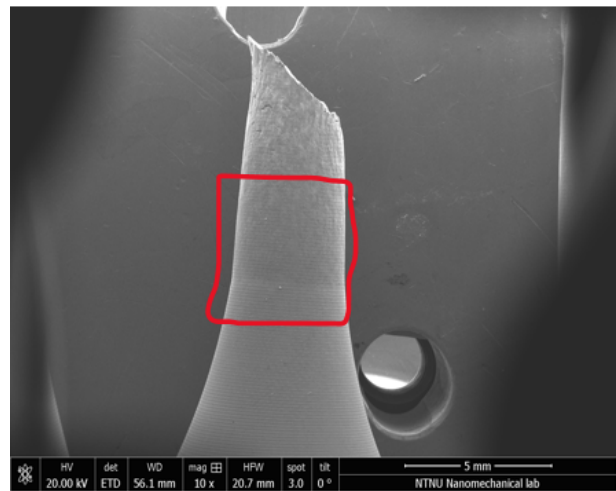
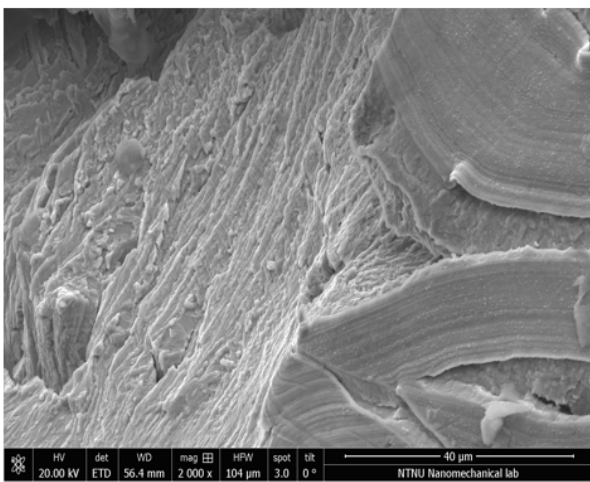
Figure 4.6.15: Overview of secondary cracking for P750-L.S from in-situ hydrogen charging in SSRT.

SCL

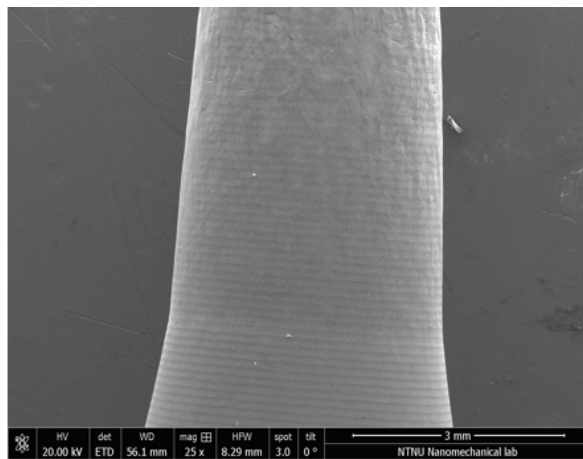
It appears from Figures 4.6.16b and 4.6.16c that a much severe transgranular cracking has occurred in fracture surfaces of secondary cracks post SCL compared to in SSRT for P750-L.S. No brittle features or secondary cracks were observed further down on the gauge section, Figure 4.6.16e.



(a) Overview of secondary cracking near fracture surface. (b) Fracture surface of secondary crack in marked area.



(c) Fracture surface of secondary crack in marked area with 2000X magnification. (d) Overview of gauge section.

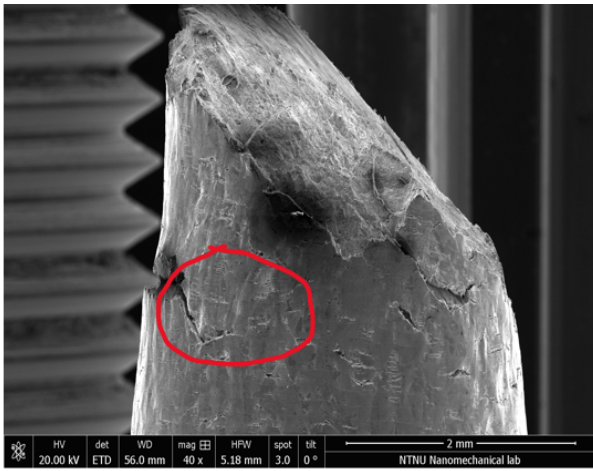


(e) Overview of gauge section with 25X magnification.

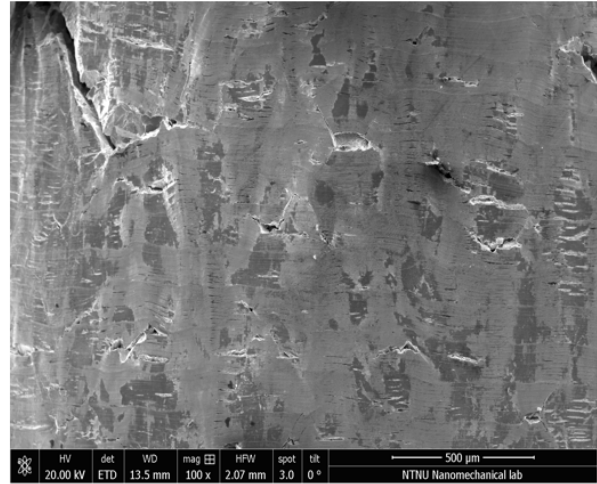
Figure 4.6.16: Overview of secondary cracking for P750-L.S from in-situ hydrogen charging in SCL.

SSRT

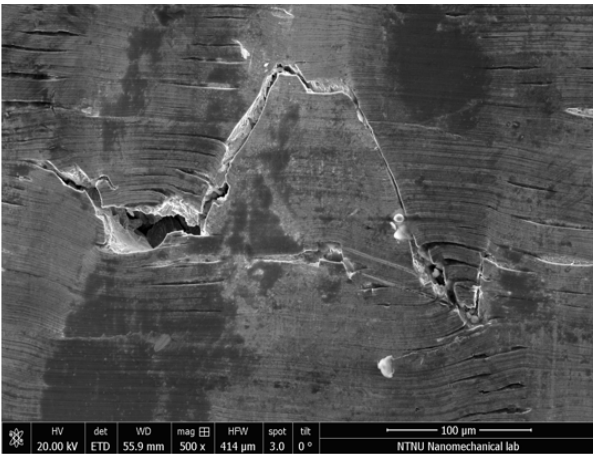
Secondary cracks have also occurred for A31+ post SSRT. In contrast to P750-L.S, not as aggressive transgranular cracking was observed on the fracture surfaces of the secondary cracks. No secondary cracks or other brittle features were observed further down the gauge section, Figure 4.6.17e.



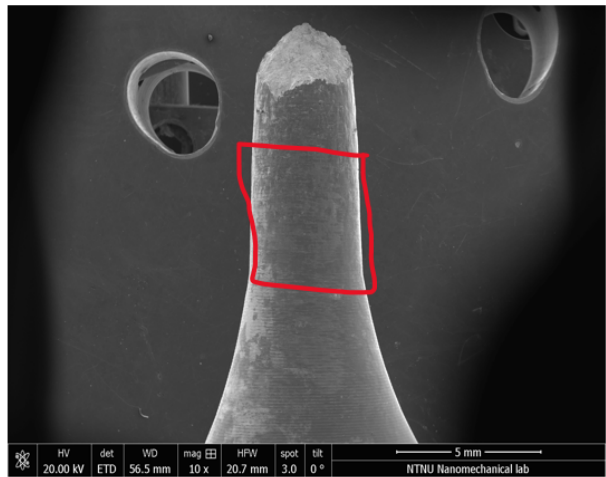
(a) Overview of secondary cracking near fracture surface.



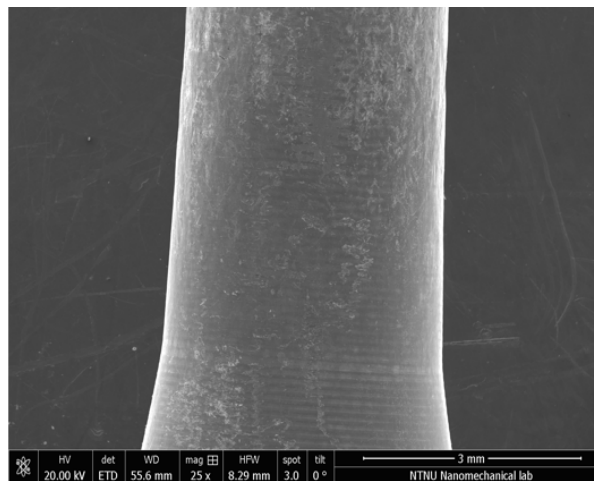
(b) Secondary cracks in marked area.



(c) Secondary cracks in marked area with 500X magnification.



(d) Overview of gauge section.

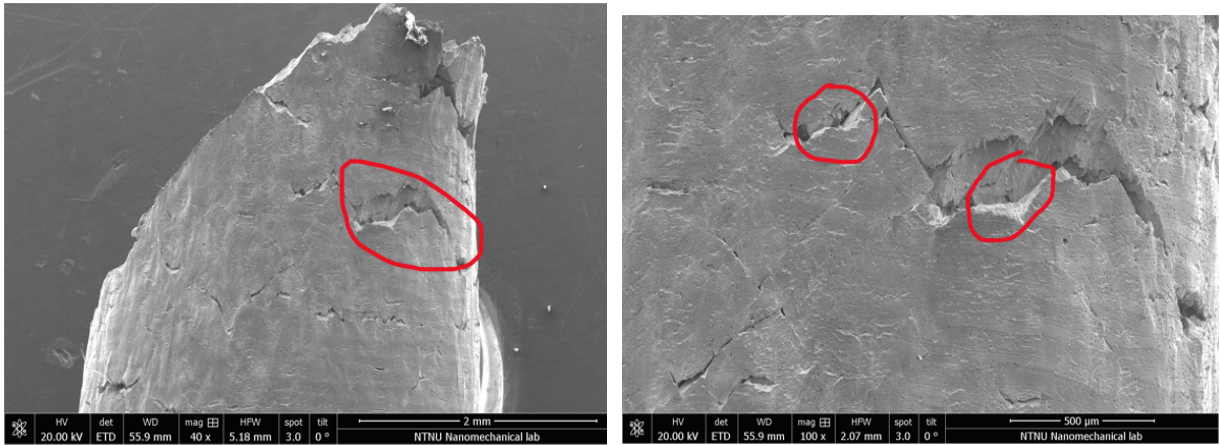


(e) Overview of gauge section with 25X magnification.

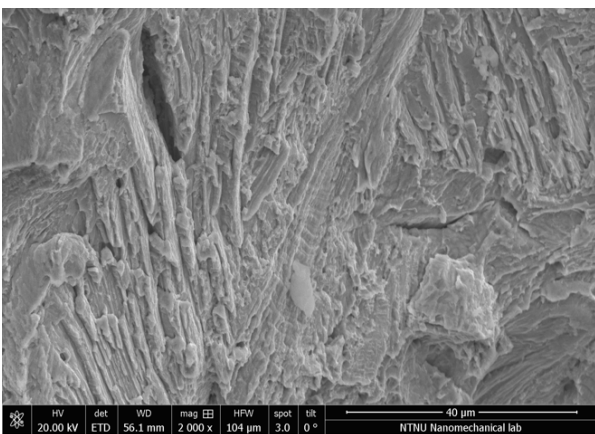
Figure 4.6.17: Overview of secondary cracking for A31+ from in-situ hydrogen charging in SSRT.

SCL

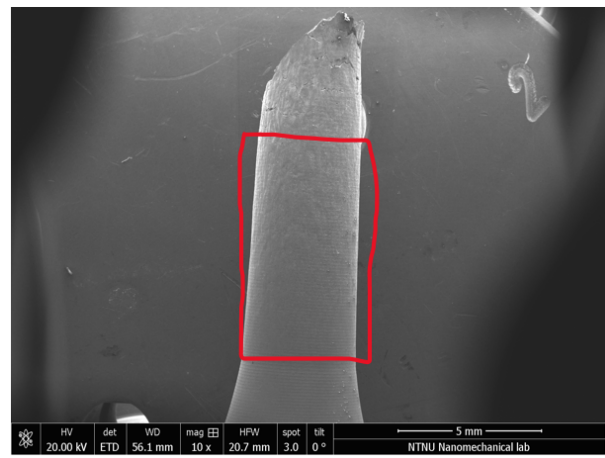
Much more aggressive transgranular cracking has occurred on the fracture surfaces of the secondary cracks for A31+ compared to post SSRT, Figure 4.6.18c. No further cracks or brittle features were observed further down the gauge section.



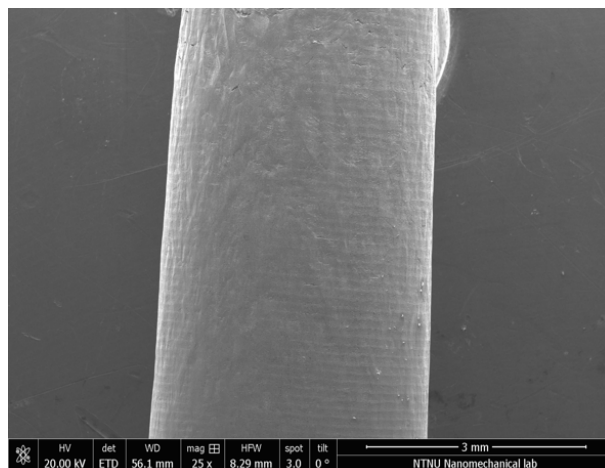
(a) Overview of secondary cracking near fracture surface. (b) Fracture surface of secondary crack in marked area.



(c) Fracture surface of secondary crack in marked area with 2000X magnification



(d) Overview of gauge section.



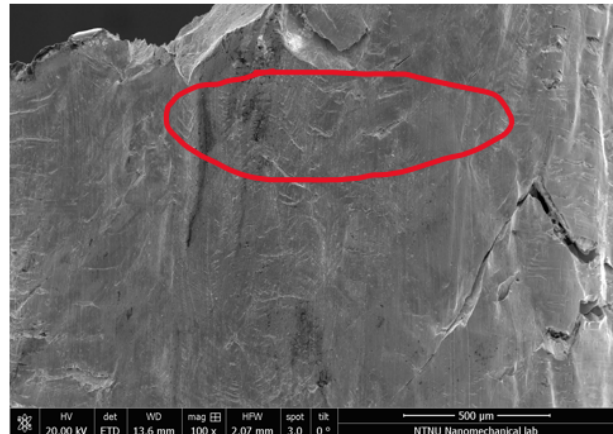
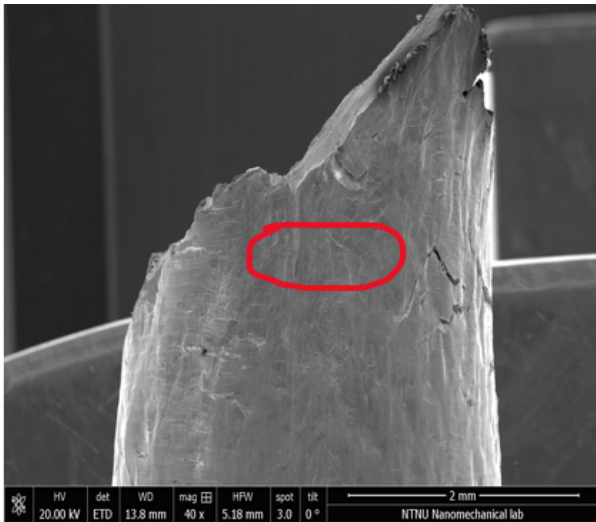
(e) Overview of gauge section with 25X magnification.

Figure 4.6.18: Overview of secondary cracking for A31+ from in-situ hydrogen charging in SCL.

Sanicro35

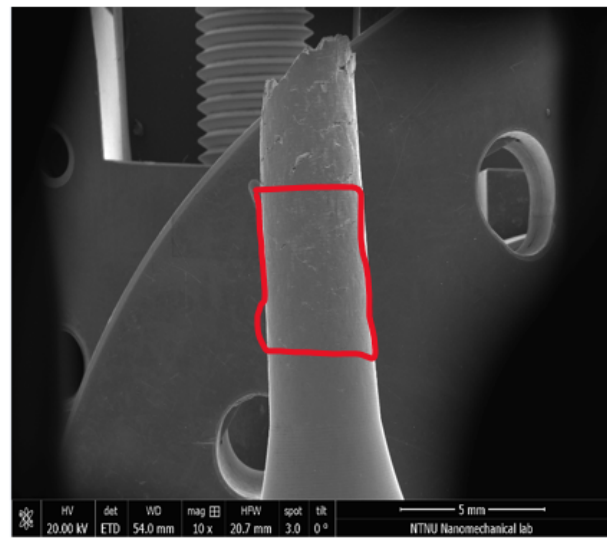
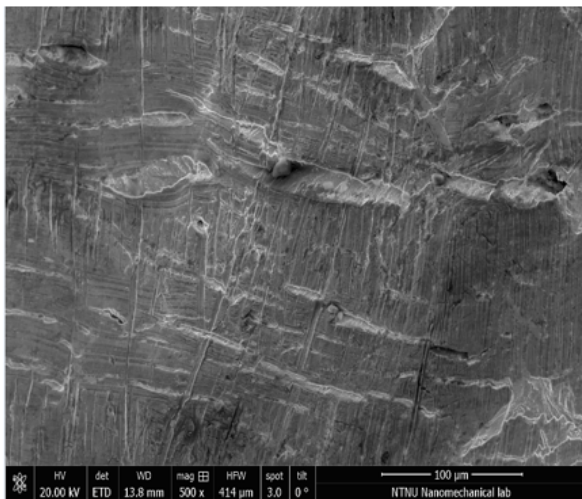
SSRT

Similarly to the P750-L.S alloy, small secondary cracks with to some extent aggressive transgranular cracking post SSRT have occurred on fracture surfaces of the secondary cracks, Figure 4.6.19c. In addition, secondary cracking was also observed further down the gauge section from the fracture surface, Figures 4.6.19d and 4.6.19e.



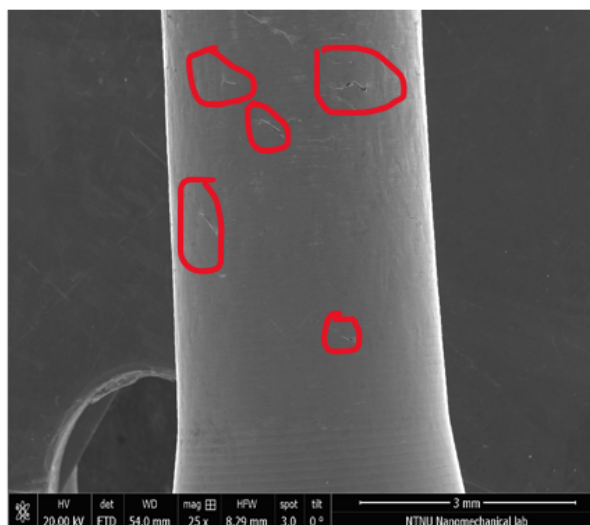
(a) Overview of secondary cracking near fracture surface.

(b) Fracture surface of the secondary cracks in marked area.



(c) Fracture surface of secondary crack in marked area with 500X magnification

(d) Overview of gauge section.

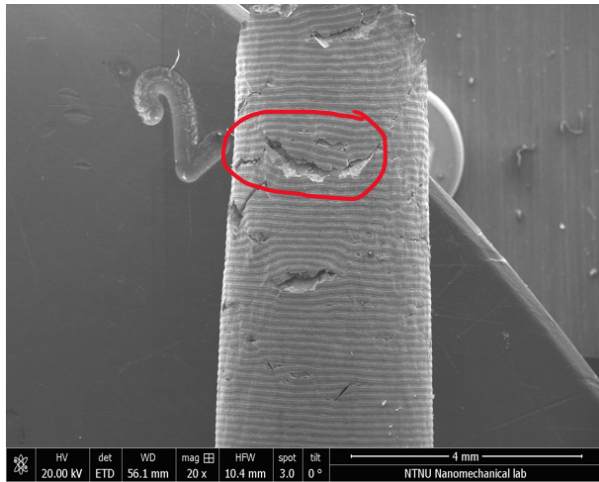


(e) Overview of gauge section with 25X magnification.

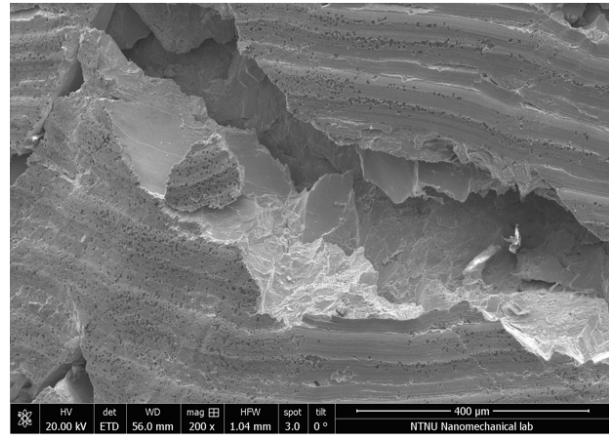
Figure 4.6.19: Overview of secondary cracking for Sanicro35 from in-situ hydrogen charging in SSRT.

SCL

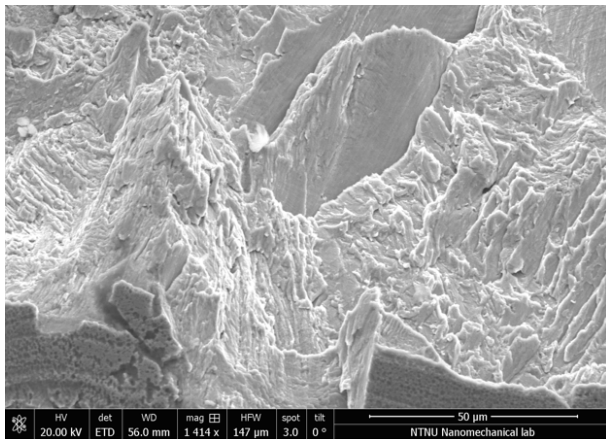
Sanicro35 post SCL compared to the other alloys suffered the most severe secondary cracking, Figure 4.6.20a. It especially appears from the Figures 4.6.20b and 4.6.20c that the Sanicro35 alloy has been subject to the most aggressive transgranular cracking in the gauge section. More secondary cracks have also been observed further down the gauge section from the fracture surface, similarly to the result post SSRT.



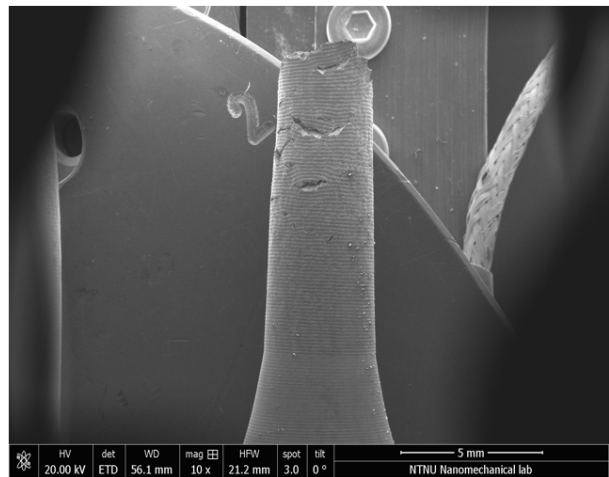
(a) Overview of secondary cracking near fracture surface.



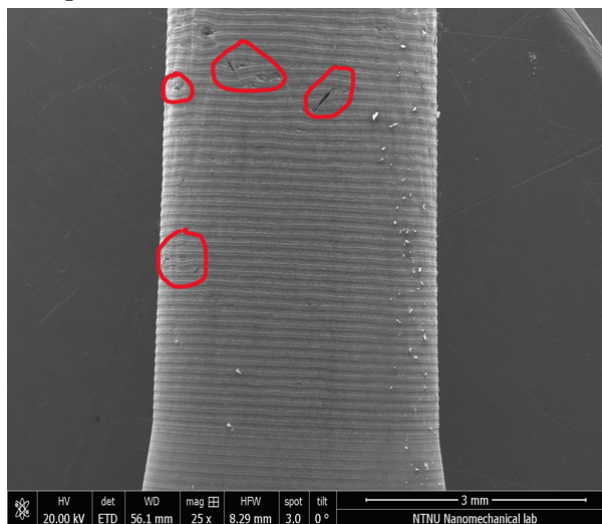
(b) Fracture surface of the secondary crack in marked area.



(c) Fracture surface of the secondary crack in marked area with 1400X magnification.



(d) Overview of gauge section.



(e) Overview of gauge section with 25X magnification.

Figure 4.6.20: Overview of secondary cracking for Sanicro35 from in-situ hydrogen charging in SCL.

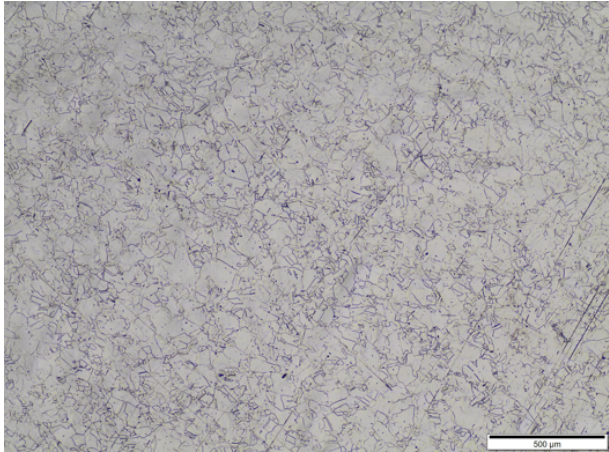
4.7 Microstructure evaluation

4.7.1 Microstructure overview

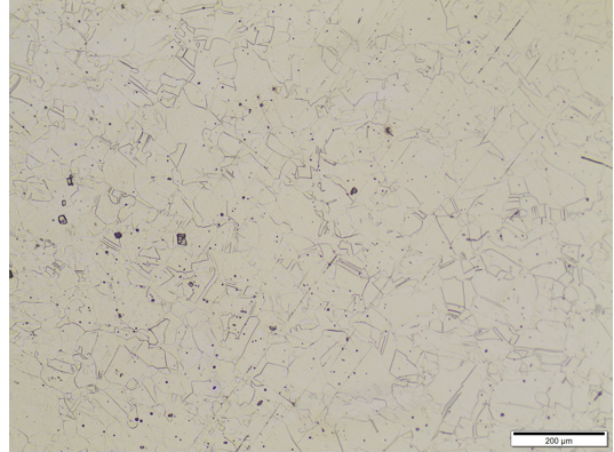
The microscopical overview has been obtained through optical microscopy with 5X, 10X and 20X magnifications for four cold worked alloys, Figures 4.7.1, 4.7.2, 4.7.3 and 4.7.4. Different etching methods were proposed by the material suppliers, but due to low clarity through the immersion techniques procedure described in section 3.11 has consistently been used for all four alloys. The grain diameter and the corresponding ASTM grain size was obtained by the means of Jeffries method in accordance with ASTM E112. When comparing the values provided in Table 4.7.1, the grain size according to ASTM E112 have correlated with the grain size provided in the alloys respective material certificates in Appendix A

Table 4.7.1: Grain diameter and the corresponding ASTM grain size for the alloys investigated.

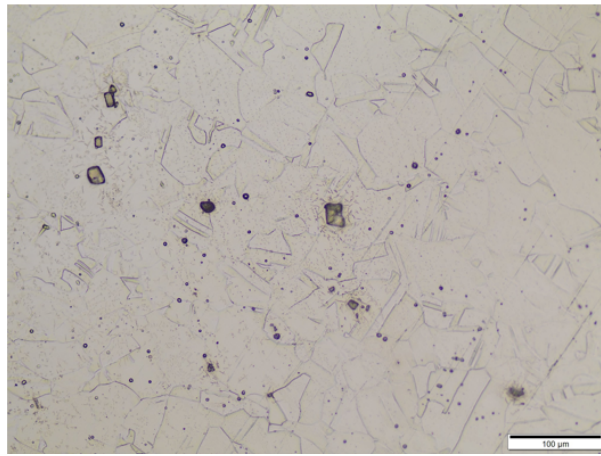
Alloy	Grain diameter (μm)	ASTM Grain size
P750-H.S	101	3.50
P750-L.S	210	1.50
A31+	180	2.00
Sanicro35	200	1.50



(a) P750-H.S at 5X magnification.

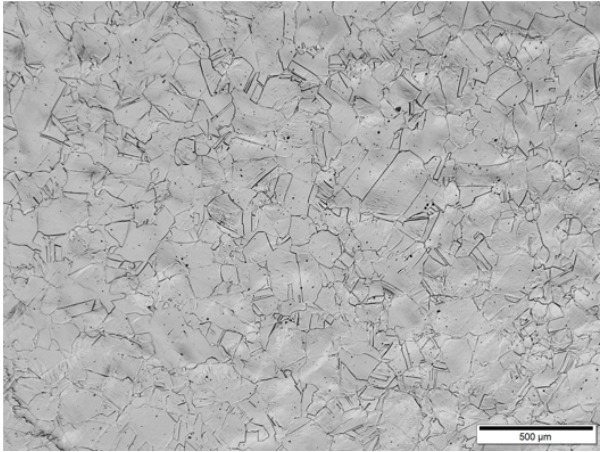


(b) P750-H.S at 10X magnification.

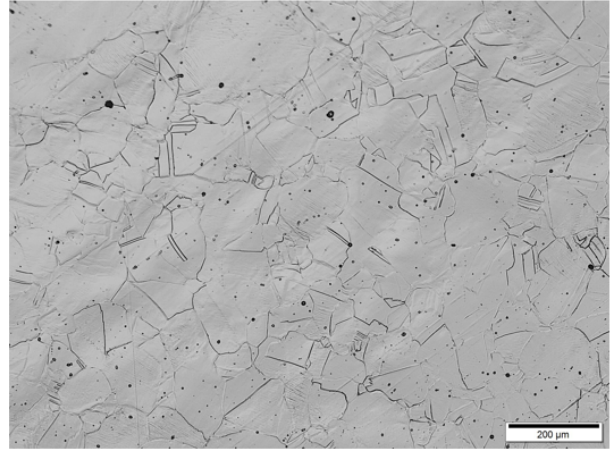


(c) P750-H.S at 20X magnification.

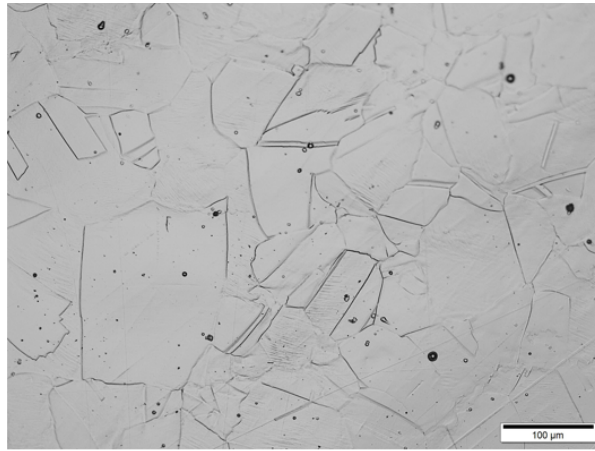
Figure 4.7.1: Microscopical overview of P750-H.S.



(a) P750-L.S at 5X magnification.

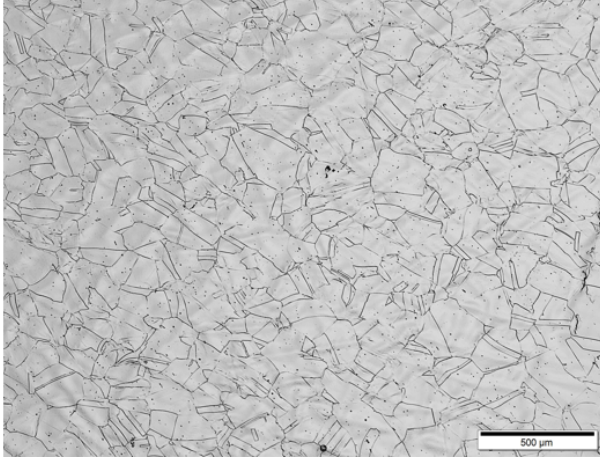


(b) P750-L.S at 10X magnification.

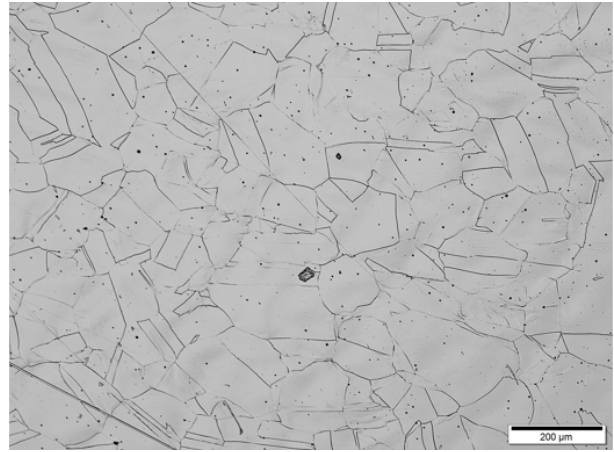


(c) P750-L.S at 20X magnification.

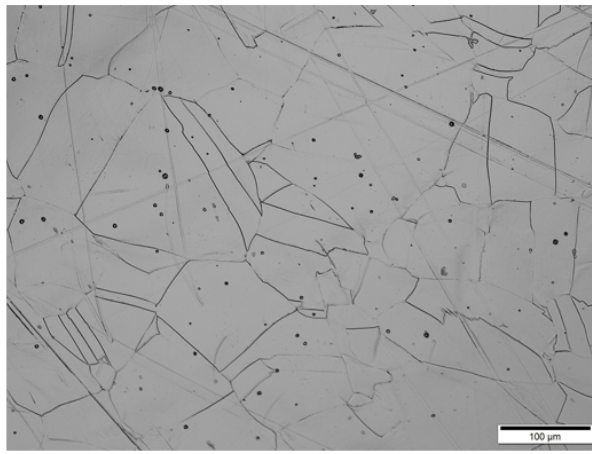
Figure 4.7.2: Microscopical overview of P750-L.S.



(a) A31+ at 5X magnification.

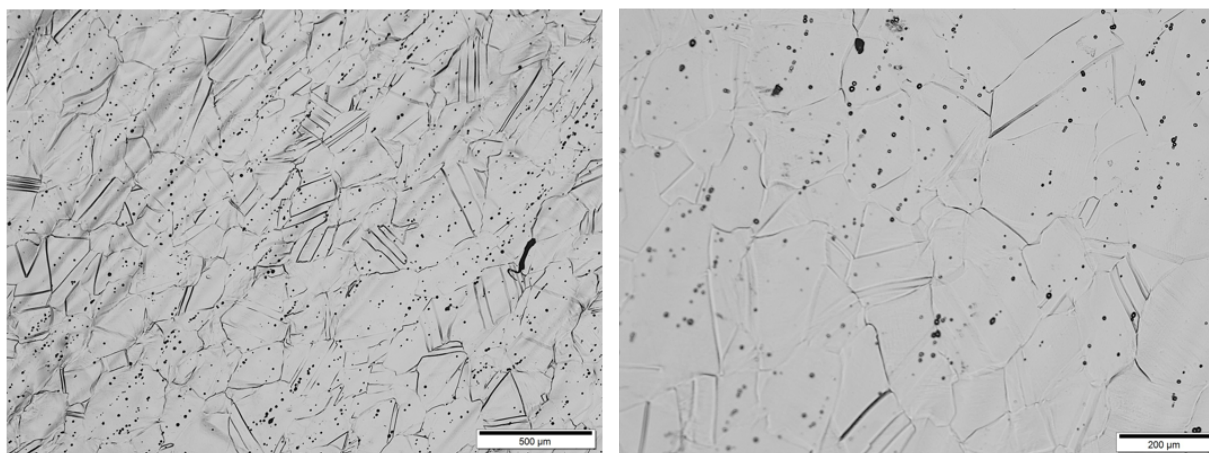


(b) A31+ at 10X magnification.



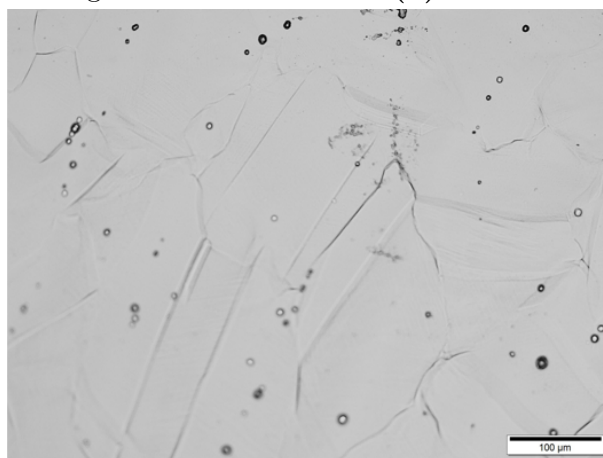
(c) A31+ at 20X magnification.

Figure 4.7.3: Microscopical overview of A31+.



(a) Sanicro35 at 5X magnification.

(b) Sanicro35 at 10X magnification.



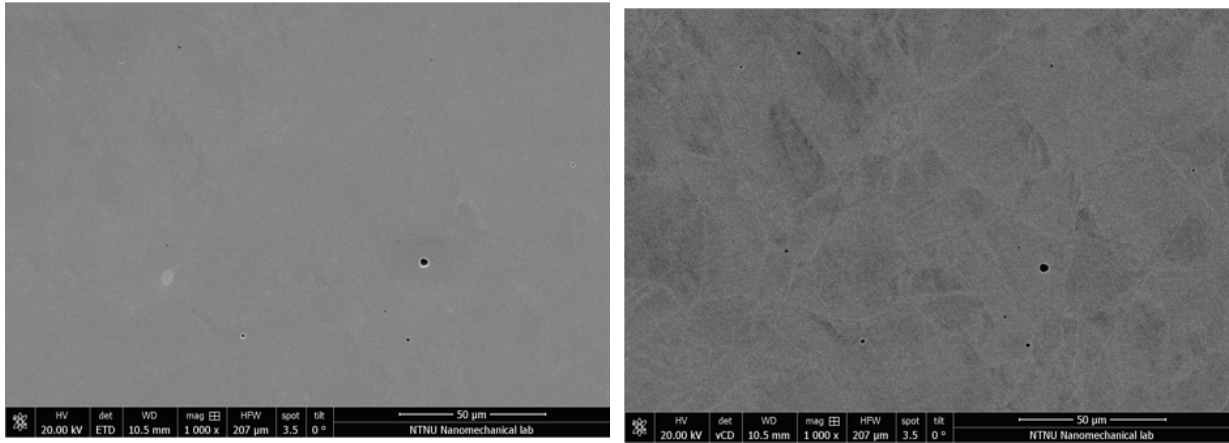
(c) Sanicro35 at 20X magnification.

Figure 4.7.4: Microscopical overview of Sanicro35.

4.7.2 EDS analysis

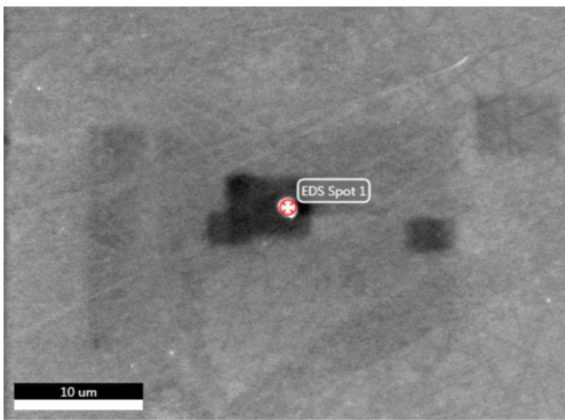
The results from chemical assessments of precipitates detected in the microstructures of the alloys investigated is provided in the following. It appears in the case of both P750 alloys from Figures 4.7.5 and 4.7.6 that the inclusions detected mainly consist of magnesium and oxygen, whereas for Sanicro35 according to Figure 4.7.10 mainly aluminium and oxygen. As the 25%Cr SDSS has been used as a reference alloy during localized corrosion testing an EDS analysis has been carried out. Similarly to the latter nickel alloys, the inclusion detected in 25%Cr SDSS mainly consisted of oxygen, chromium and aluminium, Figure 4.7.11. In contrast, according to Figure 4.7.7 both a secondary phase and inclusion is detected in the microstructure of A31+. It appears from Figure 4.7.8 that the chemical composition of the inclusion consisted of relatively higher wt% of molybdenum and chromium compared to the other alloys. In regards to the secondary phase detected in Figure 4.7.9, magnesium and oxygen is the dominating elements.

P750-H.S

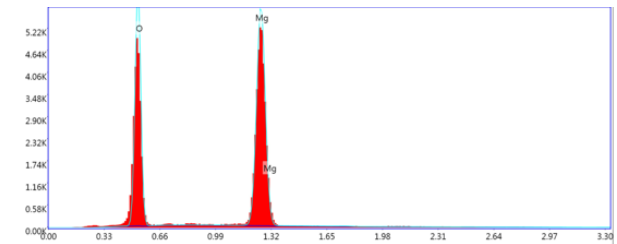


(a) Microstructure overview obtained by SE detector.

(b) Microstructure overview obtained by BSE detector.



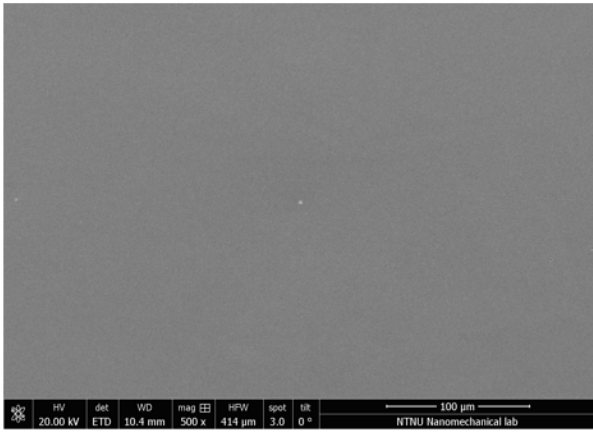
(c) Detected inclusion in microstructure.



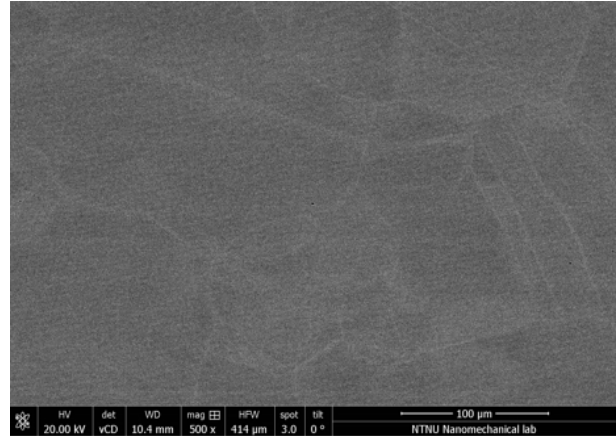
(d) Chemical assessment of detected inclusion.

Figure 4.7.5: EDS evaluation of P750-H.S.

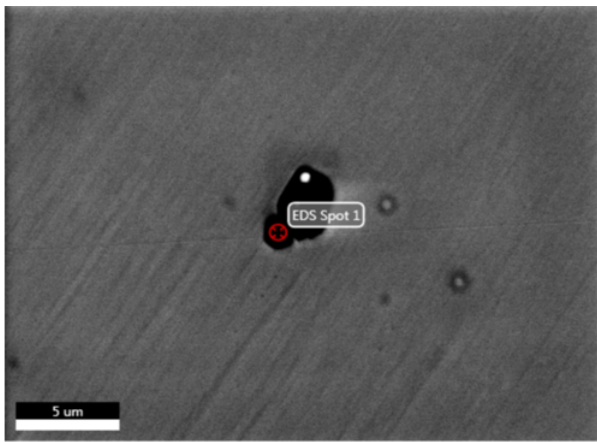
P750-L.S



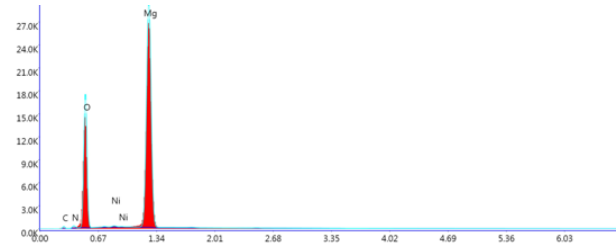
(a) Microstructure overview obtained by SE detector.



(b) Microstructure overview obtained by BSE detector.



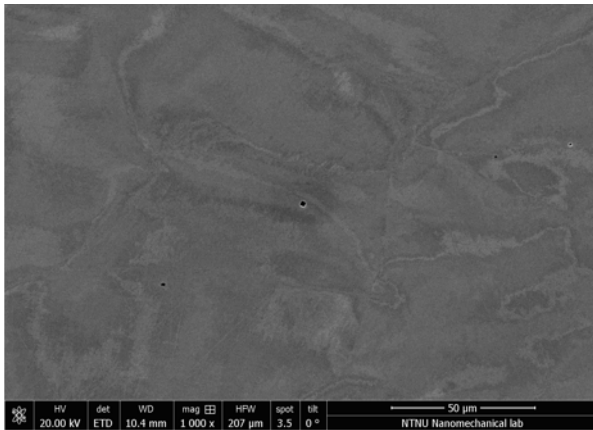
(c) Detected inclusion in microstructure.



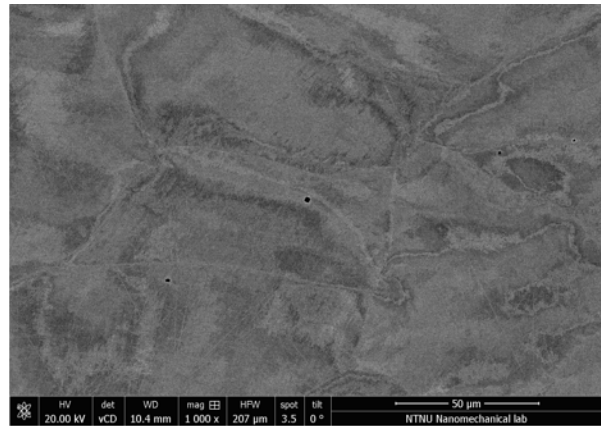
(d) Chemical assessment of detected inclusion.

Figure 4.7.6: EDS evaluation of P750-L.S

A31+



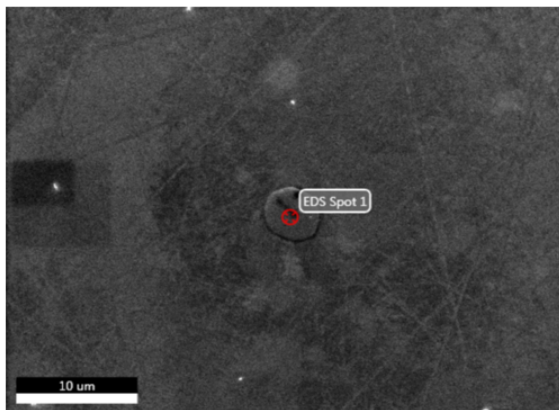
(a) Microstructure overview obtained by SE detector.



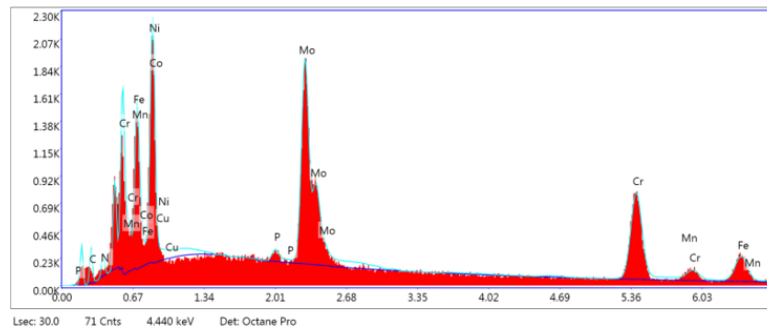
(b) Microstructure overview obtained by BSE detector.

Figure 4.7.7: Microstructure overview of A31+ obtained through SEM.

Precipitate - inclusion



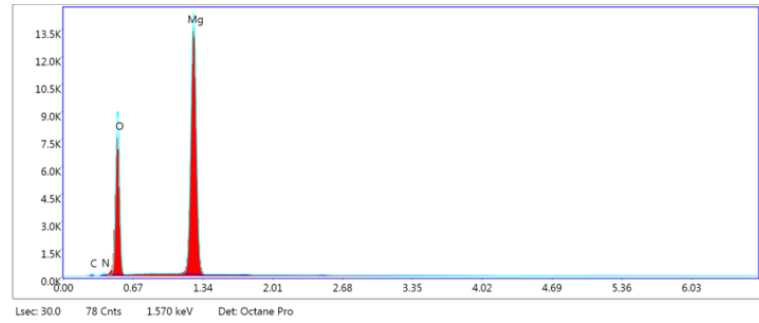
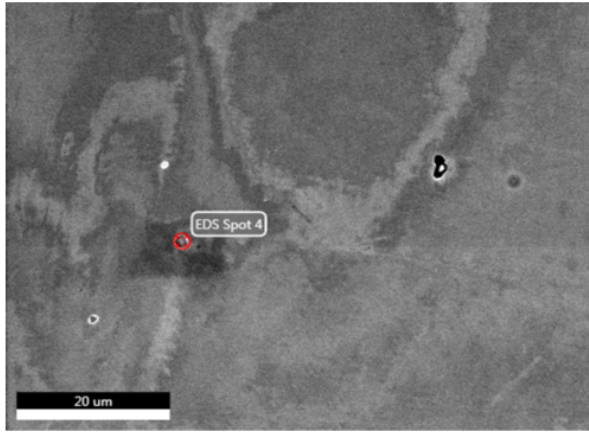
(a) Detected inclusion in microstructure.



(b) Chemical assessment of detected inclusion.

Figure 4.7.8: EDS evaluation of detected inclusion in A31+.

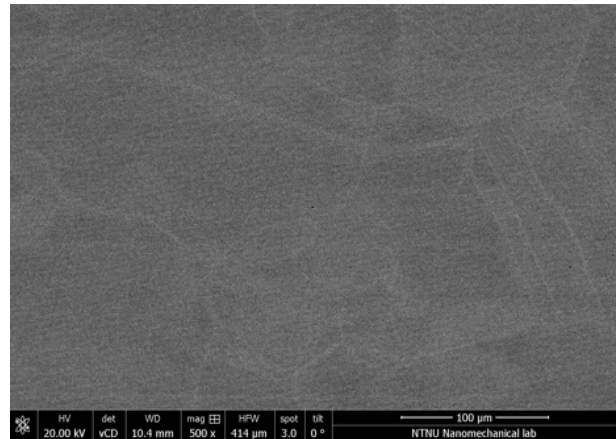
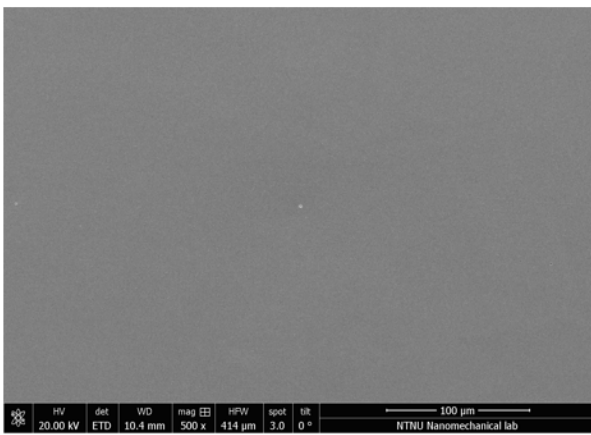
Precipitate - secondary phase



(a) Detected secondary phase in microstructure. (b) Chemical assessment of detected secondary phase.

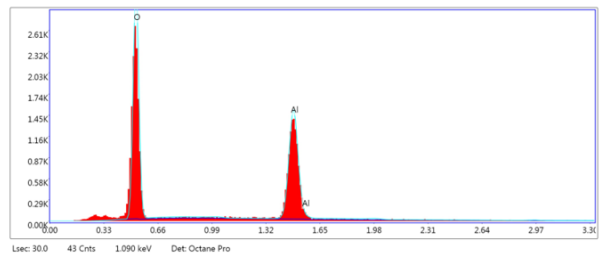
Figure 4.7.9: EDS evaluation of secondary phase detected in A31+.

Sanicro35



(a) Microstructure overview obtained by SE detector.

(b) Microstructure overview obtained by BSE detector.

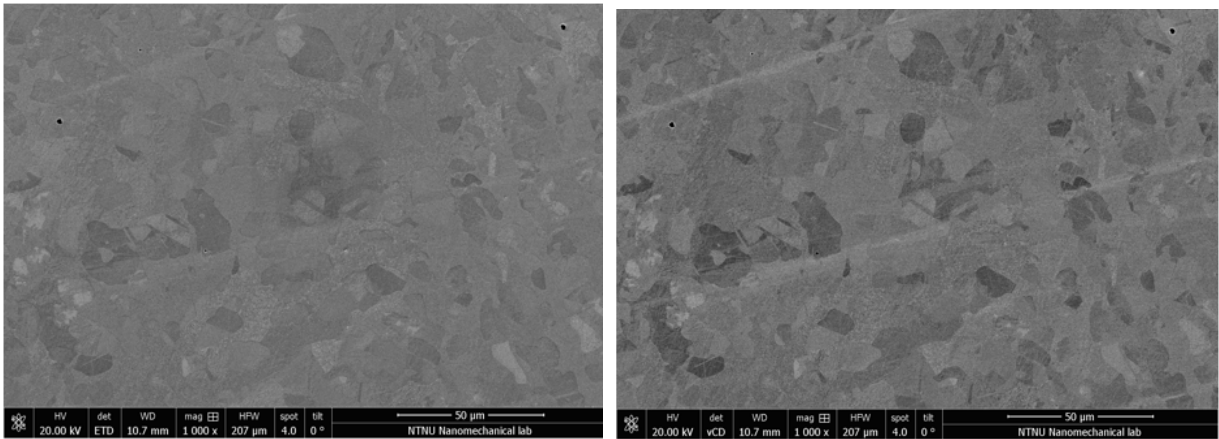


(c) Detected inclusion in microstructure.

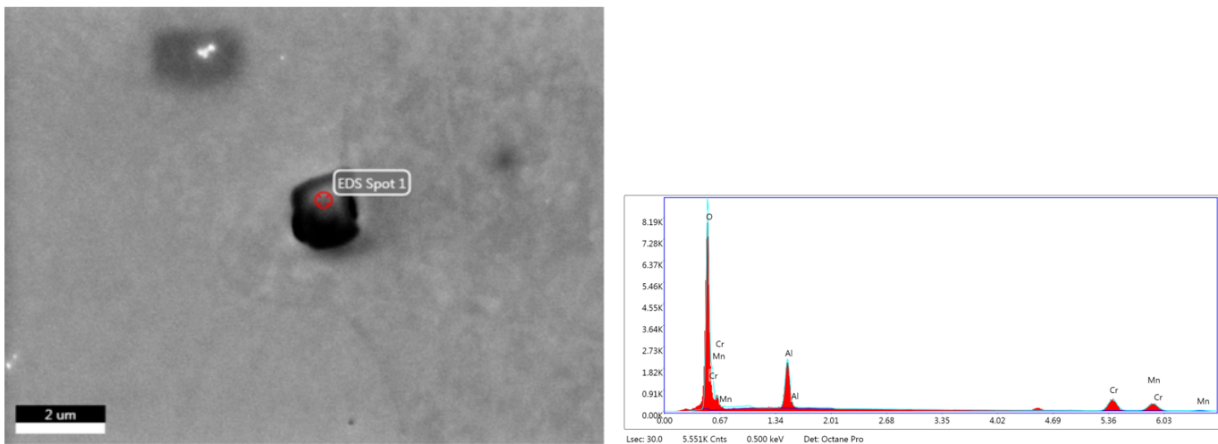
(d) Chemical assessment of detected inclusion.

Figure 4.7.10: EDS evaluation of Sanicro35.

25%Cr SDSS



(a) Microstructure overview obtained by SE detector. (b) Microstructure overview obtained by BSE detector.



(c) Detected inclusion in microstructure. (d) Chemical assessment of detected inclusion.

Figure 4.7.11: EDS evaluation of 25%Cr SDSS.

4.8 Localized corrosion testing

In the following results from ASTM G48 Method C are presented. As mentioned in section 3.9, the initiation of pitting is defined as a permanent potential drop below +450 mV_{Ag/AgCl} consequently the CPT being a temperature value corresponding to a potential drop of more than 50-100 mV. However, an individual assessment of each alloy has been made as repassivation before the final potential drop has occurred for some of the alloy samples.

In the case of P750-H.S-A sample, the potential development is steady until a temperature increase occurs from 75-80°C which results in a lasting potential fall below the defined potential threshold for pitting, Figure 4.8.1a. The P750-H.S-B sample experiences a repassivation at the same temperature increase before the lasting potential drop. Similarly, the P750-L.S-B sample experiences a minor repassivation at a lower temperature compared to P750-H.S-B followed by a lasting potential drop when temperature is increased from 70-75°C, Figure 4.8.1b. The P750-L.S-A sample has a steady potential development before experiencing the potential fall at the same temperature increase as its parallel sample. In

the case of A31-B a minor potential decline is occurring when a temperature increase from 65-70°C is performed. The final potential drop occurs immediately when temperature is increased from 70-75°C. The A31-A sample does experience the same potential decline at the temperature increase of 65-70°C, although not the final potential drop which led to pitting as the parallel sample, Figure 4.8.1c. Both 25%Cr SDSS-A and 25%Cr SDSS-B samples does in similar fashion as P750-L.S-B show tendencies to repassivation, Figure 4.8.1e. Although, this occurs at a relatively lower temperature increase of 60-65°C. The final potential drop for both samples occurs short time after a temperature increase of 65-70°C. The 25%Cr SDSS-A sample experiences a relatively smaller potential drop indicating only initiation of pitting, whereas for 25%Cr SDSS-B pitting attacks occurred on the sample surface. According to Figure 4.8.1d the Sanicro35 alloy do not experience any permanent potential drop at any of the temperature increments, hence initiation of pitting did not occur.

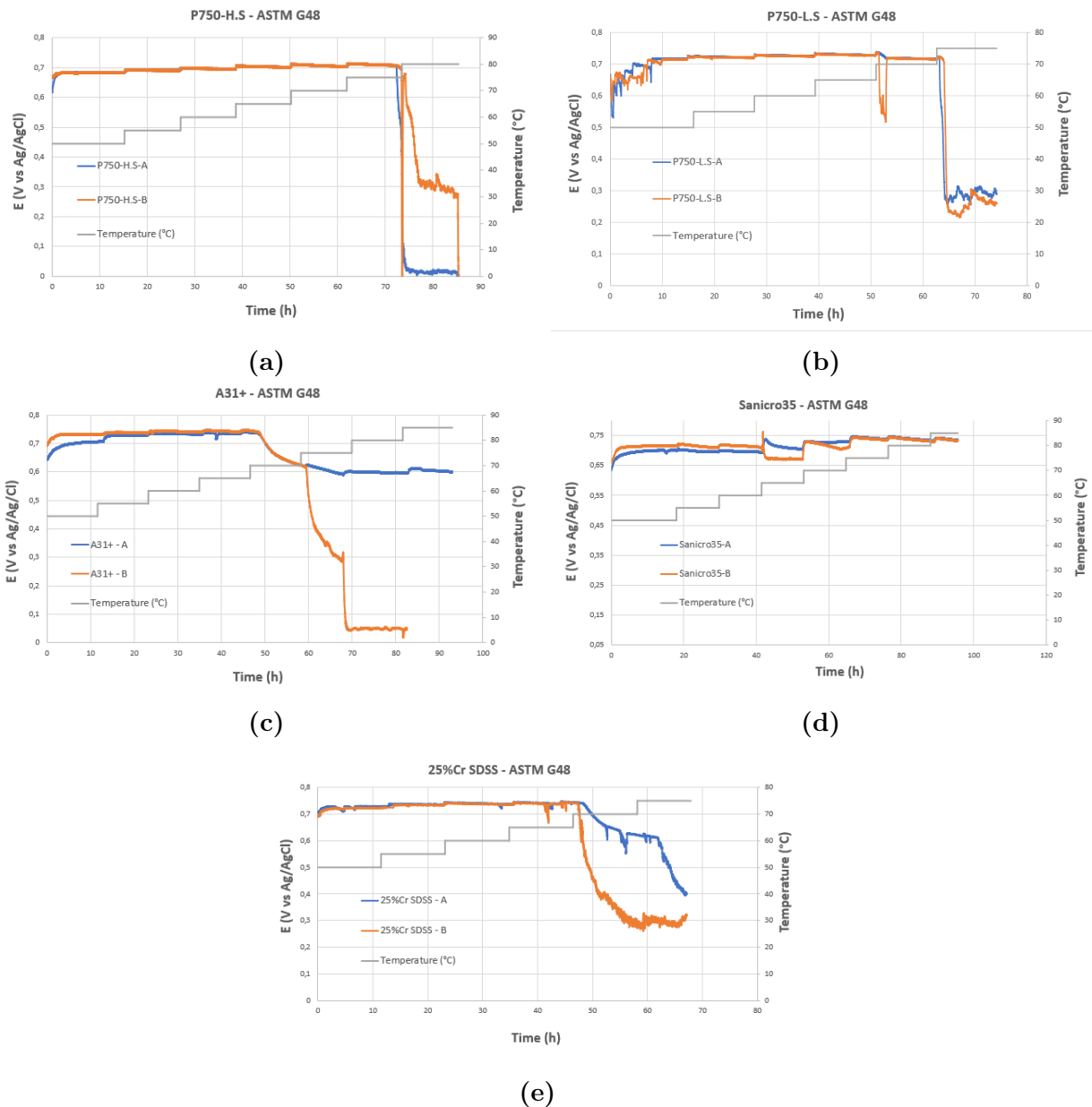


Figure 4.8.1: Potential development and temperature increase as a function of time for alloys investigated by ASTM G48 Method C.

The PREn for each alloy calculated according to equation 2.1.5, final determined CPTs with weight difference are presented in Table 4.8.1. For P750-H.S-A sample compared to its parallel sample a positive weight difference of 1.44 g has occurred, which is not consistent with the samples corrosion behavior according to Figure 4.8.1a as pitting attacks have occurred on sample surface. The weight increase is due to remaining deposit from the electrolyte solution used during testing. The weight difference for P750-H.S-B sample correlate with the corrosion behavior and CPT for the alloy have been determined to a temperature interval of 75-80°C. The 25%Cr SDSS-A sample also shows an weight increase inconsistent with corrosion behavior, which also may be due to remaining deposit on the sample surface. The parallel sample have experienced expected weight decrease according to its corrosion behavior as pitting attacks were observed on sample surface. The CPT for 25%Cr SDSS alloy have been determined to <70°C. The weight differences for A31,

Sanicro35 and P750-L.S is as expected and does correlate with their respective corrosion behaviors and with visually observed pitting attacks. The CPTs for A31, Sanicro35 and P750-L.S have been determined to be <75°C, 85°C< and <75°C, respectively.

Table 4.8.1: Overview of PREn for each alloy, weight difference and CPT achieved post ASTM G48 testing.

Alloy	Weight, before (g)	Weight, after (g)	Weight difference (g)	CPT (°C)	PREn
P750-H.S-A	22.71	24.15	1.44	75-80	42
P750-H.S-B	24.16	22.15	-2.01	75-80	42
P750-L.S-A	28.09	27.72	-0.37	<75	42
P750-L.S-B	24.26	23.85	-0.41	<75	42
A31-A	18.60	18.60	0.00	<75	52
A31-B	14.04	13.96	-0.08	<75	52
Sanicro35-A	10.78	10.76	-0.02	85<	52
Sanicro35-B	9.96	9,96	0,00	85<	52
25%Cr SDSS - A	22.06	22.35	0.29	<70	43
25%Cr SDSS - B	22.40	21.65	-0.75	<70	43

Chapter 5

Discussion

5.1 Sources of error

- As a result of time constraints, the number of samples tested during SCL has been low. Hence, the stochastic randomness becomes large leading to results specifically obtained through SCL to become a subject to uncertainty. Especially in the case of P750-H.S, the %RA was notable lower than expected where potential reasoning has been discussed. However, the latter results combined with the analysis from SSRT have been used to rate the alloys susceptibility to HISC during this study.
- The average diameter of the gauge section of specimens used for HISC testing has been $3.78 \text{ mm} \pm 0.032$ which has deviated somewhat from the machine drawing which has been in accordance with NACE TM0198. The average diameter of each gauge section was measured by the use of a caliper with an accuracy of 0.02 mm. The latter uncertainties have been included in every test carried out in SSRT and SCL and consequently may have affected the calculated stress values to some extent.

5.2 Slow strain rate testing

As expected, all four alloys investigated have been affected by HE consequently resulting in HISC, although the mechanical performance of the alloys has significantly varied. When comparing the HE indicators for all four alloys obtained from SSRT, a few interesting correlations have been observed in how variations in degree of embrittlement have affected the mechanical ductility loss. As it appears from Figures 4.2.3 and 4.2.4, both A31+ and Sanicro35 are the alloys which in regards to loss in %RA and RAR have experienced the highest degree of embrittlement. However, despite this particular similarity relatively large differences in their respective ductility loss appearing in Figure 4.2.1 have shown to be one of the core observations of interest during this work.

It has not for this study been provided any concrete information regarding the alloys respective production routes or the %CW. Therefore, each alloys respective plastic deformation behaviors from SSRT, standard tensile testing and UTS-values have been used as indications of how the dislocations densities may vary. Moreover, as the A31+ similarly to P750-H.S are the relatively stronger alloys in terms of UTS and suffered relatively smaller ductility loss during in-situ hydrogen charging in comparison to testing in air environment,

higher dislocation densities in these alloys are assumed. The latter has also correlated with their respective grain size in accordance with ASTM E112 provided in Table 4.7.1.

In the case of A31+, it is being revealed from the EDS analysis in Figures 4.7.8 and 4.7.9 that both an inclusion and secondary phase were in fact detected in the microstructure of the alloy. In addition, the relatively smaller loss in fracture strain of 1.7% describes a plastic deformation behavior consisting of a dislocation motion which has experienced more or less similar resistance both in air and during in-situ hydrogen charging. However, according to the loss in %RA of 40.96% and a RAR of 43% there is no doubt that the alloy have experienced hydrogen absorption to larger extent compared to both P750 alloys. Due to the latter observations, it becomes debatable if reversible trapping of hydrogen through dislocation motion has been the only trapping mechanism resulting in the high degree of embrittlement. As a result, it can be argued that due to the detected precipitates if irreversible trapping of hydrogen has caused the similar degree of embrittlement as the Sanicro35. The relative minimal effect of absorbed hydrogen on the mechanical performance of A31+ during SSRT in air and in-situ hydrogen charging is also according to the HE indicators in Figure 4.2.4 being confirmed. Despite being one of the alloys which experienced the relatively high degree of embrittlement arguably due to higher irreversible trapping of hydrogen, the mechanical performance according to minimal loss in fracture strain and the HE indicators has not been affected to same extent as Sanicro35 and P750-L.S. It can therefore be argued if the HEDE mechanism may not have been the case despite the irreversible trapping of hydrogen specifically for A31+.

It can be assumed in the case of Sanicro35 similarly to P750-L.S, that relatively lower dislocation density was the case in which has been considered as one of the parameters affecting the mechanical performance during the in-situ hydrogen charging. This is being confirmed by the relatively larger losses in fracture strain, as Sanicro35 and P750-L.S maintained 65% and 82% of their respective fracture strains from the testing in air environment. In comparison to the A31+ and P750-H.S which maintained 91% and 98% of their respective fracture strains from air testing, indicates a significant reduction in ductility for the relative weaker alloys despite having as high or relative higher microstructure cleanliness. From the EDS analysis in Figure 4.7.10 no secondary phases has been detected in the microstructure of Sanicro35. Hence, it can be argued in comparison to the A31+ if the dominating trapping mechanism for Sanicro35 has been the hydrogen transport through dislocation motion resulting in the highest degree of embrittlement of all four alloys. In contrast to A31+, the relatively highest degree of embrittlement in addition to the loss in fracture strain has affected the mechanical performance according to the HE indicators. It is being confirmed according to the relatively lowest plastic elongation ratio and the highest HEI that Sanicro35 has been the candidate most susceptible to HISC during in-situ hydrogen charging in SSRT.

The P750-L.S alloy has experienced the smallest degree of HE according to the smallest loss of 29.06% in terms of %RA. In contrast, the A31+, Sanicro35 and P750-H.S suffered each their respective loss of 40.96%, 40.12% and 37.31%. The low degree of embrittlement in P750-L.S, is also being confirmed with the highest RAR of 57.59% indicating low embrittlement. However, as being one of the weaker alloys similarly to Sanicro35 a relatively larger loss in ductility occurred during in-situ hydrogen charging. No precipitates other than an inclusion has been detected according to the EDS evaluation in Figure 4.7.6 indicating high microstructure cleanliness. As the alloy similarly to Sanicro35 is the weaker alloy compared to P750-H.S and A31+, higher dislocation mobility can be expected.

The latter combined with relatively high microstructure cleanliness may be indications of reversible trapping of hydrogen occurring in the microstructure. As a result, it can be argued that the relatively poor mechanical performance during in-situ hydrogen charging has been a result of hydrogen transport through highly mobile dislocations into the plastic zones of the initiated crack tips resulting in a localized softening. According to the HE indicators, the P750-L.S similarly to Sanicro35 has achieved the lowest plastic elongation ratio and the highest HEI compared to P750-H.S and A31+ suggesting relatively high susceptibility to HISC.

The P750-H.S similarly to P750-L.S in contrast to both A31+ and Sanicro35 performed well in terms of embrittlement, which is being confirmed by the relatively smaller loss in %RA and significantly higher RAR. As mentioned earlier, the loss in fracture strain during in-situ hydrogen charging has been 0.35% consequently resulting in the alloy being capable of maintaining 98% of its fracture strain obtained from testing in air. Similarly to the P750-L.S and Sanicro35, it is being revealed from the EDS evaluation in Figure 4.7.5 that high microstructure cleanliness is in fact the case for P750-H.S as well. In addition, with P750-H.S being the alloy with the highest UTS and smallest grain size according to ASTM E112 of all the alloys investigated, low dislocation mobility can be assumed. Especially the latter combined with high microstructure cleanliness indicates that irreversible trapping may not be the dominating trapping mechanism of hydrogen when compared to A31+. The hydrogen may have been transported to a small degree by dislocations in motion. From a pure mechanical point of view, it is being confirmed according to the HE indicators that the alloy obtained the highest plastic elongation ratio of 95.98% and the lowest HEI of 4.02% indicating high susceptibility to HISC.

5.3 Stepwise constant loading

In terms of how either reversible or irreversible trapping of hydrogen might have affected the mechanical performance during in-situ hydrogen charging in SSRT is also being indicated in SCL as similar results in regards to FS and fracture strain have been achieved, Table 4.4.1. As only one sample from each alloy has been investigated due to time constraints, there is not enough data collection from the SCL alone to fully confirm each alloys susceptibility to HISC. Although, the values for FS, fracture strain and %RA have appeared within the standard deviations in results obtained from SSRT in which at least indicating the similar sensitivity levels to HISC.

Due to the nature of the experimental procedure of SCL longer testing periods compared to SSRT have been the case for the alloys investigated resulting in longer exposure time to in-situ hydrogen charging. As mentioned, especially in the case of P750-H.S the testing period was 16 days before fracture occurred. It appears from Figure 4.3.2 that a %RA of 20.25% have occurred resulting in a reduction of 18.8% compared to in-situ hydrogen charging in SSRT indicating the occurrence of higher degree of embrittlement during SCL. It can be argued that this may be a result of the longer testing period consequently resulting in higher hydrogen absorption. The latter may be due to the occurrence of pre-mature secondary cracks in early increments. However, it is to be noted that despite the lower %RA occurring in SCL indicating relatively high degree of embrittlement the P750-H.S alloy still managed to obtain 101% of its FS from SSRT and no change in fracture strain occurred. The latter combined with results obtained from SSRT have strongly confirmed the alloys high susceptibility to HISC. According to Figure 4.5.1, the P750-H.S

has also been the alloy with the lowest hydrogen concentration of 39.57 ppm which has correlated well with it being the alloy which has suffered the smallest loss in fracture strain during in-situ hydrogen charging in SSRT and SCL. The P750-L.S similarly to in SSRT, achieved the highest %RA of 38.62% indicating the lowest degree of embrittlement compared to the other alloys. Similarly to P750-H.S, the alloy managed to maintain 100% of its FS from SSRT. The fracture strain suffered a minor reduction of 3.5% during SCL in comparison to fracture strain obtained from in-situ charging in SSRT. The overall mechanical performance of P750-L.S during in-situ hydrogen charging in both SSRT and SCL has been stable. The hydrogen uptake in P750-L.S of 65.70 ppm has correlated well with the alloys %RA indicating the relatively lower degree of embrittlement compared to the Sanicro35 and A31+.

The A31+ and Sanicro35 have according to Figure 4.5.1 had the highest hydrogen uptake of 78.01 ppm and 96.64 ppm, respectively. In spite of this, the alloys managed to maintain 98% and 100% of their respective FS from SSRT. In addition, the fracture strains remained the same and appeared in their respective standard deviations in results obtained from SSRT. Overall, it appears from the obtained results that the mechanical performance from SSRT was confirmed during SCL in regards to fracture strain and FS for all four alloys. Especially in terms of HE, the A31+ and Sanicro35 have been the alloys most affected during in-situ hydrogen charging both in SCL and SSRT. Although, it has been the P750-L.S and Sanicro35 which have suffered the most in terms of mechanical ductility loss due to HE resulting in final HISC.

5.4 Fracture surfaces and secondary cracking

In the following a detailed explanation of the fractography study has been provided. The main focus in the following has been on fracture surfaces of in-situ hydrogen charged specimens and the occurrence of secondary cracking in their respective gauge sections. As mentioned in section 5.3, the testing periods have been longer in SCL for all alloy samples. The higher exposure time to in-situ hydrogen charging combined with potential development of pre-mature secondary cracks due to early increments, have resulted in fractures surfaces revealing considerably more severe transgranular cracking.

For P750-H.S, the reduction of 18.8% in %RA from SSRT to SCL indicating higher degree of HE, has correlated well with the notable reduced ductile morphology in edge and central area appearing in Figure 4.6.9. In addition, considerably deeper secondary cracks have occurred in the gauge section near the fracture surface post SCL compared to SSRT which may have contributed to the increased embrittlement. It is not possible from the experimental work conducted in this study to comment the diffusion properties of the alloys. However, it seems from Figure 4.6.5 compared to Figure 4.6.9 that the hydrogen may have diffused deeper towards central sites as the brittle to ductile transition has also been notable diminished post SCL. Similarly to A31+, it is to be noted that despite the increased embrittlement according to lower %RA, considerably more severe secondary cracks and reduced ductile morphology in the fracture surface the P750-H.S still managed to maintain the ductility in terms of fracture strain during SCL. The latter being another core observation during this study. The fracture surfaces of P750-L.S with the relatively highest RAR reveal high concentration of ductile voids in central area from in-situ hydrogen charging in SSRT in contrast to the fracture surfaces post SCL. Similarly to A31+, it appears from Figure 4.6.10b that brittle facets have occurred during SCL

indicating hydrogen accumulation in central sites. The secondary cracks from SSRT and SCL have not been as severe compared to A31+ and Sanicro35. However, as the P750-L.S had larger grain size combined with relatively cleaner microstructure it can be argued that in addition to similar diffusion properties that the hydrogen may have been transported through highly mobile dislocations during the applied strain.

For A31+, brittle features such as flat facets and significantly diminished ductile morphology have been the case during in-situ hydrogen charging in both SSRT and SCL respectively, Figures 4.6.7 and 4.6.11. Especially the occurrence of brittle flat facets indicating higher hydrogen accumulation in specific sites of central and edge areas may suggest higher diffusion of hydrogen in the alloy compared to the P750-H.S. The relatively more severe secondary cracks and the considerably higher hydrogen uptake substantiates the latter assumption.

The high degree of embrittlement of Sanicro35 during both SSRT and SCL is strongly being confirmed by Figures 4.6.8 and 4.6.12 where higher concentration of flat facets have occurred in the edge areas compared to the other alloys. However, in addition to being the alloy which suffered the largest ductility loss and had the largest hydrogen uptake relatively stable ductility morphology has been maintained in the central area of the fracture surface during both SSRT and SCL in contrast to both P750 alloys and A31+. The latter may suggest that atomic hydrogen might not have managed to reach central sites through either diffusion or through dislocations in motion. In comparison to the other alloys, the Sanicro35 has severed the most aggressive secondary cracks from in-situ hydrogen charging in SCL, Figure 4.6.20. Especially in Figure 4.6.20e, more aggressive secondary cracks have occurred further down in the gauge section which has not been the case for the other alloys.

5.5 Comparison of strain hardened and PH grades.

In the following, a comparison of HISC sensitivity of alloys investigated and CRAs discussed in section 2.7 has been provided. The results obtained below are from authors which have carried out similar experimental procedures as described in this study. During this comparison, it is the acceptance criterion defined by Bothina et al.[27] for plastic elongation ratio which has been used to rate the ductility loss during in-situ hydrogen charging in SSRT. If the plastic elongation ratio would be $\geq 45\%$ for a given alloy, the acceptance criteria would be met and the candidates susceptibility to HISC would be considered acceptable. The comparison have in a chronological order from the most susceptible alloy to the least susceptible to HISC been provided in Table 5.5.1. It is to be noted that not all parameters in the provided comparison have been investigated by the authors during their respective study. Both Stefansson et al.[30] and Burille et al.[21] carried out similar experimental work on UNS N08830. As the experimental procedures in regards to hydrogen pre-charging, in-situ hydrogen charging in SSRT and hydrogen measurements conducted in this study have been more similar to Stefansson et al.[30], the results obtained from the latter authors have been used in the comparison provided below. For UNS N07718 and UNS N07725, results obtained from two different authors have been used as despite the experimental procedures have been similar in both studies, either RAR or plastic elongation ratio was not calculated in their respective studies.

In terms of the plastic elongation ratio the P750-H.S has demonstrated a superior resistance

against HISC compared to all of the mentioned PH and strain hardened nickel alloys. However, in regards to RAR and hydrogen uptake the latter would not be the case. It appears that similar correlations which have been observed in this study in terms of relatively high degree of embrittlement having a low effect on ductility, would be the case when comparing the alloys in this study to the mentioned CRAs. Both UNS N07718 and UNS N07725 had according to work carried out by Stenerud [28] the lowest hydrogen uptake and the highest RAR-values compared to the alloys investigated indicating low degree of embrittlement. However, in addition to the lowest plastic elongation ratios suggesting the relatively largest ductility losses it also appeared according to the fractography study that severe secondary cracks had occurred near the fracture surfaces verifying that the alloys were to large extent affected by HE.

Sanicro35 in contrast to all mentioned strain hardened nickel alloys had the highest sensitivity to HISC in terms of suffering the highest degree of embrittlement consequently also resulting in the largest ductility loss. Although, it seems that the ductility loss has not been as severe in comparison to the mentioned PH nickel alloys.

Table 5.5.1: An overview of RARs, hydrogen uptakes and plastic elongations ratios for strain hardened and PH nickel alloys.* = Mean value.

Hardening method	Alloy	RAR (%)	Hydrogen uptake (ppm)	RE,p (%)
Strain hardened	P750-H.S	51.14	39.57	95.98
Strain hardened	A31+	43.00	78.01	88.59
Strain hardened	A975 [31]	-	-	86.00
Strain hardened	UNS N08830 [30]	55.20	14.31	85.00
Strain hardened	P750-L.S	57.59	65.70	79.10
Strain hardened	UNS N07022 [32]	-	-	70.00
Strain hardened	Sanicro35	43.91	96.64	60.73
PH	UNS N07718[13]	-	-	53
	UNS N07718 [28]	78.08±6.13	*17.12	-
PH	UNS N07716 [13]	-	-	22
PH	UNS N07725 [13]	-	-	15
	UNS N07725 [28]	74.63±6.90	*12.05	-

5.6 Localized corrosion testing and characterization

It has through the EDS evaluations combined with ASTM G48 Method C been confirmed that the inclusions detected in the microstructures of some of the alloys have influenced the CPT. For P750-H.S, according to the EDS analysis and microstructure overview in Figure 4.7.5, neither chromium or molybdenum are being trapped by the detected inclusion. For both P750-L.S and Sanicro35 according to their respective EDS evaluations the detected inclusions similarly to P750-H.S, mainly consist of magnesium, oxygen and aluminum. Likewise P750-H.S, the microstructures according to Figures 4.7.6 and 4.7.10 for both P750-L.S and Sanicro35 respectively, also appears relatively clean in terms of precipitates affecting the CPTs. As the wt% of chromium in the latter alloys is approximately equal to 27 wt%, the relatively lower molybdenum content of 3 wt% can be argued becomes the main differentiating factor resulting in pitting in case of temperature increase above 75°C for P750-L.S and between 75-80°C for P750-H.S. Whereas, the Sanicro35 exhibits

a microstructure without notable precipitates combined with a molybdenum content approximately 6.3 wt% reaches a CPT above 85°C thus not being exposed to pitting.

According to Table 4.8.1 A31+ similar to Sanicro35 is one of the alloys with highest PREn indicating compared to both P750 alloys and 25%Cr SDSS, higher pitting resistance. Although, the alloy is reaching relatively lower CPT than expected while being the alloy candidate with approximately twice the molybdenum content compared to P750 alloys and 25%Cr SDSS. It can be argued that the detected inclusion in A31+ in comparison to Sanicro35, which is relatively both chromium and molybdenum dense might be affecting the passive film negatively hence reducing the pitting resistance in return keeping the CPT <75°C. Similarly, the 25%Cr SDSS despite having higher PREn reaches a lower CPT of <70°C. This might be due to the detected chromium dense inclusion affecting the passive film negatively, hence reducing the pitting resistance to some extent. The correlation between CPT and PREn for alloys investigated is provided in Figure 5.6.1. It appears from the latter figure and CPTs obtained from Figure 4.8.1 that an alloy such as 25%Cr SDSS compared to the P750 alloys might has approximately the same PREn, although would perform different due to precipitates in the microstructure negatively affecting the passive film. The same can be argued for A31+ compared to both P750 alloys. As the A31+ has higher PREn, however due to microscopical precipitates the CPT is negatively impacted. As described earlier, larger PREn numbers indicate higher resistance to pitting and is a useful tool in order to benchmark alloys, however surface metallurgy is not being taken into account which has been the case for 25%Cr SDSS and A31+ during this study.

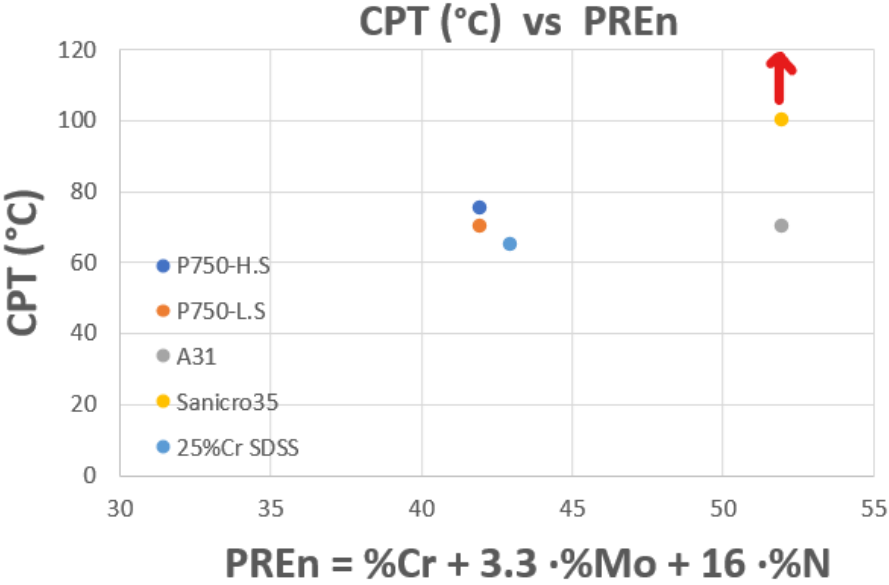


Figure 5.6.1: Correlation between CPT and PREn for alloys investigated.

Chapter 6

Conclusion

It can be based on the results obtained in this work be concluded that all alloys have been affected by HE. However, one of the core observations in this work has been that relatively high degree of embrittlement has not in all cases affected the mechanical performance in terms of ductility loss. This work draws key conclusions based on the mechanical performance on a macroscopical level. The losses in fracture strains from in-situ hydrogen charging, RARs, plastic elongation ratios and HEI-values have been used to rate each alloys susceptibility to HISC. Alloy candidates with the highest to lowest susceptibility to HISC have with their key results been provided in a chronological order in the following. The order below is first and foremost based on mechanical ductility loss as a result HE.

- The P750-H.S alloy has during this work demonstrated superior resistance against HISC in comparison to the other alloys in this work. The alloy suffered an average loss in fracture strain of 0.35% consequently maintaining 98% of the fracture strain obtained from testing in air during SSRT. Similar fracture strain was reached during SCL and 101% of the FS from in-situ hydrogen charging in SSRT was maintained. One of the highest RAR of 51.14% was reached. The highest plastic elongation ratio of 95.98% and the lowest HEI of 4.02% was achieved indicating the relatively highest susceptibility to HISC.
- The A31+ alloy has during this study been one of the alloys which has suffered the greatest degree of embrittlement with an RAR of 43%. The alloy still managed to maintain 91% of the fracture strain obtained from air testing during in-situ hydrogen charging in SSRT. The latter resulting in an average loss of 1.7% in fracture strain from in-situ hydrogen charging. During SCL, the alloy reached 98% of its FS from in-situ hydrogen charging in SSRT and minimal change in fracture strain occurred. The plastic elongation ratio and HEI of 88.59% and 11.41% respectively, was achieved.
- The P750-L.S achieved relatively lower degree of embrittlement with the highest RAR of 57.59%. Although, the alloy suffered relatively one of the largest losses in ductility with a loss of 4.19% consequently maintaining 82% of the fracture strain obtained from SSRT in air environment. During SCL, 100% of the FS from in-situ hydrogen charging in SSRT was maintained and minimal change in fracture strain occurred. The alloy reached a plastic elongation ratio and HEI of 79.10% and 20.90%, respectively.
- The Sanicro35 suffered relatively the greatest ductility loss of 8.65% from in-situ hydrogen charging in SSRT. Thus maintaining 65% of the fracture strain obtained from testing in air environment. One of the lowest RAR of 43.91% was reached. During SCL, 100% of the FS

from in-situ hydrogen charging in SSRT was reached and minimal change in fracture strain occurred. The alloy reached a plastic elongation ratio and HEI of 60.73% and 39.27% indicating the Sanicro35 to be the alloy candidate with the lowest susceptibility to HISC in comparison to the other alloys in this study.

- The overall results have demonstrated that the strain hardened nickel alloys investigated in this study exhibits superior HE resistance in regards to ductility loss when compared to UNS N07718, UNS N07725 and UNS N07716. The acceptance criterion in terms of plastic elongation ratio used in this work has been met by all alloys investigated, in contrast to the mentioned PH nickel grades.

Chapter 7

Future work

- As the alloys possess relatively high microstructure cleanliness, it would be of great interest to further investigate different parameters of the production methods which has been carried out by the suppliers. As hydrogen transport is largely affected by the dislocation density, the different production routes and %CW should be further assessed.
- Experiments regarding diffusivity should be carried out in order to obtain the temperature dependent diffusion coefficient. This with the intention to achieve a better understanding of the diffusion behaviors in regards to hydrogen absorption.
- A higher number of specimens should be tested in SCL in order to fully confirm the HISC susceptibility. In addition, experimenting with how lower potential than $-1100 \text{ mV}_{Ag/AgCl}$ during in-situ hydrogen charging in SSRT or SCL may further affect the FS and ductility of P750-H.S can be of interest to the alloys limits in regards to HISC.

Bibliography

- [1] Atle Helge Qvale and SubseaDesign As. “Strain Hardened Bridge Alloys”. en. In: *Robust Materialvalg i Energisektoren*, p. 24.
- [2] *Korrosjon og korrosjonsvern*. nob. Tapir, 1985. ISBN: 978-82-519-0700-2. URL: https://www.nb.no/items/URN:NBN:no-nb_digibok_2015073008046?page=7 (visited on June 8, 2022).
- [3] Marcel Pourbaix. “Thermodynamics and corrosion”. en. In: *Corrosion Science* 30.10 (Jan. 1990), pp. 963–988. ISSN: 0010-938X. DOI: 10.1016/0010-938X(90)90205-J. URL: <https://www.sciencedirect.com/science/article/pii/0010938X9090205J> (visited on Apr. 23, 2021).
- [4] *Galvanic Corrosion - an overview | ScienceDirect Topics*. URL: <https://www.sciencedirect.com/topics/materials-science/galvanic-corrosion> (visited on June 9, 2022).
- [5] Linn Cecilie Gjelseng. “Susceptibility to Hydrogen Induced Stress Cracking of centrifugal cast 25Cr Duplex Stainless Steel”. eng. In: (2017). Accepted: 2017-09-20T14:01:14Z Publisher: NTNU. URL: <https://ntnuopen.ntnu.no/ntnu-xmlui/handle/11250/2455848> (visited on June 9, 2022).
- [6] Zaki Ahmad. “CHAPTER 9 - SELECTION OF MATERIALS FOR CORROSIVE ENVIRONMENT”. In: *Principles of Corrosion Engineering and Corrosion Control*. Ed. by Zaki Ahmad. Oxford: Butterworth-Heinemann, 2006, pp. 479–549. ISBN: 978-0-7506-5924-6. DOI: <https://doi.org/10.1016/B978-075065924-6/50010-6>. URL: <https://www.sciencedirect.com/science/article/pii/B9780750659246500106>.
- [7] “Pitting Corrosion”. en. In: *Corrosion: Fundamentals, Testing, and Protection*. Ed. by Stephen D. Cramer and Bernard S. Covino. ASM International, 2003, pp. 236–241. ISBN: 978-1-62708-182-5. DOI: 10.31399/asm.hb.v13a.a0003612. URL: <https://dl.asminternational.org/books/book/46/chapter/549984/pitting-corrosion> (visited on Dec. 25, 2021).
- [8] Brian S DeForce. “Comparison of Pitting and Crevice Corrosion - The Effect of Alloying Elements”. en. In: (), p. 9.
- [9] Einar Bardal. *Corrosion and protection*. en. London ; New York: Springer, 2004. ISBN: 978-1-85233-758-2.
- [10] Helmuth Sarmiento Klapper, Natalia S. Zadorozne, and Raul B. Rebak. “Localized Corrosion Characteristics of Nickel Alloys: A Review”. en. In: *Acta Metallurgica Sinica (English Letters)* 30.4 (Apr. 2017), pp. 296–305. ISSN: 1006-7191, 2194-1289. DOI: 10.1007/s40195-017-0553-z. URL: <http://link.springer.com/10.1007/s40195-017-0553-z> (visited on Dec. 26, 2021).
- [11] Cristian Torres, María Sofía Hazarabedian, Zakaria Quadir, Roy Johnsen, and Mariano Iannuzzi. “The Role of Tungsten on the Phase Transformation Kinetics and its Correlation with the Localized Corrosion Resistance of 25Cr Super Duplex Stainless Steels”. en. In: *Journal of The Electrochemical Society* 167.8 (Jan. 2020).

- Publisher: The Electrochemical Society, p. 081510. ISSN: 1945-7111. DOI: 10.1149/1945-7111/ab90af. URL: <https://doi.org/10.1149/1945-7111/ab90af> (visited on June 9, 2022).
- [12] Roy Johnsen. “Hydrogen Induced Stress Cracking of Stainless Steel in Seawater – what do we know and what is still unknown?” en. In: (), p. 13.
- [13] I. Salvator, L. Alleva, D. Thierry, C. Duret-Thual, and J. W. Martin, Consultant. “Assessment of the Hydrogen Induced Stress Cracking Resistance of Precipitation Hardened Nickel-based Alloys using the Slow Strain Rate Tensile Test Method: Influence of Microstructure”. In: NACE International, 2019, p. 14.
- [14] Roy Johnsen, Bard Nyhus, and Stig Wa”stberg. “Hydrogen Induced Stress Cracking (HISC) of Stainless Steels Under Cathodic Protection in Seawater: Presentation of a New Test Method”. en. In: *Volume 6: Materials Technology; C.C. Mei Symposium on Wave Mechanics and Hydrodynamics; Offshore Measurement and Data Interpretation*. Honolulu, Hawaii, USA: ASMEDC, Jan. 2009, pp. 55–67. ISBN: 978-0-7918-4346-8. DOI: 10.1115/OMAE2009-79325. URL: <https://asmedigitalcollection.asme.org/OMAE/proceedings/OMAE2009/43468/55/337895> (visited on July 7, 2022).
- [15] W.L. Mankins and S. Lamb. “Nickel and Nickel Alloys”. In: *Properties and Selection: Nonferrous Alloys and Special-Purpose Materials*. Ed. by ASM Handbook Committee. Vol. 2. ASM International, Jan. 1990, p. 0. ISBN: 978-1-62708-162-7. DOI: 10.31399/asm.hb.v02.a0001072. URL: <https://doi.org/10.31399/asm.hb.v02.a0001072> (visited on July 7, 2022).
- [16] Roald Lilletvedt. *Superlegeringer - Lecture notes - Materialteknologi*. NTNU, Trondheim.
- [17] Liufa Liu, Katsumi Tanaka, Akio Hirose, and Kojiro Kobayashi. “Effects of precipitation phases on the hydrogen embrittlement sensitivity of Inconel 718”. In: *Science and Technology of Advanced Materials* 3.4 (Jan. 2002). Publisher: Taylor & Francis _eprint: [https://doi.org/10.1016/S1468-6996\(02\)00039-6](https://doi.org/10.1016/S1468-6996(02)00039-6), pp. 335–344. ISSN: 1468-6996. DOI: 10.1016/S1468-6996(02)00039-6. URL: [https://doi.org/10.1016/S1468-6996\(02\)00039-6](https://doi.org/10.1016/S1468-6996(02)00039-6) (visited on Dec. 27, 2021).
- [18] L Fournier, D Delafosse, and T Magnin. “Cathodic hydrogen embrittlement in alloy 718”. en. In: *Materials Science and Engineering: A* 269.1-2 (Aug. 1999), pp. 111–119. ISSN: 09215093. DOI: 10.1016/S0921-5093(99)00167-7. URL: <https://linkinghub.elsevier.com/retrieve/pii/S0921509399001677> (visited on Dec. 20, 2021).
- [19] Atle Helge Qvale, Mariano Iannuzzi, Martin M. Morra, Tone Frydenberg, Inge Osen, and Richard M. Thompson. “Hydrogen Stress Cracking of Nickel Alloy UNS N07725—Part II: Correlation between Microstructure and Hydrogen Stress Cracking Resistance of Ni-Cr-Mo-Nb age hardened alloys”. In: Phoenix: Corrosion, 2018. (Visited on June 12, 2022).
- [20] William D. Callister Jr and David G. Rethwisch. *Callister’s Materials Science and Engineering*. en. Google-Books-ID: IUjODwAAQBAJ. John Wiley & Sons, Feb. 2020. ISBN: 978-1-119-45391-8.
- [21] Airton Burille, Adriano Scheid, Daniel Correia Freire Ferreira, Luciano Santana, and Carlos Eduardo Fortis Kwietniewski. “Hydrogen embrittlement of single-phase strain-hardened nickel-based UNS N08830 alloy”. en. In: *Materials Science and Engineering: A* 803 (Jan. 2021), p. 140486. ISSN: 0921-5093. DOI: 10.1016/j.msea.2020.140486. URL: <https://www.sciencedirect.com/science/article/pii/S0921509320315495> (visited on June 8, 2022).
- [22] Afrooz Barnoush. *Hydrogen Embrittlement -Lecture notes*. NTNU, Trondheim.

- [23] Veronica Djupvik. “Hydrogen Induced Stress Cracking in Spheroidal Graphite Cast iron - MSc thesis”. In: (). (Visited on July 7, 2022).
- [24] Roy Johnsen. *Hydrogen Embrittlement - A brief introduction - Lecture notes*. NTNU, Trondheim.
- [25] Linn Cecilie Gjelseng. “Susceptibility to Hydrogen Induced Stress Cracking of centrifugal cast 25Cr Duplex Stainless Steel”. en. In: (), p. 194.
- [26] Martin Heims. “Hydrogen Induced Stress Cracking Resistance of Nickel Alloy ATI 830”. en. In: (), p. 200.
- [27] Julia Botinha, Bodo Gehrman, and Helena Alves. “Hydrogen embrittlement of Oil Patch Alloy 718 and its correlation to the microstructure”. en. In: (2021), p. 15.
- [28] Gaute Stenerud. “The Susceptibility to Hydrogen Induced Stress Cracking for Alloy 718 and Alloy 725”. eng. In: *76* (2014). Accepted: 2014-12-19T13:28:29Z Publisher: Institutt for produktutvikling og materialer, NTNU Trondheim. URL: <https://ntnuopen.ntnu.no/ntnu-xmlui/handle/11250/249561>.
- [29] Airton Burille, Adriano Scheid, Daniel Correia Freire Ferreira, Luciano Santana, and Carlos Eduardo Fortis Kwietniewski. “Hydrogen embrittlement of single-phase strain-hardened nickel-based UNS N08830 alloy”. en. In: *Materials Science and Engineering: A* 803 (Jan. 2021), p. 140486. ISSN: 09215093. DOI: 10.1016/j.msea.2020.140486. URL: <https://linkinghub.elsevier.com/retrieve/pii/S0921509320315495> (visited on June 8, 2022).
- [30] Njall Stefansson, John Dunn, Einar Strand, Roy Johnsen, Martin Heimsaeter, and Richard Birkelandsvei. “Performance of High Strength UNS N08830 in Hydrogen Stress Crack Testing to Simulate Conditions Arising from Subsea Cathodic Protection”. en. In: (), p. 15.
- [31] Ernst Plesiutchnig, Rainer Fluch, Martin Wöls, Marianne Kapp, and Greg Chitwood. “Alloy A975 Resistant to Severe Sour Environments and to Hydrogen Embrittlement”. en. In: OnePetro, Apr. 2021. URL: <https://onepetro.org/NACECORR/proceedings/CORR21/3-CORR21/D031S011R009/464020> (visited on June 28, 2022).
- [32] Jeremy L. Caron and L. Hibner. “Sour Gas and Hydrogen Embrittlement Resistance of High-Strength UNS N07022 Alloy for Oil and Gas Applications”. en. In: (Mar. 2017). URL: <https://onepetro.org/NACECORR/proceedings/CORR17/All-CORR17/NACE-2017-9479/125632> (visited on June 29, 2022).
- [33] G01 Committee. *Test Methods for Pitting and Crevice Corrosion Resistance of Stainless Steels and Related Alloys by Use of Ferric Chloride Solution*. en. Tech. rep. ASTM International. DOI: 10.1520/G0048-11R15. URL: <http://www.astm.org/cgi-bin/resolver.cgi?G48-11R15> (visited on Dec. 25, 2021).
- [34] Eivind Bruun Thorstensen. “Hydrogen Induced Stress Cracking of Inconel 625”. en. In: (), p. 114.



Chapter 8

Appendix

Appendix A: Material certificates for alloys investigated. 103
Appendix B: Data sheets for alloys investigated. 110
Appendix C: Quantitative overview from EDS analysis. 135
Appendix D: Risk assessments. 137



Appendix A

Material certificates for alloys investigated.

MATERIAL CERTIFICATION 3.1 CERTIFICATE acc. EN 10204		 SCHOELLER BLECKMANN OILFIELD TECHNOLOGY GMBH HAUPTSTRASSE 2 A-2630 TERNITZ / AUSTRIA		Approved Manufacturer acc.to ISO 9001 API-Spec. Q1 License No. 7-1-0234																			
SBOT PO No: /																							
SB – COLLAR No.: B1200 / 1			SERIAL No.:																				
Material: P 750			PART:																				
DWG No.:																							
MATERIAL SPECIFICATION:			IN ACC. WITH DATASHEET P 750, Rev. 4																				
CHEMICAL ANALYSIS:																							
Heat No.:	C	SI	MN	P	S	CR	MO	NI	N	Al	Cu												
Spec. Val.:	Y11954	0,015	0,25	2,83	0,021	0	27,25	3,22	29,37	0,28	0,012	0,12											
MECHANICAL PROPERTIES:																							
(less than 9.5-inch diameter)																							
			Specified Values		Actual Values (1)																		
TENSILE STRENGTH			min. 150 KSI		184,2 KSI																		
YIELD STRENGTH			min. 140 KSI		178,1 KSI																		
ELONGATION			min. 17 %		17 %																		
REDUCTION IN AREA			min. 50 %		72 %																		
IMPACT STRENGTH (Charpy V)			min. 100 ft.lb		170 ft.lb																		
HARDNESS BRINELL			300-400 BHN		380 , 370 BHN																		
FATIGUE STRENGTH (100000 cycl.)					315763 ,304156																		
(1) Specimen are taken in longitudinal direction.																							
GRAIN SIZE			3 - 4		ASTM																		
MAGNETIC PERMEABILITY			1,001		max.																		
CORROSION TEST																							
ASTM A262, PRACT A			Step		<table border="1" style="margin: auto;"> <thead> <tr> <th colspan="3">Inclusion Rating</th> </tr> <tr> <th>Type</th> <th>Thin</th> <th>Heavy</th> </tr> </thead> <tbody> <tr> <td>A</td> <td></td> <td></td> </tr> <tr> <td>B</td> <td>0,5</td> <td>1</td> </tr> <tr> <td>C</td> <td></td> <td></td> </tr> <tr> <td>D</td> <td>0,5</td> <td>1</td> </tr> </tbody> </table>	Inclusion Rating			Type	Thin	Heavy	A			B	0,5	1	C			D	0,5	1
Inclusion Rating																							
Type	Thin	Heavy																					
A																							
B	0,5	1																					
C																							
D	0,5	1																					
ASTM A262, PRACT E			pass																				
RESIDUAL MAGNETISM			passed																				
ULTRASONIC TEST			passed																				
DIMENSIONAL TEST			in acc. with order																				
SURFACE TREATMENTS:																							
OUTSIDE:			--																				
INSIDE:			--																				
MARKING:			B1200																				
																							
Date: 06.07.2020		P750-4-kl		Christoph Kopinits / Quality Department																			

Appendix A

Material certificates for alloys investigated.

MATERIAL CERTIFICATION 3.1 CERTIFICATE acc. EN 10204		 SCHOELLER BLECKMANN OILFIELD TECHNOLOGY SCHOELLER BLECKMANN OILFIELD TECHNOLOGY GMBH HAUPTSTRASSE 2 A-2630 TERNITZ / AUSTRIA	
SBOT PO No: /			
SB – COLLAR No.: B1580 / 4		SERIAL No.:	
Material: P 750		PART: 140 x 500 mm	
DWG No.:			
MATERIAL SPECIFICATION:		IN ACC. WITH DATASHEET P 750, Rev. 4	
CHEMICAL ANALYSIS:			
Heat No.:	C	SI	MN P S CR MO NI N
Spec. Val.:	max 0.03	0.1 - 0.4	1.5 - 3 max 0.05 max 0.01 26.5 - 29.5 2 - 4 28 - 31.5 0.2 - 1
K10448	0,013	0,33	2,51 0,019 0 27,19 3,15 29,48 0,28
MECHANICAL PROPERTIES: (less than 9.5-inch diameter)			
			Actual Values (1)
TENSILE STRENGTH			142,7 KSI
YIELD STRENGTH			133,4 KSI
ELONGATION			26 %
REDUCTION IN AREA			75 %
IMPACT STRENGTH (Charpy V)			240 ft.lb
HARDNESS BRINELL			308 , 310 BHN
(1) Specimen are taken in longitudinal direction.			
GRAIN SIZE	1 - 3	ASTM	
MAGNETIC PERMEABILITY	1,001	max.	
CORROSION TEST			
ASTM A262, PRACT A	Step		
ASTM A262, PRACT E	pass		
RESIDUAL MAGNETISM	--		
ULTRASONIC TEST	--		
DIMENSIONAL TEST	--		
SURFACE TREATMENTS:			
OUTSIDE:	--		
INSIDE:	--		
MARKING:	B1580/4		
Date: 13.10.2021		P750-4-kl	
		 Christoph Kopinits / Quality Department	

Appendix A

Material certificates for alloys investigated.

VDM Metals GmbH
on behalf of VDM Metals International GmbH

VDM Metals

Inspection certificate 229202/0
DIN EN 10204/01.05 3.1

Page: 1 / 2
printed: 07. OCT 2021

Order No.
LAGER

VDM Metals GmbH
Produktionsbereich
Plettenberger Str. 2
D - 58791 Werdohl



Trademark
VDM Alloy 31 Plus®
NICROFER 3426 HMO ESU
2.4692
Product
Bar, round, forged, unannealed, peeled

Specification

Material

Item	Pcs	Weight [kg]	Dimension [mm]	Cast	Lot
32			200,00 Ø x RL	344059	9400024437

Analysis (weight %)

LE=combustion analysis analysed corresponding to ASTM E1019-18

RF=X-ray fluorescence spectroscopy analysed corresponding to ASTM E572-21, ASTM E1085-16, ASTM E1621-21, ASTM E2465-19

Cast	Melting Pr.		C	S	N	Cr	Ni	Mn	Si	Mo	Cu	Fe	P
344059	EF/VD/ESR	top	0,004	<0,002	0,23	26,5	34,0	2,04	0,01	6,58	1,21	R29,1	0,013
		Meth	LE	LE	LE	RF	RF	RF	RF	RF	RF	RF	RF

Cast	Melting Pr.		W	Co
344059	EF/VD/ESR	top	0,04	0,06
		Meth	RF	RF

Sample Condition		Tensile Test								Hardness Test	
unannealed		1 ASTM E8/E8M - 21 (acc) / longitudinal specimen								1 ASTM E18 - 20 (acc)	
Lot	Sample No.	Temp [°C]	Yield0.2% [MPa]	Yield1.0% [MPa]	Tensile [MPa]	Elongation A [%]	RoA [%]	HRC			
9400024437	101-F04	1 RT	960	1064	4D	28,4	64	1 31,8 25mm from OD			
9400024437	101-F04	1 RT	1037	1117	4D	18,5	66				
9400024437	101-K04	1 RT	995	1090	4D	23,7	67				
9400024437	104-K04	1 RT	962	1058	4D	24,5	65				

Sample Condition		Notched Bar Impact Testing							Grain size	
unannealed		1 ASTM E23 - 18 (acc)Charpy-V/long.specim./1" below surface / KV _s 450/10							1 ASTM E112 - 13 (acc)	
Lot	Sample No.	Temp. [°C]	KV [J]	aK [J/cm ²]	Lateral Exp. [mm]				No	
9400024437	101-F04	1 21	202	207	205	1,86	1,84	1,82	1 No 1.5	
9400024437	101-F04									
9400024437	101-K04	1 21	197	193	202	1,73	1,84	1,83	1 No 2	
9400024437	104-K04									

Sample Condition		Microstructure/Precipitates	
unannealed		1	
Lot	Sample No.		
9400024437	101-F04	1 Conforming to requirements.	
9400024437	101-F04		
9400024437	101-K04	1 Conforming to requirements.	
9400024437	104-K04		

We herewith certify, that the material is in conformance with the above mentioned specifications	Mark of the Inspector	E	Enclosures: 1
authorized inspection representative	E-Mail	Q	* 229202 - 0 - E *

This certified test report shall not be reproduced except in full, without the written approval of VDM Metals. The recording of false, fictitious or fraudulent statements or entries on the certificate may be punished as a felony under federal law.

VDM Metals GmbH
Division Bar and Forgings
Plettenberger Straße 2, D-58791 Werdohl
Postfach 18 20, D-58778 Werdohl
Telephon: +49 2392 550
Internet: www.vdm-metals.com

Chairman of the Supervisory Board: Bernardo Velázquez Herreros
Management Board: Dr. Nicias Müller (Chairman),
Daniel Aspizarre Zemp, Frank Morris, Rolf Schencking
Commercial register: Iserlohn local court, #5327
Company domicile: Werdohl

Appendix A

Material certificates for alloys investigated.

VDM Metals GmbH
on behalf of VDM Metals International GmbH

VDM Metals

Inspection certificate 229202/0
DIN EN 10204/01.05 3.1

Page: 2 / 2
printed: 07. OCT 2021

Order No.
LAGER

Spectrographic analytical mixup test/PMI check: without objection
Dimensional and visual inspection performed: without objection

No mercury contamination; no Radium, Luminous or Alpha source materials were used in the manufacture or testing of the items furnished.

No weld repairs performed.

For dimensions greater 20mmØ we use samples for tensile testing, that are standard ASTM specimens with 12.5 mm diameter, taken from a prolongation of the bars.

MACROETCHING: conducted as per ASTM A 604, etchant 'Aqua Regia', sample taken from top and bottom of ingot after hot forming.
Rating: better or equal severity A, in all 4 classes.

—

—

VDM Metals GmbH
Division Bar and Forgings
Plettenberger Straße 2, D-58791 Werdohl
Postfach 18 20, D-58778 Werdohl
Telephon: +49 2392 550
Internet: www.vdm-metals.com

Chairman of the Supervisory Board: Bernardo Velázquez Herreros
Management Board: Dr. Nicias Müller (Chairman),
Daniel Azpilarte Zemp, Frank Morris, Rolf Schencking
Commercial register: Iserlohn local court, #5327
Company domicile: Werdohl

Appendix A

Material certificates for alloys investigated.

VDM Metals GmbH

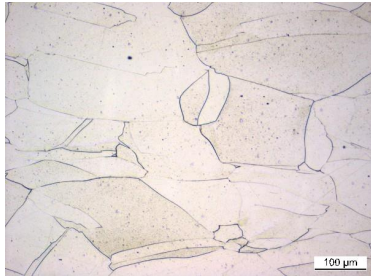
VDM Metals
A company of ACERINOX

Microstructure Examination

Metallography Job No.: 180368
Lot No.: 9400024437
Heat: 344059

Inspection Certificate No.: 229202

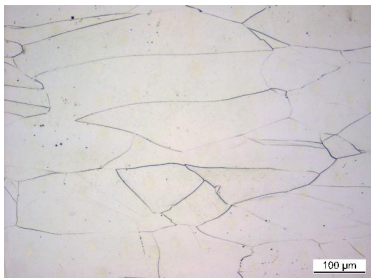
Enclosure: 1
Page: 1 of 1



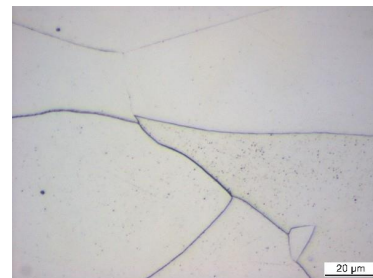
100:1VDM Alloy 31 Plus® / Nicrofer 3426HMO
ESU 101K04 Rand
Salz Salpeter 6:1 03.08.2021 10:44:39



500:1VDM Alloy 31 Plus® / Nicrofer 3426HMO
ESU 101K04 Rand
Salz Salpeter 6:1 03.08.2021 10:44:41



100:1VDM Alloy 31 Plus® / Nicrofer 3426HMO
ESU 101F04 Rand
Salz Salpeter 6:1 03.08.2021 11:05:19



500:1VDM Alloy 31 Plus® / Nicrofer 3426HMO
ESU 101F04 Rand
Salz Salpeter 6:1 03.08.2021 11:05:20

Adress: VDM Metals GmbH, Kleffstrasse 23, D-58762 Altena, P.O. Box 12 51, D-58742 Altena
Telephone: +49 2392 55-0 Fax: +49 2392 55-2217 Internet: www.vdm-metals.com
Chairman of the Supervisory Board: Bernardo Velázquez Herreros
Management Board: Dr. Niclas Müller, Chairman; Daniel Azpitarte Zemp, Frank Morris, Rolf Schencking
Company domicile: Werdohl Commercial register: Iserlohn local court, HRB 5327

Appendix A

Material certificates for alloys investigated.

Materials information

Material: Cold worked bar material

Grade: Sanicro 35
UNS N08935

Heat: 560812

Chemical composition:

C	Si	Mn	P	S	Cr	Ni	Mo	Ti	Cu	N	Fe
≤0.030	0.2	0.9	≤0.030	≤0.020	27.2	35.1	6.3	≤0.01	0.2	0.28	balance

PRE = 52.5

Mechanical properties:

Tensile properties according to ISO 6892-1 at room temperature and hardness according to ISO 6508-1.

Rp0.2	Rp1.0	Rm	A	Hardness
917 MPa	994 MPa	1067 MPa	28,9 %	33 HRC

Appendix B

Data sheets for alloys investigated.

Technical Information



Data sheet P 750 HS

Revision 1

1. CHEMICAL COMPOSITION

„P750 HS“ is a high pitting corrosion resistant nonmagnetic, austenitic Cr-Ni-N-steel, specifically developed for oilfield applications.

C	Mn	Cr	Ni	Mo	N
max. 0,03	1,50-3,00	26,50-29,50	28,00-31,50	2,00-4,00	min. 0,20

2. MECHANICAL PROPERTIES

Following mechanical properties (tested at room temperature) are achieved by a special cold-working process over the full length of the collar:

Yield Strength (min.): OD max. 6“ 0,2%-offset method	175 ksi	1208 N/mm ²
Tensile Strength (min.):	180 ksi	1242 N/mm ²
Elongation (min.):	10%	10%
Reduction of area (min.):	50%	50%
Impact energy (min.):	80 ft.lb	110 J
Endurance Strength / N=10 ⁵ (min.):	± 80 ksi	± 550 N/mm ²
Hardness Brinell:	300-420 HB	300-420 HB

3. MAGNETIC PROPERTIES

Relative permeability: ≤ 1,001.

4. CORROSION RESISTANCE

- **Transgranular SCC:** Prevented by special surface treatments (Hammer peening, roller burnishing, shot peening).
- **Intergranular SCC:** The occurrence of material sensitization is prevented by quenching after warmforging. Each collar is tested according to ASTM A 262, Pract.A and E, last edition.
- **Pitting Corrosion:** Due to a high chromium-, nickel- and nitrogen contents an excellent resistance to pitting corrosion comparable to nickelbase alloys is given.

5. NON-DESTRUCTIVE TESTING

- **Magnetic inspection:** Drill collars are 100% tested by a proprietary probe-testing process using a Förster Magnetomat 1.782. (“Hot Spot“-test). Magnetic permeability of each collar is certified with the printout of probe-testing.
- **Ultrasonic inspection:** Each collar is ultrasonically inspected over 100% of the volume according to ASTM E 114, last edition as a minimum level.

P750 HS Non-Magnetic Drill Collars meet all requirements of API Spec. 7.1, last edition.
All tests are carried out according to ASTM-Standards, last editions.
Prepared / released: B. Holper
Date: June, 2013

We provide the leading edge

Appendix B

Data sheets for alloys investigated.

VDM Metals

A company of ACERINOX

VDM Alloy 31 Plus®
Nicrofer 3426 hMo

Material Data Sheet No. 4063 Revision 04
November 2020

Appendix B

Data sheets for alloys investigated.

November 2020

VDM Alloy 31 Plus®

2

VDM Alloy 31 Plus®

Nicrofer 3426 hMo

VDM Alloy 31 Plus® is a Nickel-Iron-Chromium-Molybdenum alloy with a controlled addition of nitrogen. For an improved metallurgical stability the alloy has an optimized nickel content compared to VDM® Alloy 31.

VDM Alloy 31 Plus® is characterized by:

- high corrosion resistance similar to VDM® Alloy 31
- improved lower solution annealing temperature
- excellent corrosion resistance to sulfuric acids
- excellent corrosion resistance to phosphoric acids
- ease of working and processing
- good weldability
- approval for pressure vessels according to ASME Code Section VIII Div 1; Section VIII Div 2, Class 1 applications

Designations

Standard	Material designation
D	2.4692
ISO	NiFeCr27Mo6CuN
UNS	N08034

Standards

Product form	ASTM	VdTUEV	Others
Strip	B 625	583	ASME Code Case 2991*
Sheet and plate	B 625	583	ASME Code Case 2991*
Rod and bar	B 581 B 649		ASME Code Case 2991*
Wire	B 649		
Forging	B 564		ASME Code Case 2991*

*Valid for Solution Annealed alloy

Table 1 – Designations and standards

Appendix B

Data sheets for alloys investigated.

November 2020

VDM Alloy 31 Plus®

3

Chemical composition

	Ni	Cr	Fe	S	Si	Mn	P	Mo	Cu	N	C	Al
Min.	33,5	26,0	balance			1,0		6,0	0,5	0,10		
Max.	35,0	27,0		0,01	0,1	4,0	0,02	7,0	1,5	0,25	0,01	0,30

Table 2 – Chemical composition (%)

Physical properties

Density	Melting range	Relative magnetic permeability at 20 °C (68 °F)
8.08 g/cm ³ (0.292 lbs/in ³) at 20 °C (68 °F)	1,350-1,370 °C (2,460-2,500 °F)	1.001

Temperature		Specific heat capacity		Thermal conductivity		Modulus of elasticity		Average linear expansion coefficient	
°C	°F	$\frac{J}{Kg \cdot K}$	$\frac{Btu}{lb \cdot ^\circ F}$	$\frac{W}{m \cdot K}$	$\frac{Btu \cdot in}{sq. ft \cdot h \cdot ^\circ F}$	GPa	10 ⁶ psi	$\frac{10^{-6}}{K}$	$\frac{10^{-6}}{^\circ F}$
20	68	431 ¹⁾	0.103 ¹⁾	10.3 ¹⁾	5.95 ¹⁾	199	28.9	14.3 ¹⁾	7.94 ¹⁾
100	212	447	0.107	11.6	6.70	195	28.3	14.8 ¹⁾	8.22 ¹⁾
200	392	468	0.112	13.4	7.74	189	27.4	15.4	8.56
300	572	480	0.115	14.9	8.61	181	26.3	16.0	8.89
400	752	488	0.117	16.3	9.42	174	25.2	16.3	9.06
500	932	488	0.117	17.6	10.17	168	24.4	16.3	9.06

1) Extrapolated

Table 3 – Typical physical properties of VDM Alloy 31 Plus® at room temperature and elevated temperatures

Appendix B

Data sheets for alloys investigated.

November 2020

VDM Alloy 31 Plus®

4

Microstructural properties

VDM Alloy 31 Plus® has a face-centered cubic structure. The nitrogen and nickel content reduces the tendency for precipitation of intermetallic phases and stabilizes the austenitic microstructure.

Mechanical properties

The data for the 0.2 % yield strength $R_{p0.2}$, 1.0 % yield strength $R_{p1.0}$, elongation at fracture A_5 , A_{80} and notch impact toughness KV_2 are minimum values. They apply for the solution-annealed and quenched condition independent of the sampling location and the sample position for the sample direction longitudinal (l) and transverse (q).

Temperature		Yield strength $R_{p0.2}$		Yield strength $R_{p1.0}$		Tensile strength R_m		Elongation A
°C	°F	MPa	ksi	MPa	ksi	MPa	ksi	%
20	68	280	40.6	310	45	650 to 850	94.3 to 123	40
100	212	210	30.5	240	34.8			
200	392	180	26.1	210	30.5			
300	572	165	23.9	195	28.3			
400	762	150	21.8	180	26.1			
500	932	135	19.6	165	23.9			

Table 4 – Mechanical short-term properties at room and elevated temperatures for the product form plate, plate thickness ≤ 30mm (minimum value)

ISO V-notch impact energy

Average value, room temperature: ≥ 150 J

Average value, -196 °C (-320.8 °F): ≥ 110 J

Cut axis perpendicular to the surface, sheet thickness ≤ 30 mm average value from 3 samples. The minimum average value may only fall below by a single value, namely no more than 30%. These values only apply for normal samples according to DIN EN ISO 148-1. For undersized samples according to DIN EN ISO 148-1, the minimum values indicated for the notch impact toughness linear to the sample cross-section in the gap must be reduced. For undersized samples < 5 mm according to DIN EN ISO 148-1, the values for the individual case must be agreed separately with the manufacturer. The values also apply for the heat affected zone in welded joints.

Corrosion resistance

The material is resistant to inter-crystalline corrosion in the delivery condition and when welded according to the test procedure according to ASTM-G 28, Method A. The corrosion rate determined via the mass loss according to ASTM-G 28, Method A (test period 24 hours), is maximum 0.5 mm/a (0.020 mpy) in the delivery condition and when welded. A very good resistance is also provided against crevice corrosion and pitting. The corrosion resistance is comparable with the material VDM® Alloy 31.

Fields of application

Typical fields of application for VDM Alloy 31 Plus® are:

- Chemical processes with sulfuric acid
- Treatment of sulfuric acids from waste
- Components for flue gas desulfurization plants
- Clad tanks
- Plants for the production of phosphoric acid via the wet digestion process
- Ocean water and brackish water applications
- Evaporation and crystallization of salts
- Pickling plants for sulfuric acid and for nitric-hydrofluoric acid
- Hydrometallurgy, e.g. digestion of laterite ores in the HPAL process
- Fine chemicals, special chemicals and organic acids
- Components for the cellulose and paper industry

Fabrication and heat treatment

VDM Alloy 31 Plus® can be easily formed both hot and cold and can also be machined.

Heating

It is important that the workpieces are clean and free of any contaminants before and during heat treatment. Sulfur, phosphorus, lead and other low-melting-point metals can result in damage during the heat treatment of the material. This type of contamination is also contained in marking and temperature-indicating paints or pens as well as in lubricating grease, oils, fuels and similar materials. The sulfur content of fuels must be as low as possible. Natural gas should contain less than 0.1% by weight of sulfur. Heating oil with a maximum sulfur content of 0.5% by weight is also suitable. Electric furnaces are to be preferred due to precise temperature control and lack of contaminants due to fuel. The furnace atmosphere should be set between neutral and slightly oxidizing and should not change between oxidizing and reducing. The workpieces must not come in direct contact with flames.

Hot forming

VDM Alloy 31 Plus® should be hot-formed in a temperature range of 1,200 to 1,050 °C (2,192 to 1,922 °F) with subsequent rapid cooling in water or in air. For heating up, workpieces should be placed in a furnace that has been heated up to the maximum hot-forming temperature (solution annealing temperature). Once the furnace has reached its temperature again, the workpieces should remain in the furnace for around 60 minutes per 100 mm (3.94 in) of thickness. After this, they should be removed from the furnace immediately and formed within the temperature range stated above, with reheating necessary once the temperature reaches 1,050 °C (1,922 °F). Heat treatment after hot forming is recommended in order to achieve optimal properties.

Cold forming

The workpieces should be in the annealed condition for cold forming. VDM Alloy 31 Plus® has a significantly higher work hardening rate than other widely used austenitic stainless steels. This must be taken into account during the design and selection of forming tools and equipment and during the planning of forming processes. Intermediate annealing is necessary for major cold forming work. For cold forming of > 15%, a final solution annealing must be conducted.

Heat treatment

Solution annealing should take place at temperatures between 1,140 and 1,170 °C (2,084 and 2,138 °F). The retention time during annealing depends on the semi-finished product thickness and can be calculated as follows:

- For thickness $d \leq 10$ mm (0.39 in), the retention time is $t = d \cdot 3$ min/mm
- For thickness $d = 10$ to 20 mm (0.39 to 0.79 in), the retention time is $t = 30$ min + $(d - 10$ mm) $\cdot 2$ min/mm
- For thickness $d > 20$ mm (0.79 in), the retention time is $t = 50$ min + $(d - 20$ mm) $\cdot 1$ min/mm

The retention time commences with material temperature equalization; longer times are generally considerably less critical than retention times that are too short.

For maximum corrosion resistance, the workpieces must be quickly cooled from the annealing temperature particularly through the range of 1,100 to 500 °C (2,012 to 932 °F) with a cooling rate of >150 °C/min (>302 °F/min). The material must be placed in a furnace that has been heated up to the maximum annealing temperature before any heat treatment. The cleanliness requirements listed under "Heating" must be observed. For strip products, the heat treatment can be performed in a continuous furnace at a speed and temperature that is adapted to the strip thickness.

Descaling and pickling

Oxides formed on VDM Alloy 31 Plus® and discoloration adjacent to welds are more adherent than on stainless steels. Grinding using extremely fine abrasive belts or grinding discs is recommended. It is imperative that grinding burns be avoided. Before pickling in nitric-hydrofluoric acid mixtures, the oxide layers should be disrupted by abrasive blasting or

fine grinding, or pre-treated in in a fused salt bath. The pickling baths used should be carefully monitored with regard to concentration and temperature.

Machining

VDM Alloy 31 Plus® should be machined in the heat-treated condition. Because of the considerably elevated tendency toward work hardening in comparison with low-alloy austenitic stainless steels, a low cutting speed and a feed level that is not too high should be selected and the cutting tool should be engaged at all times. An adequate depth of cut is important in order to cut below the previously formed strain-hardened zone. Optimum heat dissipation through the use of large quantities of suitable, preferably aqueous, lubricants has considerable influence on a stable machining process.

Welding information

When welding nickel alloys and special stainless steels, the following information should be taken into account:

Safety

The safety recommendations of the manufacturer of welding consumables have to be taken into consideration especially to avoid dust and smoke exposure.

Workplace

A separately located workplace, which is specifically separated from areas in which C-steel is being processed, must be provided. Maximum cleanliness is required, and drafts should be avoided during gas-shielded welding.

Auxiliary equipment and clothing

Clean fine leather gloves and clean working clothes must be used.

Tools and machines

Tools that have been used for other materials may not be used for nickel alloys and stainless steels. Only stainless steel brushes may be used. Processing and treatment machines such as shears, punches or rollers must be fitted (felt, cardboard, films) so that the workpiece surfaces cannot be damaged by the pressing in of iron particles through such equipment, as this can lead to corrosion.

Edge preparation

Welding seam preparation should preferably be carried out using mechanical methods through lathing, milling or planing. Abrasive waterjet cutting or plasma cutting is also possible. In the latter case, however, the cut edge (seam flank) must be cleanly reworked. Careful grinding without overheating is also permissible.

Striking the arc

Appendix B

Data sheets for alloys investigated.

The arc should only be struck in the seam area, such as on the weld edges or on an outlet piece (extension tab), and not on the component surface. Arc strikes are areas in which corrosion more easily occurs.

Included angle

Compared to C-steels, nickel alloys and special stainless steels exhibit lower heat conductivity and greater heat expansion. These properties must be taken into account by larger root openings or root gaps (1 to 3 mm, 0.039 to 0.118 in). Due to the viscosity of the welding material (compared to standard austenitic stainless steels) and the tendency to shrink, opening angles of 60 to 70° – as shown in Figure 5 – have to be provided for butt welds.

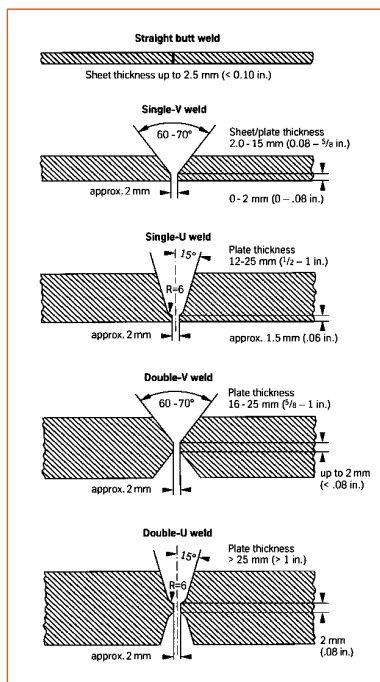


Figure 1 – Seam preparation for welding nickel alloys and special stainless steels

Cleaning

Cleaning of the base material in the seam area (both sides) and the welding filler (e.g. welding rod) should be carried out using acetone.

Welding technique

VDM Alloy 31 Plus® can be welded in most applications with VDM® FM 59 using conventional processes. This includes TIG and MAG welding. Pulsed arc welding is preferred for gas-shielded welding processes. For welding, VDM Alloy 31 Plus® should be in a solution-annealed condition and free of scale, grease and markings. When welding the root, care should be taken to achieve best quality root protection using pure argon, purity 99.99% or better so that the welding edge is free of oxides after welding the root. Root protection is also recommended for the first and, in certain cases depending on the welded construction, also for the second intermediate layer weld after root construction. Any tempering colors must be removed while the welding edge is still hot, preferably using a stainless steel brush.

Appendix B

Data sheets for alloys investigated.

Welding filler

The use of the following fillers is recommended for gas-shielded welding methods:

Welding rods and wire electrodes:

VDM® FM 59 (material no. 2.4607)

UNS N06059 AWS A5.14: ERNiCrMo-13

DIN EN ISO 18274: S Ni 6059 (NiCr23Mo16)

It is recommended to contact the manufacture for application in strongly oxidizing media.

Welding parameters and influences

It must be ensured that work is carried out using targeted heat application and low heat input as listed in Table 6 as an example. The stringer bead technique is recommended. The interpass temperature should not exceed 120 °C (248 °F). In principle, checking of welding parameters is necessary.

Heat input Q can be calculated as follows:

$$Q = \frac{U \cdot I \cdot 60}{v \cdot 1,000} \left(\frac{\text{kJ}}{\text{cm}} \right)$$

U = arc voltage, volts

I = welding current strength, amperes

v = welding speed, cm/min

Post-treatment

For the optimal performance of the work, insert the brush immediately after welding, i.e., while still warm, without additional pickling to the desired surface condition, i.e., discoloration can be removed completely. Pickling, if required, should generally be the last operation in the welding process. Information contained in the section entitled "Descaling and pickling" must be observed. Heat treatments are normally not required before or after welding.

Thickness	Welding technique	Filler material	Intermediate and final passes		Welding speed	Shielding gas	
			I in (A)	U in (V)		Type	Rate (l/min)
mm (in)		Diameter (mm)			(cm/min)		
8 (0.314)	v- TIG	1.2 (0.047)	150-170	11	19	I1	8-13
25 (0.984)	TIG	1.2 (0.047)	190-210	23-25	24,5	I1	12-16

Table 5 – Welding parameters

Appendix B

Data sheets for alloys investigated.

Availability

VDM Alloy 31 Plus® is available in the following standard semi-finished forms:

Sheet

Delivery condition: Hot- or cold-rolled, heat-treated, de-scaled or pickled

Condition	Thickness mm (in)	Width mm (in)	Length mm (in)	Piece weight Kg (lb)
Cold rolled	1-7 (0.04-0.28)	≤ 2,500 (98.43)	≤ 12,500 (492.13)	
Hot rolled*	3-30 (0.118-1.181)	≤ 2,500 (98.43)	≤ 12,500 (492.13)	≤ 1,650 (3,637.63)

* 2 mm (0.08 in) thickness on request

Strip

Delivery condition: Cold-rolled, heat-treated, pickled or bright annealed

Thickness mm (in)	Width mm (in)	Coil - inside diameter mm (in)			
0.03-0.15 (0.00118-0.006)	4-230 (0.16-9.06)	300 (11.811)	400 (15.748)	500 (19.685)	–
0.15-0.25 (0.006-0.01)	4-720 (0.16-28.34)	300 (11.811)	400 (15.748)	500 (19.685)	–
0.25-0.6 (0.01-0.024)	6-750 (0.24-29.5)	–	400 (15.748)	500 (19.685)	600 (23.622)
0.6-1 (0.024-0.0393)	8-750 (0.32-29.5)	–	400 (15.748)	500 (19.685)	600 (23.622)
1-2 (0.0393-0.0787)	15-750 (0.6-29.5)	–	400 (15.748)	500 (19.685)	600 (23.622)
2-3 (0.078-0.118)	25-750 (0.98-29.5)	–	400 (15.748)	500 (19.685)	600 (23.622)

Rolled sheet – separated from the coil – are available in lengths from 250 to 4,000 mm (9.84 to 157.48 in).

Other shapes and dimensions (such as rods, wires, discs, rings, seamless or longitudinally welded pipes and forgings) can be requested.

Appendix B

Data sheets for alloys investigated.

Publications

The following technical literature has been published about the material VDM Alloy 31 Plus®:

H. Alves, R. Behrens, F. Winter: "UNS N08031 and UNS N08031 Plus, multipurpose alloys for the chemical process industry and related applications", CORROSION 2016, Paper No. 7563, NACE International, Vancouver, British Columbia, 2016.

H. Alves, R. Behrens, L. Paul: "Evolution of Nickel Base Alloys – Modification to Traditional Alloys for Specific Applications", CORROSION 2014, Paper No. 4317, NACE International, San Antonio, Texas, 2014.

R. Behrens, F. Stenner, H. Alves: "New developed 6-Mo super-austenitic stainless steel with low sigma solvus temperature and high resistance to localised corrosion", CORROSION 2013, Paper No. 2228, NACE International, Orlando, Florida, 2013.

Legal notice

23.11.2020

Publisher

VDM Metals International GmbH
Plettenberger Strasse 2
58791 Werdohl
Germany

Disclaimer

All information contained in this data sheet is based on the results of research and development work carried out by VDM Metals International GmbH and the data contained in the specifications and standards listed available at the time of printing. The information does not represent a guarantee of specific properties. VDM Metals reserves the right to change information without notice. All information contained in this data sheet is compiled to the best of our knowledge and is provided without liability. Deliveries and services are subject exclusively to the relevant contractual conditions and the General Terms and Conditions issued by VDM Metals. Use of the most up-to-date version of this data sheet is the responsibility of the customer.

VDM Metals International GmbH
Plettenberger Strasse 2
58791 Werdohl
Germany

Phone +49 (0)2392 55 0
Fax +49 (0)2392 55 22 17

vdm@vdm-metals.com
www.vdm-metals.com

Appendix B

Data sheets for alloys investigated.

Technical Information



Data sheet P 750

Revision 3

1. CHEMICAL COMPOSITION

„P750“ is a high pitting corrosion resistant nonmagnetic, austenitic Cr-Ni-N-steel, specifically developed for oilfield applications.

C	Mn	Cr	Ni	Mo	N
max. 0,03	1,50-3,00	26,50-29,50	28,00-31,50	2,00-4,00	min. 0,20

2. MECHANICAL PROPERTIES

Following mechanical properties (tested at room temperature) are achieved by a special cold-working process over the full length of the collar:

Yield Strength (min.):	OD up to 9 1/4"	140 ksi	965 N/mm ²
0,2%-offset method	OD 9 1/2" and larger	130 ksi	900 N/mm ²
Tensile Strength (min.):		150 ksi	1035 N/mm ²
Elongation (min.):		15%	15%
Reduction of area (min.):		50%	50%
Impact energy (min.):		100 ft.lb	135 J
Endurance Strength / N=10 ⁵ (min.):		± 80 ksi	± 550 N/mm ²
Hardness Brinell:		300-400 HB	300-400 HB

3. MAGNETIC PROPERTIES

Relative permeability: ≤ 1,001.

4. CORROSION RESISTANCE

- **Transgranular SCC:** Prevented by special surface treatments (Hammer peening, roller burnishing, shot peening).
- **Intergranular SCC:** The occurrence of material sensitization is prevented by quenching after warmforging. Each collar is tested according to ASTM A 262, Pract.A and E, last edition.
- **Pitting Corrosion:** Due to a high chromium-, nickel- and nitrogen contents a excellent resistance to pitting corrosion comparable to nickelbase alloys is given.

5. NON-DESTRUCTIVE TESTING

- **Magnetic inspection:** Drill collars are 100% tested by a proprietary probe-testing process using a Förster Magnetomat 1.782. ("Hot Spot"-test). Magnetic permeability of each collar is certified with the printout of probe-testing.
- **Ultrasonic inspection:** Each collar is ultrasonically inspected over 100% of the volume according to ASTM E 114, last edition as a minimum level.

P750 Non-Magnetic Drill Collars meet all requirements of API Spec. 7.1, last edition.
All tests are carried out according to ASTM-Standards, last editions.
Prepared / released: B. Holper
Date: June, 2013

We provide the leading edge

Appendix B

Data sheets for alloys investigated.



Sanicro® 35 is an alloy combining the best features of a super austenitic stainless steel and a nickel alloy. The grade has excellent corrosion resistance, for service in sea-water applications and other highly corrosive environments.

The grade is characterized by:

- Excellent resistance to pitting and crevice corrosion
- Excellent resistance to stress corrosion cracking (SCC)
- High resistance to general corrosion in acid and caustic environments
- High resistance to erosion-corrosion
- Very high mechanical strength
- Good weldability using nickel alloy consumables

STANDARDS

- UNS: N08935
- Compliance with NACE MR0175/ISO 15156-3:2015, (Petroleum, Petrochemical, and Natural Gas Industries - Materials for Use in H₂S-Containing Environments in Oil and Gas Production - Part 3: Cracking-Resistant CRAs (Corrosion-Resistant Alloys) and Other Alloys) for type 4a and type 4c materials.
- Compliance with ANSI/NACE MR0103/ISO 17495-1:2016, (Petroleum, petrochemical and natural gas industries-Metallic materials resistant to sulfide stress cracking in corrosive petroleum refining environments) for highly alloyed austenitic stainless steels and nickel alloys.

PRODUCT STANDARDS

- Seamless tube and pipe: ASTM B163

APPROVALS

- ASME Code Case 2982. Boiler and Pressure Vessel Code, Section VIII, Division I and II.
- Pre-approval for Particular Material Appraisal (PMA), TÜV file 1326W043219

CHEMICAL COMPOSITION (NOMINAL)

Chemical composition (nominal) %

C	Si	Mn	P	S	Cr	Ni	Mo	Cu	N
≤0.030	≤0.5	0.8	≤0.030	≤0.020	27	35	6.5	0.2	0.3

APPLICATIONS

Due to its extremely good pitting and crevice corrosion properties, Sanicro® 35 is particularly suitable for applications where seawater is used for cooling or heating. Sanicro® 35 also has a high resistance to general

Datasheet updated 2/2/2021 4:51:43 PM (supersedes all previous editions)

Appendix B

Data sheets for alloys investigated.

corrosion in acid environments, making it suitable for a variety of applications.

CORROSION RESISTANCE

General corrosion

Sanicro® 35 has good resistance to hydrochloric acid compared to stainless steels with a lower chromium and molybdenum content and can, therefore, be useful in environments where hydrochloric acid is present. See Figure 1.

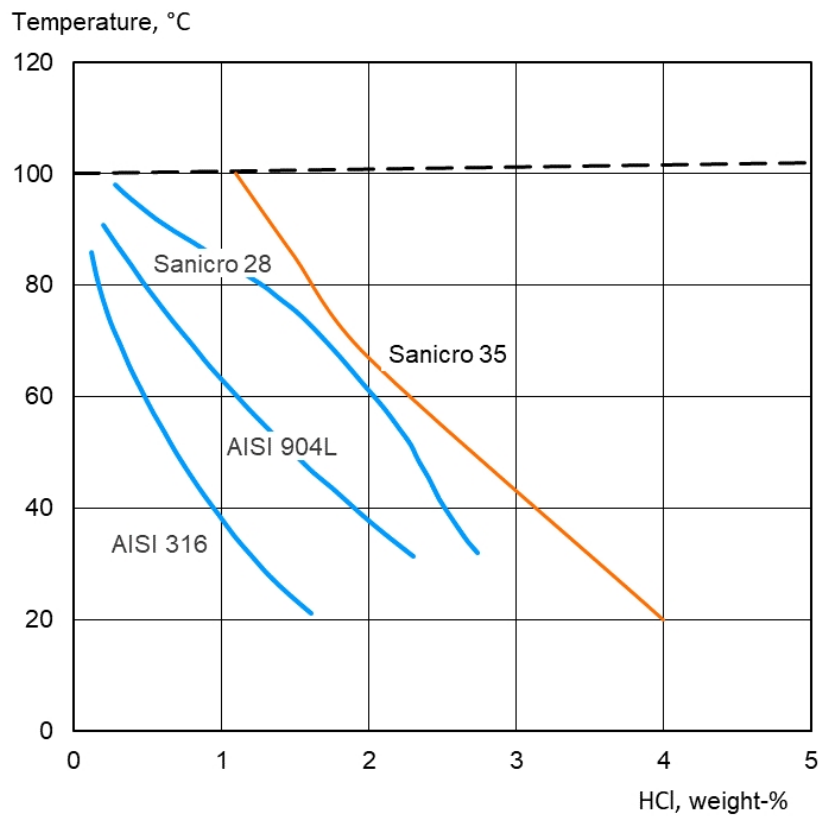


Figure 1. Isocorrosion in hydrochloric acid. The curves represent a corrosion rate of 0.1 mm/year.

Sanicro® 35 has a high resistance to sulfuric acid and nitric acid. Isocorrosion diagrams can be seen in Figure 2 and Figure 3.

Datasheet updated 2/2/2021 4:51:43 PM (supersedes all previous editions)

Appendix B

Data sheets for alloys investigated.

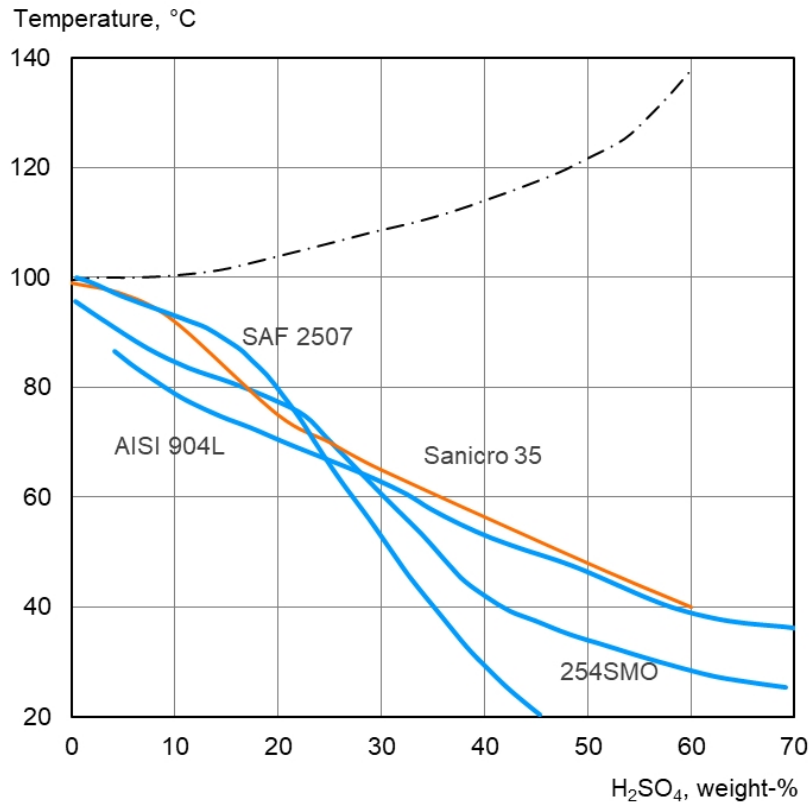


Figure 2. Isocorrosion in naturally aerated sulfuric acid. The curves represent a corrosion rate of 0.1 mm/year.

Datasheet updated 2/2/2021 4:51:43 PM (supersedes all previous editions)

Appendix B

Data sheets for alloys investigated.

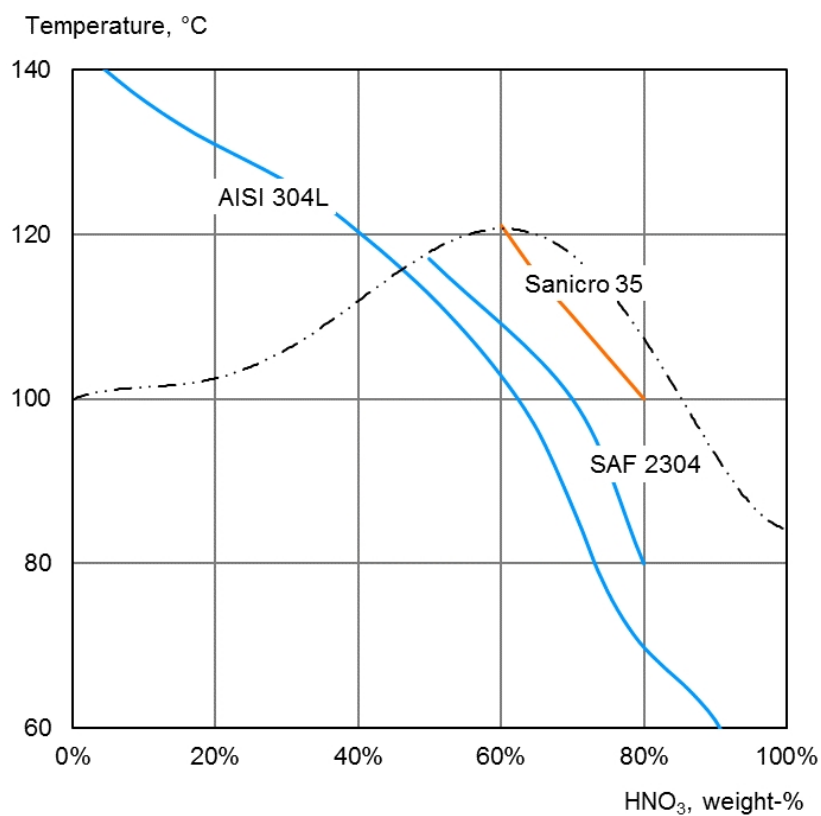


Figure 3. Isocorrosion in nitric acid. The curves represent a corrosion rate of 0.1 mm/year.

Sanicro® 35 also performs well in mixtures of formic acid and acetic acid, see Table 1.

Table 1. Corrosion rate of Sanicro 35 in mixtures of acetic acid (CH₃COOH) and formic acid (HCOOH) at boiling conditions.

Concentration CH ₃ COOH, %	50	50	50	50
Concentration HCOOH, %	10	15	20	25
Corrosion rate, mm/year	0.00	0.00	0.00	0.01

Sanicro® 35 performs well also in alkaline conditions showing high corrosion resistance in caustic solutions, see Table 2.

Table 2. Corrosion rate of Sanicro® 35 in sodium hydroxide (NaOH) at various concentrations and temperatures.

Concentration NaOH %	40	50	60	70
----------------------	----	----	----	----

Appendix B

Data sheets for alloys investigated.

Temperature (°C)	120	120	120	130
Corrosion rate, mm/year	0.06	0.05	0.03	0.01

Pitting corrosion

One of the main advantages of Sanicro® 35 is that it has excellent resistance to pitting corrosion. The pitting resistance comes from the high contents of chromium, molybdenum, and nitrogen. The PREN-number can be used to compare and rank alloys with respect to the chemical composition and possibility to resist pitting. The PREN is defined as, in weight-%;

$$\text{PREN} = \%Cr + 3.3 \times \%Mo + 16 \times \%N$$

The nominal PREN value for Sanicro® 35 is ~52, comparable to the nickel alloy Sanicro® 625 (Alloy 625). This is significantly higher than e.g. the PREN values for super duplex and 6 Mo austenitic grades which are commonly used in seawater applications. For reference, Sandvik SAF 2507® and Sandvik 254 SMO have a minimum PREN-value of 42.5.

The critical pitting temperature (CPT) has been determined in 6% FeCl₃ according to ASTM G48 practice C. The CPT has also been determined in a potentiostatic test in a 3M MgCl₂ solution. The test was performed in a modified ASTM G150 test where the solution was changed from 1M NaCl to allow the CPT-measurement of highly alloyed materials. The measured CPT-values can be seen in Table 3.

Table 3. CPT-values for Sanicro® 35 compared to Sandvik 254 SMO. The CPT was measured on coupons with P120 surface for the ASTM G48 test and P600 surface for the G150 mod. test.

Alloy	CPT (°C)	
	Mod. G150 in 3M MgCl ₂	ASTM G48 method C
Sanicro® 35	110	>85 ¹⁾²⁾
Sandvik 254 SMO	67	65 ³⁾
Alloy C276	N/A	>85 ¹⁾²⁾
Alloy 625	N/A	>85 ¹⁾²⁾

¹⁾ According to the standard ASTM G48, the method was developed to be used up to 85°C.

²⁾ Method C

³⁾ Method E

Crevice corrosion

Crevice corrosion resistance is equally as important as pitting resistance since crevices can rarely be totally avoided. Sanicro® 35 has excellent crevice corrosion resistance in chloride environments. The critical crevice temperature (CCT) has been determined by potentiostatic tests in 1M NaCl according to standard ASTM G150 and by immersion tests in 6% FeCl₃ test solution acidified with HCl according to ASTM G48, see Table 4.

Table 4. CCT-values for Sanicro® 35 compared to some alloys according to various test methods. The applied potential was 700 mV vs. SCE as per ASTM G150. Flat coupons were tested with surfaces wet ground with P600 grit paper for the ASTM G150 test and with P120 for the ASTM G48 tests.

Alloy	CCT (°C)		
	ASTM G150 ¹⁾	ASTM G48 method D ²⁾	ASTM G48 method F ³⁾
Sanicro® 35	100	52.5	45
Alloy C276		52.5	42.5
Alloy 625		45	25
Sandvik 254 SMO	75		35

Appendix B

Data sheets for alloys investigated.

- ¹⁾ crevice formers according to ISO 18070 with applied momentum of 3 Nm
²⁾ applied momentum of 0.28 Nm
³⁾ applied momentum of 1.58 Nm

Testing in seawater

Accelerated laboratory tests are very good for ranking different alloys, however, real application environment tests are also valuable. Materials are often used in a seawater environment which is very corrosive for many alloys. Sanicro® 35 has been tested for 90 days in natural seawater at 30°C where a biofilm is active and also in 0.5 ppm chlorinated seawater at elevated temperatures.

Table 5. Flat specimens with surfaces ground with P120 grit paper tested in real seawater.

Test condition	Pitting corrosion	Crevice corrosion ¹⁾
30°C natural seawater	No	No
80°C chlorinated seawater (0.5 ppm residual Cl)	No	N/A

- ¹⁾ crevice formers according to ISO 18070 with applied crevice pressure of 3 N/mm²

Stress corrosion cracking

Ordinary austenitic steels of the ASTM 316 type are susceptible to chloride-induced stress corrosion cracking (SCC) in chloride bearing solutions at temperatures above about 60°C (140°F). This susceptibility declines with increasing nickel content. Chromium contents above 20% can also be beneficial. Sanicro® 35 has excellent resistance to SCC. This is demonstrated in Table 6, which shows the results of SCC tests in a 40% calcium chloride solution. The grade showed no cracking or corrosion after 500 hours of constant load testing, corresponding to 90% of the actual ultimate tensile strength at 100°C. It should be noted that the high loading of 90% of UTS naturally causes plastic deformation of the specimens.

Table 6. Result of stress corrosion cracking test of different alloys in aerated 40% CaCl₂, at 100°C (210°F), pH 6.5

Alloy	% of UTS	Time to failure (h)	Remark
Sanicro® 35	90	>500	No attack
Sanicro® 28	90	>500	No attack
ASTM TP 316	90	<70	Pitting and cracking

Sanicro® 35 does not suffer from SCC in a NACE MR 0175 / ISO 15156 Test Level VI environment. Slow strain rate testing (SSRT) was performed on cold worked Sanicro® 35 material (140 ksi and 180 ksi), according to NACE TM0198. The environment had partial pressures of 500 psia H₂S and 500 psi CO₂. 20 wt-% sodium chloride was used as test solution and the temperature was 175°C ± 3°C. For both the 140 ksi and 180 ksi materials, two specimens were tested in the corrosive environment and one in nitrogen. All tests were carried out at the same baseline temperature. Both materials show ductile fractures with ratios of ≥92% for time to failure, elongation to failure, plastic strain to failure and reduction in area compared to inert environment, which indicates no SCC.

Hydrogen embrittlement

Sanicro® 35 shows as expected excellent resistant to hydrogen embrittlement since it has high austenitic phase stability. Sanicro® 35 is not a precipitation-hardened grade which the latter may experience hydrogen embrittlement.

Sanicro® 35 solution annealed material experienced no cracking in constant load testing at 4°C in 3% NaCl at -1050 mV_{SCE} at two different loads present in Table 7. This indicates that the alloy is not prone to hydrogen embrittlement and is a viable option for subsea applications.

Table 7. Sanicro® 35 results from constant load testing at 4°C in 3% NaCl at -1050 mV_{SCE}

Appendix B

Data sheets for alloys investigated.

Load/Yield strength, %	Load, MPa	Time to failure, h	Cracking, Yes/No
100	427	>500	No
120	509	>500	No

FABRICATION

Bending

The force needed for bending Sanicro® 35 is higher than that for standard austenitic stainless steels which is a natural consequence of the higher yield strength. The excellent formability of the grade permits cold bending to tight bending radii.

Expanding

Sanicro® 35 can be expanded into tube sheets in the same way as standard austenitic stainless steels.

FORMS OF SUPPLY

Sanicro® 35 can be supplied as seamless tube and pipe.

HEAT TREATMENT

Tubes are delivered in solution annealed condition. If additional heat treatment is needed after further processing, please contact Sandvik.

MECHANICAL PROPERTIES

The following figures apply to material in the solution annealed condition.

At 20°C (68°F)

Metric units

Proof strength	Tensile Strength	Elongation
R _{p0.2} ^a	R _m	A ₂ ^c
MPa	MPa	%
≥425	≥750	≥35

Imperial units

Proof strength	Tensile Strength	Elongation
R _{p0.2} ^a	R _m	A ₂ ^c
ksi	ksi	%
≥62	≥109	≥35

1 MPa = 1 N/mm²

a) R_{p0.2} and R_{p1.0} corresponds to 0.2% and 1.0% offset yield strength.

b) Based on L₀ = 5.65 √S₀ where L₀ is the original gauge length and S₀ the original cross-section area.

At high temperatures

Intermetallic phases are precipitated at temperatures above 600°C (1110°F). Therefore, the steel should not be exposed to these temperatures for prolonged periods.

Metric units

Temperature	Proof strength	Tensile strength	Elongation
	R _{p0.2}	R _m	A

7 SANICRO® 35

Datasheet updated 2/2/2021 4:51:43 PM (supersedes all previous editions)

Appendix B

Data sheets for alloys investigated.

°C	MPa	MPa	%
	Min.	Min.	Min.
100	350	680	35
200	300	620	35
300	275	600	35
400	250	580	35

Imperial units

Temperature	Proof strength	Tensile strength	Elongation
	Rp0.2	Rm	A
°F	ksi	ksi	%
	Min.	Min.	Min.
200	51	98	35
400	43	90	35
600	39	87	35
800	36	84	35

PHYSICAL PROPERTIES

Density: 8.1 g/cm³, 0.29 lb/in³

Thermal conductivity

Temperature, °C	W/(m °C)	Temperature, °F	Btu/(ft h °F)
20	10.0	68	6.0
100	12.0	200	7.0
200	13.5	400	8.0
300	15.5	600	9.0
400	17.0	800	10.0

Specific heat capacity

Temperature, °C	J/(kg °C)	Temperature, °F	Btu/(lb °F)
20	450	68	0.11
100	470	200	0.11
200	500	400	0.12
300	510	600	0.12
400	530	800	0.13

Thermal expansion

Metric units, x10⁻⁶/°C

Temperature, °C	30-100	30-200	30-300	30-400
Sanicro® 35	14.0	14.5	15.0	15.5
Carbon steel	12.5	13.0	13.5	14.0
ASTM 316L	16.5	17.0	17.5	18.0

Appendix B

Data sheets for alloys investigated.

Imperial units, x10⁻⁶/°F

Temperature, °C	86-200	86-400	86-600	86-800
Sanicro® 35	8.0	8.0	8.5	8.5
Carbon steel	7.0	7.0	7.5	8.0
ASTM 316L	9.5	9.5	10.0	10.0

Resistivity

Temperature, °C	μΩm	Temperature, °F	μΩinch
20	1.0	68	39

Modulus of elasticity, x10³

Temperature, °C	MPa	Temperature, °F	ksi
20	190	68	28.0
100	185	200	27.0
200	180	400	26.0
300	175	600	25.0
400	170	800	24.5

WELDING

The weldability of Sanicro® 35 is good and a suitable method for fusion welding is TIG welding (GTAW).

Welding should be undertaken with low heat input, maximum 1.2 kJ/mm, and interpass temperature 100 °C maximum. A stringer welding technique should be used. Preheating and post-weld heat treatment are not necessary. To maintain full corrosion resistance of the welded joint, welding must be followed by thorough cleaning to ensure the removal of all oxides and heat tint. Ar + 2 %N₂ is recommended as shielding gas and backing gas with TIG welding to achieve the best combination of mechanical properties and corrosion resistance of the welded joints.

Welding of fully austenitic stainless steels and nickel-base alloys often involves the risk of hot cracking in the welded joints if the weldment is under constrain. Sanicro® 35, however, possesses very high purity, and is thereby less prone to hot cracking than most of the nickel-base alloys.

Nickel alloy UNS N06059 (ERNiCrMo-13, NiCr23Mo16) wire or rod is recommended as filler material for gas shielded arc welding. Welding without filler material should be avoided in the as-welded condition.

Disclaimer: Recommendations are for guidance only, and the suitability of a material for a specific application can be confirmed only when we know the actual service conditions. Continuous development may necessitate changes in technical data without notice. This datasheet is only valid for Sandvik materials.

materials.sandvik/contact-us
MATERIALS.SANDVIK



Datasheet updated 2/2/2021 4:51:43 PM (supersedes all previous editions)

Stainless Steel Grade Super Duplex 2507 (UNS S32750)

Stainless Steel Grade Super Duplex 2507 (UNS S32750)

Jun 21 2013

Topics Covered

Introduction
Chemical Composition
Physical Properties
Applications

Introduction

Stainless steel Super Duplex 2507 is designed to handle highly corrosive conditions and situations where high strength is required. High molybdenum, chromium and nitrogen content in Super Duplex 2507 help the material withstand pitting and crevice corrosion. The material is also resistant to chloride stress corrosion cracking, to erosion corrosion, to corrosion fatigue, to general corrosion in acids. This alloy has good weldability and very high mechanical strength.

The following sections will discuss in detail about stainless steel grade Super Duplex 2507.

Chemical Composition

The chemical composition of stainless steel grade Super Duplex 2507 is outlined in the following table.

Element	Content (%)
Chromium, Cr	24 – 26
Nickel, Ni	6 – 8
Molybdenum, Mo	3 – 5
Manganese, Mn	1.20 max
Silicon, Si	0.80 max
Copper, Cu	0.50 max
Nitrogen, N	0.24 – 0.32
Phosphorous, P	0.035 max
Carbon, C	0.030 max

Saved from URL: <https://www.azom.com/article.aspx?ArticleID=9185>

Appendix B

Data sheets for alloys investigated.

Stainless Steel Grade Super Duplex 2507 (UNS S32750)

Sulfur, S	0.020 max
Iron, Fe	Balance

Physical Properties

The physical properties of stainless steel grade Super Duplex 2507 are tabulated below.

Properties	Metric	Imperial
Density	7.8 g/cm ³	0.281 lb/in ³
Melting point	1350°C	2460°F

Applications

Super Duplex 2507 is widely used in the following sectors:

- Power
- Marine
- Chemical
- Pulp and paper
- Petrochemical
- Water desalinization
- Oil and gas production

Products made using Super Duplex 2507 include:

- Fans
- Wire
- Fittings
- Cargo tanks
- Water heaters
- Storage vessels
- Hydraulic piping
- Heat exchangers
- Hot water tanks
- Spiral wound gaskets
- Lifting and pulley equipment
- Propellers, rotors, and shafts

Appendix C

Quantitative overview from EDS analysis.

P750-H.S

Table S1: Key values from EDS analysis on P750-H.S

Element	Weight %	Atomic %	Net Int.	Error %	Kratio	Z	A	F
O K	36.31	46.42	880.55	5.40	0.3522	1.0736	0.9034	1.0000
MgK	63.69	53.58	1214.37	5.48	0.5906	0.9579	0.9678	1.0002

P750-L.S

Table S2: Key values from EDS analysis of P750-L.S

Element	Weight %	Atomic %	Net Int.	Error %	Kratio	Z	A	F
C K	1.58	2.65	30.28	13.89	0.0047	1.1212	0.2634	1.0000
N K	1.35	1.95	37.65	11.20	0.0072	1.0882	0.4856	1.0000
O K	34.76	43.89	2569.43	5.19	0.2576	1.0598	0.6994	1.0000
NiL	0.53	0.18	20.71	16.52	0.0042	0.7985	0.9878	1.0000
MgK	61.78	51.33	6248.96	3.34	0.5275	0.9622	0.8872	1.0002

A31+

Precipitate - Inclusion

Table S3: Key values from EDS analysis of detected inclusion in the microstructure of A31.

Element	Weight %	Atomic %	Net Int.	Error %	Kratio	Z	A	F
C K	1.69	7.59	32.53	13.55	0.0076	1.4255	0.3178	1.0000
N K	1.39	5.36	24.60	14.92	0.0072	1.3878	0.3703	1.0000
FeL	13.91	13.44	171.34	9.22	0.0646	1.0120	0.4591	1.0000
CoL	0.32	0.30	4.62	68.28	0.0016	0.9902	0.4973	1.0000
NiL	16.91	15.54	303.46	8.02	0.0939	1.0255	0.5414	1.0000
CuL	0.00	0.00	0.02	99.99	0.0000	0.9758	0.4996	1.0000
P K	0.18	0.31	8.89	67.96	0.0018	1.1690	0.8520	1.0068
MoL	22.34	12.56	550.85	4.12	0.1914	0.8821	0.9703	1.0011
CrK	43.25	44.89	353.02	6.59	0.4511	1.0269	0.9893	1.0266
MnK	0.01	0.01	0.03	99.99	0.0001	1.0041	0.9905	1.0275

Precipitate - Secondary phase

Table S4: Key values from EDS analysis of detected secondary phase in the microstructure of A31.

Element	Weight %	Atomic %	Net Int.	Error %	Kratio	Z	A	F
C K	1.54	2.57	14.65	15.70	0.0046	1.1193	0.2658	1.0000
N K	1.18	1.69	16.29	14.38	0.0063	1.0863	0.4898	1.0000
O K	35.94	45.09	1317.66	5.28	0.2685	1.0580	0.7060	1.0000
MgK	61.34	50.65	3052.80	3.42	0.5238	0.9604	0.8889	1.0002

Sanicro35

Table S5: Key values from EDS analysis of Sanicro35.

Element	Weight %	Atomic %	Net Int.	Error %	Kratio	Z	A	F
O K	46.19	59.14	483.43	6.06	0.4391	1.0854	0.8759	1.0000
AlK	53.81	40.86	368.56	6.41	0.4870	0.9261	0.9769	1.0004

25% Cr SDSS

Table S6: Key values from EDS analysis of 25%Cr SDSS.

Element	Weight %	Atomic %	Net Int.	Error %	Kratio	Z	A	F
O K	25.04	49.41	1345.32	4.64	0.2382	1.2184	0.7808	1.0000
AlK	10.62	12.43	533.54	5.77	0.0856	1.0685	0.7534	1.0017
CrK	36.75	22.31	227.74	6.76	0.3366	0.8990	1.0009	1.0178
MnK	27.58	15.85	115.02	9.63	0.2426	0.8753	0.9999	1.0046

Appendix D

Risk assessments of the experimental work conducted in this study.



Faculty of Engineering (IV)
Department of Mechanical and Industrial Engineering (MTP)

Date created
XXXX

Last Revision
XXXXX

1 of 6

RISK ASSESSMENT

ONLY VALID FOR DETAILED ACTIVITIES LISTED IN SECTION 4

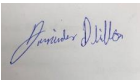

1. Identification

Laboratory name: Corrosion lab	Room number: 104A
User's name: Amrinder Pal Singh Dhillon	<input checked="" type="checkbox"/> Master <input type="checkbox"/> PhD <input type="checkbox"/> Post-Doc <input type="checkbox"/> SINTEF <input type="checkbox"/> Other:
User's e-mail: apdhillo@stud.ntnu.no	User's Phone: 91702713
Supervisor: Roy Johnsen	Supervisor's phone: 932 45 101
Project number: 70442887	
Period: 01.02.22- 30.06.22	

Description of the project and needs:
Hydrogen pre-charging of specimen used for slow strain rate testing (SSRT).

2. Signatures

The user and the supervisor are aware of all the risks involved in the lab activities that are going to be performed. Additionally, the user confirms that he/she will follow the preventive measures described in this form to minimize all the risks that have been identified.

User's signature	Supervisor's signature
Signature: 	Signature: 
Name: Amrinder Pal Singh Dhillon	Name: Roy Johnsen
Date: 08.02.22	Date: 16.02.2022

Approved by:

	Signature:	Name:	Date:
Room responsible:		Cristian Torres	

Note: a pdf copy with all signatures shall be sent to everyone who has signed above.

Appendix D

Risk assessments of the experimental work conducted in this study.



Faculty of Engineering (IV)
Department of Mechanical and Industrial Engineering (MTP)

Date created
XXXX

Last Revision
XXXXX

2 of 6

3. Administration

Answer: Yes, No or NR (Not relevant)

Is the work order signed? (only for external work)	NR
Will the operator receive the required courses/training on the equipment?	Yes
Has the operator followed the safety courses? (Mandatory)	Yes
Can the work be done alone?	Yes
- If not, the work may have to be done under special conditions (evaluated in section 4)	NR
Does an expert have to check the start of the experiment?	No
- If yes, who?	NR

4. Description of the activity

The risk assessment is a living document during the duration of your project, you must update it with new activities that might arise along the project period. This is not once in a lifetime task; it needs to be reviewed regularly!

For each activity performed in the lab, health risks affecting the user or others need to be identified. For each risk identified, a preventive measure must be performed, and the final risk value calculated with the “risk matrix”. Explanation of the “risk matrix” can be found in the last page of this form.

The following page must be replicated for each different activity performed in the lab. Activities involving the use of chemicals must be filled together with section 4.2 “Chemical risk assessment”.

Appendix D

Risk assessments of the experimental work conducted in this study.



Faculty of Engineering (IV)
Department of Mechanical and Industrial Engineering (MTP)

Date created
"XXX

Last Revision
XXXXX

3 of 6

Activity: Hydrogen pre-charging with heating plate

Risk overview: (mark with X the risk that applies for the activity)

Big loads		Danger of fire	
Heavy lifting		Working at heights	
Hanging load		Hydraulic pressure	
Gas pressure		Water pressure	
High temperature	X	Low temperature	
Parts at high velocity		Chemicals (fill up section 4.2)	X
Sudden acceleration at fracture/failure		Pre-tensioned components	
Dangerous dust		Severe noise	
Danger of pinching		Rotating parts	

Detailed risk evaluation:

Risks	Preventive measures
1. Burning your hands	Wait for test cell to cool down before working with it after test. No touch test cell during testing
2. Setting things on fire	Hold objects away from the heating plate.
3 Chemical spill	Patient execution of the experiment.

Risk matrix after preventive measures of the activity:

Risk	Probability (P) (1-5)	Consequence (C)				Risk value (P x C)
		Health (1-5)	Material values (1-5)	Environment (1-5)	Reputation (1-5)	
1	1	1	1	1	1	1
2	1	1	1	1	1	1
3	1	1	1	1	1	1

Required safety equipment: (mark with X the equipment needed to perform the activity)

Safety goggles	X	Safety shoes	
Helmet		Gloves	X
Screen/Visor		Lifting equipment	
Ear protection		Hazard suit	

Appendix D

Risk assessments of the experimental work conducted in this study.



Faculty of Engineering (IV)
Department of Mechanical and Industrial Engineering (MTP)

Date created
"xxx

Last Revision
xxxxx

4 of 6

Harness ropes, other measures to prevent falling		Fume hood	
--	--	-----------	--

4.2. Chemical Risk Assessment:

Only for activities involving the use of chemicals (except ethanol and acetone for cleaning).

This page must be replicated for each different chemical activity performed in the lab.

Activity: Hydrogen pre-charging, solution used for reference electrode

Chemicals used:	KCl
Mixture:	Saturated
Will the mixture be stored in the cabinet for future uses?	Yes

Risk	Prevention Measure
1. Causes skin irritation	Wear gloves

Chemical disposal procedure:
Pour as chemical waste in a container specifically for this chemical.

Risk matrix after preventive measures of the chemical activity:

Risk	Probability (P) (1-5)	Consequence (C)				Risk value (P x C)
		Health (1-5)	Material values (1-5)	Environment (1-5)	Reputation (1-5)	
1	1	1	1	1	1	1
2	1	1	1	1	1	1
3	1	1	1	1	1	1

Required safety equipment: (mark with X the equipment needed to perform the activity)

Safety goggles	X	Safety shoes	
Helmet		Gloves	X
Screen/Visor		Lifting equipment	
Ear protection		Hazard suit	
Harness ropes, other measures to prevent falling		Fume hood (during solution preparation)	

Appendix D

Risk assessments of the experimental work conducted in this study.



Faculty of Engineering (IV)
Department of Mechanical and Industrial Engineering (MTP)

Date created: XXX
Last Revision: XXXX

5 of 6

Activity: Hydrogen pre-charging, solution for main container

Chemicals used:	NaCl
Mixture:	3.5 wt% NaCl
Will the mixture be stored in the cabinet for future uses?	Yes

Risk	Prevention Measure
1. Causes skin irritation	Wear gloves

Chemical disposal procedure:
Pour as chemical waste in a container specifically for this chemical

Risk matrix after preventive measures of the chemical activity:

Risk	Probability (P) (1-5)	Consequence (C)				Risk value (P x C)
		Health (1-5)	Material values (1-5)	Environment (1-5)	Reputation (1-5)	
1	1	1	1	1	1	1
2	1	1	1	1	1	1
3	1	1	1	1	1	1

Required safety equipment: (mark with X the equipment needed to perform the activity)

Safety goggles	X	Safety shoes	
Helmet		Gloves	X
Screen/Visor		Lifting equipment	
Ear protection		Hazard suit	
Harness ropes, other measures to prevent falling		Fume hood	

5. Comments

--

Appendix D

Risk assessments of the experimental work conducted in this study.



Faculty of Engineering (IV)
Department of Mechanical and Industrial Engineering (MTP)

Date created
XXXX

Last Revision
XXXXX

6 of 6

Risk matrix explanation

		Health	Material values	Reputation	Environment
Grade	1	Minor injury/strain that requires simple treatment. Reversible injury. Short recovery time.	Operational shutdown, or shutdown of activities <1 day.	Little effect on credibility and respect.	Negligible injury and short recovery time.
	2	Injury/strain that requires medical treatment. Reversible injury/strain. Short recovery time.	Operational shutdown, or shutdown of activities <1 week.	Negative effect on credibility and respect.	Minor injury and short recovery time.
	3	Serious injury/strain that requires medical treatment. Lengthy recovery time.	Operational shutdown, or shutdown of activities <1 month.	Reduced credibility and respect.	Minor injury and lengthy recovery time.
	4	Serious injury/strain that requires medical treatment. Possible disability /permanent disability.	Operational shutdown > 1/2 year. Shutdown of activities up to 1 year.	Credibility and respect considerably reduced.	Long-lasting injury. Lengthy recovery time.
	5	Death or disability / permanent disability.	Operational shutdown, or shutdown of activities >1 year.	Credibility and respect considerably and permanently reduced.	Very long-lasting and irreversible injury.

Consequence (C)	Very serious	5	10	15	20	25
	Serious	4	8	12	16	20
	Moderate	3	6	9	12	15
	Little	2	4	6	8	10
	Very little	1	2	3	4	5
		Very little	Little	Medium	Big	Very big
		Probability (P)				

Red	Unacceptable risk. Measures need to be implemented.
Yellow	Medium risk. Measures need to be considered.
Green	Acceptable risk. Measures can be considered.

Appendix D

Risk assessments of the experimental work conducted in this study.



Faculty of Engineering (IV)
Department of Mechanical and Industrial Engineering (MTP)

Date created Last Revision 1 of 14

RISK ASSESSMENT

ONLY VALID FOR DETAILED ACTIVITIES LISTED IN SECTION 4

1. Identification

Laboratory name: Metallography lab	Room number: 161
User's name: Amrinder Pal Singh Dhillon	<input checked="" type="checkbox"/> Master <input type="checkbox"/> PhD <input type="checkbox"/> Post-Doc <input type="checkbox"/> SINTEF <input type="checkbox"/> Other:
User's e-mail: apdhillo@stud.ntnu.no	User's Phone: 91702713
Supervisor: Roy Johnsen	Supervisor's phone: 932 45 101
Project number: 70442887	
Period: 01.02.22- 30.06.22	

Description of the project and needs:
HISC testing by the use of SSRT. Etching of nickel alloys

2. Signatures

The user and the supervisor are aware of all the risks involved in the lab activities that are going to be performed. Additionally, the user confirms that he/she will follow the preventive measures described in this form to minimize all the risks that have been identified.

User's signature	Supervisor's signature
Signature: 	Signature: 
Name: Amrinder Pal Singh Dhillon	Name: Roy Johnsen
Date: 28.03.22	Date: 28.03.2022

Approved by:

	Signature:	Name:	Date:
Room responsible:		Cristian Torres	

Appendix D

Risk assessments of the experimental work conducted in this study.



Faculty of Engineering (IV)
Department of Mechanical and Industrial Engineering (MTP)

Date created Last Revision 2 of 14

Note: a pdf copy with all signatures shall be sent to everyone who has signed above.

3. Administration

Answer: Yes, No or NR (Not relevant)

Is the work order signed? (only for external work)	NR
Will the operator receive the required courses/training on the equipment?	Yes
Has the operator followed the safety courses? (Mandatory)	Yes
Can the work be done alone?	Yes
- If not, the work may have to be done under special conditions (evaluated in section 4)	NR
Does an expert have to check the start of the experiment?	No
- If yes, who?	NR

4. Description of the activity

The risk assessment is a living document during the duration of your project, you must update it with new activities that might arise along the project period. This is not once in a lifetime task; it needs to be reviewed regularly!

For each activity performed in the lab, health risks affecting the user or others need to be identified. For each risk identified, a preventive measure must be performed, and the final risk value calculated with the “risk matrix”. Explanation of the “risk matrix” can be found in the last page of this form.

The following page must be replicated for each different activity performed in the lab. Activities involving the use of chemicals must be filled together with section 4.2 “Chemical risk assessment”.

Appendix D

Risk assessments of the experimental work conducted in this study.



Faculty of Engineering (IV)
Department of Mechanical and Industrial Engineering (MTP)

Date created 3 of 14
Last Revision

Activity: Slow strain rate testing (SSRT) in two different environments; air and NaCl solution.

Risk overview: (mark with X the risk that applies for the activity)

Big loads	X	Danger of fire	
Heavy lifting		Working at heights	
Hanging load		Hydraulic pressure	X
Gas pressure		Water pressure	
High temperature		Low temperature	
Parts at high velocity		Chemicals (fill up section 4.2)	
Sudden acceleration at fracture/failure	X	Pre-tensioned components	
Dangerous dust		Severe noise	
Danger of pinching		Rotating parts	

Detailed risk evaluation:

Risks	Preventive measures
1. Metal splash due to incorrect use of the machine and not according to the set standard.	Follow testing standard and step-by-step procedure.
2. Crush injuries due to incorrect use of the machine and not according to the set standard	Follow testing standard and step-by-step procedure.

Risk matrix after preventive measures of the activity:

Risk	Probability (P) (1-5)	Consequence (C)				Risk value (P x C)
		Health (1-5)	Material values (1-5)	Environment (1-5)	Reputation (1-5)	
1	1	1	1	1	1	1
2						
3						

Required safety equipment: (mark with X the risk that applies for the activity)

Safety goggles	X	Safety shoes	
----------------	---	--------------	--

Appendix D

Risk assessments of the experimental work conducted in this study.



Faculty of Engineering (IV)
Department of Mechanical and Industrial Engineering (MTP)

Date created Last Revision 4 of 14

Helmet		Gloves	X
Screen		Lifting equipment	
Ear protection		Hazard suit	
Harness ropes, other measures to prevent falling		Fume hood	

Activity: Etching procedure 1 - Electrolytic etching in Oxalic acid at 3 V and 5 A for up to 12 seconds.

Risk overview: (mark with X the risk that applies for the activity)

Big loads		Danger of fire	
Heavy lifting		Working at heights	
Hanging load		Hydraulic pressure	
Gas pressure		Water pressure	
High temperature		Low temperature	
Parts at high velocity		Chemicals (fill up section 4.2)	X
Sudden acceleration at fracture/failure		Pre-tensioned components	
Dangerous dust		Severe noise	
Danger of pinching		Rotating parts	

Detailed risk evaluation:

Risks	Preventive measures
1. Chemical spill during experiment setup and sample handling.	Follow testing standard and step-by-step procedure patiently. The process is not to be rushed.

Risk	Probability (P) (1-5)	Consequence (C)				Risk value (P x C)
		Health (1-5)	Material values (1-5)	Environment (1-5)	Reputation (1-5)	
1	1	1	1	1	1	1

Appendix D

Risk assessments of the experimental work conducted in this study.



Faculty of Engineering (IV)
Department of Mechanical and Industrial Engineering (MTP)

Date created Last Revision 5 of 14

2						
3						

Risk matrix after preventive measures of the activity:

Required safety equipment: (mark with X the risk that applies for the activity)

Safety goggles	X	Safety shoes	
Helmet		Gloves	X
Screen		Lifting equipment	
Ear protection		Hazard suit	
Harness ropes, other measures to prevent falling		Fume hood	

Activity: Etching procedure 2 - HNO₃ + HCl (6:1). The sample is etched by immersion for up to 2-5 minutes

Risk overview: (mark with X the risk that applies for the activity)

Big loads		Danger of fire	
Heavy lifting		Working at heights	
Hanging load		Hydraulic pressure	
Gas pressure		Water pressure	
High temperature		Low temperature	
Parts at high velocity		Chemicals (fill up section 4.2)	X
Sudden acceleration at fracture/failure		Pre-tensioned components	
Dangerous dust		Severe noise	
Danger of pinching		Rotating parts	

Detailed risk evaluation:

Risks	Preventive measures
1. Chemical spill during sample handling and immersion	Follow testing standard and step-by-step procedure patiently. The process is not to be rushed.

Appendix D

Risk assessments of the experimental work conducted in this study.



Faculty of Engineering (IV)
Department of Mechanical and Industrial Engineering (MTP)

Date created Last Revision 6 of 14

--	--

Risk matrix after preventive measures of the activity:

Risk	Probability (P) (1-5)	Consequence (C)				Risk value (P x C)
		Health (1-5)	Material values (1-5)	Environment (1-5)	Reputation (1-5)	
1	1	1	1	1	1	1
2						
3						

Required safety equipment: (mark with X the risk that applies for the activity)

Safety goggles	X	Safety shoes	
Helmet		Gloves	X
Screen		Lifting equipment	
Ear protection		Hazard suit	
Harness ropes, other measures to prevent falling		Fume hood	

Activity: Etching procedure 3 – 100ml H₂O, 300ml HCl, 15ml H₂O₂ (30%)

Risk overview: (mark with X the risk that applies for the activity)

Big loads		Danger of fire	
Heavy lifting		Working at heights	
Hanging load		Hydraulic pressure	
Gas pressure		Water pressure	
High temperature		Low temperature	
Parts at high velocity		Chemicals (fill up section 4.2)	X
Sudden acceleration at fracture/failure		Pre-tensioned components	
Dangerous dust		Severe noise	
Danger of pinching		Rotating parts	

Detailed risk evaluation:

Appendix D

Risk assessments of the experimental work conducted in this study.



Faculty of Engineering (IV)
Department of Mechanical and Industrial Engineering (MTP)

Date created 7 of 14
Last Revision

Risks	Preventive measures
1. Chemical spill during sample handling and immersion	Follow testing standard and step-by-step procedure patiently. The process is not to be rushed.

Risk matrix after preventive measures of the activity:

Risk	Probability (P) (1-5)	Consequence (C)				Risk value (P x C)
		Health (1-5)	Material values (1-5)	Environment (1-5)	Reputation (1-5)	
1	1	1	1	1	1	1
2						
3						

Required safety equipment: (mark with X the risk that applies for the activity)

Safety goggles	X	Safety shoes	
Helmet		Gloves	X
Screen		Lifting equipment	
Ear protection		Hazard suit	
Harness ropes, other measures to prevent falling		Fume hood	

Activity: Optical microscopy

Risk overview: (mark with X the risk that applies for the activity)

Big loads		Danger of fire	
Heavy lifting		Working at heights	
Hanging load		Hydraulic pressure	
Gas pressure		Water pressure	
High temperature		Low temperature	
Parts at high velocity		Chemicals (fill up section 4.2)	
Sudden acceleration at fracture/failure		Pre-tensioned components	

Appendix D

Risk assessments of the experimental work conducted in this study.



Faculty of Engineering (IV)
Department of Mechanical and Industrial Engineering (MTP)

Date created 8 of 14
Last Revision

Dangerous dust		Severe noise	
Danger of pinching		Rotating parts	

Detailed risk evaluation:

Risks	Preventive measures
No risks.	

Risk matrix after preventive measures of the activity:

Risk	Probability (P) (1-5)	Consequence (C)				Risk value (P x C)
		Health (1-5)	Material values (1-5)	Environment (1-5)	Reputation (1-5)	
1	1	1	1	1	1	1
2						
3						

Required safety equipment: (mark with X the risk that applies for the activity)

Safety goggles		Safety shoes	
Helmet		Gloves	
Screen		Lifting equipment	
Ear protection		Hazard suit	
Harness ropes, other measures to prevent falling		Fume hood	

4.2. Chemical Risk Assessment:

Only for activities involving the use of chemicals (except ethanol and acetone for cleaning).

Appendix D

Risk assessments of the experimental work conducted in this study.



Faculty of Engineering (IV)
Department of Mechanical and Industrial Engineering (MTP)

Date created 9 of 14
Last Revision

This page must be replicated for each different chemical activity performed in the lab.

Activity: Slow strain rate testing (SSRT) while cathodically polarizing the specimen using NaCl solution.

Chemicals used:	NaCl
Mixture:	3.5wt% NaCl
Will the mixture be stored in the cabinet for several uses?	Yes

Risk	Prevention Measure
1. Causes skin irritation	Wear gloves and protective clothes

Chemical disposal procedure:
Pour as chemical waste in a container specifically for this chemical

Risk matrix after preventive measures of the chemical activity:

Risk	Probability (P) (1-5)	Consequence (C)				Risk value (P x C)
		Health (1-5)	Material values (1-5)	Environment (1-5)	Reputation (1-5)	
1	1	1	1	1	1	1
2	1	1	1	1	1	1
3	1	1	1	1	1	1

Required safety equipment: (mark with X the risk that applies for the activity)

Safety goggles	X	Safety shoes	
Helmet		Gloves	X
Screen		Lifting equipment	
Ear protection		Hazard suit	
Harness ropes, other measures to prevent falling		Fume hood	

Appendix D

Risk assessments of the experimental work conducted in this study.



Faculty of Engineering (IV)
Department of Mechanical and Industrial Engineering (MTP)

Date created 10 of 14
Last Revision

Activity: Etching procedure 1 – Ni alloy: Sanicro35

Chemicals used:	Oxalic acid
Mixture:	
Will the mixture be stored in the cabinet for several uses?	Yes

Risk	Prevention Measure
1. Harmful if swallowed or in contact with skin	Wear gloves and protective clothes. Wash skin thoroughly after handling.
2. Can causes serious eye damage	Eye protection

Chemical disposal procedure:
Pour as chemical waste in a container specifically for this chemical

Risk matrix after preventive measures of the chemical activity:

Risk	Probability (P) (1-5)	Consequence (C)				Risk value (P x C)
		Health (1-5)	Material values (1-5)	Environment (1-5)	Reputation (1-5)	
1	1	1	1	1	1	1
2	1	1	1	1	1	1
3	1	2	1	1	1	2

Required safety equipment: (mark with X the risk that applies for the activity)

Safety goggles	X	Safety shoes	
Helmet		Gloves	X
Screen		Lifting equipment	
Ear protection		Hazard suit	
Harness ropes, other measures to prevent falling		Fume hood	X

Activity: Etching procedure 2 – Ni alloy: A31

Chemicals used:	HNO3 and HCl
------------------------	--------------

Appendix D

Risk assessments of the experimental work conducted in this study.



Faculty of Engineering (IV)
Department of Mechanical and Industrial Engineering (MTP)

Date created 11 of 14
Last Revision

Mixture:	HNO ₃ + HCl (6:1-ratio)
Will the mixture be stored in the cabinet for several uses?	Yes

Risk	Prevention Measure
1. Harmful if swallowed or in contact with skin	Wear gloves and protective clothes. Wash skin thoroughly after handling.
2. Can cause serious eye damage	Eye protection

Chemical disposal procedure:
Pour as chemical waste in a container specifically for this chemical

Risk matrix after preventive measures of the chemical activity:

Risk	Probability (P) (1-5)	Consequence (C)				Risk value (P x C)
		Health (1-5)	Material values (1-5)	Environment (1-5)	Reputation (1-5)	
1	1	1	1	1	1	1
2	1	1	1	1	1	1
3	1	2	1	1	1	2

Required safety equipment: (mark with X the risk that applies for the activity)

Safety goggles	X	Safety shoes	
Helmet		Gloves	X
Screen		Lifting equipment	
Ear protection		Hazard suit	
Harness ropes, other measures to prevent falling		Fume hood	X

Activity: Etching procedure 3 – Ni alloy: P750

Chemicals used:	HCl + H ₂ O ₂ (30%)
------------------------	---

Appendix D

Risk assessments of the experimental work conducted in this study.



Faculty of Engineering (IV)
Department of Mechanical and Industrial Engineering (MTP)

Date created 12 of 14
Last Revision

Mixture:	100ml H ₂ O, 300ml HCl, 15ml H ₂ O ₂ (30%)
Will the mixture be stored in the cabinet for several uses?	Yes

Risk	Prevention Measure
1. Harmful if swallowed or in contact with skin	Wear gloves and protective clothes. Wash skin thoroughly after handling.
2. May cause fire, strong oxidizer	Keep away from heat/sparks/open flames/hot surfaces. -

Chemical disposal procedure:
Pour as chemical waste in a container specifically for this chemical

Risk matrix after preventive measures of the chemical activity:

Risk	Probability (P) (1-5)	Consequence (C)				Risk value (P x C)
		Health (1-5)	Material values (1-5)	Environment (1-5)	Reputation (1-5)	
1	1	1	1	1	1	1
2	1	1	1	1	1	1
3	1	2	1	1	1	2

Required safety equipment: (mark with X the risk that applies for the activity)

Safety goggles	X	Safety shoes	
Helmet		Gloves	X
Screen		Lifting equipment	
Ear protection		Hazard suit	
Harness ropes, other measures to prevent falling		Fume hood	X

Appendix D

Risk assessments of the experimental work conducted in this study.



Faculty of Engineering (IV)
Department of Mechanical and Industrial Engineering (MTP)

Date created 13 of 14
Last Revision

5. Comments

Appendix D

Risk assessments of the experimental work conducted in this study.



Faculty of Engineering (IV)
Department of Mechanical and Industrial Engineering (MTP)

Date created 14 of 14
Last Revision

Risk matrix explanation

		Health	Material values	Reputation	Environment
Grade	1	Minor injury/strain that requires simple treatment. Reversible injury. Short recovery time.	Operational shutdown, or shutdown of activities <1 day.	Little effect on credibility and respect.	Negligible injury and short recovery time.
	2	Injury/strain that requires medical treatment. Reversible injury/strain. Short recovery time.	Operational shutdown, or shutdown of activities <1 week.	Negative effect on credibility and respect.	Minor injury and short recovery time.
	3	Serious injury/strain that requires medical treatment. Lengthy recovery time.	Operational shutdown, or shutdown of activities <1 month.	Reduced credibility and respect.	Minor injury and lengthy recovery time.
	4	Serious injury/strain that requires medical treatment. Possible disability /permanent disability.	Operational shutdown > 1/2 year. Shutdown of activities up to 1 year.	Credibility and respect considerably reduced.	Long-lasting injury. Lengthy recovery time.
	5	Death or disability / permanent disability.	Operational shutdown, or shutdown of activities >1 year.	Credibility and respect considerably and permanently reduced.	Very long-lasting and irreversible injury.

Consequence (C)	Very serious	5	10	15	20	25
	Serious	4	8	12	16	20
	Moderate	3	6	9	12	15
	Little	2	4	6	8	10
	Very little	1	2	3	4	5
		Very little	Little	Medium	Big	Very big
		Probability (P)				

Red	Unacceptable risk. Measures need to be implemented.
Yellow	Medium risk. Measures need to be considered.
Green	Acceptable risk. Measures can be considered.

Appendix D

Risk assessments of the experimental work conducted in this study.



Faculty of Engineering (IV)
Department of Mechanical and Industrial Engineering (MTP)

Date created 18.11.2020
Last Revision 03.09.2021

1 of 7

RISK ASSESSMENT

ONLY VALID FOR DETAILED ACTIVITIES LISTED IN SECTION 4

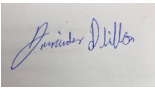

1. Identification

Laboratory name: Nanomechanical lab	Room number: 160
User's name: Amrinder Pal Singh Dhillon	<input checked="" type="checkbox"/> Master <input type="checkbox"/> PhD <input type="checkbox"/> Post-Doc <input type="checkbox"/> SINTEF <input type="checkbox"/> Other:
User's e-mail: apdhillo@stud.ntnu.no	User's Phone: 91702713
Supervisor: Roy Johnsen	Supervisor's phone: 932 45 101
Project number: 70442887	
Period: 01.02.22- 30.06.22	

Description of the project and needs:
Master thesis where the student will be using the SEM with the EDS and Optical microscopy

2. Signatures

The user and the supervisor are aware of all the risks involved in the lab activities that are going to be performed. Additionally, the user confirms that he/she will follow the preventive measures described in this form to minimize all the risks that have been identified.

User's signature	Supervisor's signature
Signature: 	Signature: 
Name: Amrinder Pal Singh Dhillon	Name: Roy Johnsen
Date: 09.02.22	Date: 16.02.2022

Approved by:

	Signature:	Name:	Date:
Room responsible:		Cristian Torres	

Note: a pdf copy with all signatures shall be sent to everyone who has signed above.

Appendix D

Risk assessments of the experimental work conducted in this study.



Faculty of Engineering (IV)
Department of Mechanical and Industrial Engineering (MTP)

Date created 18.11.2020
Last Revision 03.09.2021

2 of 7

3. Administration

Answer: Yes, No or NR (Not relevant)

Is the work order signed? (only for external work)	NR
Will the operator receive the required courses/training on the equipment?	Yes
Has the operator followed the safety courses? (Mandatory)	Yes
Can the work be done alone?	Yes
- If not, the work may have to be done under special conditions (evaluated in section 4)	NR
Does an expert have to check the start of the experiment?	No
- If yes, who?	NR

4. Description of the activity

The risk assessment is a living document during the duration of your project, you must update it with new activities that might arise along the project period. This is not once in a lifetime task; it needs to be reviewed regularly!

For each activity performed in the lab, health risks affecting the user or others need to be identified. For each risk identified, a preventive measure must be performed, and the final risk value calculated with the “risk matrix”. Explanation of the “risk matrix” can be found in the last page of this form.

The following page must be replicated for each different activity performed in the lab. Activities involving the use of chemicals must be filled together with section 4.2 “Chemical risk assessment”.

Appendix D

Risk assessments of the experimental work conducted in this study.



Faculty of Engineering (IV)
Department of Mechanical and Industrial Engineering (MTP)

Date created 18.11.2020
Last Revision 03.09.2021

3 of 7

Activity: SEM and EDS

Risk overview: (mark with X the risk that applies for the activity)

Big loads		Danger of fire	
Heavy lifting		Working at heights	
Hanging load		Hydraulic pressure	
Gas pressure		Water pressure	
High temperature		Low temperature	
Parts at high velocity		Chemicals (fill up section 4.2)	
Sudden acceleration at fracture/failure		Pre-tensioned components	
Dangerous dust		Severe noise	
Danger of pinching		Rotating parts	

Detailed risk evaluation:

Risks	Preventive measures
1. No perceivable hazards in this activity	
2.	
3.	

Risk matrix after preventive measures of the activity:

Risk	Probability (P) (1-5)	Consequence (C)				Risk value (P x C)
		Health (1-5)	Material values (1-5)	Environment (1-5)	Reputation (1-5)	
1	1	1	1	1	1	1
2						
3						

Required safety equipment: (mark with X the risk that applies for the activity)

Safety goggles		Safety shoes	
Helmet		Gloves	X
Screen		Lifting equipment	
Ear protection		Hazard suit	
Harness ropes, other measures to prevent falling		Fume hood	

Appendix D

Risk assessments of the experimental work conducted in this study.



Faculty of Engineering (IV)
Department of Mechanical and Industrial Engineering (MTP)

Date created 18.11.2020
Last Revision 03.09.2021

4 of 7

Activity: Optical microscopy

Risk overview: (mark with X the risk that applies for the activity)

Big loads		Danger of fire	
Heavy lifting		Working at heights	
Hanging load		Hydraulic pressure	
Gas pressure		Water pressure	
High temperature		Low temperature	
Parts at high velocity		Chemicals (fill up section 4.2)	
Sudden acceleration at fracture/failure		Pre-tensioned components	
Dangerous dust		Severe noise	
Danger of pinching		Rotating parts	

Detailed risk evaluation:

Risks	Preventive measures
1. No perceivable hazards in this activity	
2.	
3.	

Risk matrix after preventive measures of the activity:

Risk	Probability (P) (1-5)	Consequence (C)				Risk value (P x C)
		Health (1-5)	Material values (1-5)	Environment (1-5)	Reputation (1-5)	
1	1	1	1	1	1	1
2						
3						

Required safety equipment: (mark with X the risk that applies for the activity)

Safety goggles		Safety shoes	
Helmet		Gloves	X
Screen		Lifting equipment	
Ear protection		Hazard suit	
Harness ropes, other measures to prevent falling		Fume hood	

Appendix D

Risk assessments of the experimental work conducted in this study.



Faculty of Engineering (IV)
Department of Mechanical and Industrial Engineering (MTP)

Date created 18.11.2020
Last Revision 03.09.2021

5 of 7

4.2. Chemical Risk Assessment:

Only for activities involving the use of chemicals (except ethanol and acetone for cleaning).

This page must be replicated for each different chemical activity performed in the lab.

Activity:	
Chemicals used:	
Mixture:	
Will the mixture be stored in the cabinet for several uses?	

Risk	Prevention Measure
1.	
2.	
3.	

Chemical disposal procedure:

Risk matrix after preventive measures of the chemical activity:

Risk	Probability (P) (1-5)	Consequence (C)				Risk value (P x C)
		Health (1-5)	Material values (1-5)	Environment (1-5)	Reputation (1-5)	
1						
2						
3						

Required safety equipment: (mark with X the risk that applies for the activity)

Safety goggles		Safety shoes	
Helmet		Gloves	
Screen		Lifting equipment	
Ear protection		Hazard suit	
Harness ropes, other measures to prevent falling		Fume hood	

Appendix D

Risk assessments of the experimental work conducted in this study.



Faculty of Engineering (IV)
Department of Mechanical and Industrial Engineering (MTP)

Date created Last Revision
18.11.2020 03.09.2021

6 of 7

5. Comments

Appendix D

Risk assessments of the experimental work conducted in this study.



Faculty of Engineering (IV)
Department of Mechanical and Industrial Engineering (MTP)

Date created 18.11.2020
Last Revision 03.09.2021

7 of 7

Risk matrix explanation

		Health	Material values	Reputation	Environment
Grade	1	Minor injury/strain that requires simple treatment. Reversible injury. Short recovery time.	Operational shutdown, or shutdown of activities <1 day.	Little effect on credibility and respect.	Negligible injury and short recovery time.
	2	Injury/strain that requires medical treatment. Reversible injury/strain. Short recovery time.	Operational shutdown, or shutdown of activities <1 week.	Negative effect on credibility and respect.	Minor injury and short recovery time.
	3	Serious injury/strain that requires medical treatment. Lengthy recovery time.	Operational shutdown, or shutdown of activities <1 month.	Reduced credibility and respect.	Minor injury and lengthy recovery time.
	4	Serious injury/strain that requires medical treatment. Possible disability /permanent disability.	Operational shutdown > 1/2 year. Shutdown of activities up to 1 year.	Credibility and respect considerably reduced.	Long-lasting injury. Lengthy recovery time.
	5	Death or disability / permanent disability.	Operational shutdown, or shutdown of activities >1 year.	Credibility and respect considerably and permanently reduced.	Very long-lasting and irreversible injury.

Consequence (C)	Very serious	5	10	15	20	25
	Serious	4	8	12	16	20
	Moderate	3	6	9	12	15
	Little	2	4	6	8	10
	Very little	1	2	3	4	5
		Very little	Little	Medium	Big	Very big
		Probability (P)				

Red	Unacceptable risk. Measures need to be implemented.
Yellow	Medium risk. Measures need to be considered.
Green	Acceptable risk. Measures can be considered.

